**Proceedings of:**

# *Machines and Processes for Micro-scale and Meso-scale Fabrication, Metrology and Assembly*

## *2003 Winter Topical Meeting*

*January 22-23, 2003*

*J. Wayne Reitz Union, University of Florida*
*Gainesville, Florida*

*The American Society for Precision Engineering (ASPE) is a multidisciplinary professional and technical society concerned with research and development, design, manufacture and measurement of high accuracy components and systems. ASPE activities encompass relevant aspects of mechanical, electronic, optical and production engineering, physics, chemistry, and computer and materials science. Membership is open to anyone interested in any aspect of precision engineering.*

*Founded in 1986, ASPE provides a new focus for a diverse but important community. Other professional organizations have covered aspects of precision engineering, always as a sideline to their principal goals. ASPE is based on the core of generic concepts necessary to achieve precision in any application; independent of discipline, ASPE intends to be the focus for precision technology -- and to represent all facets from research to application.*

*ASPE -- The American Society for Precision Engineering*
*301 Glenwood Avenue, Suite 205, Raleigh, NC 27603*
*P.O. Box 10826, Raleigh, NC 27605*
*Telephone: (919) 839-8444 Fax (919) 839-8039*
*Web site: http://www.aspe.net*

# *Preface*

*This book comprises the proceedings of the 2003 Winter Topical Meeting. The contributions reflect the authors' opinions and are published as presented to ASPE, without change. Their inclusion in this publication does not necessarily constitute endorsement by the ASPE, or its editorial staff.*

*Individual readers of this book and nonprofit libraries acting for them are permitted to make fair use of the material contained in this book to be used in teaching or research; provided they copy said paper in total, as written by the author. Permission is granted to quote excerpts from the scientific or technical works in this book with proper acknowledgment of the source to include: The author's name, the book name, and the ASPE tag line. Reproduction of figures and tables is likewise permitted from the contents of this book, provided that the same acknowledgment of the same source and content is permitted.*

*Any other type reproduction, systematic copying or multiple reproduction of any material in this book is expressly prohibited except with the written permission of the ASPE editorial staff, addressed to the Society's headquarters.*

*ISBN 1-887706-30-5*

*2003*

*American Society for Precision Engineering*
*301 Glenwood Avenue, Suite 205*
*Raleigh, NC 27603*

*Printed in the United States of America*

# 2003 Winter Topical Meeting
## Contents


Preface ..... ii

Contents ..... iii

Foreword ..... v

**Keynote Presentation**

***Dr. Jan van Eijk**, Brouwer, D. and Franse, J.*
*Phillips CFT*
*Eindhoven, Netherlands*
***Challenges in Applying Minature Devices in a Number of Domains; Component Fabrication, Metrology, and Assembly Aspects*** ..... 1

***Session I***
**Material Removal Processes**
*Wednesday, January 22, 2002, 8:30AM – 10:00AM*

1. ***Cut it out. Shaping the Micrometer (Invited paper)*** ..... 8
   *Schaller, T., Pflegling, W., and Hlavac, M (Industrial Forum for Microfabrication Technologies (FIF) Karlsruhe Research Center)*
2. ***Mesoscale and Microscale Manufacturing Processes: Challenges for Materials, Fabrication, and Metrology*** ..... 14
   *Dow, T., and Scattergood, R. (North Carolina State University)*
3. ***Introducing Meso-scale Channels on Ceramics by Machining*** ..... 20
   *Shin, H.W., Kok, C.K., Case, E. and Kwon, P. (Michigan State University)*
4. ***Straightness and Roughness Analysis of Micro-Shaft Machined with Wire Electrode Discharge Grinding*** ..... 26
   *Morgan, C.J., Shreve, S., and Vallance, R. (University of Kentucky)*

***Session II***
**Forming, Molding, & Additive Processes**
*Wednesday, January 22, 2002, 10:30AM – 12:00PM*

1. ***Mastering and Replication of Precision Micro-Structured Surfaces (Invited paper)*** ..... 32
   *Morris, G.M. (Corning Rochester Photonics)*
2. ***Growing Up, Additive Processes in MEMS Fabrication and Packaging (Invited paper)*** ..... 36
   *Goetzen, R. ( microTEC mbh)*
3. ***Material Behavior in Microforming at Elevated Temperatures*** ..... 37
   *Egerer, E. and Engel, U. (University of Erlangen-Nuremberg)*
4. ***The Reliability of Dynamic Interfaces in LIGA Microsystems*** ..... 43
   *Prasad, S., Christenson, T., Dugger, J., Michael, J., and Vanacek, C. (Sandia National Laboratory)*

***Session III***
**Probe Based Metrology**
*Wednesday, January 22, 2002, 1:30PM – 3:00PM*

1. ***Small Volume Metrology (Invited paper)*** ..... 48
   *Smith, S., and Seugling, R. (University of North Carolina at Charlotte)*
2. ***Measuring in Three Dimensions at the Mesoscopic Scale*** ..... 53
   *Peggs, G., Lewis, A., and Leach, R. (National Physical Laboratory)*
3. ***Uncertainty in Measurements of Micro-patterned Thin Film Thickness Using Nanometrological AFM*** ..... 58
   *Misumi, I., Gonda, S., et. al. (National Institute of Advanced Industrial Science and Technology)*
4. ***Probe Force Calibration Experiments Using the NIST Electrostatic Force Balance*** ..... 64
   *Pratt, J., Newell, D. et.al. (National Institute of Standards and Technology)*

*Session IV*

***Machines, Sensors, & Actuators***

*Wednesday, January 22, 2002, 3:30PM – 5:00PM*

1. ***Meso-Scale Metrology Tools:***
   ***A Survey of Relevant Tools and a Discussion of Their Strengths and Weaknesses*** ..... *70*
   *Hibbard, R., and Bono, M. (Lawrence Livermore National Laboratory)*
2. ***Micromachined Interferometer for MEMS Metrology*** ..... *73*
   *Kim, B., Razavi, A., Degertekin, L., and Kurfess, T. (Georgia Institute of Technology)*
3. ***Design and Fabrication of the Meso-Mill:***
   ***A Five-axis Milling Machine for Meso-scaled Parts*** ..... *79*
   *Werkmeister, J., and Slocum, A. (Massachusetts Institute of Technology)*
4. ***Advances in Fast Nano-Precision Motion Technologies: Practical Parallel Kinematics*** ..... *83*
   *Jordan, S. (Polytec PI, Inc.)*

*Session V*

***Optical Metrology***

*Thursday, January 23, 2002, 8:30AM – 10:00AM*

1. ***Optical Metrology (Invited paper)*** ..... *87*
   *Roth, J., Felkel, E., and DeGroot, P. (Zygo Corporation)*
2. ***Analysis of Microstructures with Confocal Laser Scanning Microscopy*** ..... *93*
   *Uhlmann, E., and Oberschmidt, D. (Technical University of Berlin)*
3. ***Silicon Wafer Thickness Variation Using Infrared Interferometry*** ..... *98*
   *Schmitz, T., Davies, A., and Evans, C. (University of Florida)*
4. ***Dynamic MEMS Measurement Using a Strobed Interferometric System***
   ***with Combined Coherence Sensing and Phase Information*** ..... *104*
   *Novak, E., Wan, D., Unruh, P., and Schmit, J. (Veeco Instruments, Inc.)*

*Session VI*

***Assembly***

*Thursday, January 23, 2002, 10:30AM – 12:00PM*

1. ***Micro/meso Robotic Assembly (Invited paper)*** ..... *108*
   *Stephanou, H. (Rennselaer Polytechnic Institute)*
2. ***PZN Based Nanopositioning Systems*** ..... *113*
   *Woody, S. (University of North Carolina at Charlotte)*
3. ***Hybrid Micro-Assembly System for Tele-Operated and Automated Micro-Manipulation*** ..... *119*
   *Zaeh, M., Jacob, D., Ehrenstrasser, M., and Schilp, J. (Technische Unversitaet München)*
4. ***Production of Direct Drive Cylindrical Targets for***
   ***Inertial Confinement Fusion Experiments*** ..... *125*
   *Elliot, N., Day, R., et.al. (Los Alamos National Laboratory)*

*Session VII*

***Applications***

*Thursday, January 23, 2002, 1:30PM – 3:00PM*

1. ***Non–destructive Characterization Technologies for***
   ***Metrology of Micro/mesoscale Devices (Invited paper)*** ..... *131*
   *Martz, H., and Albrecht, G. (Lawrence Livermore National Laboratory)*
2. ***Laser Contouring Method for Wall Thickness***
   ***Metrology in OMEGA Shock Breakout Targets*** ..... *142*
   *Sebring, R., Bartos, J., et.al. (Los Alamos National Laboratory)*
3. ***Manufacturing of Micro-asperities on Thrust Surfaces Using UV Photolithography*** ..... *148*
   *Kortikar, S., Stephens, N., et.al. (University of Kentucky)*
4. ***Aluminide Microchannel Arrays for High-temperature***
   ***Microreactors and Microscale Heat Exchangers*** ..... *154*
   *Paul, B., and Kanlayasiri, K. (Oregon State University)*

# *Foreword*

*The continuing trend toward miniaturization of manufactured systems has heightened the need for increasingly small mechanical components and assemblies. Numerous applications of such systems currently exist in fields ranging from aerospace to biotechnology. Many projected applications require new materials and more complex, three-dimensional geometries and motions than can be produced using conventional planar, lithography-based, surface micro-machining techniques. For this reason, researchers are exploring the issues involved in fabrication, metrology, and assembly of components with important length scales ranging from fractions of a micrometer to a few millimeters. This two day conference will focus on new developments in micro-scale and meso-scale manufacturing processes, equipment, and applications.*

*The objective of this meeting is to bring together researchers and practitioners from industry, government and academia to provide a forum for the exchange of ideas. In addition to paper and poster presentations, we will have a panel discussion on current industry needs and the perceived relationship between those needs and current research.*


***2003 Winter Topical Meeting Committee***

*John C. Ziegert, Chair, University of Florida*

*Keith Carlisle, Lawrence Livermore National Laboratory*
*Steven C. Fawcett, Axsun Technologies, Inc.*
*Bernard Jokiel, Sandia National Laboratory*
*Don A. Lucca, Oklahoma State University*
*Eric R. Marsh, The Pennsylvania State University*
*Newman M. Marsilius, Moore Tool Company*
*Tony L. Schmitz, University of Florida*
*Alexander H. Slocum, MIT*
*E. Clayton Teague, NIST*
*Daniel C. Thompson, Production Technologies*
*R. Ryan Vallance, University of Kentucky*

# A Systems Approach towards Business Creation

Jan van Eijk [1,2], Dannis M. Brouwer [1], Jelm Franse [1]
(1) Philips Center for Industrial Technolgy (CFT), Eindhoven, The Netherlands
(2) Technical University Delft, Advanced Mechatronics, Delft, The Netherlands

## Introduction

MEMS are becoming a large market with revenues in 2001 being $3.9B. The MEMS market represents 2.5% of the total semiconductor market. In spite of the downturn of the semiconductor market by 12.9 % from 2000 to 2002 the MEMS market has increased in the same time span by 13.2 %. The largest end markets in 2001 in terms of revenues are Automotive 31%, IT peripherals and (Bio) medical. The MEMS projection is a growth of 20% annually of which actuator are becoming increasingly important. Between 2002 and 2004 commercialization of several MEMS devices are expected: gas sensors, valves, nozzles, photonics & displays, biosensors, RF & wireless, rate sensors, micro relays. For commercialization the focus should be on customer benefits rather than (impressive) scientific features.
The opportunities are clear. What contribution can the Precision Engineering community deliver and how can we create superior value. In this presentation some ideas from the Philips Electronics company will be presented.

## System engineering

The emergence of new applications strongly depends upon a collaborative engineering approach. When large numbers, targeted for consumers, are concerned this starts with strong market knowledge. In combination with mechanical and electrical technology system designs can be developed. As the precision engineer is trained in multi-discipline, or Mechatronic, approach they may form a catalyst in this process. They may form the link between market and manufacturing technologists.

## Parts Manufacturing

The enthusiasm for micro-parts started from technologies in semiconductor manufacturing. Since 25 years engineers have worked on manufacturing of mechanical structures in silicon. Research driven from material science and processing technologies. In these fields established companies, like Sandia Lab spin-off MEMX, are now occurring. Although we feel that the capabilities in parts manufacturing have reached a high level, Precision Engineering can contribute in this field. Different aspects of accuracy and yield in manufacturing may be improved. When a wafer must be processed on two sides the alignment of different layers must be secured. In specially developed lithography tools solutions for such issues are implemented.

Thin film processing for MEMS is in many aspects different compared to mainstream silicon semiconductor technology. Requirements such as double sided processing, thick-resist processing and imaging, large device manufacturing and high topologies are becoming standard in MEMS manufacturing. ASML Special Applications has developed an options package fulfilling these demands. By measuring markers on the backside of double sided wafers (Figure 1) alignment from front-to-back is better than 500 nm (+/-3sigma) resulting in less yield losses. It also allows for thick layer processing without the need for re-alignment schemes. Stitching enables production of large size

devices with high resolution, while still using the relatively small fields of the reduction stepper. Boundary field stitching errors of as low as 150 nm can easily be achieved with this option. 3D Metrology (Figure 2) enables alignment on a plane other than the focusing plane. This capability is especially useful when processing structures with deep trenches or high topologies, while maintaining minimal overlay.

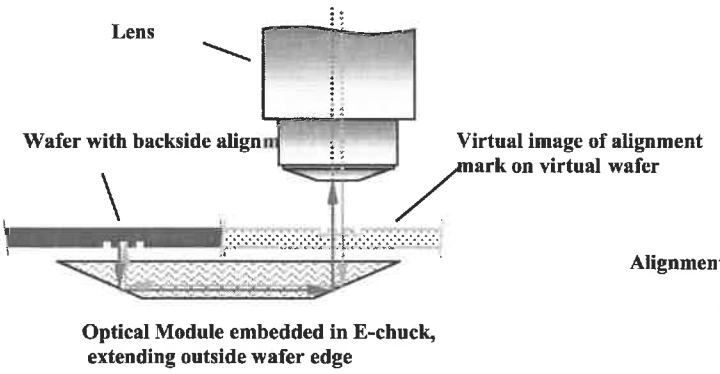
Lens
Wafer with backside alignm
Virtual image of alignment mark on virtual wafer
Optical Module embedded in E-chuck, extending outside wafer edge

**Figure 1:** 3DAlign functionality

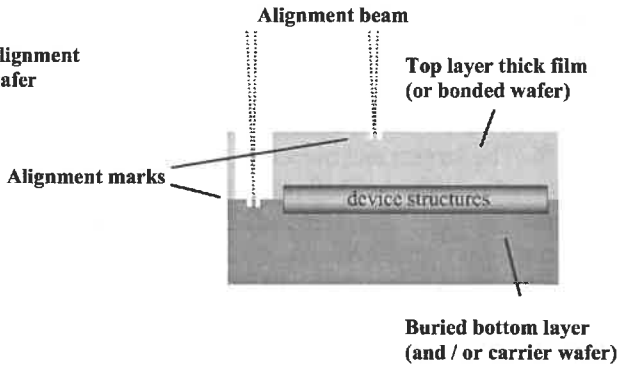
Alignment beam
Top layer thick film (or bonded wafer)
Alignment marks
device structures
Buried bottom layer (and / or carrier wafer)

**Figure 2:** 3DMetrology functionality for a bonded wafer

## Assembly of Hybrid Products

In most cases one attempts to produce complete systems on one wafer. Combining mechanical parts with electronic functionality is desirable. The compatibility of processes however is often complicating this. Combining CMOS and MEMS technology on one die for example is challenging. Sometimes a 3D-structure is obtained through assembly of micro-parts. In both cases a low cost solution for mass scale assembly is needed.

Micro assembly by traditional picking and placing is costly. Measuring, bonding and gripping / releasing are specific competences which need dedicated solutions. To ease measuring it helps to create references at process accuracy (grinding or litho/etching). Although sub-micron accuracy can be achieved by manipulation, bonding can distort the alignment by several microns. Design for bonding is a must, or after bonding adjustments have to be made, by laser adjustment for example.

**Accuracy derived from a process**

Laser adjustment is a proven sub-micron accuracy adjustment. For example a video head consisted of two magnetic sensors, which had to be aligned with respect to each other. The alignment was especially difficult as the head had to spin at 150 revolutions per second in order to measure the right positions, as the gyroscopic effect of turning stabilizes the head. With vision the height difference between the sensors was determined. Short shutter times to prevent blurring required flashing at high intensity. Two laser pulses are aimed at a micro adjustment bending mechanism during spinning. The actuated sensor bends up. The height difference between the two sensors is made smaller. Several pulses are required to reach the accuracy of sensor alignment of 0.5 μm. Other applications are alignment of reed contacts and Optical Pick-Up (OPU) units.

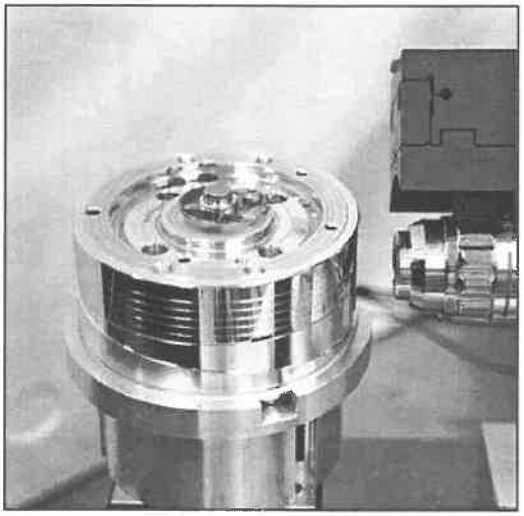

**Figure 3**: Laser adjustment on spinning video head by vision metrology

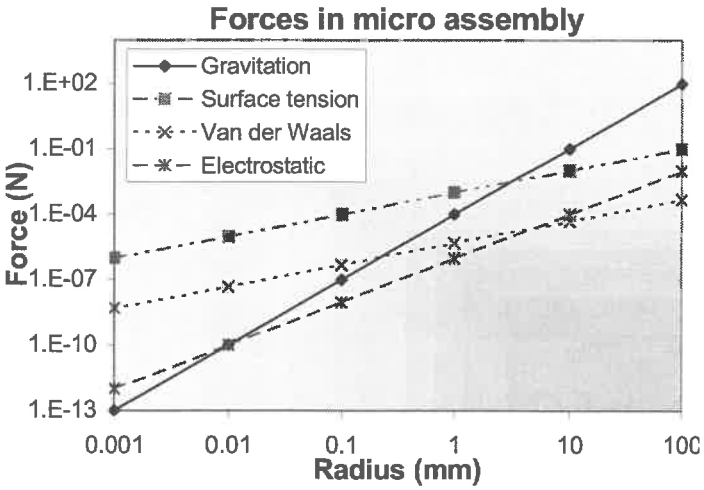


**Figure 4**: Micro forces dominate in the micro world

## Physical aspects in the micro world

In handling particles with dimensions in the order microns some differences with handling objects in the macro world have to be considered. One major difference is the forces acting on the particle. Forces normally negligible with regard to the gravitation become significant. Surface tension effects arise from interactions of layers of absorbed moisture on two surfaces. When the surfaces are close enough liquid bridges can be formed. The Van der Waals force is a force acting between atoms. It is also called atomic force caused by orientation effect, excitation effect and dispersion effect. Electrostatic forces are based on the capacitive interaction associated with a contact potential. This potential is due to the difference between the work functions of two bodies and even exists in the absence of applied voltage.

Figure 4 shows the primary forces acting on a silicon sphere as a function of the radius [1]. As the gravitation force decreases proportionally with the radius to the third power, it decreases faster than micro forces: Surface Tension, Van der Waals and Electrostatic.

### Gripping

Error diagnostics in IC production requires handling of 20 x 10 x 2 μm samples (Figure 4). The sample can be grabbed and lift out by a gripper. The sample is milled out by a focussed ion beam (FIB) at sub micron precision. Preferably a Scanning Electron Microscope (SEM) is used for process feedback and hence a combined machine like the FEI dual-beam machine is used. The small sample size requires both delicate and small gripper fingers. The gripper is to be shielded from both ion and electron beam, to prevent deviation of the beams. The grippers operation should also be unaffected by the presence of the beam and the sample should be visible during FIB milling.

A consortium of MESA+, FEI and Philips CFT, built an electrostatic driven MEMS gripper (Figure 5) for lift-out of a sample. Figure 6 shows the angled grabbing of the sample by the MEMS gripper. Details on the gripper will be released shortly.

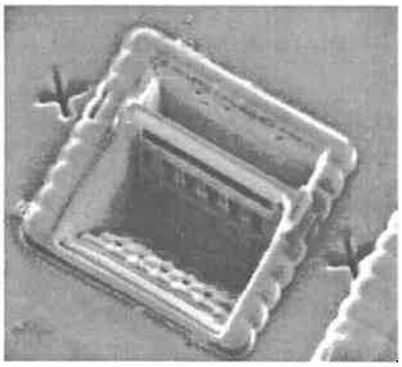

**Figure 4:** FIB milled out sample 20 x 10 x 2 μm

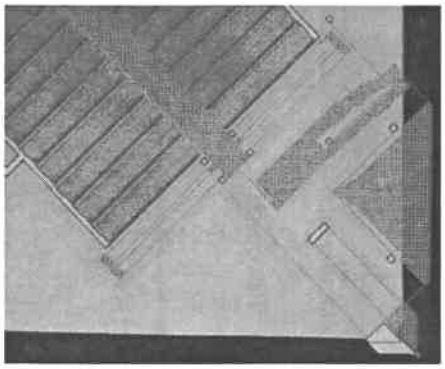

**Figure 5:** Electrostatic comb driven MEMS gripper

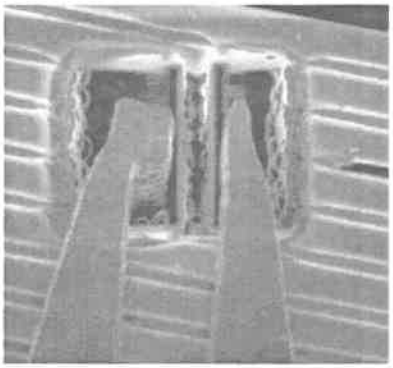

**Figure 6:** Grabbing the sample

Another development was a gripper made by precision grinding, driven piezo electrically. This gripper compared to the MEMS gripper proved to be tougher (material), larger force generating (piezo), though sufficiently small enough, but very labor costly.

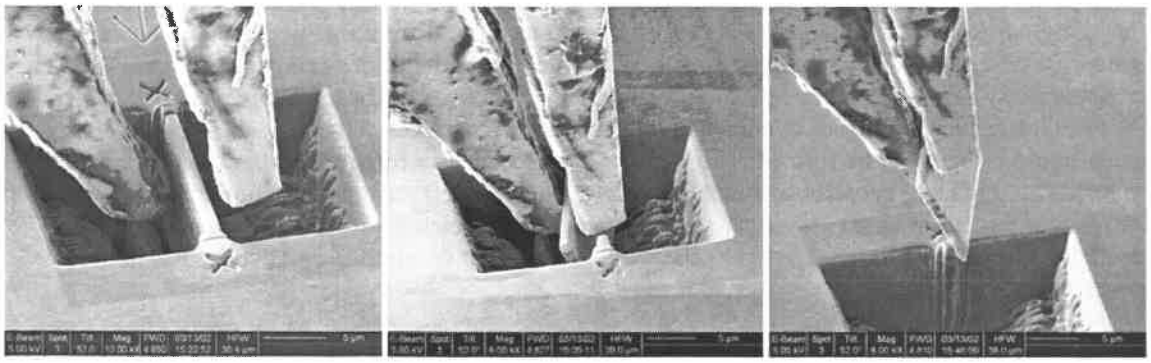

**Figure 7:** Successful lift out of sample by 'conventionally' made gripper

**Contactless transfer**

Gripping can sometimes also be overcome, for example by contactless transfer. For components of dimensions smaller than 250 μm the conventional pick-and-place technology is not applicable anymore. Electrostatic forces dominate gravitation force. Therefore contactless laser transfer technology is being investigated which enables the assembly of large numbers of micro components at high production speed . The laser pulses at a transfer foil at which the die is adhesively bonded. The foil bursts and the die is shot perpendicular to the foil, if shot at the center. Components of 1 to 100 μm will be placed at an accuracy of around 3-4 μm.

On a lab scale the most beautiful MEMS structures are created. Reproducing these in large volumes is a huge challenge. Good examples are the development of methods to produce opto-electronic devices. Although the present market indicates that the hype in this field is over companies that achieve breakthroughs in precision assembly of opto-electronic systems have serious business opportunities.

In many cases low-cost assembly can only be obtained when batch processes are used. Combinations of thousands of electronic systems, diodes and amplifiers, with the same number of optical elements

must be made and wafer scale bonded. The separation and wire bonding is done after the joining step. Thus huge cost differences may be obtained. This becomes clear when mass assembly of electromagnetic bearings for diskdrives is considered [2]. At EPFL in Lausanne functioning systems were developed, now the economic assembly of the products forms an interesting challenge.

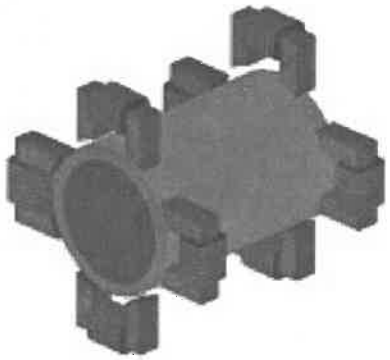

**Figure 8:** Principle of micro magnetic bearing of a shaft

## Packaging and interconnecting MEMS

When fully functional systems have been assembled a stable and protective packaging solution must be found. Securing the proper position during this step and avoiding thermal or mechanical stresses form a challenge.

As the wafer diameter is projected to increases to 400 mm in 2012, the thickness is projected to increase to 850 μm because of dynamical and fabrication technical reasons. The die thickness, on the contrary, decreases rapidly to 50 μm, as constraints on size are ever increasing. Wafers need to be thinned increasingly!
The space usage of IC is downscaling especially for portable devices. Smart-Cards require ultra thin IC's. The size of IC's is no longer determined by the feature size of the silicon technology, but by the amount of silicon needed to accommodate the bond pads. The bond pad pitch for wire bonding is in the process of shrinking from 100 μm to 80 μm and further down to 40 μm. Flip chip technology has specific advantages being more compact and having better EMC performance, but still cannot follow the drive towards smaller bond pad pitch. The present flip chip technology doesn't allow pad pitches below 200-150 μm.

As part of a European Project "Cirrius" the flip chip pitch was brought down to 40 μm [3]. This implied the development of adequate bumping technology, development of substrates of sufficient quality and fine flip chip interconnects. The ultra thin IC package developed uses an ultra thin Ball Grid Array (BGA), has 168 IOs and measures 9x9 mm. An IC of 5x5 mm has been used with a bondpad pitch of 100 μm. The package has a standardized board interface with ball pitch of 0.5 mm. The ultimate height reduction has been achieved through the use of a thinned die (150 μm) with low flip chip bumps (20μm) in combination with anisotropic conductive adhesives. The resulting height after solder reflow on the motherboard is less than 300 μm.

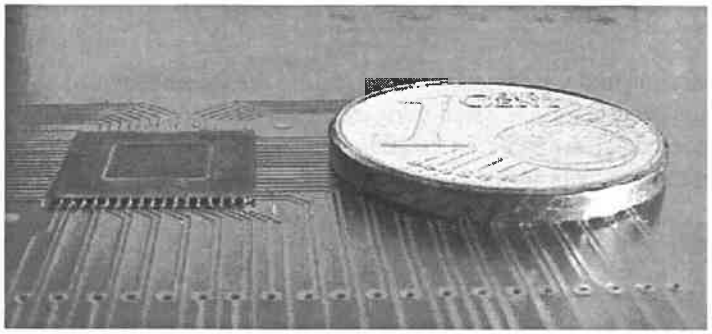

**Figure 9:** Ultra thin flip chip and a 1 cent Euro coin

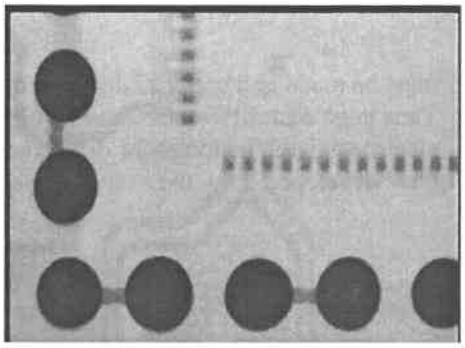

**Figure 10:** X-ray picture showing first and second level interconnect

At a larger scale 3D interconnect technology enables to increase the number of features in a certain volume. Figure 11 shows a 3D interconnect with a pitch of 100 μm, a conductor line thickness of 10 μm and the edge radius of 100 μm.

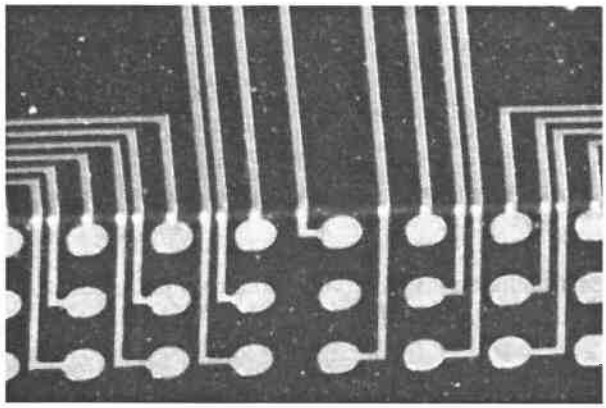

**Figure 11:** By 3D interconnect the envelope accommodating the bondpads is decreased

## Metrology

In metrology there is an increasing demand for either functional measurement or vision feedback. Functional measurement is application dependant and can be seen in fibre coupling, or DVD optical path alignment. Vision is used for inspection (off-line) or outer loop calibration of robotics. As the processor speed increases, vision image interpretation will speed up, and higher bandwidths of robotics are attained. Vision is also successfully implemented at accurately measuring fast processes, droplet formation and ejection from, a print head for example.
In flight droplet analysis, developed by Philips Research and CFT, can in principle measure, droplet volume (20 pL), small angular deviations of jetted droplets (10 mRad) and the droplet speed (3-8 m/s). A large magnification and a short illumination time obtain the required volumetric accuracy. A short 400ns short illumination burst by a LumiLED prevents excessive smearing, while the camera can be kept relatively simple. Electronically the time to transfer a image limits the number of frames per second. Blob or threshold analysis is used to interpret a frame and convert it into a volume. The accuracy of the test system was determined to be better than 0.25 pL. The droplet travels through the field of view (from top to bottom) in 0.15ms.

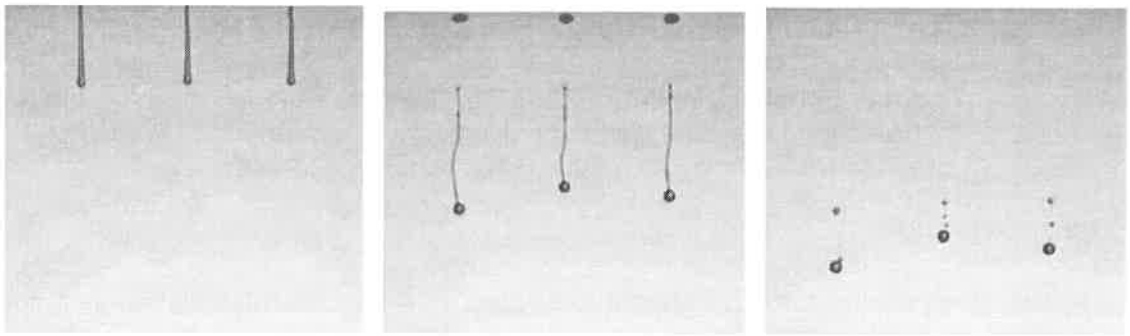

**Figure 12:** Droplet formation

## Conclusion

Developing business based upon new MEMS-applications has appealing opportunities. Full-scale players will combine market knowledge with integral system engineering competences. Many contributions from the Precision Engineering community can be made to enable robust, mass manufacturing solutions for assembly and packaging

## Acknowledgments

G. Krijnen, Mesa+ Research Institute, University of Twente, the Netherlands
Sebastian von Harrach, FEI
Hans Krikhaar, ASML
Frits Dijksman, Philips Research
Rine Dona, Willem Hoving, Marc Meuwese, Edjoe Osinski, Rene Sanders, Marc de Samber, Herman Soemers, Co van Veen, Thijs Wijnakker, Willem Jan de Wijs,
Philips Center for Industrial Technology

## References

[1] H. Van Brussel, J. Peirs, D. Reynaerts, A. Delchambre, G. Reinhart, N. Roth, M. Weck, E. Zussman, Assembly of Microsystems, Keynote paper, Annals of the CIRP Vol.49/2/2000, p451-471
[2] A. Boletis, R. Vuillemin, C. Aymon, M. Kümmerle, B. Aeschlimann, R. Moser, H. Bleuler, A six magnetic Actuator Integrated Micromotor, Proceedings of the 7th International Symposium of Magnetic Bearings, August 2000, Zürich
[3] Co van Veen, Esther Janssen, Barbara Pahl, Juergen Guenther,"Cirrus: Fine pitch flip chip interconnect, European Microelectronics Packaging and Interconnection Symposium, Cracow, Poland 16-18 June 2002, p207-212

# CUT IT OUT. SHAPING THE MICROMETER

**Thomas Schaller[1], Wilhelm Pfleging[1], Marcus Hlavac[2]**
[1] Forschungszentrum Karlsruhe, Karlsruhe, Germany
[2] Braunschweig Tech. University, Braunschweig, Germany

## ABSTRACT

This contribution gives an overview of material removing, maskless microfabrication techniques such as microcutting (drilling, turning, grinding, milling, slotting), electro-discharge machining (EDM), laser machining (drilling, cutting, ablation) and focused ion beam machining. Feasibility and commercial relevance of the techniques – including combining manufacturing technologies – will be shown by examples of microstructures and applications.

## INTRODUCTION

Using a tool for shaping bulk material is nothing new, but one of the oldest arts of manufacture. An artist sees his sculpture in a block of marble or wood while he is cutting it out with a chisel or a drawknife. Splinters or chips are covering the floor, and finally a masterpiece is finished.

Nowadays, nothing has changed in principle, only techniques have changed a little: The workpiece can be seen virtually as a CAD model, and the structure is cut out of a block by modern CNC machining centers and laser systems. It is production rather than art, but knowledge and experience still are the key to excellent results, particularly in microcutting of hard-to-see structures, using a variety of tools. Shaping the micrometer means to touch the limits of technical feasibility, and sometimes there seems to be no difference between micro-structures and artwork.

Due to the wide range of available techniques, tools, machines, materials, structure geometries, process variants, and individual adaptations, the overview of techniques cannot be complete. Although they may be material removal processes, some techniques are missing, e.g. electro-chemical machining, lithography (developing irradiated structures), and etching techniques; our exclusion criterion is the absence of a "tool" for cutting, even in a broad sense. It could be worth the effort to compare several microfabrication techniques with respect to workpiece materials, structure dimensions and accuracy, industrial relevance, and others.

## TOOLS & TECHNIQUES

The use of tools for material removal is not restricted to "real" cutting tools, such as end-mills, profiled cutters or grinding wheels. We also consider a laser or ion beam a cutting tool, as well as sparks for electro-discharge machining. Due to the different nature of the tools, applicability of the methods covers a wide range of workpiece materials, material removal rates, surface finishes, structure geometries, structure detail dimensions and aspect ratios, and more. To be counted as a microfabrication technique here, the only precondition is that the tools and structures are in sub-millimeter range, typically some tens or hundreds of micrometers.

Each microfabrication technique has its own advantages and disadvantages. In order to achieve best results for a specific microstructuring problem, you have to pick the most suitable and economical technique or, if needed, to combine several techniques. None of the techniques is "good" or "bad", but you can make a good or a bad choice. *Table 1* is listing some characteris-

*Table 1: Characteristics of material removing microfabrication techniques*

| ***Technique*** | **Cutting**<br>D: drilling<br>T: turning<br>F: flycutting<br>M: milling<br>(slotting[a]) | **Grinding** | **Electro-Discharge Machining (EDM)** | **Laser Machining**<br>drilling<br>cutting<br>ablation | **Focused Ion Beam Machining (FIB)** |
|---|---|---|---|---|---|
| ***Machining principle*** | mechanical ablation (defined cutting edge) | mechanical ablation (undefined cutting edges) | plasma ablation by electric sparks | thermal / chemical ablation | ion sputtering |
| ***Tool type*** | drills (D)<br>profiled tools (T,F)<br>end-mills (M) | grinding wheels and pins | wires or shaped electrodes | pulsed or continuous wave laser radiation | ion beam |
| ***Tool material*** | tool steel (D,T)<br>tungsten carbide (D,T,F,M)<br>diamond (T,F,M) | abrasive coatings/grains (CVD diamond, CBN, ...) | copper, tungsten, and alloys | photons | ions |
| ***Min. tool size*** | 30...50 µm (D)<br>< 50...100 µm (T,F)<br>< 50...100 µm (M) | > 15 µm (wheels)<br>> 60 µm (pins) | < 50 µm | < 5 µm (focus diameter) | < 1 µm (focus diameter) |
| ***Workpiece material*** | ductile materials: polymers, copper & aluminum alloys, graphite, green ceramics, steel | brittle or hard materials: glass, ceramics, silicon, tungsten carbide, steel | conductive materials: metals, (ceramics) | polymers, metals, steel, ceramics, glass, (almost any material) | PMMA, brass, aluminum, steel, tungsten carbide, ... |
| ***Removal rate / Machining time for typical applications*** | medium...low / hours...days | fast...medium / minutes...hours | medium / hours | fast...low / seconds... hours | low / minutes... hours |
| ***Min. structure details*** | > 5 µm (sub-µm for SPDT[b]) limited by tool geometry | > 10 µm limited by tool geometry | > 10 µm limited by tool geometry | < 5 µm limited by beam diameter and shape | < 5 µm limited by beam diameter and shape |
| ***Max. aspect ratio*** | typically 10 | > 10 | > 100 | < 50 | ≈ 2 |
| ***Accuracy*** | 1...3 µm (sub-µm for SPDT[b]) | < 5 µm | 1...3 µm | 1...5 µm | < 1 µm |
| ***Surface finish ($R_a$)*** | < 0.1 µm (≈10 nm for SPDT[b]) | < 0.2 µm | < 0.1 µm | < 0.2 µm | < 0.1 µm (estimated) |
| ***Microstructure application examples*** | prototyping and molds for fluidics, sensors, and actuators (optical surfaces for SPDT[b]) | prototyping, wear-resistant molds | prototyping, punching tools, molds | prototyping, molds, vias, gratings, etching, membranes | mask repair, diagnostic tools, direct ablation, micro cutting tools |
| ***Academic / commercial use*** | academic / commercial | academic | commercial | academic / commercial | academic / commercial |

*Notes:*

a Microslotting is a new, kind of "exotic" technique under development. By steering the cutting edge of profiled tools to the actual cutting direction, the relative robustness of profiled tools is combined with the versatility of milling and the ability of cutting arbitrary structures. Features are trenches less than 20 µm wide, cutting of steel using diamond tools, and machinable structure details, such as sharp inner edges.

b Single-point diamond turning (SPDT) is an ultra-precision cutting technique for optical surfaces and of nanometer accuracy, but limited geometric variability. Workpiece material limitations (usually no ferrous materials when using diamond tools) and structure limitations (rotational symmetry, large radius of diamond tool) can be reduced by using ultrasonic tool excitation and a fast-tool servo, respectively.

tics of micro "cutting" techniques. It should not be understood to be a ranking of competing techniques, but a representation of the state of the art.

All techniques (except for FIB) are well-established in the "macro" world, and for specific products considerable knowledge exists in industry, pushing production processes with high yields at simultaneously small tolerances. An obvious example is producing thousands of square meters of microstructured reflector foils by the 3M company (and others) using an elaborate diamond flycutting process and microreplication technologies. Other techniques are adapted and perfected by specialized companies according to the needs of a market for microstructured devices, such as microcutting (e.g. by KERN [1]), EDM (e.g. by CHRISTMANN [2] or ROLLA Micro-Synthetics AG [3]), and laser machining (e.g. by LPKF Laser & Electronics AG [4], BARTELS [5] or EUROFLEX SCHUESSLER [6]). Further progress is made by academic institutions (e.g. IMF-1 Karlsruhe [7], IWF Braunschweig [8], and many others all over the world) developing new techniques [9] and providing understanding of machining principles, such as cutting steel using diamond tools, grinding of microstructures, improving accuracy in laser ablation, or fabrication of cutting tools by FIB machining.

Many micromachining problems require more than one technique, not to forget the measurement equipment. A combination of techniques in a process chain can be established by cooperation and mutual support of industrial and academic partners. The growing networks of excellence, e.g. to be promoted within the Sixth Framework Program of the European Union, is an obvious sign of the need for collaboration. In Germany, an industrial forum (FIF) has been established at the Forschungszentrum Karlsruhe to close the gap between research and industry: The forum is open to companies, provides networking in the microfabrication scene, and renders consultancy and technical support for specific microfabrication problems [10,11].

## EXAMPLES

The following examples of structures and microfabrication techniques cover directly fabricated parts and mold making for mass replication of microstructures and components. No matter if you want to have machined just one prototype or if you want to start a mass production: It's always a good choice to cut it out.

### *Milling*

Figure 1 shows three micromilled turbine wheels for micro fluid pumps, machined into ceramic and vespel®. Sample diameters are 7/4/2 mm. In 5-axes machining, a circumference tolerance of 2 µm is achieved. These parts are commercially produced, which demonstrates that even tough material and dimension specifications can be met in a production environment.

*Fig. 1: Micromilled parts*
*Source: KERN Micro- und Feinwerktechnik GmbH, Murnau-Westried, Germany*

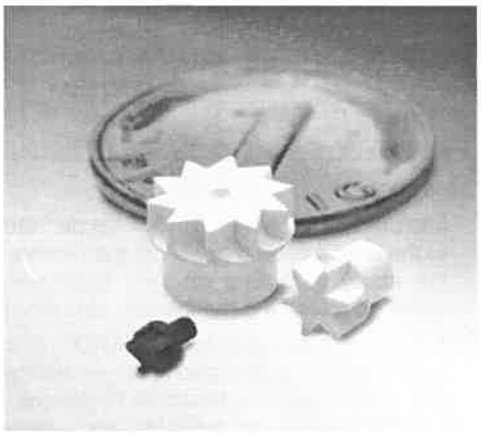

But there are many combinations of structure size, material choice, and surface quality that require further investigations on tools, materials and processes [12], e.g. cutting of steel or burr removal. And there is still a gap to be closed between high-precision machining in the micrometer range and ultra-precision cutting of optical surfaces with nanometer accuracy.

### *Grinding*

Figure 2 shows a test structure ground into hardened steel (X 155 CrVMo 1 2 1). The tool used is a CBN micro grinding wheel B15 (hard resin bond), cutting width 100 µm [13]. Grinding wheels are available with various grain materials and bonds. They can be used for machining of microstructures with high aspect ratios. The smallest cutting width is 15 µm.

Arbitrary structures can be machined by using grinding pins which are available in various shapes. Best surface qualities are achieved with CVD coatings due to their small grain size. The smallest pin diameter is 60 µm.

A characteristic effect of grinding brittle materials is the appearance of chipping, which is a factor limiting the the size of structure details (cf. burrs in milling): By applying optimum cutting parameters, chipping can be reduced to 1 µm and less.

### *EDM*

Figure 3 shows two parts of a micro gear pump, and a dandelion pollen for comparison. The parts are cut out of tungsten carbide by wire-EDM. The wire diameter is 100 µm, structure tolerance is ± 1 µm, and the roughness of the machined surface is < 0.1 µm.

In the fabrication of EDM parts, micrometer accuracy can be achieved using commercial EDM machines. For complex geometries, plunge-EDM can be applied which requires electrodes with the inverse structure. The electrodes can be machined by any microfabrication technique: EDM, milling, laser machining or others. For some types of microstructures, even elaborate LIGA microstructures may be suitable for use in a production environment [14].

### *Laser Machining (and Combination with Other Microfabrication Techniques)*

It is impossible to give an impression of the variability of laser drilling, cutting, and ablation in just one paragraph. There is hardly any material, geometry or microfabrication task that could not be done with laser machining [15]. Another benefit of the broad application range is the easy combination with other microfabrication techniques. Figure 4 shows a bioreactor (left) for growth of three-dimensional cell cultures in tissue engineering [16,17]. The process chain of fabrication

*Fig. 2: Ground microstructure*
*Source: IWF, Tech. University, Braunschweig, Germany*

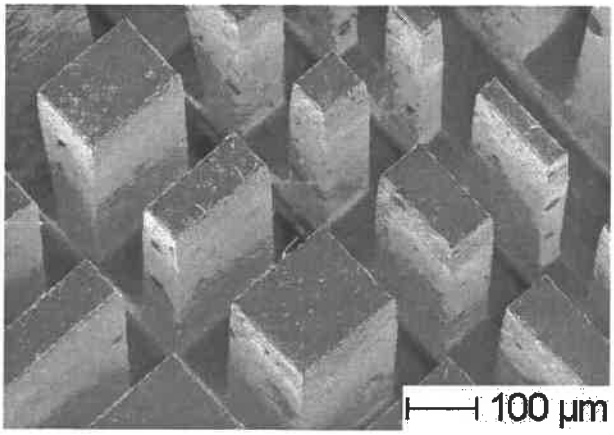


*Fig. 3: EDM parts*
*Source: Helmut CHRISTMAN GmbH, Birkenfeld, Germany*

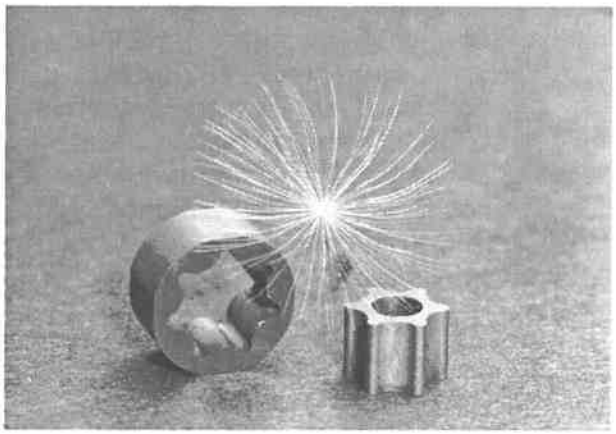

*Fig. 4: Bioreactor*
*Source: Forschungszentrum Karlsruhe, IMF-1*

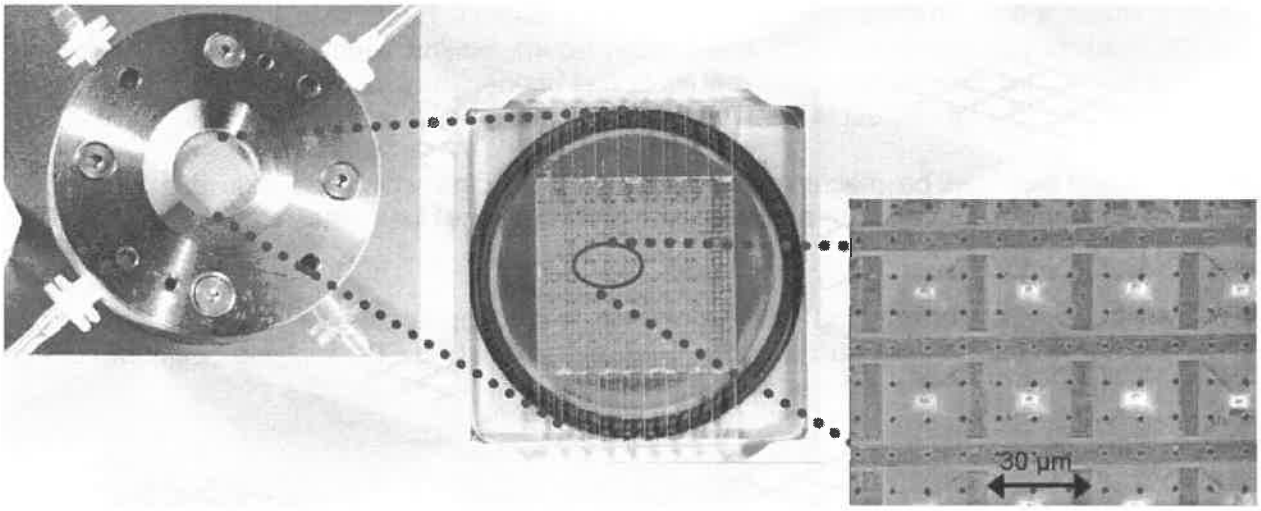


starts with micromilling and flycutting of a brass mold, followed by micro injection molding for mass replication of the structure. The molded polycarbonate parts accomodate approximately 300 container structures per square centimeter (middle). The bottom of each container is microstructured with pyramidal pits (right). In a final process step, the bottom has to be perforated by excimer laser machining to ensure nutrient supply to the cells in the containers. Specifications of the pores: diameter < 3 µm, length < 100 µm, pitch 15 µm.

### *FIB*

FIB is commonly used as an analysis and machining tool, mainly in electronic and electro-optic device fabrication. Besides direct machining, FIB proved to be a suitable technique for fabricating ultra-small cutting tools [18].

Profiled tools and end-mills can be used for turning [19] and milling trenches less than 20 µm wide. Figure 5 shows a profiled tool made of tungsten carbide [20].

*Fig. 5: Profiled cutting tool*
*Source: Louisiana Tech University, Ruston, LA, USA*

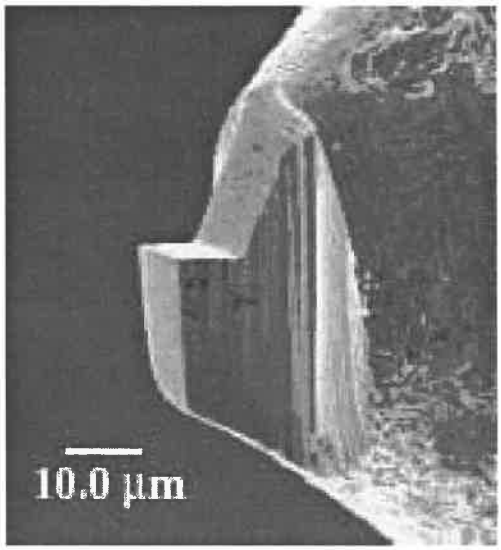


## CONCLUSION

Many techniques are available for maskless material removal on a micrometer scale. Most of them are suitable for both fabrication of prototypes and the industrial production of microstructured components. Part of research and development should be the implementation of new techniques and solutions in industrial processes. The growing number of networks of excellence is a sign of the need for interdisciplinary cooperation which should include cooperation of research and industry.

## ACKNOWLEDGEMENTS

The authors are grateful to all colleagues and companies who contributed information, figures and all kind of support. Success in microcutting depends on teamwork, and we feel that we are part of a powerful "micro" community.

## LITERATURE & WWW REFERENCES

[1] KERN Micro- und Feinwerktechnik GmbH & Co. KG www.kern-microtechnic.com
[2[ Helmut CHRISTMAN GmbH www.christmann-gmbh.de
[3] ROLLA Micro-Synthetics AG www.rolla.ch
[4] LPKF Laser & Electronics AG www.lpkf.de
[5] BARTELS Mikrotechnik GmbH www.bartels-mikrotechnik.de
[6] Euroflex Schuessler GmbH www.nitinol.de
[7] Forschungszentrum Karlsruhe, IMF-3 www.fzk.de/imf
[8] Braunschweig Tech. University, IWF www.iwf.ing.tu-bs.de
[9] Schaller Th, Schubert K: Micromachining by CNC Slotting Using a Steered Tool. Proceedings of the ASPE 16th Annual Meeting (2001) 469–472
[10] Bley P, Fahrenberg J, Czolk R: The Link between Laboratory and Market: Forschungszentrum Karlsruhe's Industrial Forum for Microfabrication Technologies (FIF). Proceedings of The Commercialization of Microsystems (2000)
[11] Forschungszentrum Karlsruhe, Industrial Forum (FIF) www.fzk.de/fif
[12] Schaller Th, Heckele M, Ruprecht R, Schubert K: Microfabrication of a Mold Insert Made of Hardened Steel and First Molding Results. Proceedings of the ASPE 14th Annual Meeting (1999) 224–227
[13] Hoffmeister HW, Hlavac M: Grinding of Microstructures in Hardened Steel with CBN Tools. Proceedings of the ASPE 17th Annual Meeting (2002) 490–494
[14] Takahata K, Gianchandani YB: Batch Mode Micro-EDM For High-Density And High-Throughput Micromachining. Proceedings of IEEE MEMS (2001) 72–75
[15] Pfleging W, Hanemann T, Torge M, Bernauer W: Rapid Fabrication and Replication of Metal, Ceramic and Plastic Mold Inserts for Application in Microsystem Technologies. Accepted (19.08.02) for publication in Journal of Mechanical Engineering Science, Proc. Instn Mech. Engrs. Vol 217 Part C
[16] Pfleging W: Laser material processing for applications in medical and microsystem technologies. LaserOpto 31(5) (1999) 54–57
[17] Knedlitschek G, Schneider F, Gottwald E, Schaller T, Eschbach E, Weibezahn KF: A Tissue-Like Culture System Using Microstructures – Influence of Extracellular Matrix Material on Cell Adhesion and Aggregation. Journal of Biomechanical Engineering 121 (1999) 35–39
[18] Vasile MJ, Nassar R, Xie J, Guo H: Microfabrication techniques using ion beams and emergent applications. Micron 30 (1999) 235–244
[19] Adams DP, Vasile MJ, Krishnan ASM: Microgrooving and microthreading tools for fabricating curvilinear features. Precision Engineering 24 (2000) 347–356
[20] Adams DP, Vasile MJ, Picard YN: Focused Ion Beam Shaped Micro-cutting tools for Fabricating Curvilinear Features. Proceedings of the ASPE 15th Annual Meeting (2000) 176–179

# Mesoscale and Microscale Manufacturing Processes: Challenges for Materials, Fabrication and Metrology.

*T. A. Dow and R. O. Scattergood*
*Precision Engineering Center*
*North Carolina State University, Raleigh, NC 27695-7918*

## Introduction

Length scales for processes and materials are generally classified as nanoscale (< 100 nm), microscale (100 nm to 100 $\mu$m) and mesoscale (> 100 $\mu$m). The length can be an external dimension of a component, or the internal dimension of a material such as the crystalline grain size. A comprehensive summary of the recent state-of-the art for Micro Meso Mechanical Manufacturing ($M^4$) is given in the NSF workshop report [1]. Material properties play an important role for all of the manufacturing processes. The $M^4$ report concludes that "understanding mechanics and physics of materials at the microscale is essential", and that "material can no longer be considered homogeneous when the process size dimensions approach the material grain size". The overview presented in this paper will focus on material properties, and in particular the structural properties of metals that will be used for the production of miniaturized mechanical components and assemblies. Many of the other papers in this conference will address the specific fabrication processes or metrology methods for manufacturing down to the microscale or nanoscale.

## Mechanical Micromachining and Materials

Milling, drilling, turning or grinding are basic mechanical manufacturing processes used for the production of complex 3D components. Metallic materials used are steels and nonferrous alloys of aluminum, copper, titanium and other metals. These engineering materials provide the range of mechanical properties required for fabrication and end use. Manufacturing at the microscale using mechanical processes, ie., mechanical micromachining, requires suitable adaptation of the conventional processes. Fig. 1a shows an example of miniaturized tooling used to turn the demonstration microgrooves in 6061 aluminum shown in Fig. 1b [2]. Fig. 2 shows commercially micromachined components with overall dimensions on the order of 1-2 mm [3]. The need for further miniaturization of components will require that internal features on assembled components of this size, or smaller, be the order of 20 $\mu$m or less, similar to the features shown in Fig. 1. What kind of engineering materials will be best suited for these applications ? A general engineering guideline for materials selection is that the grain size be at least two orders of magnitude smaller than the section or feature size for the component of interest. Otherwise, the material response will not be uniform or predictable. Uniformity of material response in this context means

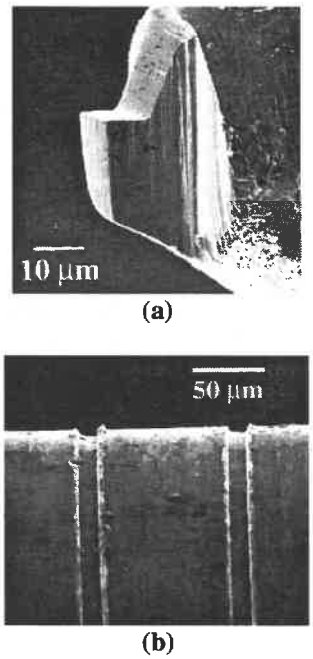


**Figure 1.** a) Miniature cutting tool. b) Grooves cut with the tool.

that directional-dependent (anisotropic) material properties must be averaged over a sufficiently large number grains so that fluctuations over the length scale of interest are negligible. Both the elastic and plastic properties of crystalline materials are anisotropic with very few exceptions. Fig. 3 shows an example of grooves produced in a very large grain-size, high-purity tin lap plate by diamond turning [4]. The tin is soft and very ductile which leads to extensive burr formation on the groove overlaps. The burr formation is produced by dislocation-controlled plastic deformation (slip) and this is strongly dependent on the local crystal orientation. Nonuniform material response is manifest as dramatic changes in the extent of burr formation when a grain boundary is crossed in Fig. 3. If the tin grain size were reduced below 1 $\mu$m, burr formation viewed at the same magnification would appear quite uniform. Furthermore, burr size could be substantially reduced because fine-grained tin is harder and less ductile.

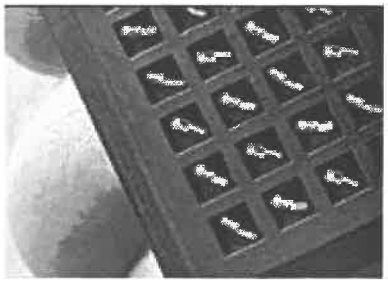

**Figure 2.** Micromachined parts. Note the scale with respect to the fingers on the hand.

Currently, one of the most hotly pursed research areas in materials science is the synthesis of nanocrystalline (nc) materials with grain sizes in the nanoscale size range. If mechanical micromachining techniques are developed which push section sizes down to 10 $\mu$m or less, the guidelines discussed above for uniformity and predictability of properties points to the need for nc metals and alloys, ie., grain sizes < 100 nm. Furthermore, optimal process development will require interdisciplinary research efforts between precision engineers and material scientists. This has not yet been undertaken in a concerted fashion. In the following sections, a brief overview of the synthesis and properties of nc metals and alloys will be given with the aim of introducing the precision engineering community to this novel class of materials and hopefully encouraging more interdisciplinary research for mesoscale and microscale manufacturing processes.

## Synthesis of Nanocrystalline Metals and Alloys

Research on nc materials includes the synthesis of particles, thin or thick films and bulk material along with the characterization of their properties. The state of the art is described in recent reviews [5]. Materials can be metals, ceramics or polymers. Since mechanical micromachining is a bulk fabrication process for metallic materials, only bulk synthesis techniques for metals are relevant. There are two type of processing methods in widespread use. They are classified as two-step or one-step synthesis techniques. Two-step techniques involve the production of a powder, which must then be compacted. Powder production has been done using condensation of a gas to form nanoscale particles or high-energy ball milling to produce powders from the starting materials. In the case of milling, the final powder size can be large, on

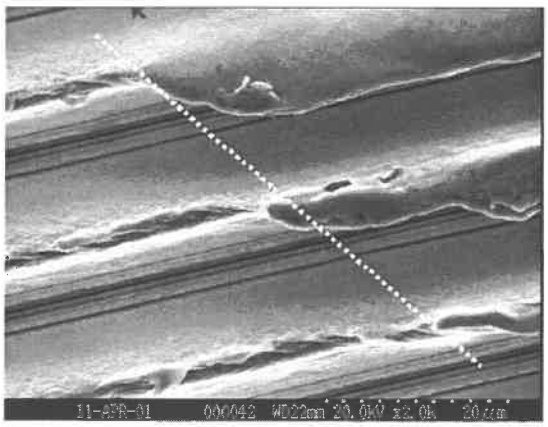

**Figure 3.** Burrs formed along grooves cut in a tin plate. A grain boundary lies along the dashed line.

the order of 1-100 $\mu$m, but the crystalline grain size within each powder particle is nanoscale. Milling is quite versatile since any composition can be made, and the alloys produced can be a non-equilibrium mixture of normally insoluble constituents. The second part of the two-step technique is compaction of the powder into a fully dense solid. Compaction requires application of pressure for densification combined with elevated temperature to promote plastic deformation and diffusion processes that lead to interparticle bonding and removal of porosity. The primary difficulty for nc materials is that temperatures must be kept low to avoid extensive grain growth during compaction. Since a large fraction of the atoms in nc materials are in high-energy grain boundaries, there is a large driving force for grain growth. For example, at a grain size of 5 nm, about 50 % of the atoms are grain boundaries. Much of the early work on nc metals produced by two-step methods was inconclusive due to processing defects introduced by poor compaction. One-step synthesis techniques avoid the compaction step. The most widely used one-step techniques are electrodeposition of thick films which can be stripped from substrates, large-strain plastic deformation, and crystallization of metallic glasses. Each of these has limitations. Varying composition is difficult with electrodeposition. Large plastic strain techniques based on rolling or extrusion can be used with ductile starting materials, but it is usually difficult to get the grain size below 100 nm. Certain zirconium-based, aluminum-based or iron-based alloys can be cast in bulk form as fully amorphous metallic glasses. These can then be crystallized to form nc alloys.

## Mechanical Properties of Nanocrystalline Metals and Alloys

The mechanical properties of nc metals and alloys will be a key factor in determining their success as optimum materials for manufacturing. For machining, properties such as strength, ductility and work-hardening capacity determine tool forces, surface finish and features such as shear localization or burr formation. For end use of a component or an assembly, performance can be limited by properties such as fatigue life, wear resistance and fracture toughness. Although a large number of studies have been done on the mechanical properties of nc materials, a fundamental understanding of the deformation mechanisms and a reliable database of the engineering properties is just beginning to emerge [6,7]. As already noted, many of the earlier results are inconclusive due to processing defects introduced during synthesis. In addition, there is the fact that laboratory-scale synthesis methods generally produce small quantities of nc material, insufficient to make standard-size specimens for mechanical testing. However, the state of the art is improving because better synthesis techniques and small-scale mechanical testing techniques are being developed.

A very large increase in yield strength and hardness due to a reduction in grain size is the most striking and best understood effect for nc metals. For example the yield strength of 20 $\mu$m grain size, high purity annealed copper is about 50 MPa and the strength approaches 1 GPa when the grain size is reduced to 16 nm. This is a result of a grain-size strengthening mechanism that inhibits the motion of dislocations on slip planes. The increase in yield strength $\sigma_y$, or the hardness $H \approx 3\ \sigma_y$, as a function of grain size is given by the Hall-Petch relation [8],

$$\sigma_y = \sigma_o + \frac{k}{\sqrt{d}} \qquad (1)$$

where d is the grain size and $\sigma_o$ and k are material constants which depend on the temperature and strain rate. Extrapolating the Hall-Petch relation for conventional grain size materials (d ≈ 5 - 50 $\mu$m) to the nanoscale size range predicts large increases in the strength. Large increases are observed for nc metals. Moreover, as shown by the Hall-Petch plot in Fig. 4, when the grain size decreases, the strength passes through a maximum at a critical value of the grain size and then decreases. Considerable controversy has surrounded this inverse Hall-Petch effect since processing defects might also cause the strength reduction. However, there are now reliable measurements, like those shown in Fig. 4, which confirm the inverse effect and imply that a new plastic deformation mechanism becomes operative at very small grain sizes A number of different mechanisms have been proposed [6]. It appears that dislocations no longer control plastic deformation in nc metals with grain sizes less than about 10-20 nm. Alternate mechanisms depend on plastic deformation controlled by grain-boundary diffusion processes that do not involve dislocation motion. The simplest picture for a mechanism transition follows from the well-known equation for plastic deformation due to grain-boundary controlled diffusion creep [8],

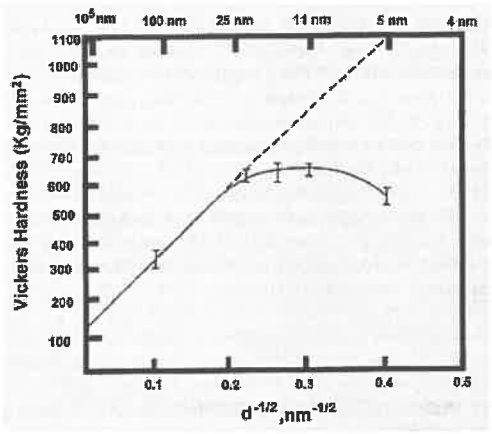


**Figure 4.** Hall-Petch plot of hardness vs. $1/\sqrt{d}$ for electrodeposited nc nickel. The straight line represents eq. (1) for large grain-size nickel [6].

$$\frac{d\varepsilon}{dt} = \frac{A\sigma}{d^3} e^{-\frac{Q_b}{RT}} \qquad (2)$$

where $d\varepsilon/dt$ is the strain rate, $\sigma$ is the applied stress, $Q_b$ is the activation energy for grain-boundary diffusion, R is the gas constant and A is a material constant. The yield strength of a material is always measured at a specified temperature and strain rate. Assuming that plastic deformation is controlled by the diffusion creep mechanism, $\sigma = \sigma_y$ in equation (2) and thus $\sigma_y$ is proportional to $d^3$ at a fixed temperature and strain rate. In contrast, equation (1) shows that $\sigma_y$ is inversely proportional to $\sqrt{d}$ for the dislocation-controlled plastic deformation mechanism. Consequently, as grain size decreases the yield strengths for the two mechanisms must cross over such that the diffusion mechanism would be favored below a critical grain size.

The effects of grain size on mechanical properties other than yield strength or hardness remain uncertain at this time. The data in Fig. 5 indicate that the ductility in tension for nc metals decreases as the grain size decreases. This loss in ductility is not desirable, but there is encouraging evidence that ductility can be improved at the

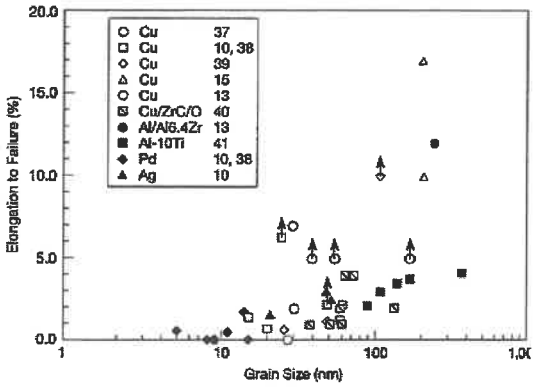


**Figure 5.** Plot of ductility in tension vs. grain size for the nc metals indicated [9].

smallest grain sizes in multi-phase alloys [9]. The effect of grain size on properties such as work hardening capacity, fatigue life and fracture toughness have not yet been established. There is conflicting evidence for the presence or lack of work hardening capacity in pure nc metals. Iron shows very low work hardening over a wide range of nanoscale grain sizes whereas nc copper and zinc generally do work harden. Improved fatigue life has been reported for some nc metals. Establishing the effects of grain size is complicated by the fact that the synthesis techniques for nc metals often produce a rather wide distribution of grains sizes. It has been suggested that this results in a superposition type response wherein the larger grains will deform by dislocation mechanisms and the small grains deform by diffusion mechanisms.

The effects of alloying been studied for various nc metals [10]. As in the case of larger grain-size materials, multi-phase microstructures can produce beneficial changes in the mechanical properties. For example, two-phase nc alloys produced by partial crystallization of metallic glasses or by mechanical milling can exhibit high strength along with good ductility at very small grain sizes. The metallic glasses are rather unique in that the fully amorphous glass has no work hardening-capacity. Such glasses fail catastrophically with zero ductility in a tensile test because of shear localization. When fully crystallized to form an nc alloy, the glasses are usually very brittle and will fracture. Intermediate structures formed by partial crystallization consist of nc grains in an amorphous glass matrix. These alloys have shown excellent combinations of strength, ductility, toughness and resistance to shear localization. Furthermore, they are fully dense with no processing defects. More research is needed to explore the benefits of multi-phase microstructures in nc alloys.

## Modeling

Because of the nanoscale grain size, nc materials are suited to molecular dynamics modeling. A large number of very small nano-grains can be incorporated into the computational cell. The structure of the grain boundaries has been studied extensively using modeling and high-resolution electron microscopy [11]. The nature of the boundaries depends in part on the synthesis technique and subsequent thermal treatments. The boundaries can be sharp with a well defined structure and relatively stable, or they can be more diffuse, analogous to a thin amorphous layer surround the grains, and less stable. It is thought that the latter type of boundaries are present in materials with very small nano-grains and that these boundaries promote the diffusion-based plastic deformation mechanisms discussed earlier [6]. Simulations of the dynamic stress-strain response are also being done to provide insight into the

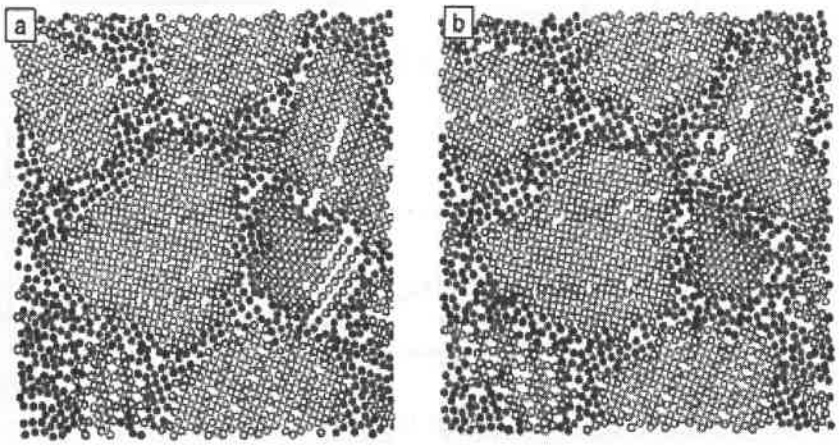


**Figure 6.** Simulation of the deformation of nc copper (5.2 nm grain size). a) initial configuration. b) after 3% strain [7].

deformation mechanism. The results must be carefully interpreted since molecular dynamics simulations correspond to very high strain rates. Changes in the grain structure and the plasticity mechanisms can be observed in these simulations. Fig. 6 shows typical results for a simulation of the deformation in pure copper [7].

## Summary

The development of new nc metals and alloys is actively being pursed by materials scientists. One can anticipate that a reliable database of their properties will emerge from this work. Because of the very fine grain size, this class of materials should be well suited to the needs of mesoscale and microscale manufacturing and in particular to mechanical micromachining of very small section sizes and features. Coatings produced by electroplating, for example, copper and electroless nickel, have had wide application for diamond turning. The nanoscale grain size of such coatings produces high hardness, good uniformity of properties at small size scales and excellent surface finish. Encouraged by this, precision engineers and materials scientists can look forward to a wider range of new nc metals and alloys that will enhance the development of mesoscale and microscale manufacturing.

## References


1. K. F. Ehmann, R. E. deVor, S. G. Kapoor and J. Ni., *Micro/Meso-Mechanical Manufacturing $M^4$*, NSF Workshop, May 16-17 (2000).
2. D. P. Adams, M. J. Vasile and A. S. M. Krishnan, Precision Engineering, 24 [4], 347 (2000).
3. Remelle Engineering, Inc., New Brighton, MN, 55112.
4. D. A. Kametz, PhD thesis, NC State University (2001).
5. C. C. Koch, ed., *Nanostructured Materials: Processing, Properties and Potential Applications*, Noyes Publications (2002).
6. J. R. Weertman, in ref. 4, 397 (2002).
7. J. R. Weertman, D. Farkas, K. Hemker, H. Kung, M. Mayo and H. Van Swygenhoven, MRS Bulletin, 24, 44 (1999).
8. T. H. Courtney, Mechanical Behavior of Materials, McGraw Hill (2000).
9. C. C. Koch, D. G. Morris, K. Lu and A. Inoue, MRS Bulletin, 24, 54 (1999).
10. J. Eckert, in ref 4, 423 (2002).
11. V. Vitek, *Stability of Materials - NATO Advanced Science Institute*, A. Gonis et al, eds., Plenum Press, 53 (1996).

# Introducing Meso-scale channels on Ceramics by Machining

H-W Shin, C.K. Kok, E. Case*, and P. Kwon
Department of Mechanical Engineering
Department of Chemical Engineering and Materials Science*
Michigan State University
East Lansing, Michigan

## EXTENDED ABSTRACT

Conventional wisdom dictates that ductile metals are easier to machine than brittle materials such as engineering ceramics, glasses, semiconductors, diamonds, and metal composites. In fact, Sreejith et al. [1] attributed the ease of machining metals to their inherent properties such as their non-directional bonding, high symmetry of crystal structure, high thermal conductivity, low density, zero porosity, high fracture toughness, large strain to fracture and high impact energy. They also explained the nature of bonding impact with material removal mechanism. Ceramics, on the other hand, possess many important attributes that cannot be attained from metals. Most covalent-bonded ceramics are hard, strong, and possess high melting temperature, exhibiting low symmetry of crystal structure, limited or inadequate slip systems for plastic deformation, low thermal conductivity, low fracture toughness and low breaking energy. Due to the brittleness of ceramics, the requirements on high-temperature processing, and the difficulty in traditional forming and machining techniques, the use of ceramic materials for engineering applications has been severely limited. As the usages of advanced ceramics are growing increasingly for applications in aerospace, automotive and electronics industries, one of most important key issues hindering the utilization of ceramic materials is in its processing. The present study tackles this problem by exploring a novel technique to shape ceramic materials by combining traditional ceramic-powder processing techniques with those of machining and joining.

The recent studies [1, 2, 3] show that it is possible to machine brittle materials like ceramics in a ductile manner under certain machining parameters. Bifano et al. [4] explain when the critical resolved shear stress within a brittle material exceeds the elastic yield stress during machining, it is possible to change the mechanism of deformation. Kumbera et al. [2] analyzed the process by running the numerical simulation. They showed that silicon carbide change its phase from brittle to ductile under high pressure at contact interface between the work piece and the cutting tool by investigating the effects of cutting speed, tool tip radius, rake angle and feed on the machining of silicon carbide. By increasing the cutting speed, temperature and pressure can be increased, which causes thermal softening of materials. As the silicon nitride material undergoes a high-pressure phase transformation at about its hardness value of 22GPa under hydrostatic stress state conditions.

In conjunction with our current research in the fabrication of a meso-scale heat exchanger, we have explored the processing possibility of introducing meso-scale channels on the surface of ceramics. The motivation for the complex network of channels is to circulate cooling fluids in the meso-scale heat exchangers to be developed. In our previous work, internal meso-scale channels have been introduced in the bulk of ceramic materials by embedding a fugitive phase inside the ceramic powder during compaction. During sintering, the fugitive phase burns away leaving the channels in the bulk of ceramics. A similar process has been used to make surface channels as well. The materials with the surface channels can be joined to form internal channels. However, this technique possesses a major disadvantage as it is only capable to make simple channels. As the shape of the channels becomes complex, powder flow around the complex fugitive phase becomes increasingly limited. This leads to the forming of large cracks around the fugitive phase in the final ceramic parts.

By testing with tungsten carbide drills and a diamond grinding wheel, David et al. [5] showed that two-phase mixtures of consisting of refractory oxides, such as $Al_2O_3$, $ZrO_2$, Mullite, and rare-earth phosphates, such as $LaPO_4$, $CePO_4$, can be cut and drilled due to the weakness of their bonding and formation and linking of cracks at the weak interfaces between the two phases. Similar to our work, Halcomb et al. [6] and Klocke et al. [7] machined advanced ceramics before final sintering and was able to reduce the expensive cost of processing hard materials. To demonstrate this, they successfully carried out the machining of green compact, for which a binder phase was use to consolidate the compact for machining, and white compact, which is the product after pre-sintering. The advantage of machining before final sintering is attributed to the lower inherent strength and hardness of green and white compacts as compared to their finally sintered counterparts. In addition, the desirable surface quality was obtained by decreasing the feed rate in green and white machining and increasing the feed rate increases relative wear and decreases tool life [8]. During machining, the powder-debris from the specimen can cause wear damage on sideways and bearings. Therefore, the debris should be cleaned by extraction equipment such as vacuum removal for good machining precision. Increasing the revolution speed (in rpm) of the cutting tool not only decrease the machining time, but also reduce the amount of tool wear [9] because tool loads are higher at the slower cutting speeds thus it is desirable to machine in high cutting speed.

Most engineering ceramic materials after they have been fully sintered are too brittle and hard to machine with conventional machine tools. Mixing a binder phase with the powder and Binder-burnout are undesirable. A new meso-scale processing method is needed to introduce a complex network of channels in a ceramic material. One of the flexible methods of achieving this objective is the CNC milling process. Machining is controlled to arrive at the specific component shape, size for application, desired finish and strength, and so on, at a low cost. Therefore, we have prepared partially sintered ceramics (PSC) that have barely formed necks among the powders. Fig. 1 shows the partially stabilized zirconia samples about the size of a dime with the complex channels machined and subsequently sintered. PSC are easily handled and mounted on a conventional table-top CNC machine.

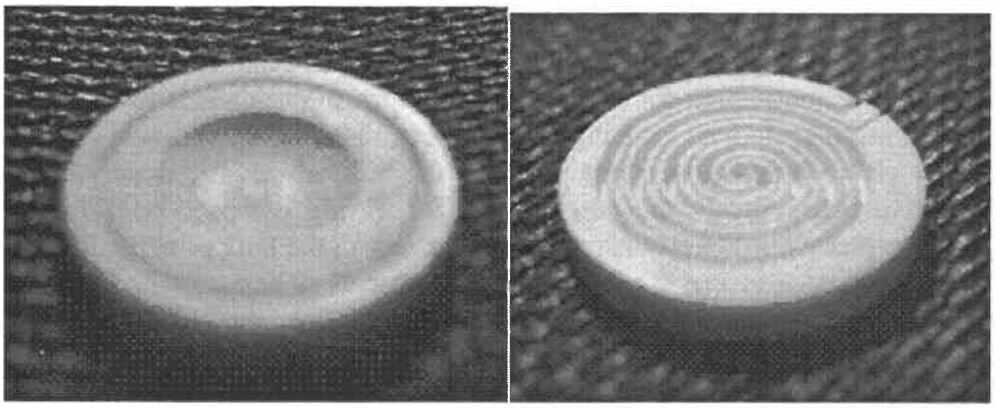

Figure 1: Complex Channels and Cavity Achieved by CNC Milling

In our work, a range of machining parameters including various pre-sintering temperatures, RPM and feed rates have been tried to determine the optimal processing condition. In particular, pre-sintering temperatures of 600, 800, 1000°C, feed-rate increments between 2.5 to 25 mm/min, and rpm varying from 500 to 2500, have been used to mill a series of channels on pre-sintered ceramic specimens made of partially stabilized zirconia (PSZ). The milling tool used in this study was made of stainless steels and the diameter is 0.625mm. This allows us to observe the finished surfaces in and near the channels at various rpm and feed rate in order to narrow down the recommended processing range.

In our experiments, the green compacts without binder phase are too unwieldy for machining. Not only they are hard to handle but also they have a tendency to fragment during machining. Consequently, green machining is discounted in making a meso-scale heat exchanger. A set of recommended parameters governing both pre-sintering and machining processes is arrived based on SEM observations on fully sintered samples. Fig. 3 and 4 shows two extreme cases. As shown in Fig. 4, the finished channels would lead to the absence of surface fractures near the edges of the channels. Based on the observations, higher rpm, low feed rate and pre-sintering at a temperature above 800°C for 4 hrs are generally recommend for machining the pre-sintered PSZ. Even though more experimental data are needed to understand machining the pre-sintered alumina samples, the similar machining condition may be recommended except there was a major difference in the recommended pre-sintering temperature. The channels on the samples pre-sintered at 600°C were much better. Fig. 5 shows the cross-section of the channel.

Machining, more specifically milling of channels, causes some effect on the material near the channels. The SEM observations were made on the surfaces inside of channels and the surface away from the channels. Unlike typical machining of metals, machining the PSC does not cause plastic deformation but breaking of the necks formed during the pre-sintering process. Because the PSC are subsequently fully sintered (typically up to 98% theoretical density), the samples undergo substantial shrinkage (about 50% in volume or about 80% in length) during sintering. However, the shrinkage on the size of channels was much larger (around 47% reduction in size) than the shrinkage of the overall samples (around 25% reduction in diameter) in all our samples.

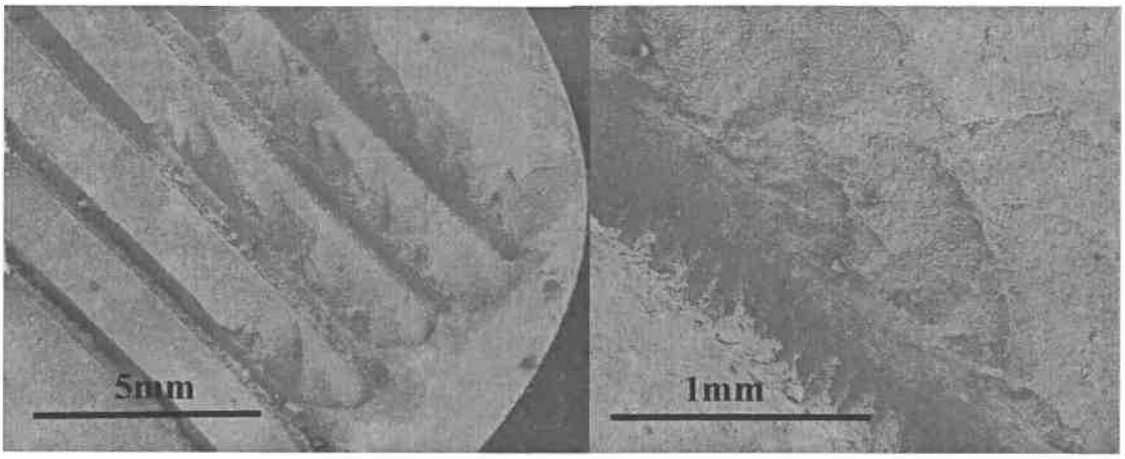


Figure 2: Excessive Surface Damage Caused by Milling at 500rpm and feed rate of 25mm/min on the Pre-sintered sample at 600oC for 4 hr.

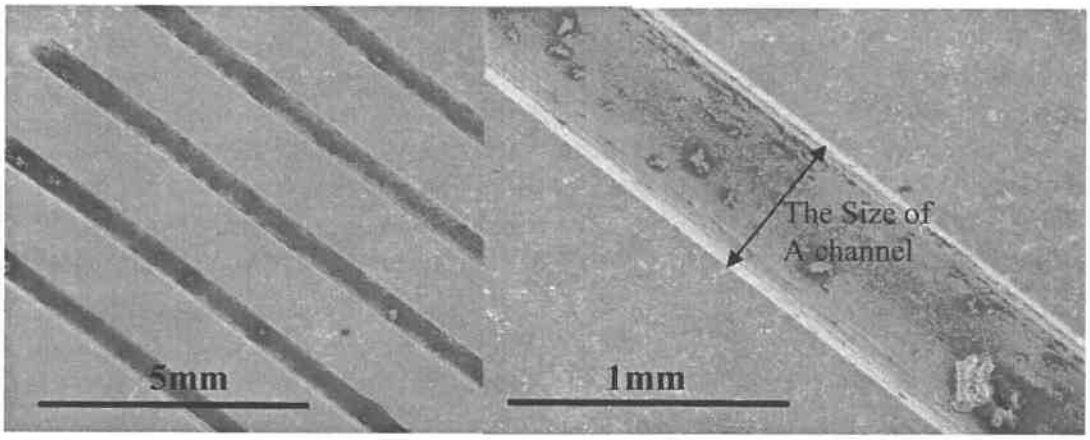


Figure 3: No Pronoun Surface Damage Caused by Milling at 1500rpm and feed rate of 25mm/min on the Pre-sintered sample at 1000°C for 4 hr.

The discrepancy may come from the subsurface damage around the channels during machining. Depending on the pre-sintering temperature, the extent of neck formation between the powders affects the integrity of the samples. Milling PSCs cause the small subsurface cracks around the cracks. Final sintering heals these cracks as the cracks after final sintering cannot be observed. After milling with the milling tool with the same diameter (0.625mm) used in the experiment, the sizes of the channels after pre-sintering for all samples (processes at different sintering temperature were practically the same between 0.713mm and 0.794mm. After final sintering the size between 0.516mm and 0.605mm were observed. The data were profoundly depended on the pre-sintering temperature. This can be explained by the difference in the region affected by small subsurface cracks.

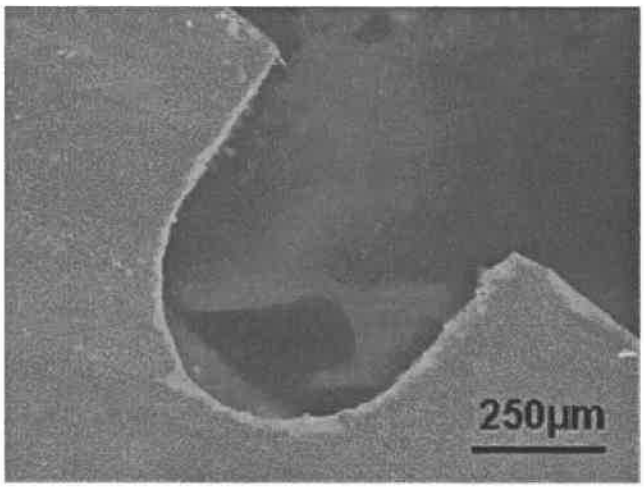


Figure 4: The Cross-section of a Channel

In the meso scale machining of metals, the major problem lies in the plastic deformation of the metals. Extensive burr formation [10] or chip formation [11] has been observed even with the special machine tool designed to rotate up to 670,00 rpm for meso-scale machining. Machining PSCs does not suffer from these problems. To form complex networks of internal channels, the specimens are joined which can be used to circulate coolants. Joining requires a precursor of silicate film, which is deposited on to the surfaces to be joined. Silicate film spin-coated from a liquid containing silicate is then cured. Joining takes place with MaCor® on the conventional oven at around 1400°C. The joined sample is then sectioned to observe the integrity of the join via SEM as shown in Fig. 5.

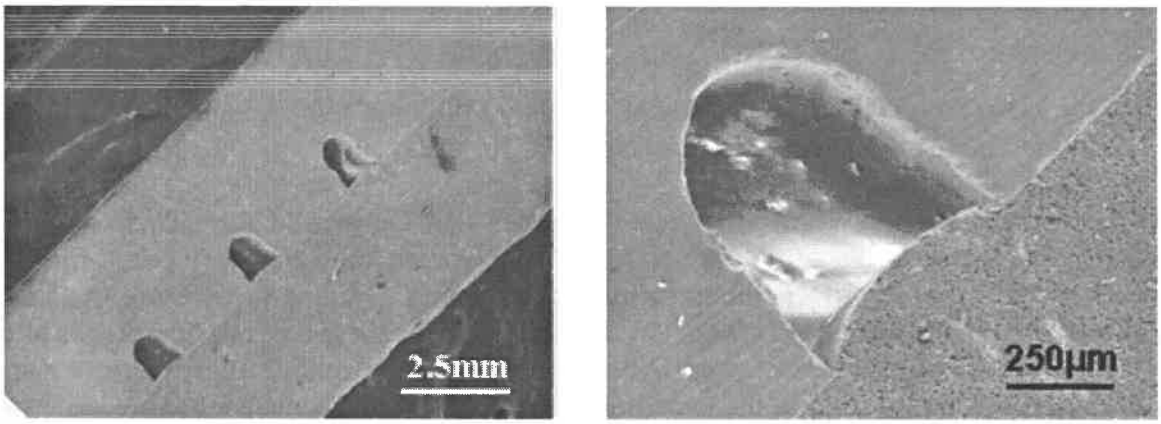


Figure 5: The Cross-section of the Joined Sample

[1] Kumbera, T.G., Cherukuri, H.P., Patten, J.A., Brand, C.J. and Marusich, T.D., 2001, "Numerical simulations of ductile machining of silicon nitride with a cutting tool of defined geometry," Machining Science and Technology, 5[3], pp. 341-352.

[2] Morris, J.C., Callahan, D.L., Kulik, J., Patten, J.A., and Scattergood, R.O., 1995 "Origins of the Ductile Regime in Single-Point Diamond Turning of Semiconductors," J. Am. Ceram. Soc., 78[8], pp. 2015-2020.
[3] Chandra, A., Wang, K., Huang, Y., Subhash, G., Miller, M.H., and Qu, W., 2000, "Role of Unloading in Machining of Brittle Materials," Journal of Manufacturing Science and Engineering, 122, pp. 452-462.
[4] Bifano, T.G., Dow, T.A. and Scattergood, R.O., 1991, "Ductile-regime Grinding: A New Technology for Machining Brittle materials," *Journal of Engineering for Industry*, 113[2], pp. 184-189
[5] Davis, J. B., Marshall, D. B., Housley, R. M., and Morgan, P. E. D., 1998, "Machinable Ceramics Containing Rare-Earth Phosphates," Journal American Ceramic Society, 81[8], pp. 2169-2175.
[6] Halcomb L. D. and Rey, M. C., 1982, "Ceramic Cutting Tools for Machining Unsintered Compacts of Oxide Ceramics," Ceramic Bulletin, 61[12], pp. 1311-1314.
[7] Klocke, F., Gerent, O. and Schippers, C., 1997, "Machining Advanced Ceramics in the Green State," Ceramic Forum International(CFI) /Berichte der DKG, 74[6], pp.288-290,.
[8] King, A. G. and Wheildon, W. M., Ceramics in Machining Processes, Academic Press, 1966.
[9] Klocke, F., Gerent, O. and Schippers, C., 1999, Machining of Ceramics and Composites, ed. Jahanmir, S., Ramulu, M., Koshy, P., Manufacturing Engineering and Materials Processing, Marcel Dekker, pp. 1-10.
[10] Lee, K. and Dornfeld, D. A., A Experimental Study on Burr Formation in Micro Milling Aluminum and Copper, Transactions of NAMRI, XXX, pp. 255-262.
[11] Kim, C.-J., Bono., M. and Ni, J., 2002, Experimental Analysis of Chip Formation in Micro-Milling, Transactions of NAMRI, XXX, pp. 247-254

# PRECISION OF MICRO SHAFTS MACHINED WITH WIRE ELECTRO-DISCHARGE GRINDING

**Chris Morgan, Shelby Shreve, and R. Ryan Vallance,**
Precision Systems Laboratory, University of Kentucky, Lexington, KY *

## Abstract

This paper presents an experimental study of the straightness error and surface roughness developed during wire electro-discharge grinding (WEDG) of a micro-shaft. Shafts with a nominal diameter of 50 microns were fabricated with various machining conditions. Edge profiles of the shafts were measured with a 3D surface profilometer and analyzed numerically to determine straightness and $R_a$ values. A statistical analysis reveals the sensitivity of roughness to discharge energy and $R_a$ values down to 67 nm were achieved. Straightness ranged between 3.05 and 12.04 μm, and an error model suggests the dependence of straightness on machine/process errors rather than process conditions during WEDG.

**Keywords:** micro shaft, micro EDM, WEDG, metrology, straightness, surface roughness

## Introduction

Wire electro-discharge grinding (WEDG) is a micro fabrication process that uses electrical discharges in a dielectric fluid to erode material from conductive wires and produce micro shafts. A typical tungsten micro shaft produced with WEDG is illustrated in Fig 1; the diameter and length are approximately 80 μm and 300 μm, respectively. These shafts are finding increasing application in both microstructures and as tools in subsequent micro fabrication processes. For instance, cutting tools produced with WEDG were recently used to drill holes in silicon [1], and grinding wheels were made from polycrystalline diamond [2].

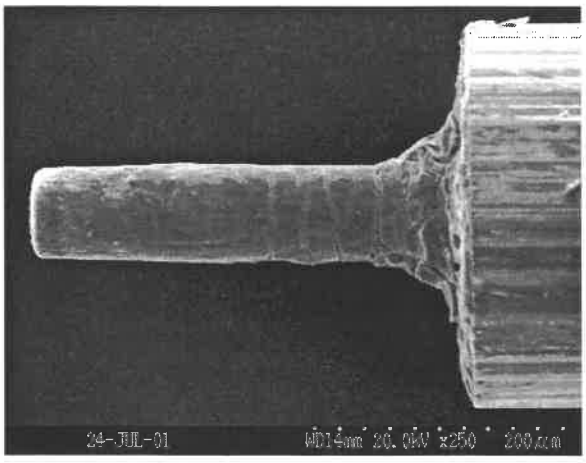

**Fig 1. Micro shaft produced with WEDG**

In these applications, the accuracy and precision of the micro shafts produced by WEDG are crucial for achieving accuracy and precision in the subsequent processes. However, it is visually evident in Fig 1 that variation in the diameter of the shaft and surface defects can exist. Despite this, studies have not related process conditions during WEDG or machine errors to the precision or accuracy of micro shafts. Therefore, the objectives of this work were to measure the variation in a set of micro shafts and subsequently relate the variation to process conditions and machine errors.

The paper presents the fabrication and metrology of 81 micro shafts produced with various process conditions. The sensitivity of the shafts' roughness and straightness was assessed with statistical box plots. The analysis reveals the precision of the WEDG process. Furthermore, the results suggest that the roughness of the shaft depends mainly upon process conditions, and the straightness appears to be dominated by machine and process errors. An error model and an analysis of variation support this conclusion.

## Background and Literature Review

Electro-discharge machining (EDM) is well suited for micro machining high-strength conductive materials since neither mechanical contact nor cutting is necessary. In 1985, Masuzawa [3] described wire electro-discharge grinding (WEDG) as a means to manufacture micro cylindrical electrodes, and Sato [4] described a method for drilling micro-scale holes using cylindrical electrodes. Since then, research on micro EDM has concentrated on either characterizing the process or applying the process to manufacture

* *Precision Systems Laboratory, Mechanical Engineering, University of Kentucky, 015 Ralph G. Anderson Building, Lexington, KY 40506. http://www.engr.uky.edu/psl.*

particular microstructures. Two applications of micro EDM include micro pipes/nozzles [5] and ink jet nozzles [6].

The WEDG process, illustrated in Fig 2, is similar to turning on a lathe. A simple RC circuit generates pulses that produce electrical discharges between the workpiece (cathode) and a $\varphi$100 μm brass wire (anode). The discharges occur across a small gap (~ 2μm) filled with dielectric oil. The workpiece is held vertically in a mandrel that rotates at 3000 RPM, and its position is slowly fed in the z-direction. The wire is supported on a wire guide, and its position is controlled in the x- and y-directions.

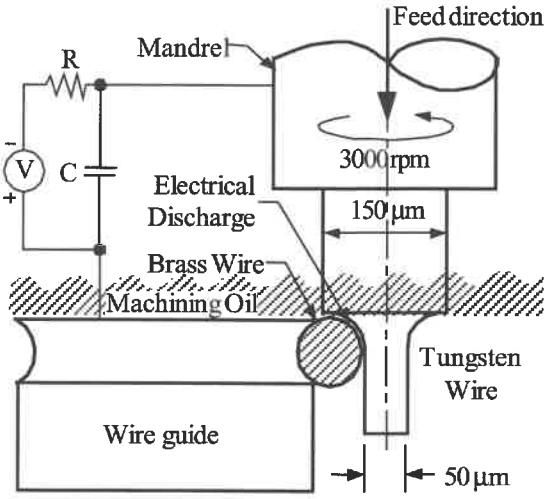


**Fig 2. Wire Electro-Discharge Grinding**

Each electrical discharge erodes material from the workpiece and the anode wire. To prevent discharges from worn regions of the anode wire, the wire travels at around 340 μm/s, and is fed from a reel and take-up system as illustrated in Fig 3.

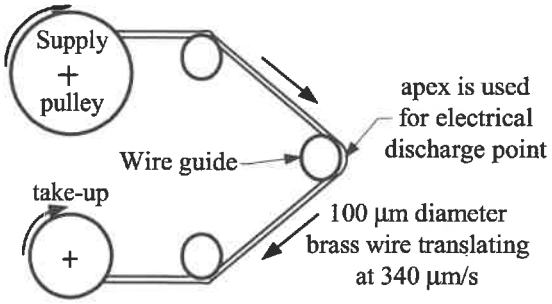


**Fig 3. Traveling Wire in WEDG**

A micro shaft is usually produced in three consecutive steps as illustrated in Fig 4. In the first step, the workpiece is positioned above the traveling wire, and the end of the shaft is machined by feeding the wire/guide in the x-direction. The second step is to rough cut the shaft and reduce the diameter of the stock material by feeding the workpiece in the z direction. The final step is to finish cut the shaft.

| Operation | Geometry | Process Conditions |
|---|---|---|
| Step 1: Flat End | 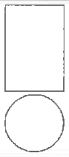 | V = 100 V<br>C = 1<br>Fh = 30 μm/s<br>Fl = 2 μm/s |
| Step 2: Rough Cut | 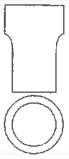 | V = 110 V<br>C = 1<br>Fh = 30 μm/s<br>Fl = 3 μm/s |
| Step 3: Finish Cut | | V = 70-80 V<br>C = 4<br>Fh = 20 μm/s<br>Fl = 30 μm/s |

**Fig 4. Typical Steps and Conditions for WEDG**

A high material removal rate (MRR) is achieved during the rough cut by increasing the energy in each discharge, which depends upon the energy stored by the capacitor as given in Eq 1. During the finish cut, the voltage and capacitance are reduced to achieve improved dimensions and surface finish. Although the multi-step process is based on the premise that improved precision is obtained by reducing the capacitance and voltage, a numerical relation for straightness or roughness is not available.

$$E = \frac{1}{2}CV^2 \qquad (1)$$

Substantial effort has concentrated on the precision of holes or cavities machined by micro EDM using cylindrical electrodes made by WEDG. Masuzawa et al. [7,8] used a vibroscanning method to measure holes drilled by micro EDM, and Yu et al. [9,10] developed the uniform wear method to reduce inaccuracy arising from electrode wear when micro-machining cavities. Yu et al. [11] later studied the influence of current, voltage, layer depth, and feed on the material removal rate, electrode wear ratio, and gap during contour milling with a cylindrical electrode.

## *Fabrication of Micro Shafts*

Tungsten micro shafts were produced by WEDG using a Panasonic MG-ED82W micro EDM machine, patented by Masaki et al. [12]. The stock tungsten wires ($\phi$ 150 μm) were machined down to a nominal diameter of about $\phi$ 50 μm with a single cut.

Three different lengths were manufactured to achieve aspect ratios (L/D) of approximately 10, 20, and 30.

The process variables for this experiment were voltage (V), capacitance (C), and feed rate of the tungsten workpiece. The values of each variable (Table 1) were chosen based on machine capabilities and experience. For each shaft a computer program was written to control the variables and record the time of machining. 81 shafts were machined to cover all possible combinations of the variables.

**Table 1: Summary of Experimental Variables**

| | |
|---|---|
| Voltage, V | 70, 80, 100 |
| Capacitance, pF | 10, 220, 3300 |
| Feed Rate, μm/s | 1, 3, 5 |
| Shaft Length, μm | 500, 1000, 1500 |
| Shaft Diameter, μm | 50 |

Fig 5 shows the dependence of material removal rate on the energy per discharge, for each shaft. The machining time increases as the discharge energy decreases. Also, in most cases, the higher the feed rate the higher the material removal rate, but excessive feed rates cause shorting, which dramatically increases machining time.

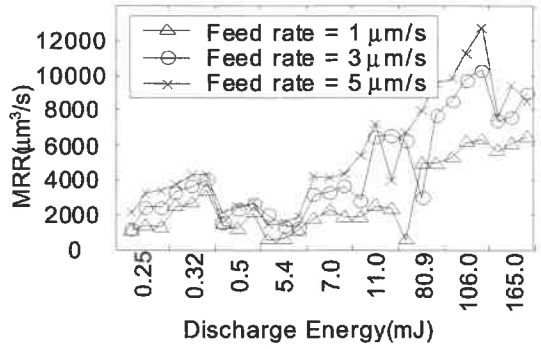


**Fig 5. Dependence of Material Removal Rate on Discharge Energy**

## *Metrology of Micro Shafts*

Each micro-shaft edge profile was measured with a 3D surface profilometer (Zygo NewView 500). The profilometer has ultra fine height resolution (sub-nanometer), which makes it acceptable for surface roughness and straightness measurements. The CCD camera was set to 640x480 resolution, and a 10x objective was used. This provided a lateral resolution of 0.64 μm.

Sample 3D data acquired for a single shaft is plotted in Fig 6. The scan region was typically about 20 μm wide and equal to the machined length. 2D profiles were obtained from the 3D data by selecting a scan line, drawn over the length of the shaft in the x direction. The 2D profiles had repeatable form error across a wide region of the scanned data; therefore precise placement of the scan line was not necessary. Each micro shaft was scanned twice at random locations around the circumference of the shaft.

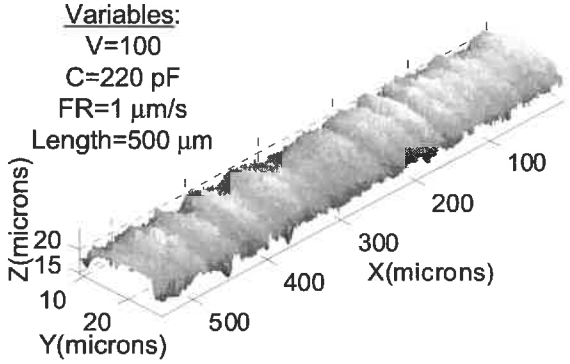


**Fig 6. 3D Scan of Shaft Surface Acquired with Zygo NewView 500**

After measuring all shafts with the profilometer, the data was analyzed with a Matlab script that determined straightness and roughness. The first step was to filter the data with a low-pass filter and separate waviness form errors from shaft roughness [13]. Standard wavelengths for separating these components are not available for micro shafts. Therefore, a spectral analysis was performed on the profile data, but dominant wavelengths were not apparent. A 10 μm cutoff wavelength was therefore chosen based on visual observation of the profiles. A roughness profile was obtained by subtracting the filtered profile from the raw profile. The average roughness of each shaft, $R_a$, was calculated using Eq (2) and data points, $Z_i$, from the roughness profile.

$$R_a = \frac{|Z_1| + |Z_2| + |Z_3| + \ldots + |Z_N|}{N} \qquad (2)$$

The straightness of a shaft was determined from the raw profiles by a method similar to that described by Weber et al. [14]. A least-squares line was determined that minimized the squared deviations of the orthogonal distance $(d_i)$ between the line and profile. The least-squares straightness tolerance was then calculated using Eq (3) as the difference between the minimum and maximum distances.

$$S = \max(d_i) - \min(d_i) \qquad (3)$$

The shafts and measurements shown in Fig 7 illustrate the range of values observed for roughness and straightness. In general, the SEM images correlate well with the measured profiles.

| Process Conditions | Scanning Electron Microscope Images of Micro Shafts | Profile Data (Raw, Filtered, Roughness) |
|---|---|---|
| V=70 V<br>C=10 pF<br>L=500 μm<br>FR=5 μm/s | 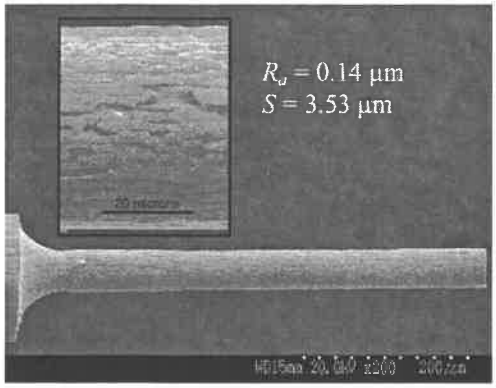 | 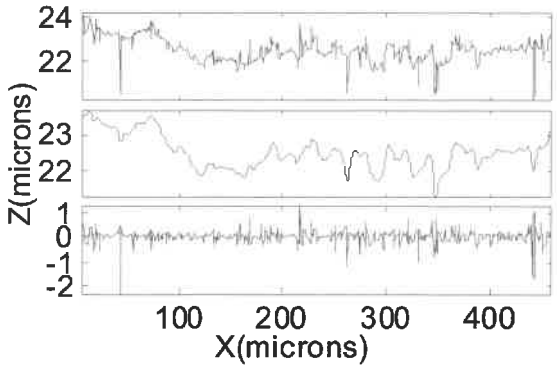 |
| V=100 V<br>C=220 pF<br>L=500 μm<br>FR=1 μm/s | 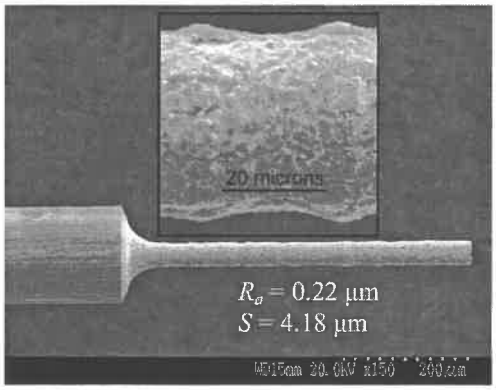 | 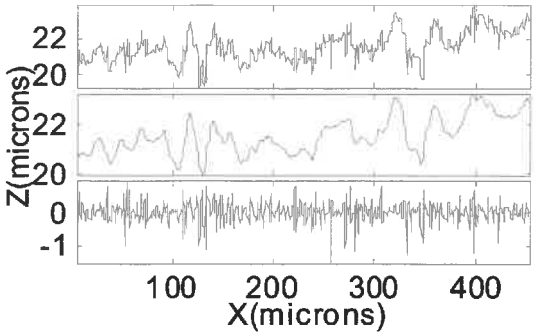 |
| V=70 V<br>C=3300 pF<br>L=500 μm<br>FR=1 μm/s | 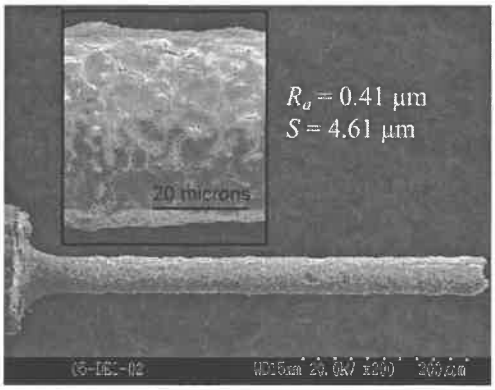 | 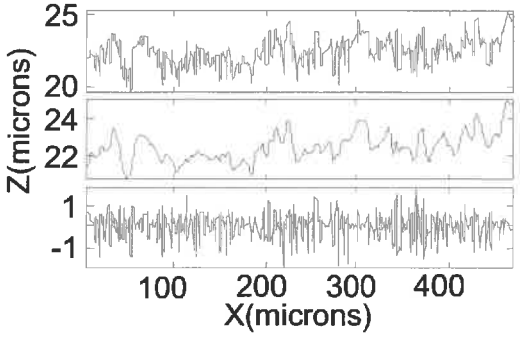 |

**Fig 7. Range of Roughness and Straightness Measured using 2D Profiles of Micro Shaft s**

### *Sensitivity Analysis*

The straightness and roughness of the micro shafts were grouped into categories and plotted on statistical box plots. An ANOVA analysis is performed on each group to test the hypothesis that the data is from same population or that one treatment is different from the others [18]. At the 5% level of significance, the graphs show that $R_a$ was independent of feed rate and aspect ratio. As expected, $R_a$ is dependent on voltage and capacitance. It was expected that surface roughness should increase with capacitor energy, but mean comparison tests suggest that the lowest surface roughness can be achieved with a capacitance of 10 pF, and a voltage of 80. Therefore surface roughness does not decrease with discharge voltage and an optimal value may exist.

The statistical tests show that straightness was independent of voltage, capacitance, and feed rate. But, as the length of the shaft increased, straightness errors increased. This indicates that machine errors likely dominate the straightness of the micro shafts.

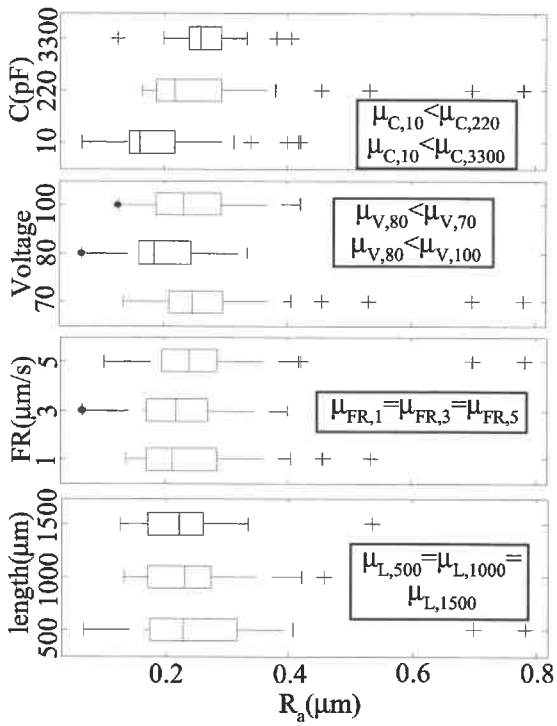


**Fig 8. Box Plots of variables versus micro shaft $R_a$, and mean comparison results using a 5% statistical level of significance**

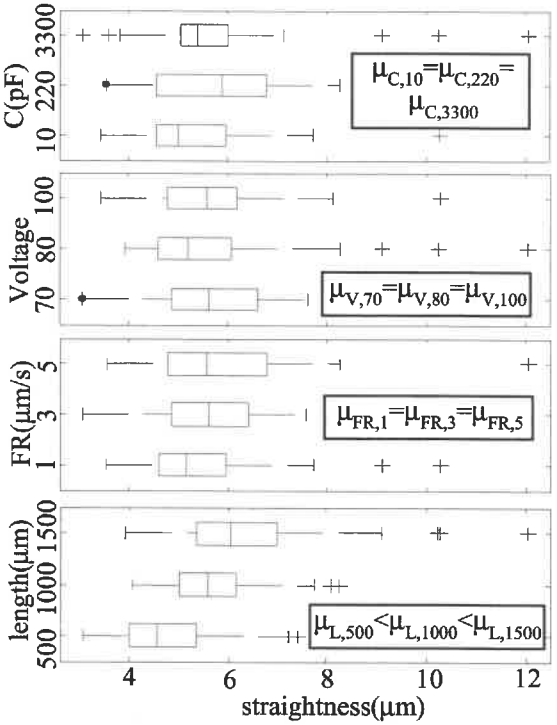


**Fig 9. Box Plots of variables versus straightness, and mean comparison results using a 5% statistical level of significance**

## *Model of Process and Machine Errors*

Errors during the WEDG process likely produce form errors in the micro shafts. Therefore, errors in the sensitive direction are modeled as shown in Fig 10. The straightness of edge profiles is essentially variation in shaft radius. The radius of the shaft, $R$, depends upon the relative position between the wire guide and workpiece, $X$, diameter of the wire, $D_w$, and gap, $G$, as given in Eq (4).

$$R = X - D_w - G \tag{4}$$

If these are continuous and independent random variables, then the variance in $R$ is simply the sum of the variances in $X$, $D_W$, and $G$ as given in Eq (5).

$$\sigma_R^2 = \sigma_X^2 + \sigma_{D_w}^2 + \sigma_G^2 \tag{5}$$

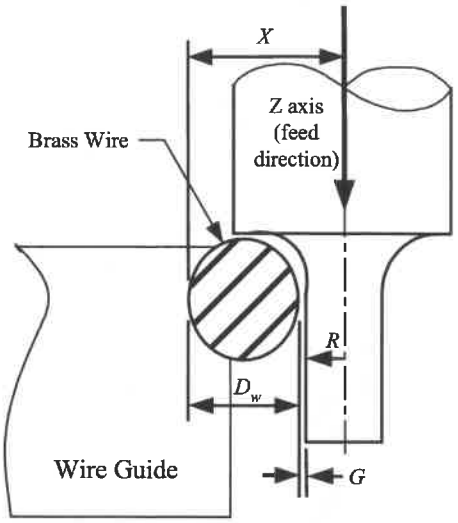


**Fig 10. Errors in WEDG Process**

The variance in $X$ is a primarily a combination of error motion in the machine's z-axis, spindle radial error motion, vibration, and thermal drift. The spindle's radial error motion has not been measured yet. Neglecting spindle radial error motion, the variance in $X$ is given by Eq (6).

$$\sigma_X^2 = \sigma_{z-axis}^2 + \sigma_{thermal}^2 + \sigma_{vibration}^2 \tag{6}$$

The variance in the gap is difficult to measure and is also assumed negligible. Substituting Eq (6) into Eq (5) provides an expression for $\sigma_R^2$.

$$\sigma_R^2 = \sigma_{z-axis}^2 + \sigma_{thermal}^2 + \sigma_{vibration}^2 + \sigma_{D_w}^2 \tag{7}$$

The variances on the right hand side of Eq (7) were measured and the 95% confidence interval estimators were calculated. Table 2 lists a summary of the standard deviation and 95% confidence intervals for these error sources and the predicted variance in the radius of the micro shafts. The

variation in the wire diameter dominates since it is an order of magnitude above the other error sources and the roughness values.

**Table 2. Process Errors and Predicted Variation in Radius of Micro Shaft**

| Error Source | Standard Deviation & 95% Confidence Intervals | | |
|---|---|---|---|
| | Lower Limit (μm) | Std. Dev. (μm) | Upper Limit (μm) |
| Z-axis | 0.08 | 0.089 | 0.097 |
| Thermal | 0.149 | 0.1644 | 0.181 |
| Vibration | 0.0146 | 0.0147 | 0.0148 |
| Wire ($D_W$) | 0.655 | 0.726 | 0.797 |
| **Radius, $R$** | 0.676 | 0.75 | 0.823 |

The results of the error model suggest that $\sigma_R$ should lie between 0.676 and 0.823 μm. To verify this result the filtered micro shaft profiles (excludes roughness) are used to calculate the standard deviation of the entire population. The standard deviation of the distances, $d_i$, from the least-squares line is found to be $\sigma_d$=0.823 μm. This value is within the predicted standard deviation interval and implies the dependence of edge straightness on machine/process errors rather than process variables.

## Conclusion

This paper reports the precision of micro shafts manufactured with wire electro discharge grinding (WEDG). The precision was assessed by measuring the roughness and straightness of edge profiles for 81 shafts, machined with various process conditions. The average surface roughness, $R_a$, varied between 0.067 and 0.781 μm and depended upon capacitance and voltage. The straightness varied between 3.05 and 12.04 μm but was independent of all process conditions except aspect ratio. Straightness variation corresponded well to the predicted variation in shaft radius as determined by combining variation in machine errors and the diameter of the anode wire.

## References


[1] Egashira, K. and K. Mizutani. "Micro-Drilling of Monocrystalline Silicon Using a Cutting Tool". *Precision Engineering*. V. 26, N. 3. July, 2002. p. 263-268.

[2] Wada, T, T. Masaki, and D. Davis. "Development of Micro Grinding Process using Micro EDM Trued Diamond Tools". *ASPE Proceeding, Annual Meeting*. 2002. p. 16-19.

[3] Masuzawa, T. "Wire Electro-Discharge Grinding for Micro-Machining". *Annals of the CIRP*. Vol. 34, No. 1. 1985. p. 431-434.

[4] Sato, T., T. Mizutani, and K. Kawata. "Electro-Discharge Machine for Micro Hole Boring". *National Technical Report*. Vol. 81, No. 5. Oct. 1985. p. 105-113.

[5] Masuzawa, T., C.-L. Kuo, and M. Fujino. "A Combined Electrical Machining Process for Micronozzle Fabrication". *Annals of the CIRP*. V. 43, N. 1. 1994, p 189-192

[6] Allen, D.M. and A. Lecheheb. "Micro Electro-Discharge Machining of Ink Jet Nozzles: Optimum Selection of Material and Machining Parameters". *Journal of Materials Processing Technology*. Vol. 58. 1996. p. 53-66.

[7] Masuzawa, T., Y. Hamasaki, and M. Fujino. "Vibroscanning Method of Nondestructive Measurement of Small Holes". *Annals of the CIRP*. V. 42, N. 1. 1993. p. 589-592.

[8] Masuzawa, T., B.J. Kim, C. Bergaud, and M. Fujino. "Twin-probe Vibroscanning Method for Dimensional Measurement of Microholes". *Annals of the CIRP*. V. 46, N. 1. 1997. p. 437-440.

[9] Yu, Z., T. Masuzawa, and M. Fujino. "Micro-EDM for Three Dimensional Cavities - Development of Uniform Wear Method". *Annals of the CIRP*. Vol. 47, No. 1. p. 169-172.

[10] Yu, Z., T. Masuzawa and M. Fujino. "3D Micro EDM with Simple Shape Electrode: Part 1 -- Machining of Cavities with Sharp Corners and Electrode Wear Compensation". *International Journal of Electrical Machining*. No. 3. p. 7-12. 1998.

[11] Yu, Z., K.P. Rajurkar, and P.D. Prabhuram. "Study of Contouring Micro EDM Characteristics". *Proc. of the 10th Int. Conf. on Precision Engineering*. Japan Society for Precision Engineering (JSPE). Yokohama, Japan. July 18-20, 2001. Kluwer Academic Publishers, Boston, MA. P. 199-203.

[12] Masaki, T., T. Mizutani, K. Yonemaochi, and A. Tanaka. "Electric Discharge Machining Method and Apparatus for Machining a Microshaft". United States Patent and Trademark Office. Patent Number 4,900,890. Feb. 13, 1990.

[13] Raja, J., B. Muralikrishnan, S. Fu. "Recent Advances in Separation of Roughness, Waviness, and Form". *Precision Engineering*. V. 26, N. 2. 2002. p. 222-235.

[14] Weber, T., S. Motavalli, B. Fallahi, and S.H. Cheraghi. "A Unified Approach to Form Error Evaluation". *Precision Engineering*. V. 26, N. 3. July 2002. p. 269-278.

[16] Wada, T, T. Masaki, D. Davis. "Development of Micro Grinding Process using Micro EDM trued Diamond Tools". *ASPE Proceeding, Annual Meeting*. 2002. p. 16-19..

[17] Estler, Tyler. "Calibration and Use of Optical Straightedges in the Metrology of Precision Machines". *Optical Engineering*. V. 24, N. 3. 1985, p. 372-379.

[18] Serrano, Sergio. *Engineering Uncertainty and Risk Analysis*. Hydro Science Inc., 2001.

# MASTERING AND REPLICATON OF PRECISION MICRO-STRUCTURED SURFACES

Dr. G. Michael Morris
Corning Rochester Photonics Corporation, 115 Canal Landing Blvd., Rochester, NY 14626
e-mail: MorrisGM@corning.com

*Abstract*

Precision surface-relief optical elements with depths up to 160 micrometers are created using a single-point laser pattern generator. A thick photoresist layer is exposed using a focused beam from a helium-cadmium laser. Development of the photoresist yields the desired surface profile. The transfer characteristics for the various steps of the mastering and replication process are described. The laser pattern generator provides a new and powerful system for fabrication of arbitrary, continuous-relief structured surfaces, including microlenses (spheres, cylinders, aspheres, hyperbolas, toroids), diffractive and refractive phase plates, display screens, beam homogenizers, prism arrays, and master elements for a variety of printing processes.

## The Fabrication Process

In this paper we will highlight recent advances in laser pattern generation (LPG) techniques for mastering of precision structured surfaces. A system diagram and photograph of an LPG system is shown in Fig. 1. The LPG method involves focusing a laser beam onto a substrate coated with a thick layer of photoresist. As the focused beam is scanned under computer control across the surface in a raster-scan format, the intensity is varied so as to expose the photoresist in a specified and continuous manner. Development of the photoresist yields the desired surface profile. The photoresist master can then be used to create a tool suitable for a variety of replication processes, e.g., a nickel electroform or a silicone-rubber replica, etc.

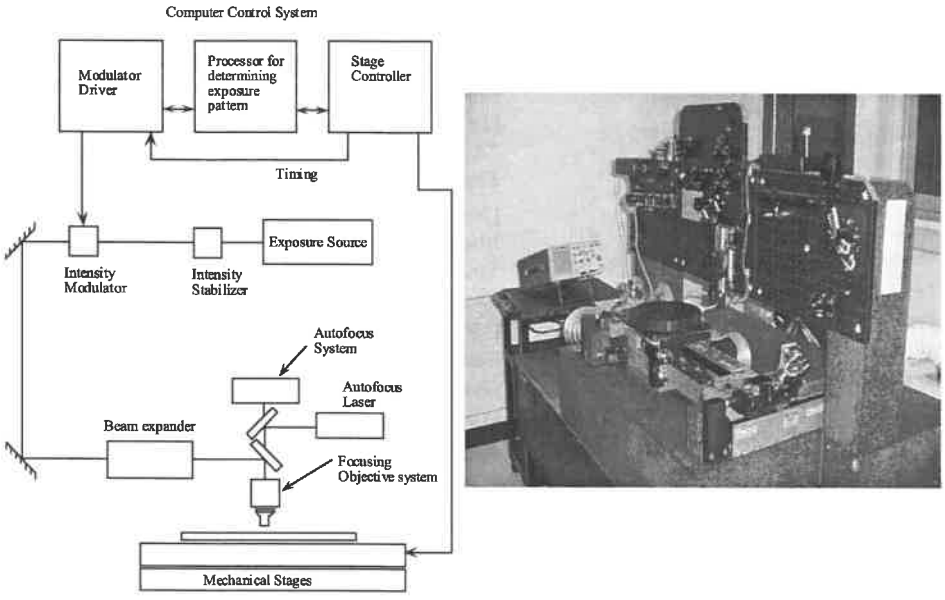


Fig. 1. Schematic and photograph of a single-point laser pattern generator.

A flow chart for the mastering and replication process is illustrated in Fig. 2. In this process a thick layer of photoresist is deposited on a substrate. The photoresist layer is then exposed using a focused laser beam that is scanned across the surface in an x-y raster format using air-bearing translation stages. As the beam is scanned the intensity of the beam is varied. The photoresist is then developed to obtain the desired surface-relief profile. Precision surfaces profiles have been obtained for depths up to 160 micrometers with surface profile accuracies in the range of 0.1 μm to 0.2 μm, and rms surface roughness less than approximately 50 nanometers. To our knowledge these are the deepest micro-structures that have been produced using LPG methods.

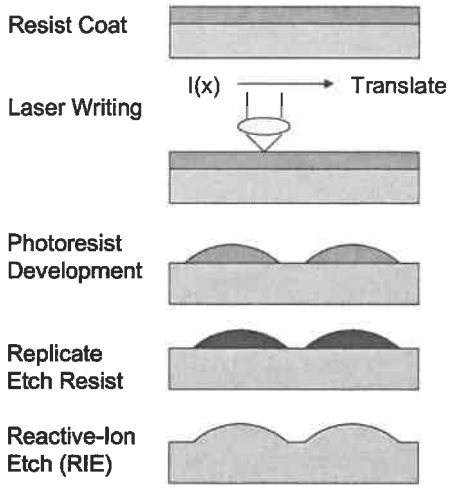


Fig. 2. Flow chart for the LPG mastering and replication process.

The developed photoresist, or "grand master," can then be used to create a hard or soft tooling suitable for a particular replication process.

Tooling for a variety of replication processes have been created, including tools for compression and injection molding, "cast-and-cure" replication using UV-cured and thermally cured epoxies and photopolymers, and replication of an etch resist for use in a reactive-ion etching (RIE) system, which is used to transfer of the desired surface-relief pattern directly into a substrate material, such as fused silica, silicon, germanium, etc.

Results of the entire LPG mastering and replication process are illustrated in Figs. 3 and 4. Figure 3 contains photographs of the surface finish of a refractive, 1.3-mm diameter microlens with surface sag of 116 μm. The photographs were taken at 50X magnification.

Figure 4 illustrates the surface-profile accuracy that can be obtained using the LPG fabrication process. The fused-silica microlens in this measurement has a surface sag of 68 μm. The theoretical surface profile, obtained from a commercial lens-design program, is depicted in Fig. 4(a) using a thin black line. The measured surface profile, is illustrated by the broad (green) line, which overlays the theoretical curve. In Figure 4 (b), the measured surface-sag error is plotted versus the radial position across the microlens. Note that the measured surface-sag error is less than approximately 0.2 μm over the entire 600-μm-diameter clear aperture of the microlens.

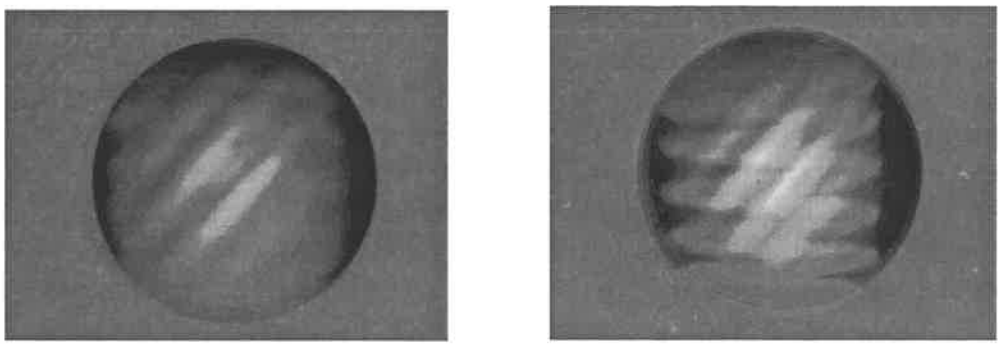

(a) (b)

Fig. 3. Nomarski microscope photograph of (a) top surface of a microlens replicated in an etch resist [pre-etch surface finish], and (b) top surface of the same microlens after transfer into a fused silica substrate [post-etch surface finish]. Note that the spiral-shaped pattern in the photographs is the image of the illumination filament.

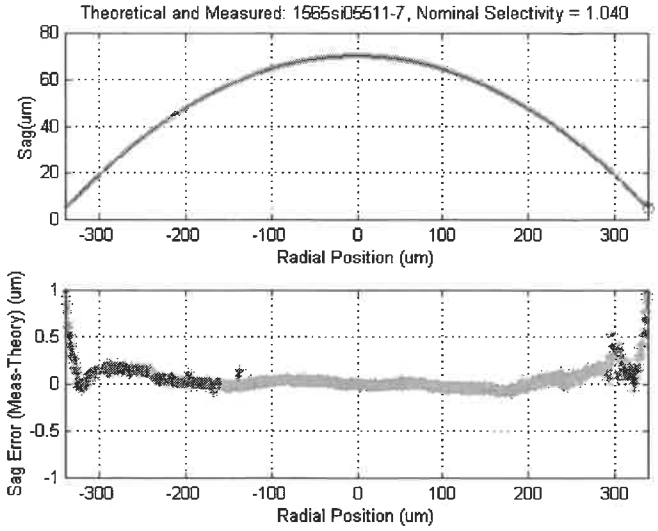


Fig. 4. Surface profile plots of a fused silica microlens the LPG fabrication process. In the top graph, the thin black line is the theoretical (desired) surface profile, and the broad green curve, which overlays the theoretical curve is the measured surface profile for the lens. The bottom graph is a plot of the sag error (measured – theory) as a function of the radial position across the lens.

## An Application – Engineered Diffusers™

The LPG process outlined above provides a powerful way to fabricate entirely new classes of large-area structured surfaces for a variety of applications that could not be created previously. Basically, the LPG system allows one to start with a "clean sheet of paper" and create a precision structured surface that produces all of the desired attributes for the particular application.

An important application that illustrates the features of the LPG fabrication process is the creation of new high-performance screens for projection display systems.

Screens for the high-performance projection systems based on micro-display technology need incorporate the following design requirements:

- Light Management (light where the viewer is)
- High Transmission
- High Resolution
- No Color Effect/Artifacts
- No Image Effects/Artifacts (Moiré patterns)
- No/Low Speckle
- Reasonable Manufacturing Tolerances

An interesting design that satisfies all of the above design requirements utilizes the concept of random microlens arrays. To achieve scattering angles on the order of +/- 75 to 80 degrees horizontally and +/- 25 degrees in the vertical direction, the toroidal-shaped microlenses in the array must have steep surface profiles and sharp transitions between the microlenses. The positional coordinates (x y, z) and radius of curvature of the microlenses can all be randomized. Randomization of these variables permits one to shape and homogenize the light-scattering distribution and to eliminate image and color artifacts, which are present when a regular array of microlenses is used. Finally the size of each microlens is chosen to be small enough to provide high resolution, yet large enough so that average diameter is greater than the coherence length of the light source, thereby greatly reducing (or eliminating) any speckle effects in the display. The performance of this new class of Engineered Diffusers™ will be described during the presentation.

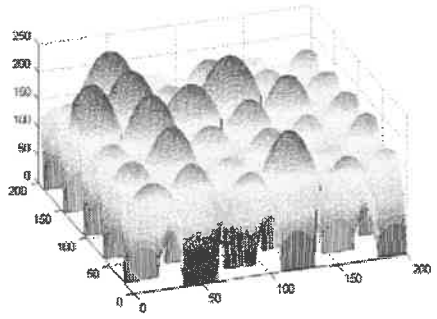

(a)

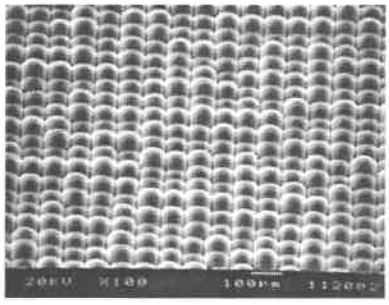

(b)

Fig. 5. (a) 3-D plot of an Engineered Diffuser™ (random microlens array) for a high-performance projection display, and (b) SEM photo of an LPG-produced random microlens array, replicated in silicone. [Engineered Diffusers™ is a registered trademark of Corning Rochester Photonics Corporation.]

*Acknowledgement:* Special thanks to the entire Corning Rochester Photonics team, particularly T. Sales, G. Gretton, D. Mauer, T. Tiberio, E. Prince, S. Chakmakjian, D. Schertler, S. Ward, and M. Evans.

**Growing Up, Additive Processes in MEMS Fabrication and Packaging**

Reiner Götzen, CEO microTEC Gesellschaft für Mikrotechnologie mbH Germany
www.microtec-d.com

The most important growth factor in nature is light. Its secrets have been the basis of several technological revolutions. Growth through light is the paragon of generative technology.

Light can not only be used for the polymerization of organic materials, but also for the structured growth of inorganic structures. Thus, light provides us with an ideal and cheap tool for production.

For the production of MEMS, we need the capability to combine organic and inorganic materials with their different properties in the smallest possible space. The mechanical, electrical, optical, chemical and biological functions can be deposited from the gaseous or liqued state with nanometer scale accuracy according to the desired property using light.

Today, the question posed by Richard Feynmann at the annual meeting of the American Physical Society at the California Institute of Technology: „Is there a physical process for the synthesis of any arbitrary chemical substance?" can be answered with „yes".

The relevant physical processes span a range from the well-known photopolymerization process to the deposition of molecules induced by focused electromegnetic radiation and the two-photon process for polymerization.

An important condition for the economic application of these processes is a build-up rate appropriate to the desired volume, or, figuratively put, „small bricks for small houses and big bricks for big houses". Also of importance is the compatibility fo the physical processes and conversion to a batch (large-scale, mass-production) process.

The RMPD technologies have combined these principles, offering the possibility of the integration of electronic parts using 3D-CSP, the integration of electrical, optical biological and chemical functions using RMPD-multimat while possesing a build-up rate appropriate to the volume scale.

University of Florida, 2003 Winter Topical Meeting, January 22-23, 2003
Machines and Processes for Micro-scale and Meso-scale Fabrication, Metrology and Assembly, Session II Forming, Molding, & Additive Processes

# MATERIAL BEHAVIOR IN MICROFORMING AT ELEVATED TEMPERATURE

Emil Egerer, Ulf Engel
LFT – Chair of Manufacturing Technology, Erlangen, Germany

## Abstract

The application of metal forming to the manufacturing of microparts is still not widespread. One reason is that the know-how of conventional forming cannot be simply transferred to the microscale. This is due to the so called size effects, which in cold forging can be observed in terms of effects on material flow, on tribological behavior and on working accuracy. Investigations at cylindrical microparts at stainless steel (X4CrNi18-10) produced by cold upsetting reveal that there is a transition in the observed material behavior from homogeneous to inhomogeneous continuum being one of the reasons for a very unstable processes. The forming behavior mainly depends on the part's individual grain constellation leading to a rather unpredictable forming result and making a process design impossible. One possibility to counteract the inhomogeneous material character is to process at elevated temperature. During forming at elevated temperature additional slip systems are activated with the effect to reduce the dependency on single grains. This improves not only the material flow but also the reproducibility of process variables like the flow stress.

## Introduction

The trend towards higher integrated functional density and miniaturization in electronic and micro mechanical products is still unbroken causing an increased demand for metallic parts of smallest dimensions and closest tolerances. Many modern products like mobile phones, hand held computers or navigation systems contain such small parts. According to the actual NEXUS market analysis the world wide total turnover of microsystems for the year 2005 is estimated to be in the range of 68 billion US$ [1]. The production of these components demands for technologies which enable to produce high numbers of pieces economically, environmentally friendly and reliably. Metal forming technology meets these demands and is already occasionally applied for the production of smallest parts like springs, screws, gears, rivets, contacts and shafts. Microforming is defined as the production of metallic parts by forming with at least two part dimensions in the sub millimeter range, which in the following will be termed by microparts [2]. However, facing the fact how many of those parts are produced today by machining, the break through of the new technology of microforming is still missing. One reason for this is the lack of an appropriate system technology. Another reason concerns the process itself and is due the fact that the know-how of conventional forming cannot be simply transferred to the microscale because of so called miniaturization effects influencing the material flow behavior, tribological conditions and working accuracy. Up to now the realization of microforming processes is still characterized by empirical process design, which especially in this case is confronted with problems regarding tool design and process control. It is well recognized that in order to facilitate a more extensive use of the microforming technology, an improved understanding of the mechanisms causing the size effect is indispensable. Therefore a fundamental basis for the design of micro metal forming processes has been created. This paper takes as a basis that in microforming the continuum cannot be regarded as a homogeneous one as it is done in the case of conventional forming, being the main reason for the observed scatter of process variables [3]. In order to counteract this problem, warm forging is investigated expecting an ho-

mogenizing effect. First results will show that in fact scatter can be reduced by forging at elevated temperature, which is regarded as an important presupposition for improved working accuracy. Furthermore the investigation shows a temperature influence on mechanical properties like work hardening. In addition a distinct temperature effect on the homogeneity of deformation is observed.

## Experimental Methods and Set-Up

All the investigations reported here are done on cylindrical specimens of stainless steel (X4CrNi18-10, diameter 0.48 mm, height 0.72 mm). This alloy has an high industrial relevance since it is quite frequently used for microparts in the field of fine mechanics and medicine technology due to its favorable mechanical properties (e.g. strength, machinability). In terms of the experimental investigations it is important that the grain size of the material can be varied by by heat treatment in a range of approximately 10 µm to 100 µm. Specimens were machined from drawn wire and finished by the highest possible accuracy in order to minimize geometrical effects. For the cold and warm forging experiments a mechanically driven material testing system (type MTS Synergy 100 (0.5 kN nominal press load)) has been used (Fig. 1a). The procedure of material tests especially in warm microforming necessitates a manipulation unit for the handling of microparts. In this case a properly designed automatic handling system is used, which is first of all due to the necessity of the operator safety considering the high process temperatures. Besides, the automated operating sequence guarantees the reproducibility of heating conditions i. e. temperature and heat-up time. Furthermore, an exact positioning of the specimen guaranteed by this handling stage leads to a reduction of perturbations, which e.g. lowers scattering of the flow stress evaluated by upsetting tests. The technology of the handling system used in this experimental setup was already developed by the authors as a so called cross transport system in an former project and successfully implanted in a prototype of a micro former. The handling system consists of a linear translation stage for the part transfer and a special designed vacuum pipette for the gripping of the part (Fig. 1c). The advantages of this system are the excellent dynamic behavior, the high speed and the high precision [4, 5].

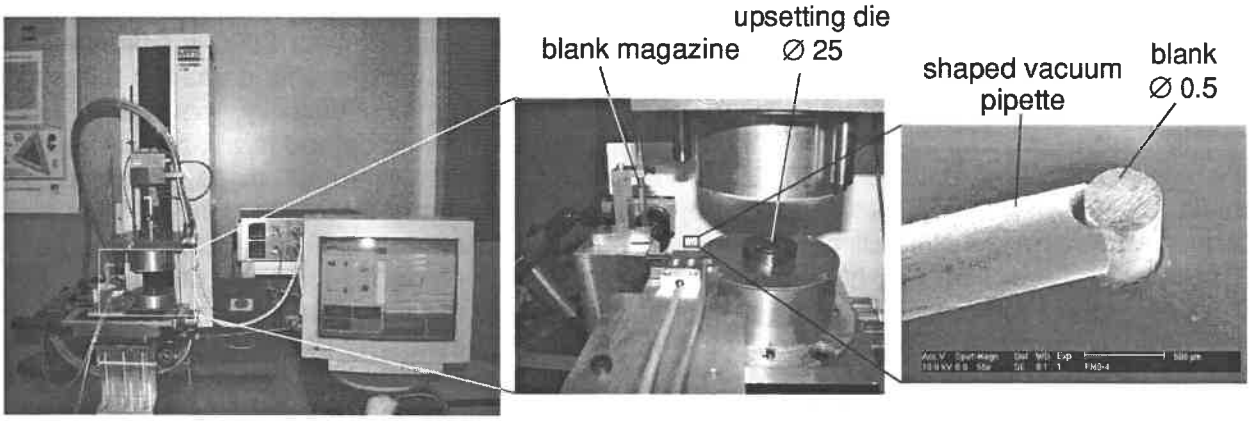


**Fig. 1:** different views of the experimental set-up. a) total view, b) tool area with dies, blank magazine and handling unit and c) vacuum pipette with a blank

In contrast to macro forging processes the micro part cannot be heated up outside of the tool area, because the high ratio of surface to volume favors the heat dissipation with the result that the micropart will be cooled down before starting the forming process. In order to reach a controllable temperature within the part the tools are heated up by special heating elements so that the micropart itself is warmed up purely by conduction within seconds to get a sufficient ho-

mogenous temperature distribution. Finally, hardness measurements used to identify the inhomogeneity of work hardening on a micro structural scale were done with a special set-up to measure the so called universal hardness HU0.1 (Fischerscope H100VP, indentation force 0.1 N) with a scanning facility [6].

## Scatter of process variables

The flow curve is one of the most important criterions for the design of bulk metal forming processes and is gained by upsetting tests. One result of the investigations on geometrically similar scaled upsetting tests at room temperature is that the scatter of the flow stress increases with decreasing specimen size [7]. With respect to the process stability and reliability the increase of scatter is rather problematic. The reason is the following: Depending on the grain size, in microforming the whole work piece or single work piece structures to be shaped may consist of only a few grains. This means that the forming result is strongly depending on the orientation even of single grains. Former investigations showed that the material cannot be considered as a homogeneous continuum like in conventional forming but as a inhomogeneous one. One countermeasure to this material behavior is to perform the forming process at elevated temperature as done in warm forming. In this context warm forming is defined as - considering economical reasonable terms - forming above room temperature while hardening effects still occur [8] and recrystallization may not take place during forming. As shown in Fig. 2 the investigations of micro upsetting tests at different temperatures bring up two results.

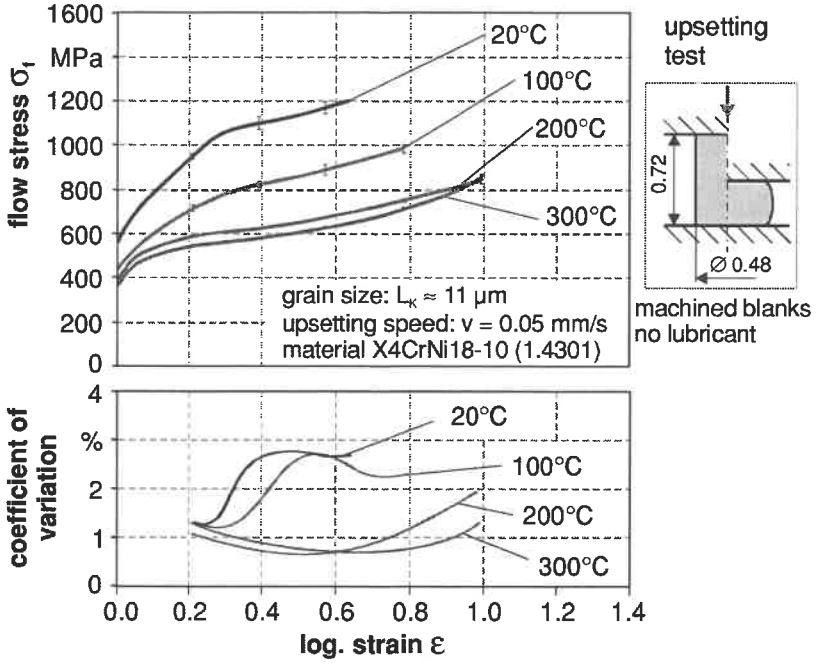


**Fig. 2:** flow stress and scatter at different temperatures gained by upsetting test

The first result is the reduction of the flow stress with increasing temperature as expected from macro forming. The second effect is the reduction in scatter of the flow stress. As a measure for the scatter the coefficient of variation (standard deviation in relation to mean value) was calculated and is depicted in the lower diagram of Fig. 2. Compared to room temperature the reduction of the coefficient of variation of the flow curve at a moderate temperature level of 200°C is approximately 70% at a strain of 0.6.

## Mechanical properties

A further effect regarding the mechanical properties of cold microformed parts is the inhomogeneous forming behavior characterized by distinctly different deformations of neighbored grains. To get knowledge about the local forming status hardness measurements at forged specimen were performed. Actually the cross sections of cylindrical specimens were scanned with micro

hardness measurements. Fig. 3 shows three horizontal measurement profiles taken in the middle of the specimens which were upset at cold and warm forging conditions, room temperature and 300°C, respectively. The analysis yields two results. The first one shows that the average specimen hardness decreases with increasing temperature which also can be expected as known from conventional forming. The second effect shows, as can be seen at the spread of the hardness measurement profiles, that in both strain cases ($\varepsilon = 0.2$ and $\varepsilon = 0.6$) the scatter of the single hardness spots decrease at elevated temperature. The temperature effects that additional slip systems are activated in the material, so that the dependency of the material flow on the grain orientation and location is reduced. This influences the material behavior positively also in unfavorable orientated grains. Therefore, the temperature homogenizes the overall deformation in that way as the neighbored deformation zones are evened out.

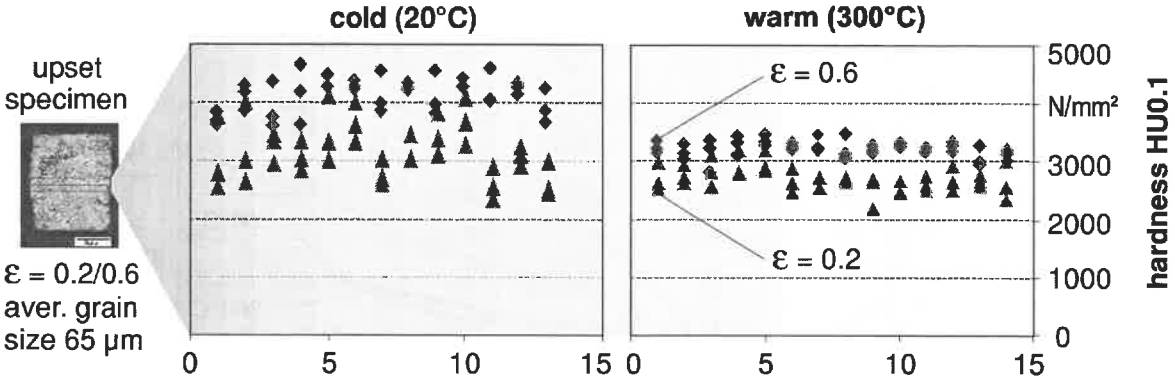


**Fig. 3:** profiles of hardness measurements at specimen of different strain and temperatures

Regarding the entire cross section area of the specimen a characteristic value is derived by statistical methods in order to characterize the degree of inhomogeneity. Starting from two adjacent points all the hardness gradients (hardness difference related to the distance of in mean 30 µm) are calculated line by line and column by column, corrected by the macroscopic contour of hardness which is approximated by a polynomial of 4$^{th}$ degree, and finally weighted by its significance dependent on its absolute value. The mean value of the resulting distribution is taken as average hardness gradient AHG characterizing the homogeneity. In Fig. 4 these values are shown for two cases of strain ($\varepsilon = 0.2$ and $\varepsilon = 0.4$) as function of the temperature which confirm the effect of temperature towards a more homogeneous deformation. The temperature increase leads to a decrease of approximately 50% at the average hardness gradient which means that homogeneity improvement is in evidence. Additionally, the average of the absolute hardness is dis-

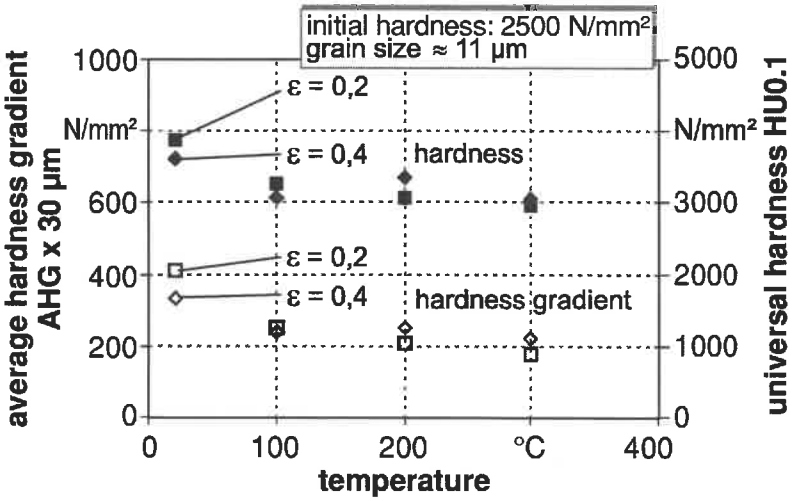


**Fig. 4:** Average hardness gradient AHG and universal hardness HU0.1 of upset cylinder specimens.

played, indicating that even though forming at high temperature work hardening still occurs. Compared to the initial hardness of 2500 N/mm² (at room temperature) the hardening effect at 300°C is approximately 20%. As it also can be seen at both the hardness as well as the hardness gradient the main step of these values takes place when increasing the temperature level from room temperature up to 100°C. A further increase of the temperature does not influence these parameters significantly although the flow stress is still decreasing at these temperatures. This result is correlating well to the investigations done by the authors on cylindrical specimens made of CuZn15 (diameter 0.5 mm, upset ratio 1.5) also processed by upsetting. Thus, it can be concluded, that by elevating the operating temperature on a moderate warm forging level of 100°C the desired effect of homogenization is reached without losing the effect of work hardening.

## Conclusion and Outlook

Because of the fact that microforming processes are characterized by the existence of only a few grains in the deformed area, the material cannot be considered as a homogeneous continuum anymore. The inhomogeneous material flow is mainly caused by the random size, location and orientation of individual grains. Therefore cold microforming processes, inter alia, are characterized by two effects. One effect is the increasing scatter of such important material parameters like the flow stress, another effect is the inhomogeneous local deformation behavior. These effects are leading to a more or less random forming behavior and almost unpredictable mechanical properties of the produced micropart and, thus, are making a process design as applied in conventional forming impossible. As a countermeasure forging at elevated temperature reduces the observed unfavorable characteristics of cold micro forming yielding a more homogeneous deformation. The different formability of the grains is evened out by thermally activating those slip systems which are not active at cold conditions. It is shown that even temperatures of moderate level are sufficient to improve the homogeneity and to reduce distinctly the scatter without losing the benefits of cold forging such as work hardening. In contrast to upsetting where the share of free surfaces is very high future investigations will be performed at the cup backward extrusion process with elevated temperature. The cup backward extrusion process is characterized by a high share of material with tool contact so that the material flow is increasingly influenced by the complex tribological conditions.

## Acknowledgement

All the research done by the Chair of Manufacturing Technology was supported by the German Research Foundation (DFG).

## References

1 WECHSUN, R. et al.: Nexus Market Analysis for microsystems 2000 - 2005. Nexus Task Force Market Analysis. Wicht Technologie Consulting. Munich, 2002.

2 GEIGER, M.; KLEINER, M.; ECKSTEIN, R.; TIESLER, N.; ENGEL, U.: Microforming. Keynote Paper. Annals of the CIRP, 50(2001)2, 445-462

3 ENGEL, U.; EGERER, E.: Basic research on cold and warm forging of microparts. In: Key Engineering Materials, 233-236(2002), 449-455

4 GEIGER, M.; EGERER, E.; ENGEL, U.: Cross Transport in a Multi-Station Former for Microparts. In: WGP (eds.): Production Engineering, 9(2002), 101-104

5 EGERER, E.; ENGEL, U.; VAN DER HEYD, G.: Handling of Microparts in a Multi-Station Former. In Balsamo, A. et al. (eds.); 2nd International Conference euspen, May 27th-31st, 2001. Turin (Italy): Augusta Edizione Mortario, 2001, pp. 836-839

6 Norm: ISO/DIS 6441-3, edition 2001-03: Paints and varnishes - Determination of micro-indentation hardness - Part 3: Determination of universal hardness and related properties using a Vickers indentor (Revision of ISO 6441:1984).

7 Tiesler, A.: Mikroumformtechnik: Miniaturisierungseffekte beim Fließpressen. In: Geiger, M.; Feldmann, K. (eds.): Reihe Fertigungstechnik Erlangen Nr. 120. Meisenbach, Bamberg, 2002.

8 ICFG Document No. 12/01: Warm Forging of Steel. In: International Cold Forging Group. Meisenbach, Bamberg, 2001, pp. 5-7

# The Reliability of Dynamic Interfaces in LIGA Microsystems

S. V. Prasad, T. R. Christenson, M. T. Dugger, J. R. Michael and C. W. Vanecek
Sandia National Laboratories
Albuquerque, NM 87185

Microelectroelectromechanical systems (MEMS) have dimensions of microns to several millimeters, depending upon the application. Due to the planar nature the fabrication methods, forces tend to be transmitted between structural elements in the plane of the device, leading to the result that sliding interactions are predominantly between sidewalls. The morphology of sidewalls and sliding interactions amongst them play a crucial role in determining the performance and reliability of MEMS (Fig. 1).

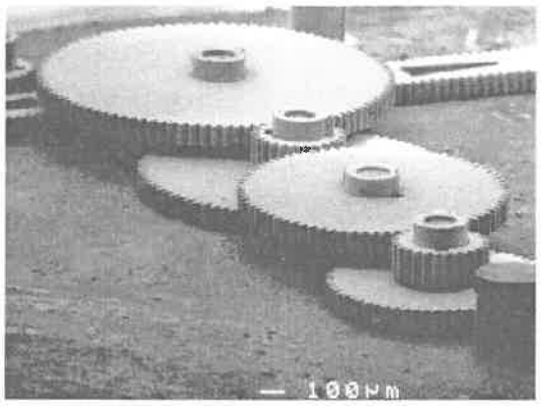


*Fig. 1 - A fully assembled LIGA gear train and track mechanism showing several sidewall-to-sidewall-to-sidewall sliding contacts. The aluminum substrate was conventionally machined to accept press-fit steel gage on which keyed bushings and gears were assemblied.*

A variety of fabrication methods are available to build Microsystems: bulk micromachining, surface micromachining (SMM), LIGA (German acronym for Lithographie, Galvanoformung und Abformung), and meso-scale machining. In LIGA [1,2] individual mechanical elements are created by deposition of material into microfabricated molds, followed by assembling the micromachine elements into a MEMS device. LIGA can be combined with electronics as a post-process.

The major objective of our work was to evaluate the tribological (friction and wear) behavior of dynamic interfaces in structures created by the LIGA process, specifically electroformed metal structures with dimensions of 0.01 to several mm, and thickness up to 500 µm. LIGA structures can be made from virtually any material that can be electroformed at low stress from solution. Ni and Ni alloys (Ni-Co, Ni-Fe) are the most commonly used materials at the present time, but a much a wider set of materials including copper, gold, and silver can be electroplated to produce LIGA parts. By incorporating particles of different materials, such as solid lubricants or hard particles into the plating bath, self-lubricating or dispersion strengthened composites can be fabricated. Alternatively, a metal micromold can be fabricated as a negative of the final part. This mold can then be filled with ceramics, polymers, or polymer composites, further expanding the materials set for design of Microsystems. In the first part of the study we have characterized the sidewall morphologies of LIGA fabricated nickel parts using scanning electron and atomic force microscopes [3]. The LIGA

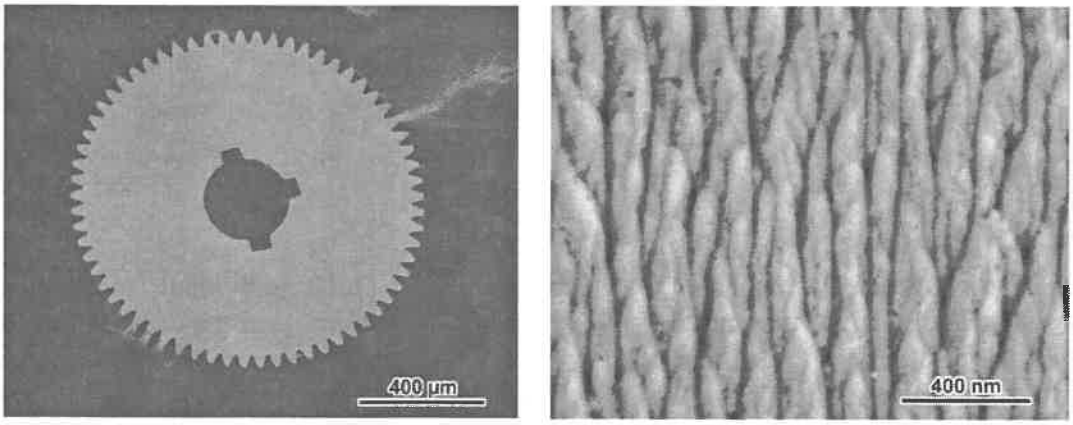


*Fig.2 – LIGA processing produces distinct sidewall morphologies. (a)SEM image of a microgear, (b)higher magnification micrograph showing typical texture-like morphology.*

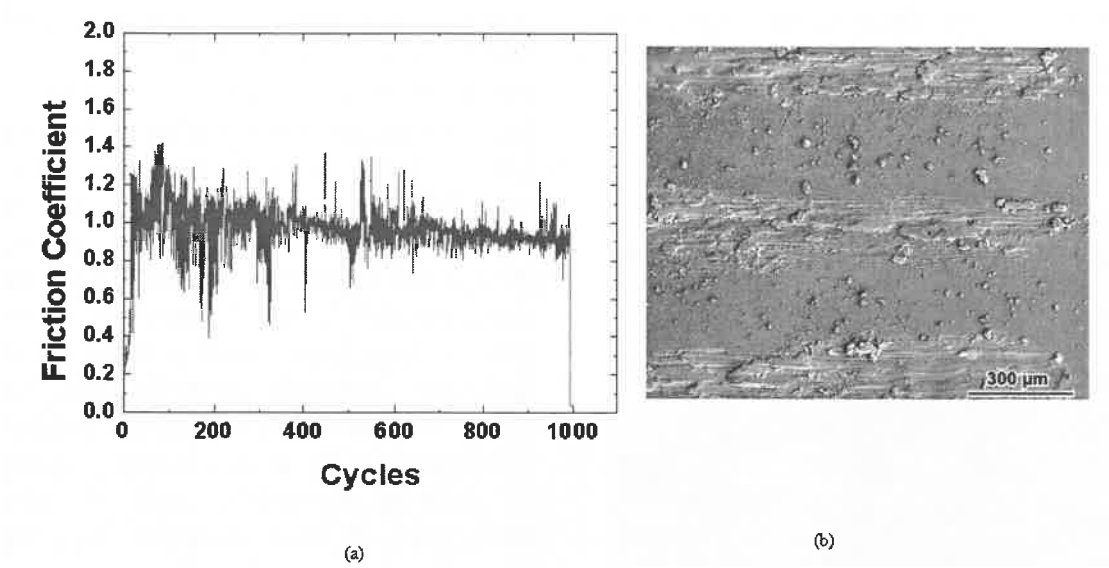


*Fig.3 – (a) Typical friction behavior of an electroplated Ni surface against a steel ball in dry nitrogen atmosphere, (b) scanning electron micrographs of wear scars showing deep grooves and particulate wear debris.*

processed parts showed unusual sidewall morphologies that are not commonly seen in macromachined parts (Fig. 2). The sidewall morphology could influence the adhesion between contacting surfaces in LIGA Microsystems.

The ideal way to evaluate the tribological behavior of LIGA Microsystems materials is to measure the friction forces between sidewall contacts in load regimes relevant to Microsystems operation. However, until such test

procedures are established, a ball-on-disk tribometer was used as a screening tool for materials evaluation. We shall also present the basic tribological measurements on electroformed nickel surfaces. Shown in Fig. 3 is a typical friction behavior of an electroplated Ni test coupon against a 440C steel ball. The test was performed in a dry nitrogen atmosphere at an applied load of 100 mN. The surface of the electroplated Ni film was metallographically polished. The high coefficient of friction (0.8 to 1.2) and large fluctuations in friction force (Fig. 3a) implies that the tribological behavior is of stick-slip type that is typical of metallic contacts. The interface adheres momentarily until sufficient shear force develops to fracture the junctions, at which time the slider advances rapidly to a new location, only to become adhered again. Additionally, generation of debris can interfere with the performance and reliability of the microsystems, specifically if the debris approaches the feature size of the elements (Fig. 3b). Since the relative maturity of Ni and Ni alloy processing make them the materials of choice for LIGA microsystems, coatings may be essential to mitigate tribological issues and improve the reliability of dynamic interfaces.

There are a variety of techniques to deposit tribological coatings on conventional machine elements, e.g. burnishing, resin bonding, physical vapor deposition, chemical vapor deposition. However, the miniature nature of LIGA MEMS elements – several hundred microns to millimeters in size – poses a tough challenge to the coatings community. Handling of individual parts is impractical, and applying coatings using such techniques as resin bonding and burnishing is not possible. Physical vapor deposition is a line-of-sight process, making it difficult to deposit material on the sidewalls where it is needed. Chemical vapor deposition of tribological coatings such as diamond, though conformal in nature, requires a high temperature process that could potentially alter the microstructure of the base Ni alloy. We have devised a novel coating strategy to circumvent these problems. Instead of coating the individual parts, the entire wafer was coated before releasing the parts, i.e. after electroplating, planarizing, and dissolving the mold material. Coatings were applied by the plasma enhanced chemical vapor deposition (PECVD) technique in which ionized species were deposited onto biased substrates thereby limiting the substrate temperatures to below 150°C. The coated wafer was backsputtered (ion etched) to remove the coating from the bare substrate to make the substrate/LIGA part interface accessible to the release agent. Since sputtering is a line-of-sight process, this only removes the coating from the planar surfaces of the parts where it is not critical, leaving the sidewalls untouched. The coated parts were subsequently released from the wafer using the standard LIGA process.

This technique has been applied to deposit a 100 nm thick diamond-like nanocomposite (Dylyn $^{TM}$) from Bekaert Advanced Coating Technologies on Ni LIGA parts. The films were deposited by the PECVD process, in which a plasma is formed from a siloxane precursor. The films contain a diamond-like network of a-C:H and a second network of Si:O with minimal bonding between the two networks. This structure is claimed to have significantly lower internal stresses than conventional DLC, resulting in good adhesion to most substrates with no

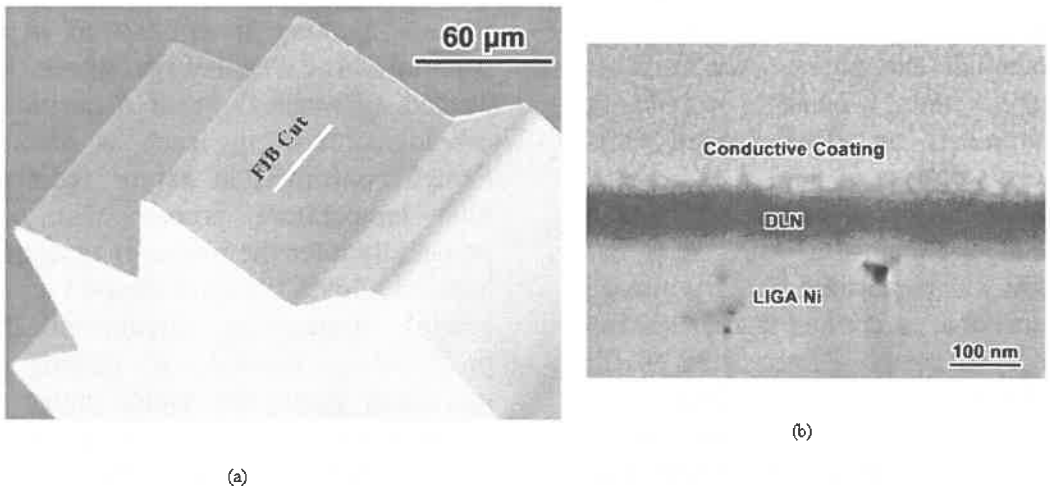


*Fig.4 – A wafer with LIGA parts that was coated with diamond like nanocomposite (DLN) after removing the PMMA mold material. The parts were still unreleased from the wafer at this stage.*

interlayer. A DLN coated LIGA Ni gear after release from the substrate is shown in Fig. 4a. A focused ion beam (FIB) cut taken from the sidewall of the coated gear confirmed that the 100 nm thick DLN coating was intact, practically unaffected during backsputtering and subsequent release. Though cross-sectional microscopy revealed that the coating was present on the sidewalls, subsequent analyses by microRaman spectroscopy revealed that the composition of the material on the sidewalls differed from than on the planar surfaces. Therefore, the deposition technique was modified to obtain the diamond-like structure on the sidewalls identical to that on the planar surfaces, by introducing planetary rotation to the substrate. The friction coefficient of DLN coated LIGA Ni coupons measured under identical conditions was reduced to 01. Nickel structures made from LIGA exhibit columnar texture that is typical of most electroplated metals. Microstructural and texture analysis on cross sections of wear scars by electron backscattered analysis showed that columnar grains could bend in the direction of sliding [4]. The DLN coating was also effective in protecting the dynamic interfaces from wear-induced microstructural changes.

In principle, the procedure described here can be applied to deposit any tribological coating. For line-of-sight processes, the substrates must be fixtured in such a way that the deposited material can form on the sidewall surfaces. Substrate rotation alone may not suffice, and planetary motion may be required to expose all sidewall surfaces to the source. Then the coating must be removed from the planar surfaces to facilitate releasing the parts and to preserve edge geometry. Backsputtering conditions and time must be optimized for the type of coating and its thickness. Finally, reactions between the release chemicals and the coating may limit the applicability of this technique to some coating materials. Ideally, the coating material should not chemically react with the LIGA release agents and change its tribological or mechanical properties.

References:


1. T. R. Christenson, "X-Ray Based Fabrication", MEMS Handbook, ed. Mohammed Gad-el-Hak (CRC Press, 2001).

2. J. Hruby, "LIGA Technologies and Applications", MRS Bulletin, 26, 337-340 (2001).

3. S. V. Prasad, A. C. Hall and M. T. Dugger, "Characterization of Sidewall and Planar Surfaces of Electroplated LIGA Parts", SAND Report, SAND2000-1702, October 2000.

4. S. V. Prasad, J. R. Michael and T. R. Christenson, "EBSD Studies on Wear-Induced Subsurface Regions in LIGA Nickel", Scripta Materialla 48, 255-260 (2003).



Acknowledgements

The authors gratefully acknowledge Chandra Venkatraman and Cindi Brodbeck of Bekaert Advanced Coating Technologies for supplying the diamond-like nanocomposite coatings. Sandia is a multiprogram laboratory operated by Sandia Corporation, a Lockheed Martin Company for the United States Department of Energy under contract DE-AC04-94AL8500.

**Key words**: LIGA, MEMS, tribology, coatings

# Overview of scaling issues: macro- to meso-scale systems

Stuart T. Smith and Richard M. Seugling, Center for Precision Engineering, UNC Charlotte, NC 28223

## Summary

This paper addresses some of the issues associated with scaling the size and accuracy of conventional machines and instruments from macro down to meso-scales and beyond. Although, small scale machine tools and instruments, such as lathes, have been built for many years in the watch-making and other industries, a limited number of these types of systems have been incorporated into modern manufacturing. Most of the small scale machine tools and instruments are merely a scaled down version of a normal machine, but the accuracy or precision is no better than that of a high-quality macro-machine/instrument. In an effort to identify areas of future research, fundamental considerations are used to assess the fidelity of possible approaches to common design problems. Key features common to the systems being considered are the ability to provide work in a controlled manner and the use of sensors for feedback of process condition, in particular, relative motions. From this we are able to consider two areas to be addressed;

1. Actuators to provide position and/or generate work.
2. Sensors for detecting surfaces and measuring relative motions.

These considerations provide a guide to those techniques that scale favorably using current technologies. However, machine systems are considerably more complex than their parts and there are a large number of other factors that must be considered. As a first step toward identifying future machine design approaches, we have undertaken an assessment of two representative systems, a coordinate measuring machine (CMM) and a lathe.

This abstract represents a condensed summary of an extensive review currently being prepared for publication.

## Overview

Precision at macroscopic scales is usually considered to start when range to accuracy or range to resolution performance is around 1 part in $10^5$ or better. A similar criterion applied to meso-systems immediately implies that total errors should be below $10^{-8}$ m or so. In many processes, to control to the relevant precision requires metrology and actuation systems of considerably better performance. Consequently, simple considerations indicate that dimensional metrology and machine design for small-scale machines must achieve reliable measurement and positional accuracy at, or approaching, nanometer levels. Major differences are

1. It is likely that the metrology system will be integrated with the manufacture and/or assembly process.
2. There are likely to be more metrology systems, possibly one for every device.
3. It must be possible to manufacture these cheaply and utilize automated assembly.
4. Power consumption must be low.

5. New methods of communication and data handling will be required.
6. It will be necessary to achieve bandwidths comparable to the manufacturing process and higher resolution than normally required of common shop-floor metrology instruments.
7. Alignments and subsequent errors will be particularly difficult to adjust and measure.
8. Measurement frames encompassing the whole instrument, and therefore modular, should not add significant cost.
9. Evaluation of force and measurement loops will be critical to the performance of the system.

As stated, to achieve precision, two major enabling technologies of meso and smaller scale systems will be small actuator and sensor systems. Fortunately, there is a limited number of possibilities enabling a reasonable assessment of the relative merits of available options in terms of the effects of scaling.

Actuator methods currently considered include; piezoelectric, electrostatic, electromagnetic, magneto-strictive, hydraulic/pneumatic, thermal and shape memory. One particular measure of the fidelity of these actuators is the theoretical maximum amount of work and/or power that can be produce per unit volume occupied by the actuator (called the work density or power density). Considering specific implementations it is found that some of these methods maintain performance (piezo-electric, hydraulic, electrostatic) as scales reduce while electromagnetic actuators tend to degrade and thermal-based actuators appear to improve. Identification of the scales at which different techniques dominate will help the designer to select the appropriate technology for a given application. Such analysis also provides information about other parametric scaling factors such as drive voltage amplitudes, forces etc. There are also a number of implementation issues that will be presented.

A similar approach has been applied to sensors for small scale systems such as optical (line scale, interferometric, diffractive, position sensitive detectors) and electromagnetic. In this later category it is necessary to split the categories into transducers and displacement sensor systems. In our study we have attempted to identify the relevant scaling parameters and assess their relative influence as scale reduces.

Below, is presented an overview of the issues that we identify when trying to reduce the scale of conventional CMM's and lathes.

## CMM

Coordinate measuring machines (CMMs) are in use by a wide range of industries covering a broad array of applications[i]. Common state-of-the art CMM systems have work volumes that are on the order of cubic meters with micrometer measurement uncertainties[ii],[iii]. There have been high accuracy, small-scale CMMs developed at The National Physical Laboratory in the U.K.[iv]. This type of precision* allows for comprehensive analysis of parts and subsequent processes at an extremely high level. This type of performance does not come without costs. To acquire this performance level, metrology systems, such as CMMs, require special environmentally stable areas and operate at a considerably slower pace than that of standard manufacturing processes. To

* Precision, in this case is defined by the ratio of operation range to the minimum detectable resolution of the system.

provide the required information, CMMs are comprised of a number of different systems working in unison. These can be differentiated into a number of different categories as shown in Table 1.

**Table 1: Scaling a coordinate measuring machine.**

| Components | Macro | Meso | Micro |
|---|---|---|---|
| Structure | Orthogonally stacked precision slides with well aligned scales. Metrology and motion control structures are the same. | Precision slides not available and alignments considerably more difficult. Metrology and motion frames have little additional material cost. | Open loop, ill defined. |
| Slide ways | Air bearings. Wide rails enable low rotation errors. Large forces, high stiffness. | Air bearing less suitable. Flexures have limited range for a small relative volume. | Use flexure |
| Probe | Large sphere on a rigid rod attached to flexure-based load cell. | Scaling macro requires novel manufacture. AFM not robust enough for a manufacturing environment. Probe and specimen mass may be comparable. | AFM made using MEMS technology. |
| Scales | Scales represent small volume of machine. | Nothing commercially available, lots of research in meso-scale optical systems. | No scales, nor metrology systems for 6 dof calibration/compensation. |
| Drives | Feedscrew, linear motors | Motors lose power in proportion to volume and radius. PZT has inadequate range. | PZT |
| Connectors | Insignificant. | Limited in size, current state of art is cell phone/laptop. Even wireless receivers are relatively large. | Significant portion of the instrument |
| Controller | Adjacent cabinet | Cell phone also state of art. Wall power supplies probably smaller than cell phone battery. | Medium sized cabinet |

## Lathe

A machine tool, almost by definition, functions as an instrument for doing work to a specimen or blank to produce a functional product. To provide work to a sample at nanometer levels the system must have high stiffness and high positional accuracy. A question arises, how much work is required to produce a part whose geometry is on the order of millimeters? For a simple lathe system as the part gets smaller the influence of the machine on the part increases quite dramatically. Deformation during the manufacturing process can cause large errors in the designed geometry and subsequently in the performance of the part in operation. Table 2 represents some of the most influential components of a common lathe and what types of systems could be used to scale the size and accuracy. A miniature machining system has been developed in Japan that machines work pieces on the order of 0.3 mm diameter[v].

**Table 2: Scaling a lathe.**

| Components | Macro | Meso | Micro |
|---|---|---|---|
| Structure | Orthogonally stacked ground and lapped slides with linear scales. Metrology and motion control structures are the same. | Precision slides not available and alignments considerably more difficult. Metrology and motion frames have little additional material cost. | Open loop, ill defined. |
| Slide ways | Hydrodynamic bearings. Wide rails enable low rotation errors. Large forces, high stiffness. | Air bearing less suitable. Flexures have limited range for a small relative volume. | Use flexure |
| Tool | Common tool steel or carbide. | Diamond tipped. | AFM tip made using MEMS technology. |
| Scales | Scales represent small fraction of machine volume. | Nothing commercially available, lots of research in meso-scale optical systems and scales. | Currently, no scales, nor metrology systems |
| Drives | Motor driven feedscrew, linear motors | Motors lose power in proportion to volume and radius. PZT has inadequate range. | PZT, Electrostrictive, Magnetostrictive. |
| Connectors | Insignificant. | Limited in size, current state of art is cell phone/laptop. Even wireless receivers are relatively large. | Significant portion of the instrument |
| Controller | Adjacent cabinet, integrated into machine cabinet. | Cell phone also state of art. Wall power supplies probably smaller than cell phone battery. | Medium sized cabinet |

## Problems with scaling of these types of machine

A major problem is that if systems are produced by the same manufacturing processes, tolerance will be independent of scale whereas the effects of these tolerances may scale unfavorably.

Examples.

1. Bearing tolerances can be accommodated by interference fits to remove play. However, as the bearing gets progressively smaller, the tolerance must scale for a given stress in the interference fit. This is not possible if the process is not refined or changed.
2. Angular errors are inversely a function of the separation of the two rails of a slideway. As the separation reduces these errors increase. However, as rotational errors increase there is a tendency for the error itself to produce misalignment forces that propagate the error.

Both of the above examples indicate the possibility that scaling not only increase the errors that exist at macroscopic scales but can also promote further, and sometimes new, disturbances that degrade performance. The information shown is a rudimentary representation of extremely complex systems, which illustrates the variability of components as they scale. Further research in these areas will need to be undertaken in order to more fully account for the issues associated with which components or technologies should be adopted and adapted for the meso-, micro- and nano-scale machinery and instrumentation.

---

[i] Bosch, J.A., 1995, *Coordinate Measuring Machines and Systems*, Marcel Dekker, Inc., New York, NY, 444 pgs., ISBN: 0824795814.

[ii] *Carl Zeiss, Inc.*, UPMC CARAT Universal Precision Measuring Centers, December 2002, <http://www.zeiss.de/us/imt/home.nsf>.

[iii] *Brown&Sharpe, Inc.*, Product Detail, PMM-C, December 2002, <http://www.brownandsharpe.com>.

[iv] Peggs, G. N., Design for a compact high-accuracy CMM, *CIRP Annuals – Manufacturing Technology*, **48** (1), pg. 417-420.

[v] Lu, Z. and Yoneyama, T., 1999, Micro cutting in the micro lathe turning system, *International Journal of Machine Tools & Manufacture*, **39** (7), pg. 1171-1183.

## Measuring in three dimensions at the mesoscopic level

Graham Peggs, Andrew Lewis, Richard Leach
National Physical Laboratory, Teddington, Middlesex, TW11 0LW. UK

### Abstract

As a first step along the path to develop metrology tools to operate in the mesoscopic regime, NPL has rapidly designed and manufactured a Small CMM with a 50 x 50 x 50 mm measuring volume and significantly sub-micrometre volumetric uncertainty. It is one of a group of such instruments being developed in several European research institutes. An overview of this research is given before looking in detail at the NPL instrument. Current work at NPL on the development of probing systems for use at even smaller scales is then described. This work is targeted at the next generation of micro-scale CMMs.

### Introduction

The key to successful manufacturing of ever smaller devices and products is proper process control, without which, useable yields will be low and failure modes poorly understood. Metrology, and in particular dimensional metrology, is fundamental to understanding and controlling such production processes [1]. But, there is a dearth of instruments capable of accurately measuring the geometry of tiny features, with steeply sloping sides, on small objects at the mesoscopic scale. An extension of the concept of Coordinate Measuring Machine (CMM) but achieving smaller uncertainties over a restricted working volume has been identified by several research groups as a possible solution to these metrology problems.

### Small CMM developments in Europe

Several different designs of Small scale CMM are being investigated. Each design has to solve the traditional CMM problems of accurate position control, overall system accuracy (including traceability) and 3D probe design and operation. The Technical University of Eindhoven [2] followed the approach of minimising kinematic positioning errors, by strict adherence to the Abbe and Bryan principles and used a probe based on a silicon flexure, designed to avoid plastic damage of the surface [3,5]. Their prototype Small CMM features a 100 x 100 x 100 mm working volume and 100 nm uncertainty. A variant has been designed with a restricted (4 mm) vertical axis and improved (25 nm) accuracy.

In Germany, PTB have been developing small opto-tactile probe systems for conventional sized CMMs [4] and also for use alongside their 3D-boss microprobe in their 3D micro measuring machine [6]. Their probe design is also based on silicon membrane technology, but using piezo-resistive elements. The measuring range of the PTB CMM is 25 x 40 x 25 nm, with target uncertainty of < 100 nm.

As well as research developments at the National Institutes, several commercial designs of Small CMM have been produced within Europe, *e.g.* the SIOS Nanopositioning machine with a 25 x 25 x 5 mm range and a resolution of 1.24 nm. This machine is designed as a nano-positioning device with interferometric readout of position – supply and operation of the probe system is the customer's responsibility.

In all these CMMs, perhaps the most difficult issue concerns the use of contacting probes. All the designs are based on miniature probe systems, using commercial probe stems and spherical tips. With the designs, calibration of the probe kinematic performance and the quality of the probe tip are of paramount importance.

## The NPL Small CMM

In order to gain a perspective of 3D metrology at the mesoscopic scale and to address the gap between conventional CMMs and nanometrology instruments, NPL designed and built a Small CMM with a 50 x 50 x 50 mm working volume and target uncertainty of 50 nm. To minimise development time, the NPL Small CMM was designed as an add-on unit to be used with a conventional CMM acting as a host. The host CMM provides motion control, programming and data analysis, whereas the add-on structure of the NPL Small CMM provides the accurate metrology and the probing systems. Figure 1 is a schematic of the Small CMM metrology systems (one axis shown), and Figure 2 shows the Small CMM mounted on the host CMM.

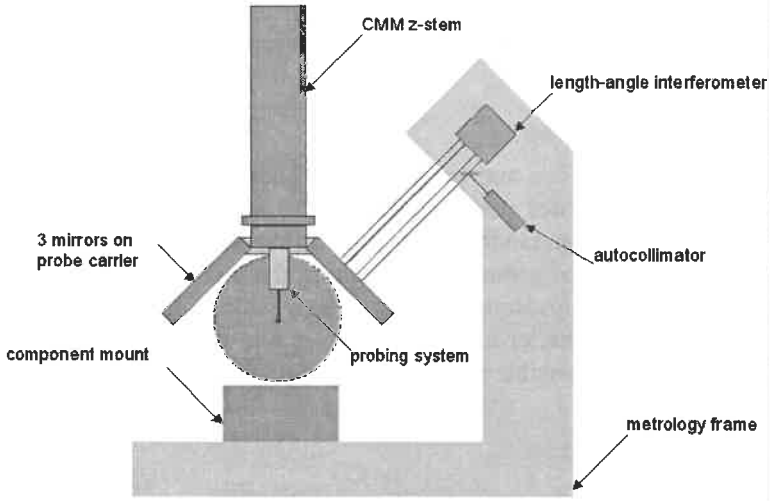


Figure 1 – Small CMM metrology systems

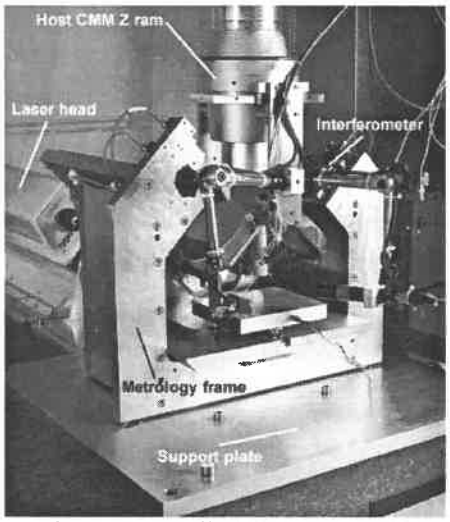


Figure 2 – Small CMM on host CMM

Some of the early design of our CMM has been presented previously [6], but a fuller description is given here. The moving structure consisting of 3 mirrors mounted on a probe carrier is attached to the Z-ram of the host CMM. The 6 degrees of freedom of this structure are continually measured using three dual-axis interferometers (linear and angular displacement) and three dual-axis position sensitive detectors (referred to as autocollimators). These interferometers and autocollimators are mounted on a low expansion metrology frame, on the table of the host CMM. From knowledge of the position and rotation of the moving structure, the 3D position of the probe head is known. The probe head uses a commercial 0.3 or 0.5 mm diameter ball ended stylus mounted in a miniature flexure system, with capacitance sensors detecting displacements of the probe tip. The probe has a 20 μm range along all three ordinate axes, a working force of 0.1 mN and a resolution of 3 nm.

Rather than try to manufacture a geometrically perfect structure, errors in the metrology and probe carrier system, including surface form of the mirrors, are compensated for by a novel self-calibration process which is performed *in situ*. The sensitivity of the dual-axis position sensitive detectors is calibrated against the accurate angular interferometers. The mutual angles between the interferometers' primary measurement beams are calculated from applying a 3D version of the Calliper principle (polygon angle determination using nominally orthogonal autocollimators). The flatness errors of the mirrors and their mutual angular separation are calibrated using a 3D process of scanning the 12 laser interferometer measurement beams (4 from each device) over the mirrors' surfaces, and using an integration of measured angle to derive the flatness at a series of grid position, spaced 3 mm apart (*i.e.* equal to the beam diameter). The deflection sensitivity of the probe head is calibrated by probing against 5 of the surfaces of a cuboid, and simultaneously acquiring probe head (capacitance gauge) data and displacement data from

the three interferometers. Careful design of the probe flexures has resulted in a probe with nearly homogenous probing force in all directions, and 3D deflection can be ascertained from resolving the 3 capacitance measurements into deflections of the flexure structure along the ordinate axes. By the above process (requiring the use of a solid cube of commercial optical flatness and orthogonality), the entire Small CMM can be self-calibrated, with full traceability to the laser wavelength used by the interferometers.

**Measurements at the mesoscopic scale**

We have used our Small CMM to make measurements of small devices and structures, some examples of which are given in Figures 3 and 4. These measurements involved mostly uni-directional probing (actually along a diagonal between the Small CMM y- and z-axes, but only using the southern cap of the probe tip for contacting the artefact surface). For these measurements, the repeatability of results was within 30 nm and the agreement with optically measured value for the step height was within 50 nm, which agrees well with a theoretical single axis uncertainty which is estimated (following *GUM* guidelines) to be 50 nm.

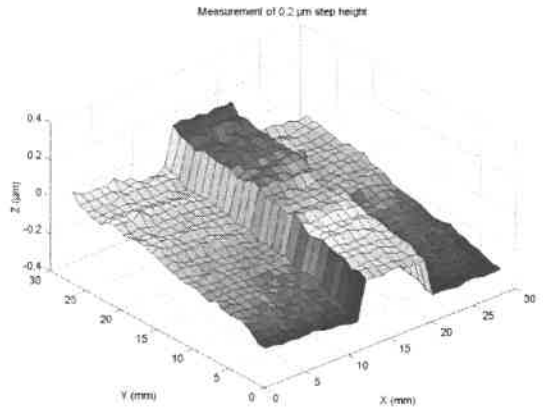


Figure 3 – measurement of a 200 nm step height

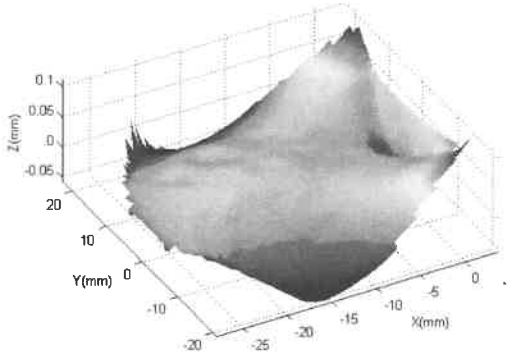


Figure 4 – measurement of defects in toroidal mould surface

As with all 3D CMMs, calibration of the probe system in 3D is necessary if 3D measurements are to be made. Using an un-calibrated probe, deviations up to 100 nm were observed in the measurement of roundness of a good quality sphere, but these were repeatable at the 30 nm level, and did not change when the test sphere was rotated between measurements, indicating a systematic probe error which could be calibrated. At the accuracy level of our Small CMM, this requires a probe calibration to better than 50 nm accuracy. Although several approaches were tried, including interferometric measurement of the probe tip, the kinematic performance of the flexures and the sphericity of the probe tip are both important in determining the probing accuracy. We have constructed probes using 1 mm diameter tips, believed to be of 'grade 1' quality (*i.e.* spherical to around 25 nm). We have made measurements using these probes of other similar 1 mm diameter spheres and re-measurement with the test sphere rotated. This has allowed us to estimate the sphericity of the probe balls and to derive an error map of the probe. For ease of integration into the Small CMM measurement software, the 1 mm probe tip is calibrated by probing against a reference sphere on a grid of points, spaced equidistantly on a rectilinear grid around the southern hemispherical cap of the probe. In this way, an error map of the entire probe system is derived. A typical error map derived by this technique is shown in Figure 5. The peak near the centre in Figure 5 corresponds to a possible wear patch on the bottom of the probe tip. Although the probe tips are spherical at the 25 nm level, the total error map of the probe system shows probing errors at the level of one or two hundred nanometres. However, these errors are repeatable at the level of ±25 nm and so can be incorporated into a probe system error map for later recall.

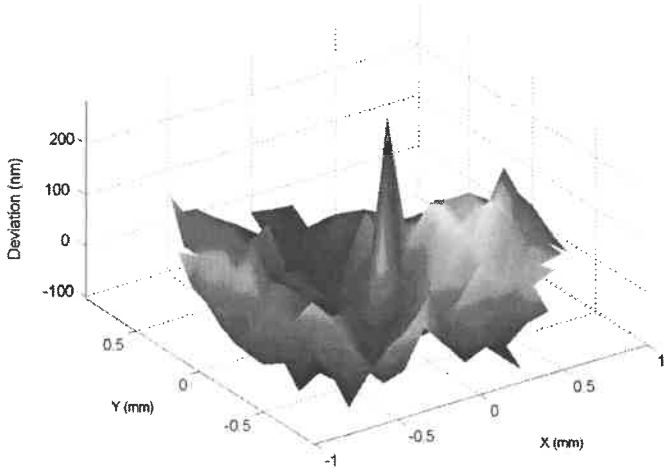


Figure 5 – probe error map - deviation from sphericity

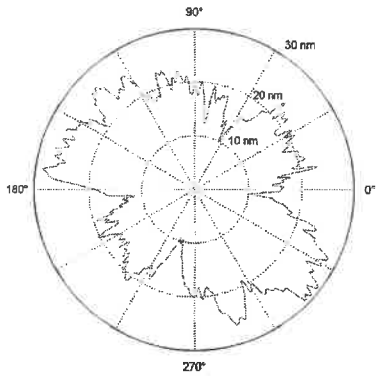


Figure 6 – precision sphere example roundness trace

We have also obtained several precision spheres of 12.7 mm diameter that have been measured using our High Accuracy Roundness instrument (Talyond73 with harmonic error separation), which achieves 5 nm uncertainty. From repeated traces of roundness at various inclinations of the spheres, we have determined that they are spherical to just under 25 nm. These are also useable as calibration spheres for calibrating the performance of the Small CMM probes. Work is ongoing to successfully incorporate the 3D error maps into the control software and to produce probes with good repeatability to use with this technique.

**Development of micro probes**

Whilst the Small CMM probe system described above is suitable for the measurement of small components, the size and mass of the probe preclude its use with MEMS-scale devices. To measure a true microstructure requires a probe size of micrometre dimensions. To date, the smallest probe sizes reported in the literature are of the order of 0.1 mm [5]. With probe stems of tens of micrometres in diameter and with probing forces greater than about 1 μN, it is very difficult to produce a sensing mechanism that is flexible enough to respond before the stem bends (or the tip compresses) significantly and, yet is stiff enough to be robust. NPL currently has a project running to design such a probe and expects first results in early 2003. The current thinking is to use a steel probe produced using micro-EDM technology [8] and micro-machined flexure structures.

The most popular commercially available systems for measuring MEMS-scale structures are stylus instruments, vertical scanning white light interferometers and confocal microscopes. However, whilst such instruments are very versatile as imaging devices they do not tend to perform well as dimensional metrology tools. Optical probes, for example, do not perform well when large slopes are present and stylus instruments struggle to measure high aspect ratio structures. A recent comparison of profiling measurements in the UK has shown a wide variation in results from laboratories with different, and in some cases, identical, measuring systems [9]. In one instance, an artefact with sinusoidal profile, with an 8 μm period and 150 nm *Ra*, was measured as having an *Ra* that varied from 20 nm to 2455 nm! The comparison exercise included using stylus instruments, interferometers, an auto-focus system and a confocal microscope. Figure 7 shows the results of the comparison. It is sobering to consider that if these instruments are struggling to achieve comparable results with well-defined structures in 2D, what is happening when they are measuring complex 3D microstructures?

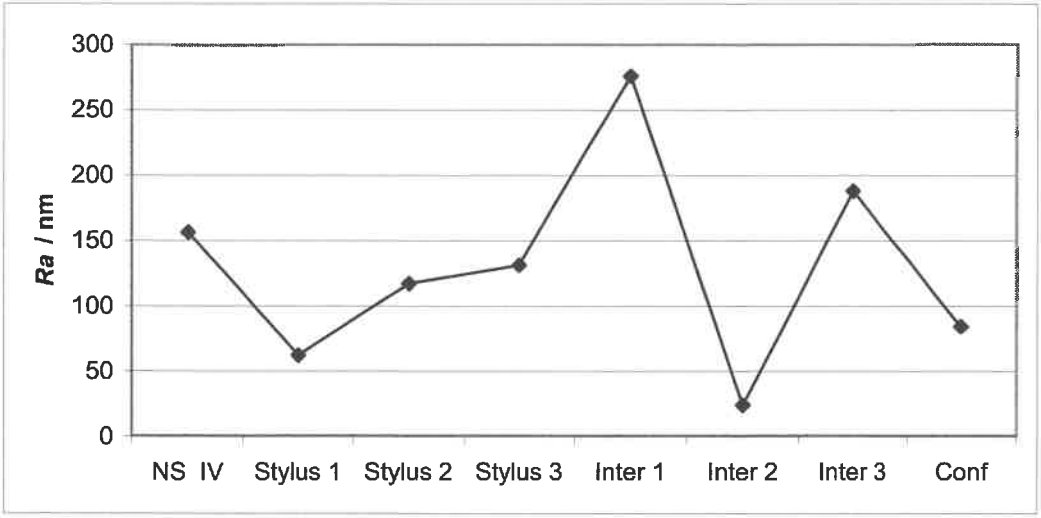


Figure 7 Results with an 8 μm nickel sinusoid (note that the 2455 nm result is off the scale)

When measuring complex 3D structures it is essential that such commercial tools are traceably calibrated and are covered by international standards. The NPL project to develop a micro-scale CMM will address this calibration deficit and an EU-funded project, MEMSTAND, co-ordinated by NPL is addressing the standards issues [10].

**Acknowledgements**

The authors would like to thank their colleagues at NPL, Leitz-Brown & Sharpe Meßtechnik GmbH Wetzlar, and acknowledge funding from the UK Government Department of Trade and Industry National Measurement System Policy Unit.

**References**

[1] R. K. Leach, *Proc. COMS2002, Sept. 8-12, Michigan, USA*, 139 (2002)

[2] M.M.P.A. Vermeulen, P.C.J.N. Rosielle, P.H.J. Schellekens, *Ann. CIRP*, **47,** 447 (1998)

[3] W.P. van Vliet, P.H. Schellekens, *Ann. CIRP*, **45**, 483 (1996)

[4] G. Ji., H. Schwenke, E. Trapet, *Proc ASPE*, **98**, 25 (1998)

[5] H. Haitjema, W.O. Pril, P.H.J. Schellekens, *Ann. CIRP*, **50**, 365 (2001)

[6] S. Cao, U. Brand, T. Kleine-Besten, W. Hoffmann, H. Schwenke, S. Bütefisch, S. Büttgenbach, *Microsys. Technol.*, **8**, 3 (2002)

[7] G.N. Peggs, A.J. Lewis, S. Oldfield, *Ann. CIRP*, **48**, 417-420 (1999)

[8] T. Masazawa, *Ann. CIRP,* **49**, 473 (2000)

[9] R. K. Leach, A. Hart, *NPL Report,* **CBTLM 15**, 1 (2002)

[10] R. K. Leach, *mst news,* **5**, 37 (2002) and *www.memstand.org*

# Uncertainty in measurements of micro-patterned thin film thickness using Nanometrological AFM
## - Reliability of parameters for base straight line -

Ichiko Misumi[1, 2], Satoshi Gonda[1], Tomizo Kurosawa[1], Yasushi Azuma[1], Toshiyuki Fujimoto[1], Isao Kojima[1], Toshihisa Sakurai[3], Tadahiro Ohmi[3], Kiyoshi Takamasu[2]

[1] National Institute of Advanced Industrial Science and Technology, National Metrology Institute of Japan (NMIJ/AIST), e-mail:misumi.i@aist.go.jp
Tsukuba Central 3 bldg, 1-1-1, Umezono, Tsukuba, Ibaraki 305-8563, Japan
[2] The University of Tokyo, [3] Tohoku University

**Abstract**
Precision measurements of thin film thickness (10, 7, 5 and 3 nm) were carried out using an atomic force microscope with three-axis laser interferometer (Nanometrological AFM). Uncertainty in measurements of thin film thickness was estimated. In estimation of uncertainty, the reliability of parameters for base straight line was considered. From the results of uncertainty estimation, less than 0.4 nm expanded uncertainty ($k = 2$) was obtained.

**Keywords**
Precision Measurement, Laser Interferometer, AFM, Calibration, Traceability, Nanometrology

### 1. Introduction

Nanometrology, dimensional metrology in nanometer-scale, is becoming increasingly important. In nanometrology, length-standard-traceable measurements are required in order to certify obtained values in measurements. National Metrology Institutes (NMIs) have developed length-standard-traceable nanometrology instruments corresponding to this requirement. National Metrology Institute of Japan, AIST (NMIJ/AIST) has developed an atomic force microscope with XYZ-axis laser interferometer (Nanometrological AFM)[1] and has measured nanometrological standards precisely using a Nanometrological AFM. The Nanometrological AFM is servo-controlled by laser interferometer signals and can realize length-standard-traceable calibration of nanometrological standards in real time. In precision measurements of one-dimensional (1D) grating standards (nominal pitch 240 nm) using the Nanometrological AFM, expanded uncertainty ($k = 2$) of approximately 0.3 nm could be obtained[2].

In this study, precision measurements of thin film thickness (Nominal thickness values: 10, 7, 5 and 3 nm) using the Nanometrological AFM were carried out. Thin films were micro-patterned for AFM measurements. Furthermore, uncertainty in thin film thickness measurements was estimated. However, the micro-patterned thin films do not have enough measured data for base straight line approximation compared with stepheight nanometrology standards. Therefore, in the estimation of measurement uncertainty, the reliability of parameters for the Gaussian associated base straight line using least squares method is considered.

## 2. Experimental methods

### 2.1 Atomic force microscope with three-axis laser interferometer (Nanometrological AFM)

Figure 1 is a photograph of an atomic force microscope system with three-axis laser interferometer (Nanometrological AFM). The Nanometrological AFM system is a stage scanning type and is operated in contact AFM mode. The Nanometrological AFM system consists of a stage unit, an AFM probe unit and an interferometer unit. The probe unit is removed in Figure 1. The stage unit is comprised of a piezo-driven XY-axis leaf spring stage and a Z-axis scanner tube-type piezo actuator. Scanning area of this stage unit is approximately 17.5 μm (X)× 17.5 μm(Y) × 2.5 μm(Z). A three-sided moving mirror for the XYZ interferometer unit is set at the top of the Z-axis scanner. The interferometer has 4 optical paths in each axis and the total resolution of the interferometer unit is approximately 0.04 nm. Atomic force applied to a cantilever under a contact-mode is detected using a conventional optical lever method. Laser sources of the interferometer unit are practical frequency-stabilized He-Ne lasers with a wavelength of 633 nm (model 117A Spectra-Physics. Ltd). The laser frequency is calibrated by an $I_2$ stabilized He-Ne laser before calibration of nanometrological standards. The stage position is servo-controlled using the interferometer signals in real-time and the Nanometrological AFM can realize the direct-length-standard-traceable calibration of nanometrological standards. Main uncertainty components in measurements of one-dimensional (1D) gratings (nominal pitch value: 240 nm) using the Nanometrological AFM are shown in Figure 2. The maximum uncertainty component was cyclic error of laser interferometer and its value was 0.115 nm.

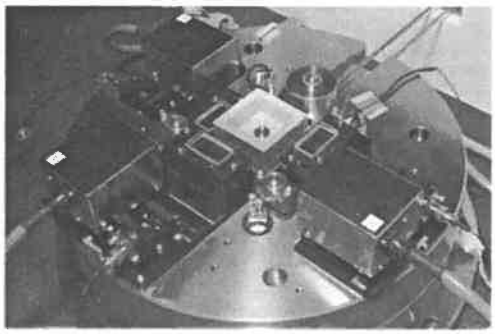

Figure 1 Atomic force microscope with three-axis laser interferometer (Nanometrological AFM)

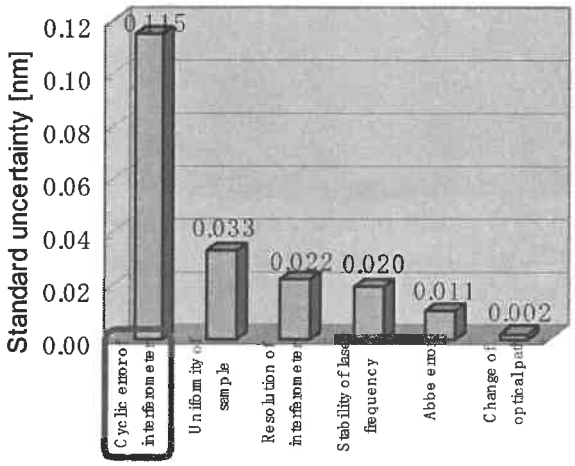


Figure 2 Main uncertainty components in pitch measurements using Nanometrological AFM.

### 2.2 Micro-patterned thin film

Thermal oxidized films of silicon substrates were wet etched precisely by buffered hydrofluoric acid and the thickness were controlled at 10, 7, 5 and 3 nm, respectively[3]. The thickness of thin films was checked using X-ray reflectivity (XRR). Furthermore, two-dimensional (2D) gratings (pitch value: approximately 3 μm) were made of thin films for AFM measurements. The size of silicon substrate was 15 mm(X)×15 mm(Y).

### 2.3 Measurement conditions and thickness calculation

Measurements of thin film thickness were operated in a temperature and humidity controlled room at 293 K and 50 %. The nanometrological AFM system was set on a vibration isolation system and covered with a shielding for stable measurements. Air temperature, neighborhood temperature of a sample, air humidity and air pressure were recorded during measurements of thin film thickness and the recorded data were used in order to compensate the refractive index of air and thermal expansion of samples.

Figure 3 is a nanometrological AFM image of micro-patterned thin film before slope correction. Scanning range and scanning lines were 5 μm(X) × 5 μm(Y) and 128 lines, respectively. Only line profiles suitable for thin film thickness calculation were selected from 128 lines obtained. Sampling interval of laser interferometer signals was approximately 6 nm. Figure 4 shows a schematic drawing of a sectional view of micro-patterned thin film. Calculation procedures of thin film thickness are as follows; (1) Slope of a line profile is calculated from the approximated straight line using measured data of Left part and Right part. (2) Slope of a line profile is corrected (3) Slope-corrected line profile is offset and base line derived from Left part and Right part becomes zero. (4) Average of measured data in Top part as a film thickness value is calculated. (5) Average and standard deviation of film thickness values of the selected line profiles are calculated as a representative value and standard deviation in the measured area.

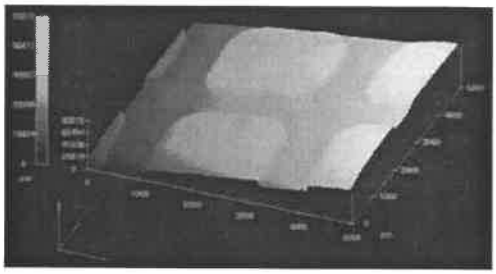

Figure 3 AFM image of micro-patterned thin film (thickness: 10 nm, measured area: 5 μm (X) x 5 μm(Y))

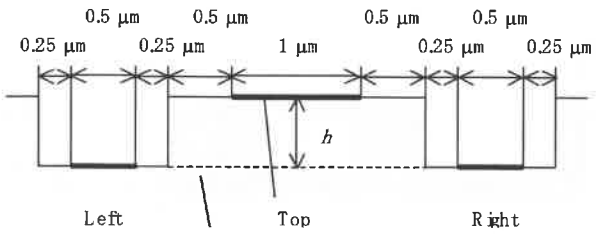


Figure 4 Schematic drawing of a sectional view of micro-patterned thin film

### 3. Reliability of base straight line parameter

Figure 5 shows a criterion for evaluation of stepheight standards in ISO 5436-1. Three times the line-width is required as a scanning range for the evaluation. However, the micro-patterned thin films do not have enough scanning range for base straight line approximation compared with the criterion. Therefore, in the estimation of measurement uncertainty, the reliability of parameters for the Gaussian associated base straight line using least squares method is considered. The calculation procedures of reliability of parameters for base straight line are as follows[4]; (1) the relation between error of measured data and error of parameters for straight line is calculated. (2) Reliability range at the position of least squares line is calculated. Jacobian matrix, **A** of straight line is expressed in eq(1);

$$\mathbf{A} = \begin{pmatrix} 1 & x_1 \\ \vdots & \vdots \\ 1 & x_n \end{pmatrix} \qquad (1)$$

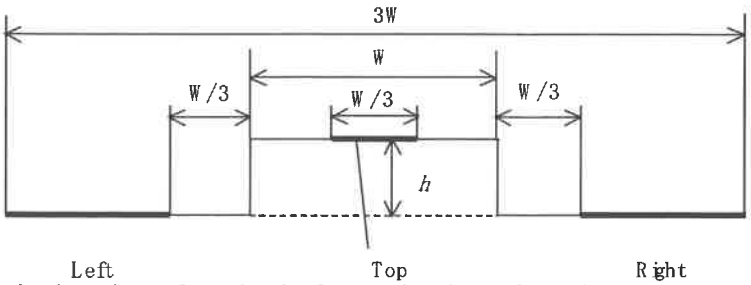

Figure 5 Schematic drawing of a criteria for evaluation of stepheight standards (ISO 5436-1).

Error matrix of parameters $\mathbf{S}_p$ is expressed in eq(2),

$$\mathbf{S}_p = \begin{pmatrix} \sigma_{p_1}^{\ 2} & \\ & \sigma_{p_2}^{\ 2} \end{pmatrix} = \left(\tilde{\mathbf{A}}\mathbf{S}^{-1}\mathbf{A}\right)^{-1} = \sigma_0^{\ 2} \begin{pmatrix} \frac{1}{n} & 0 \\ 0 & \frac{1}{\sum x_i^{\ 2}} \end{pmatrix} \tag{2}$$

where $\mathbf{S}$ is the error matrix of measured data and $\tilde{\mathbf{A}}$ is the transposed matrix of $\mathbf{A}$. Error matrix $\mathbf{S}_m$, the reliability range at any position of associated straight line, is expressed in eq(3).

$$\mathbf{S}_m = \mathbf{A}\mathbf{S}_p\tilde{\mathbf{A}} \tag{3}$$

Measured points (number: $2n$) for base straight line are located as shown in Figure 6. In this case, Jacobian matrix of straight line, $\mathbf{A}$ can be expressed simply in (4)

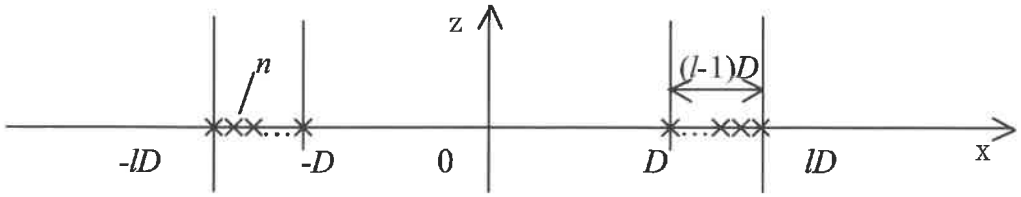

Figure 6 Measured points for base straight line.

$$\mathbf{A} = \begin{pmatrix} 1 & x \end{pmatrix} \tag{4}$$

Therefore, the reliability range at any position of associated straight line, $\mathbf{S}_m = \sigma_m$ is expressed in eq(5)

$$\sigma_m = \sqrt{\frac{1}{2n} + \frac{1}{n + (l-1)(n+1) + \frac{1}{6n}(n+1)(2n+1)(l-1)^2} \cdot \frac{x^2}{D^2}} \cdot \sigma_0 \tag{5}$$

where $\sigma_0$ is error of measured data.

Figure 7 shows the relationship between the normalized reliability range $\sigma_m/\sigma_0$ and the normalized horizontal position $x/D$ (number of measured points $2n = 100$). The solid line shows the normalized reliability range in measured data parts for base line, $l = 1.4$ (micro-patterned thin

films) and the dashed line shows the normalized reliability range in $l$ = 1.8 (ISO). The normalized reliability range $\sigma_m/\sigma_0$ in $l$ = 1.4 is slightly larger than the normalized reliability range in $l$ = 1.8. Thickness of micro-patterned thin films is calculated in the range of |x/D| < 1. The maximum reliability range in $l$ = 1.4 and |x/D| < 1, $\sigma_m/\sigma_0$ is approximately 0.15. The maximum reliability range, $\sigma_m/\sigma_0$ = 0.15 and the measured data variation for base straight line $\sigma_0$ are added as uncertainty components to the estimation of uncertainty in measurement.

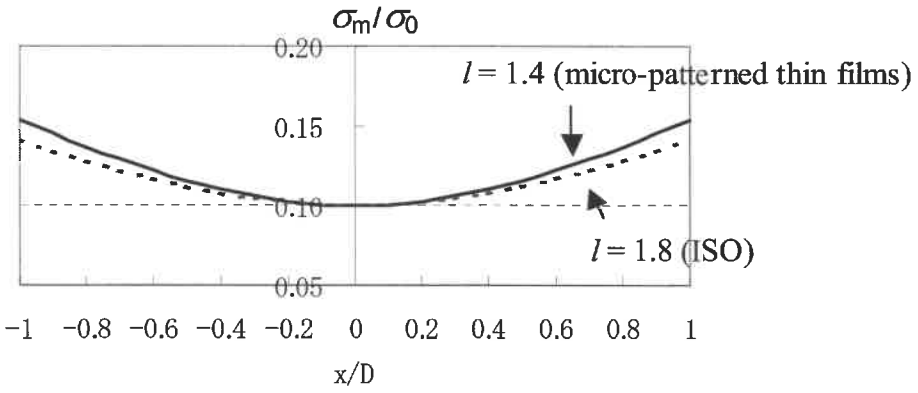


Figure 7 Reliability range versus position of approximated base straight line at number measured points $2n$ = 100.

## 4. Uncertainty in measurements

In estimation of measurement uncertainty, seventeen uncertainty components were considered. Figure 8 shows six major uncertainty components in 10 nm thickness measurement. The maximum uncertainty component is cyclic error of laser interferometer, 0.115 nm. The uncertainty of reliability range of parameters for base straight line is 0.003 nm and the sixth major uncertainty component. On the other hand, figure 9 shows major uncertainty components in 5 nm thickness measurement. The uncertainty of measured data variation for base straight line is approximately equal to the uncertainty of cyclic error of laser interferometer. The uncertainty of the reliability range of parameters for base straight line increases in proportion to the uncertainty of measured data variation for base straight line compared with the uncertainty in 10 nm thickness measurement. It becomes clear that the uncertainty of reliability range of parameters is not a negligible uncertainty component when the measured data variation for base straight line is large compared with other uncertainty components, as in the case of 5 nm thickness measurement.

Table 1 shows measured values and expanded uncertainty ($k$ = 2) in measurements of thin film thickness. Expanded uncertainty in 10, 7 and 3 nm thickness measurements is approximately 0.28 nm. On the other hand, expanded uncertainty in 5 nm thickness measurement is 0.35 nm. This is derived from the large measured data variation and the reliability range of parameters, as shown in Figure 9.

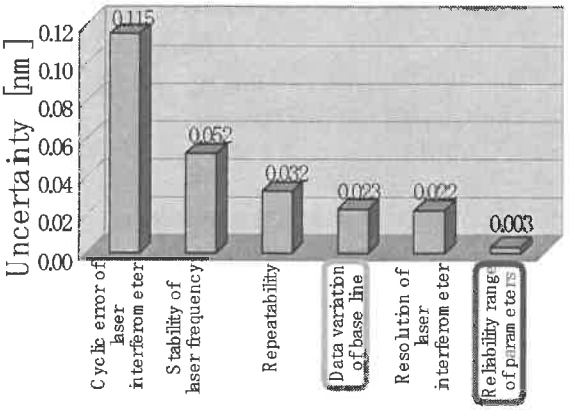


Figure 8 Major uncertainty components in 10 nm thickness measurements

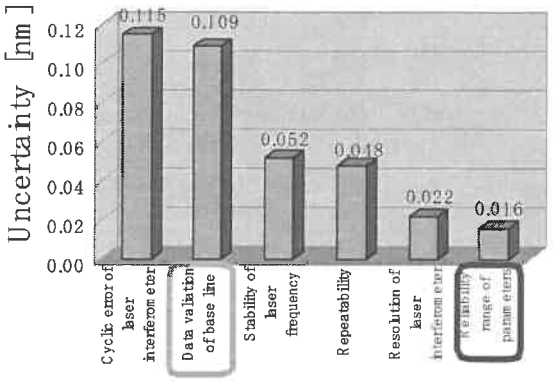


Figure 9 Major uncertainty components in 10 nm thickness measurements

Table 1 Measured values and uncertainty in measurements of thin film thickness

| Nominal thickness, [nm] | Measured value, $h$ [nm] | Expanded uncertainty, $U_{95}(p)$ [nm] |
|---|---|---|
| 10 | 10.46 | 0.27 |
| 7 | 7.72 | 0.28 |
| 5 | 5.47 | 0.35 |
| 3 | 3.63 | 0.28 |

## 5. Conclusions

Precision measurements of thin film thickness (nominal value 10, 7, 5 and 3 nm) were carried out using nanometrological AFM. Expanded uncertainty (k = 2) was less than 0.4 nm. In estimation of uncertainty, the reliability of parameters for base straight line was considered. Uncertainty of the reliability of parameters for base straight line was the sixth major uncertainty component in seventeen uncertainty components. In estimation of measurement uncertainty, it is helpful to consider the reliability of parameters for associated features.

### References

[1] S. Gonda, T. Doi, T. Kurosawa, and Y. Tanimura
N. Hisata, T. Yamagishi, H. Fujimoto, and H. Yukawa: Real-time, interferometrically measuring atomic force microscope for direct calibration of standards, *Rev. Sci. Instrum.*, **70**, (1999) 3362.
[2] I. Misumi, S. Gonda and T. Kurosawa: Precision measurements of 1D grating using metrological atomic force microscope, Proc. of 2nd **euspen** International Conference -Turin, Italy - May 27th - 31st, 2001, p474.
[3] T. Ohmi and S. Aoyama, Calibration of height in atomic force microscope images with subnanometer scale silicon dioxide steps. *Appl. Phys. Lett.* **61** (1992) 2479.
[4] K. Takamasu, R. Furutani and S. Ozono: Reliability of Parameters for Associated Features in Coordinate Metrology, *Journal of the Japan Society of Precision Engineering* **63** (1997) 1594. (in Japanese)

# Probe-force calibration experiments using the NIST electrostatic force balance

Jon R. Pratt, David Newell, John Kramar, Jonathan Mulholland*, and Eric Whitenton
National Institute of Standards and Technology, Gaithersburg, MD 20899

The sensitivity of a piezoresistive cantilever force sensor has been determined by probing the weighing pan of the National Institute of Standards and Technology's prototype electrostatic force balance. In this experiment, micronewton contact forces between a force probe and the balance's weighing pan are determined from the voltage required to maintain the null position of the force balance. The force balance incorporates length and electrical metrology so that an electrical realization of force consistent with the International System of Units may be computed from measurements of the voltage and capacitance gradient. Here, the balance serves as a primary realization of force in a continuous range between 0 and 6 x $10^{-5}$ N, allowing calibration of the sensor against a traceable standard.

## Introduction

Originally conceived as a means to image insulators [1], the atomic force microscope (AFM) has quickly distinguished itself as a useful tool for the measurement of surface forces [2] and, in more recent studies, of intermolecular forces of single macromolecules, such as DNA and proteins [3,4]. The problem of calibrating the force sensitivity of these devices is well known, and a variety of approaches have been considered in the literature [5,6].

Recently, NIST developed an electronic null balance for comparing weak forces derived from mechanical, electrical, optical, or molecular sources as part of our work to link small force measurement to the International System of Units [7]. The goal is to realize and disseminate small force through an electrostatic force balance similar to, but on a smaller scale than, voltage balances used in fundamental electrical metrology [8]. Such a balance might serve as a primary standard for probe-type force measuring instruments in the regime below $10^{-5}$ N. Eventually, the plan is to design transfer artifacts, i.e., calibrated load cells or force generators, through which we can disseminate this realized force to users in industry or academia.

In this paper, we briefly review the working principles of the electrostatic force balance and describe how it can be employed to provide a force calibration of a piezoresistive AFM cantilever. We suggest that such a cantilever can be employed directly to achieve calibrated force measurements in AFM style instruments, or indirectly by acting as a calibration specimen, or transfer artifact, that can be probed with another cantilever. As a first step in our effort to explore these possibilities, we attempt to calibrate the force sensitivity of a commercially available cantilever. The results of this proof-of-concept experiment are presented and discussed. We find encouraging repeatability in the determination of force sensitivity, with deviations below a percent for a specific contact condition; however, our ability to reproduce the measurement is limited at the level of a few percent, presumably due to inconsistencies at the contact interface. Finally, we conclude with suggestions for improvements in the procedure and apparatus that might result in higher levels of reproducibility.

## Force balance and load cell calibration

We have designed and built a prototype electrostatic force balance for realizing forces in the micronewton range, as illustrated schematically in Figure 1(a). The active electrodes are concentric cylinders, the outer serving as the reference and the inner suspended and guided by a rectilinear flexure mechanism. The geometry has been designed such that a near-linear capacitance gradient of 1pF/mm is achieved at a working overlap of 5 mm. Thus, an electrical potential across the cylinders produces an electronic realization of force along the suspension axis

$$F = \frac{1}{2}\frac{dC}{dz}V^2 \qquad (1)$$

* NSF/NIST Summer Undergraduate Research Fellow, currently at Physics Department, St. Marys College, MD

where $dC$ is the measured change in capacitance for a given change in electrode overlap $dz$, and $V$ is the applied electric potential.

Previously, we have used this force balance in an automated null-displacement mode to compare an electric realization of force with the force generated by calibrated deadweights of nominal mass 1mg, 10 mg, and 20 mg. The forces involved in this comparison were calibrated independently via traceable techniques. SI traceable determinations of capacitance, length, and voltage were used to establish the value of the electronic force, with corrections for the alignment of the interferometer, balance, and electrical axis with gravity. The mass of the deadweights was determined by comparison to the NIST working mass standards with corrections made for buoyancy. Gravity was extrapolated from an absolute gravimeter measurement taken elsewhere on campus using knowledge of the relative elevation between the two sites. Comparisons between the electrostatic and deadweight forces agreed to within a few parts in $10^4$ after including all known correction factors [9].

Now we seek to compare probe forces to the calibrated electrostatic forces by once again maintaining a null displacement. In this experiment, we probe the balance pan with a piezoresistive cantilever force sensor, as illustrated in Figure 1(b). The voltage on the electrodes is adjusted by a closed loop feedback servo that produces a compensating force to maintain the null position of the balance as the cantilever is pressed into the weighing pan. In principle, measurement of the change in voltage required to maintain null, combined with prior measurements of the capacitance gradient of the electrodes, allows direct computation of the force existing between the balance stamp and cantilever under test, within the accuracy with which null is maintained. By stepwise variation of the degree to which the sensor presses against the balance, one can map the force sensitivity of the device under test by recording its sensor output as a function of the computed null force. An example taken from our experiments with a piezoresistive cantilever is shown graphically in Figure 1(c).

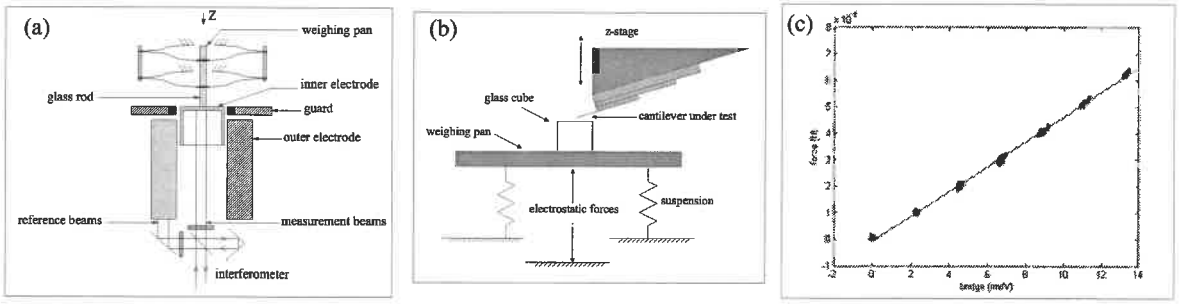


Figure 1. (a) Schematic of the NIST electrostatic force balance, (b) illustration depicting the probing of the balance with a cantilever load element, (c) typical sensitivity data for a piezoresisitive type cantilever

**Force transfer standards**

The typical macroscopic force transfer standard is a high-quality strain-gage load cell capable of reproducing changes of load within its operating range with accuracy on the order of parts in $10^6$ of its full scale value (e.g., kilonewtons). At the level of micro and, perhaps, nanonewton forces, we would like to transfer the unit of force with a more modest accuracy of a few tenths of a percent. This is the accuracy sought in draft measurement standards for instrumented indentation, and is representative of the growing metrology needs in the measurement of small force.

The notion of transferring the SI unit of force through an artifact is well developed at the macroscale and is characterized by two fundamental approaches. As an example of the first approach, consider a typical loading apparatus, such as a materials testing machine, that is equipped with a load cell to measure the magnitude of the tensile or compressive forces that it applies along its loading axis. This load cell can be removed and calibrated against a primary standard of force, such as a deadweight-loading machine. In this fashion, the unit of force is disseminated from the primary standard to the materials testing machine via direct calibration of its load cell.

In the second approach, our example machine is calibrated indirectly using a calibrated specimen. This calibrated specimen is, in fact, another load cell that has been calibrated against a deadweight machine. Once again, the unit of force is disseminated from a primary standard to the testing machine, this time through calibration of an intermediary load cell. The accuracy of this second approach is inferior to the first due to the added complexity of

interfacing the two load cells. However, the use of a secondary force standard has advantages when a large number of machines of varying geometry must be calibrated on a continuous basis, since only one load cell needs to be calibrated against a primary standard.

What we seek in a microscale load cell transfer standard is, by analogy to these conventional force practices, a device with a well-defined loading point, responsive to loads only along a well-defined axis, and possessing its own sensor for converting the load to a usable readout. This readout is preferably a voltage that is repeatable to parts in $10^4$. We further desire this load cell to be capable of use in either of the two transfer approaches, which implies that it must be compatible with both commercial AFM sensor and specimen holders. This last requirement suggests the load cell should fit within the 3.6 x 1.6 x 0.1 mm volume typical of the chips employed by commercial AFM's.

## Survey of scanning probe sensors

A review of the literature reveals a fairly limited selection of sensors in the desired micro to nanonewton force range, with the vast majority based on a cantilever elastic load element that deflects in response to the applied load. Such cantilever sensors usually have an "atomically" sharp tip that provides the requisite well-defined loading point; however, from a metrology standpoint, this arrangement fails to define a single measurement axis, since a cantilever will also respond to moments occurring at the point of contact. Ideally, a constrained load element, such as a parallelogram flexure, is preferable, though few examples of such devices exist on this scale, and none that are directly compatible with AFM instruments are available from commercial sources to our knowledge.

The detection schemes used to measure the elastic deformation of scanning-probe cantilevers, such as capacitive, interferometric, and the well-known optical lever arm techniques [10] present another set of problems for accurate force metrology. For instance, all of these techniques rely on an externally supplied metrology frame in order to monitor the deflection and produce the force readout. In particular, the popular optical lever arm requires a large housing separate from the cantilever to hold the laser light source and quadrant photo detector. Clearly, the displacement calibration of these instruments can vary greatly with set up and alignment of the cantilever with respect to the external frame of reference. Direct calibration of such devices is thus conceivable, but awkward. And it seems we cannot use these devices as an indirect calibration specimen. The only available approach for indirect calibration is to resort to calibrating the spring constant of the load element, since this can be accomplished independent of the detection hardware. However, to embrace this approach requires that the AFM's detection scheme subsequently be calibrated as a displacement consistent with the displacement measured during the primary calibration of the spring constant, a difficult task.

No existing sensor satisfies all our requirements. However, there is a cantilever sensor that avoids many of the above complications, at least as regards the detection scheme, and might be readily adapted to the problem of force transfer. This is the well-known piezoresistance approach, which we review in the following.

## Piezoresistive cantilever load cell

The variation of bulk resistivity of a material with applied stress is known as the piezoresistive effect. It has been used in various pressure detection schemes since its discovery, and has been applied successfully to the AFM to achieve atomic resolution imagery [11]. As applied in AFM, a resistor is typically doped into a region of material at the base of a silicon cantilever. The nominal resistance is a function of dopant concentration (typically boron) and can be fabricated using known relationships about semiconductor properties.

Deflection of the cantilever by an applied force causes the resistance of the doped region of the cantilever to vary about its nominal value, the sign and magnitude of deviation depending on the net change in stress experienced within the doped region. The change in resistance can be observed using a simple Wheatstone bridge or Ohm meter of sufficient resolution. Hence, this method of load detection has much in common with traditional strain-gage based load cells used as force transfer standards, albeit at a much smaller scale.

Cantilevers composed of piezoresistive material as described above are available commercially, and a photo of the type of cantilever purchased for use in our experiments is shown in Figure 2, accompanying a plot of the typical "open circuit" terminal voltage of the device. The force sensitivity is nominally 2 mΩ/nN, with a low frequency force noise of 0.4 nN (integrated between 10 and 1000 Hz) according to the manufacturer's specification. In practice, low-frequency force measurements made with these sensors seldom resolve better than $10^{-8}$ N, since the signal below 10 Hz is often dominated by 1/f noise in the detection electronics or piezoresistor itself. The plot of

"open-circuit" voltage as a function of frequency shown in Figure 2 reveals this trend. In this plot we distinguish between regimes where the noise has a predominantly 1/f character and where the noise has a flat spectrum typical of Johnson noise. So far, the low-frequency noise content has limited the application of these devices in force microscopy, with the vast majority of systems still choosing optical detection. However, there is recent evidence that careful design can manage these noise problems and produce sensors with resolutions that meet or exceed that achieved using optical detection schemes, with demonstrated low frequency resolution at or below 3 $x10^{-12}$ N [12]. Finally, we observe that both the nominal resistance and stress sensitivity of a piezoresistor may vary with temperature [13]. This temperature dependence must be quantified if such devices are to be developed as force artifacts, though it will not be addressed here.

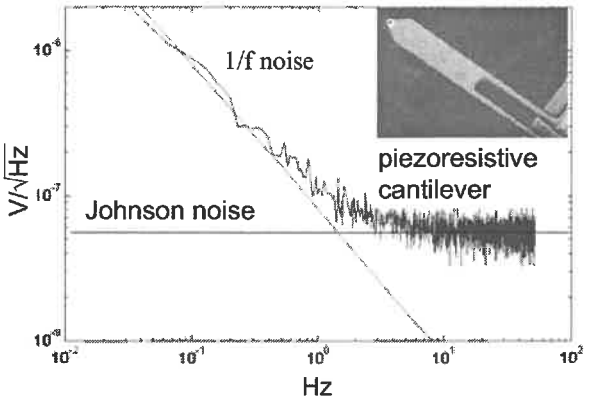


Figure 2. Typical noise signature of piezoresistive cantilever

**Proof-of-concept Experiment**

The electrostatic force balance was probed using a commercially available piezoresistive cantilever with a nominal resistance of 2 kΩ, length of approximately 3 x $10^{-4}$ m, and spring constant of 1 N/m, all according to the manufacturer's specifications. Changes in resistance were recorded using an a.c. wheatstone bridge configuration and a two-wire connection. The bridge was excited with a 1 kHz sinusoidal voltage at 1 Volt peak amplitude, and the bridge output was monitored using a lock-in amplifier. The cantilever chip came mounted on a ceramic base with gold contacts for making electrical connections to which we soldered the two wire leads.

An obvious issue to be addressed in the development of a standard load cell for AFM will be a methodology for fixing the orientation of the device with respect to the primary force balance. We chose to use the ceramic base as a reference surface, gluing the cantilever assembly to a glass microscope slide, which was then clamped in a fixture that held the assembly at an angle approximately 14 degrees from the horizontal defined by the balance weighing pan. The angle was selected as representative of the nominal angle used in typical AFM instruments, though, to our knowledge, no standard exists. The fixture was attached to a combination coarse and fine adjustment three-axis scanning stage for probing the balance. In these initial experiments, no attempt was made to align the vertical stage axis to the balance primary axis, though this too will be important in developing a standard procedure.

The cantilever was brought into contact with the top of the balance by manually turning a micrometer screw on the vertical axis of the three-axis stage. The contact region was defined using a 3 x $10^{-4}$ m polished glass cube affixed to the weighing pan. The physical contact point was observed optically to be near the edge of this cube using a long standoff microscope. Upon contact, the force was sensed by the bridge output. A nominal preload of $10^{-6}$ N was established by monitoring the balance output before re-zeroing the bridge. An automated fine motion scan was next executed using an electrostrictive actuator to drive the stage, pushing the cantilever into the balance pan. The stage was displaced a fixed increment, the balance allowed to settle for about one minute, and then the servo voltage and bridge output were sampled 150 times at nominally 3 Hz, with the average of these values being recorded as a single load point. The stage was scanned in and out through six such increments. This load and unload sequence was repeated between 30 and 40 times to yield a complete set of measurements over a period of about 3 hours. Each scan was fit using a least squares straight line to determine the slope and hence the sensitivity for a given scan. Each scan was normalized about the initial load and bridge output in an attempt to account for drift. The estimated sensitivity for the cantilever is reported as the average of the fits, with the standard deviation of the measurements indicating

the repeatability of the setup. The cantilever was then retracted from the balance along the vertical axis and then parked off to the side. This entire experiment was repeated to check for reproducibility. Results are graphed in Figure 3 and tabulated in Table 1.

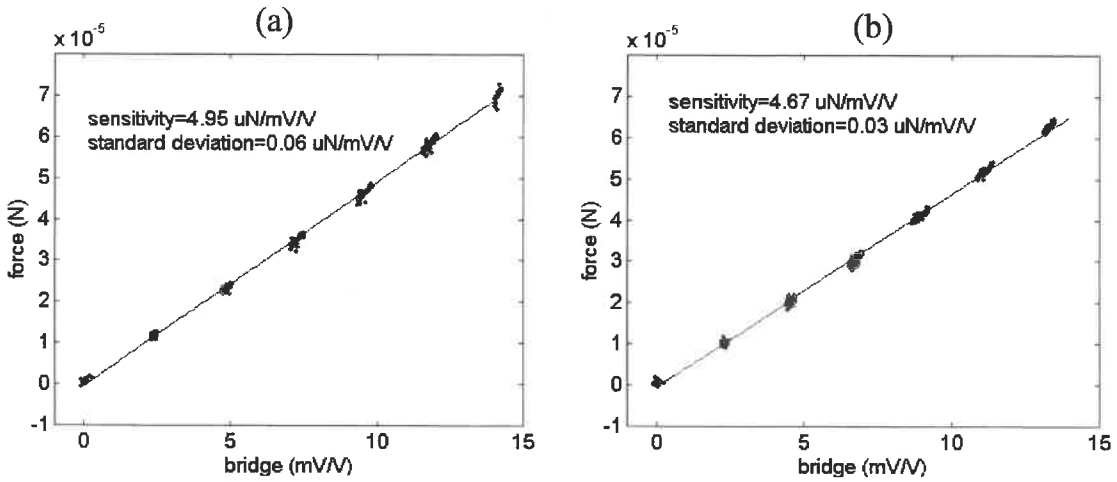


Figure 3. Null electrostatic force versus bridge output. Dots correspond to measured data. A single scan begins and ends at zero and is repeated 40 times in measurement (a) and 36 times in measurement (b). A sensitivity is determined for each scan from a least squares linear regression. The line corresponds to the mean value of sensitivities determined using a complete set of scans.

Table 1. Piezoresistive cantilever sensitivity

| Experiment | Number of force scans | Mean sensitivity (μN/mV/V) | Standard deviation (μN/mV/V, %) |
|---|---|---|---|
| a | 40 | 4.95 | 0.06 , 1 |
| b | 36 | 4.67 | 0.03 , 0.6 |

## Discussion

The repeatability within a given experiment was encouraging. These results, taken alone, suggest the potential to realize a traceable calibration of a microforce artifact at or below the percent level. Comparison between the two experiments, however, shows reproducibility is far more limited, with a discrepancy between experiments on the order of 6%. A variety of factors may contribute to this discrepancy.

*Interface uncertainty*

The actual contact condition was unobserved. The optical microscope employed lacked the resolution to monitor the fine tip of the AFM cantilever and its contact with the polished glass cube that served as the interface to the balance. For instance, we cannot say if the tip slipped along the interface due to the load. Contaminants and adsorbed water layers present at the interface may also cause variation of the surface contact angle, and this will affect the degree to which the cantilever twists out of plane in response to the applied load.

*Misalignment*

We have observed that loading the electrostatic force balance with a probe can distort the alignment of the electrodes leading to a variation of the capacitance gradient, and a change in the calibration constant of the balance. Previous investigations indicate that this effect is small (on the order of parts in $10^4$[9]), and we expect this effect should have been fairly consistent between the two experiments. Nevertheless, the orientation of the cantilever load axis with respect to the balance is unknown, and it is possible that the tangential component of force due to misalignment differs in some regard between the two experiments.

*Temperature effects*
The bridge, piezoresistor, and balance are known to drift with temperature. Temperature near the experiment was monitored and observed to drift as a function of time in a nearly linear fashion from 22° C to 21.2° C. However, the mean temperature differed by only 0.1° C between the experiments and seems an unlikely source of discrepancy.

*Zero drift*
Finally, we note that the nominal load drifted monotonically on the order of $10 \times 10^{-6}$ N in the time it took to complete a set of scans. Likewise, the sensitivities computed for each scan drift over the course of an experiment, revealing a slight dependence on preload. Unfortunately, the relative preload state of the cantilever from one experiment to the next was not accurately recorded, since the bridge was adjusted to zero after manual application of the initial preload in each case. It is always possible that an error was made in the initial setup, and that the two experiments were performed at significantly different absolute preloads of the cantilever.

## Conclusions

We have demonstrated the calibration of a piezoresistive cantilever force sensor using a specially designed null-force balance that provides null forces that are calibrated in a fashion traceable to the SI. The sensitivity of the cantilever load cell was found to be repeatable at or below the percent level in a given configuration, demonstrating its potential utility as a microforce transfer standard. The experiment was reproduced, and a systematic discrepancy on the order of 6% of the measured cantilever sensitivity was observed. The discrepancy is not surprising, since much work remains to establish standard fixtures, methods, and procedures to ensure consistent contact conditions between load cell and balance. Even given the discrepancy, this calibration technique appears to be a factor of two more precise than most previous techniques, all aimed at determining the spring constant rather than a direct force calibration (see [5]). We submit that such an approach, based on a sensor with an integrated detector, is superior because it avoids the problems inherent in calibrating displacement metrology that is external to the load element.

## Acknowledgements

Johnathan Mulholland gratefully acknowledges the support of the National Science Foundation and its Summer Undergraduate Research Fellowship program, which sponsored his research at NIST.

## References

1. Binnig G., Quate C. F., and Gerber Ch., 1986, "Atomic Force Microscope," *Phys. Rev. Lett.*, Vol. 56, no. 9, pp. 930-933.
2. N.A. Burnham, R. J. Colton, and H. M. Pollock, 1987, "Interpretation of force curves in force microscopy," *J. Appl. Phys.*, vol. 62, no. 7, pp. 2599-6022.
3. G. U. Lee, L. A. Chrisey, and R. J. Colton, 1994, "Direct measurement of the forces between complimentary strands of DNA," *Science*, vol. 266, pp. 771-773.
4. M. Rief, M. Gautel, F. Oesterhelt, J. M. Fernandez, and H. E. Gaub, 1997, " Reversible unfolding of individual titin immunoglobulin domains by AFM," *Science*, vol. 276, no. 5315, pp. 1109-1112.
5. J. D. Holbery, V. L. Eden, M. Sarikaya, and R. M. Fischer, 2000, "Experimental determination of scanning probe microscope cantilever spring constants utilizing a nanoindentation apparatus," *Review of Scientific Instruments*, vol. 71, no. 10, pp. 3769-3776.
6. L. P. Howard and J. Fu, 1997, "Accurate force measurements for miniature mechanical systems: a review of progress," SPIE Proceedings Series, vol. 3225, pp. 2-11.
7. J. A. Kramar, D. B. Newell, J. R. Pratt, 2002, "NIST Electrostatic Force Balance Experiment," *Proceedings of the joint international conference IMEKO TC3/TC5/TC20*, VDI-Berichte 1685, pp. 71-76.
8. Funck, T. and Sienknecht, V, "Determination of the Volt with the Improved PTB Voltage Balance", *IEEE Trans. on Inst. and Meas.*, **40**:2, pp. 158-161, 1991.
9. D. B. Newell, J. A. Kramar, J.R. Pratt, D. T. Smith, and E. R. Williams, 2003, "The NIST Microforce Realization and Measurement Project," CPEM special issue *of IEEE Proceedings on Instrumentation and Measurement*, accepted.
10. D. Sarid, 1994, "Scanning force microscopy", Oxford University Press.
11. M. Tortonese, R. C. Barrett, and C. F. Quate, 1993, "Atomic resolution with an atomic force microscope using piezoresistive detection," *Appl. Phys. Lett.*, vol. 62, no. 8, pp. 834-836.
12. J. Harley, 2000, "Advances in piezoresistive probes for atomic force microscopy," Ph. D. dissertation, Stanford University, Palo Alto, CA.
13. C. Smith, 1954, "Piezoresistance effect in Germanium and Silicon," *Physical Review*, vol. 94, no. 1, pp. 42-49.

# Meso-Scale Metrology Tools: A Survey of Relevant Tools and a Discussion of Their Strengths and Weaknesses

**Robin L. Hibbard, Matthew J. Bono**
**Lawrence Livermore National Laboratory**
**P.O. Box 808, MS. L-537, Livermore, CA 94550**

**Abstract**

Lawrence Livermore National Laboratory, LLNL, manufactures laser experiment targets made of cylindrical and spherical components and assemblies that are generally 2 mm in size or smaller, which are machined with micron level accuracy. The targets illustrated in Figure 1 exhibit many features that are common to typical inertial confinement fusion, ICF, and high energy density laser targets. The left side of Figure 1 illustrates a cylindrical target composed of multiple materials of various shapes, including a disk that has a multi-mode sinusoid with a 4 μm amplitude cut into it. The spherical target on the right consists of an inner capsule surrounded by four concentric hemispheres made of foams and polystyrene that are bonded together at a butt joint. Targets such as these are currently being manufactured for laser experiments conducted on the Omega Laser at the University of Rochester, and they are beginning to be fabricated for the National Ignition Facility[i],[ii], NIF. The targets need to be fully characterized with an uncertainty of +/- 1 μm, but in approximately five years, the required accuracy is expected to become +/- 0.25 μm. It is difficult to find metrology tools than can adequately measure these laser targets.

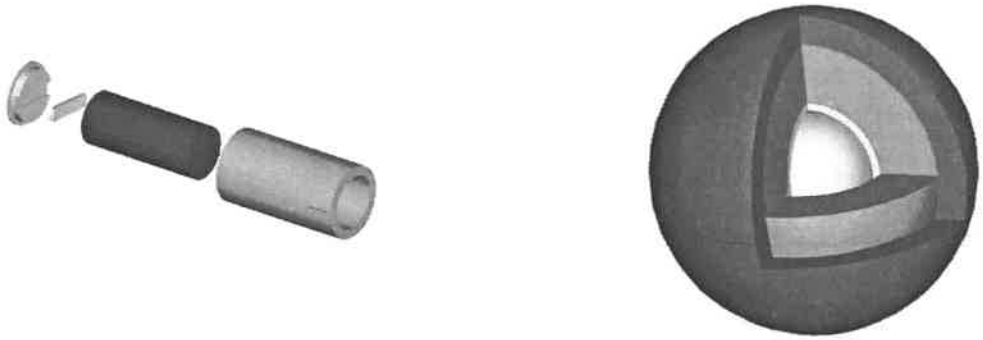

**Figure 1. Two typical laser target geometries**

The requirements for a laser experiment revolve around matching experimental laser shot results with results from predictive physics codes. The ability to provide a complete set of accurate dimensional metrology on a target is the input to the physics model. Therefore any inaccuracy or lack of data, affects the accuracy of the predictive model. In fact, it is more critical to have accurate metrology data rather than accurate manufacturing in this case. Diagnostics of the experimental results and the ability to resolve the physical behavior of the effect being modeled is the other element of the experiment cycle that is critical. Any of these errors reduces the ability to match the experimental and theoretical findings. One of the tasks of LLNL's target fabrication group is to address metrology capabilities at the meso-scale, several of which are described in the current paper.

Metrology plays a key role in fabrication and quality control on these meso-scale laser targets. Modern CNC machining equipment can provide positional resolution on the order of tens of

nanometers over lengths of several millimeters. As the target fabrication group currently has no metrology tools that can adequately measure parts on these scales, we believe that we are able to manufacture components with less uncertainty than we can measure them. Therefore, there is a critical shortcoming in dimensional metrology of these fabricated components, and new metrology tools are needed for process control and verification in meso-scale manufacturing. This paper provides a summary of current metrology capabilities at small scales and reveals a need for additional tools at the micro/meso-scale.

A survey of the capabilities of various metrology tools has been started to identify areas where metrology tools are commercially available and where tools need development. Figure 2 provides a qualitative view identifying areas where tools exist and the general capabilities for each tool category. It also identifies an area where tools may need development. LLNL would like to address a broad community knowledge base to contribute to this meso-scale metrology area and to identify other tools that are applicable in this realm. The graph focuses on commercially available tools, even though a few one-off tools are known to exist, such as the Phillips CM, and the NPL "small CMM." It would be desirable to include these types of tools on a separate graph.

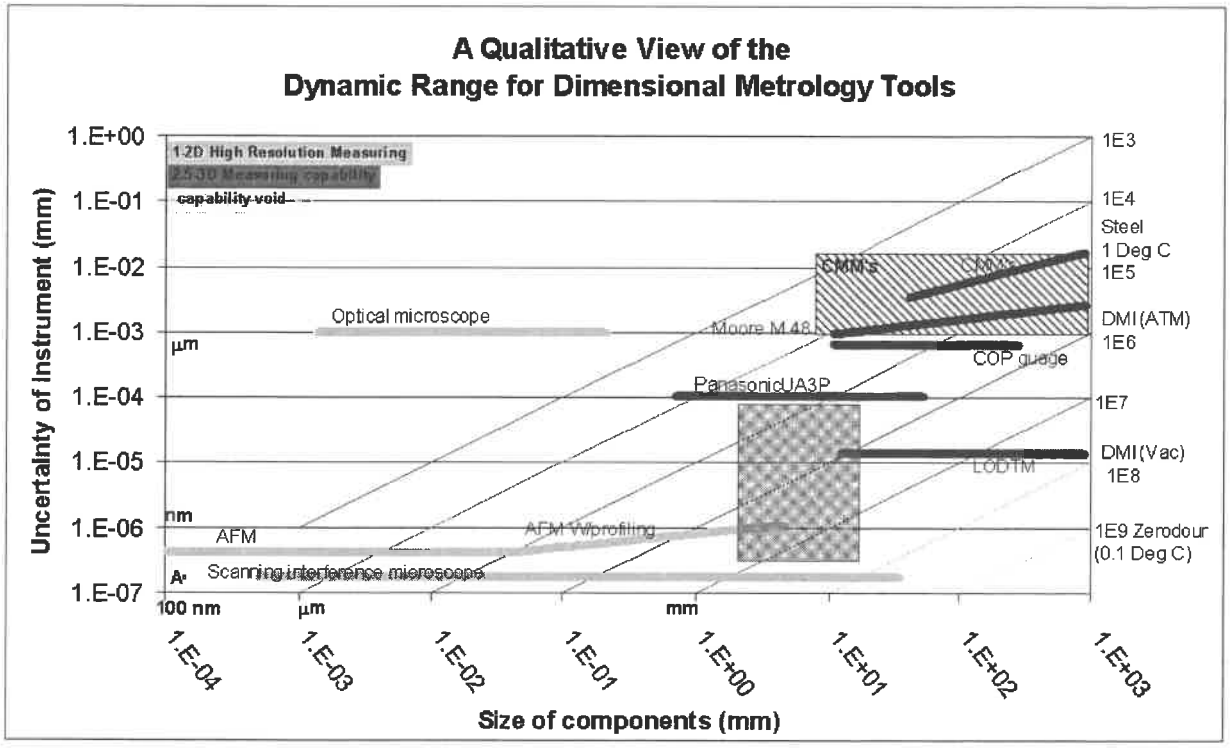


**Figure 2. A qualitative view of the dynamic range of metrology tools.**

The graph shows uncertainty of measurement versus dynamic range for various metrology tools. This type of graph is commonly used to illustrate the capabilities of precision manufacturing processes and tools. These are plotted against lines of specific accuracy (µm/M) for standard materials and measurement techniques. For example, steel would grow 1 µm/M per degree Celsius. This graph represents a qualitative look at the range and uncertainty of a broad range of metrology tools. Many of the identified tools have capabilities in 1 and 2 dimensions, and a few

claim to have 3-D capabilities, but these are really only 2.5-D devices. Some LLNL metrology tools have been included for a historical perspective.

Figure 2 illustrates a gap in metrology capabilities for the scales relevant to target fabrication. This gap falls in the meso-scale, where components range in size from tens of microns to millimeters, and accuracies range from nanometers to tenths of a micron. The current paper is intended to serve as a basis for formulating a plan for developing needed meso-scale metrology tools for target fabrication and other meso-scale applications. There is an apparent shortcoming in meso-scale metrology tools and a national need for developing them, and discussions should be initiated with interested parties and experts in the field to pursue this area of metrology development.

**Table 1. The Data set and notes on the various metrology devices.**

| | Measuring Instruments | Primary axis uncertainty - (meters) | Uncertainty in other 2 dimen. 2D | # meas dim | Min probe size mm | Feature size (M) | Min Range (M) | Max Range (M) | Notes |
|---|---|---|---|---|---|---|---|---|---|
| A | AFM w/o profiling | 1.00E-10 | ?? | 2.5D | Non Con | 5.00E-10 | 1.00E-10 | 3.00E-05 | 5 um Z limit on feature size. Time consuming |
| B | AFM w/Profiling stage | 1.00E-09 | 1.00E-08 | 2.5D | Non Con | 5.00E-09 | 1.00E-10 | 1.00E-02 | Have to stitch together many small data sets |
| C | Panasonic UA3P | 1.00E-07 | 1.00E-07 | 2.5D | 4.00E-03 | 5.00E-06 | 0.00001 | 0.05 | Acc. 0.1 um under 30deg dec. to .3 um @ 60 deg off vertical |
| D | Optical Microscope | 1.00E-06 | 1e-6&1e-5? | 2D | Non Con | 2.00E-06 | 2.00E-06 | 5.00E-05 | User views edges and estimates boundaries |
| E | "Best CMM" Moore/Leitz | 1.00E-06 | 1.00E-06 | 3D | 5.00E-01 | ?? | 0.0001 | 0.001 | 1 um over larger ranges? |
| | | 5.00E-06 | 5.00E-06 | | | | 0.001 | 1 | |
| F | Small Inexpensive CMM | 5.00E-06 | 5.00E-06 | 3D | 5.00E-01 | 1.00E-03 | 0.001 | 0.001 | Under 50K$ CMM's |
| | | 1.20E-05 | 1.20E-05 | | | | 0.001 | 0.4 | |
| G | Small Radius Gauge | 3.00E-07 | 5.00E-07 | 2D | 0.5 | 0.002 | 0.0005 | 50 | Spherical or cylindrical inner & outer contour |
| H | COP/Prism | 1.00E-06 | | 3D | 5.00E-01 | | 0.1 | 0.5 | Prefers surfaces of revolution |
| I | Taylor Hobson | 1 Ra | na | 1D | | | 0.004 | 0.12 | Surface and profile |
| j | Interference microscope | 2.50E-08 | 2.50E-08 | 2.5D | Non Con | 5.00E-07 | 5.00E-07 | 5.00E-04 | |
| k | Scanning interference microscopes | 1.00E-10 | 5.00E-07 | 2.5D | Non Con | 5.00E-07 | 5.00E-07 | 0.15 | "3D" surface Profiling. Limited by lope of surface 17deg? |
| l | Somergren interferometer | 1.00E-10 | | 2.5D | Non Con | 0.001 | 0.001 | 1 | |
| m | LODTM | 2.50E-08 | 2.50E-08 | 2.5D | 0.5 | 0.001 | 0.001 | 1.5 | 2 Axis lathe - x, z, θ coordiantes?? |

[i] "High Energy-Density Science on the National Ignition Facility", Campbell E. M., Cauble R., Remington B. A. UCRL-ID-129009, 1997.

[ii] "Conceptual Design of the National Ignition Facility", Paisner J., et al., UCRL-JC-117365

This work was performed under the auspices of the U.S. Department of Energy, by Lawrence Livermore National Laboratory, under contract W-7405-ENG-48

# MICROMACHINED INTERFEROMETER FOR MEMS METROLOGY

Byungki Kim, H. Ali Razavi, F. Levent Degertekin, Thomas R. Kurfess

G.W. Woodruff School of Mechanical Engineering,
Georgia Institute of Technology, Atlanta, GA 30332

## ABSTRACT

A microfabricated grating interferometer is described and evaluated by measuring the dynamic performance of a microfabricated microphone membrane. The device uses a phase sensitive diffraction grating for interferometric axial resolution and a microfabricated lens for improved lateral response. Experimental results show that both the transient and steady state vibration of MEMS devices can be measured and mapped using the micro interferometer. Since the interferometer is fabricated on a planar substrate and its dimensions are small, it is possible to implement interferometer arrays for parallel, fast measurement of MEMS devices and integrate optoelectronics. The integration strategy and the photodetector arrays fabricated for this purpose using CMOS technology are also discussed.

## INTRODUCTION

Significant part of MEMS research has so far concentrated on developing process technology and optimizing individual device performance. However, as the technology and market potential are being realized, a sophisticated MEMS quality control scheme needs to be developed. This requires metrology throughout the design, fabrication, wafer level test, post-package test and reliability testing processes [1].

In this paper, a microfabricated position sensing grating interferometer (μPSGI) is presented for dynamic MEMS metrology. The proposed micro interferometer measures distance using a reflective diffraction grating on a transparent substrate and a microlens fabricated using a photoresist reflow technique on the same substrate. This structure forms a phase sensitive diffraction grating to have interferometric sensitivity, while adding the capability of better lateral resolution by focusing. Figure 1 shows the schematic of a μPSGI with a photodetector. Depending on the distance between diffraction grating and target surface, diffraction pattern at the detector plane is changed. By monitoring the intensity of the certain diffraction order by the detector, the profile change of the target surface can be mapped. Detailed diffraction models of the microinterferometer have been developed to predict the device response and the location of photodetectors for integrated optoelectronics [2].

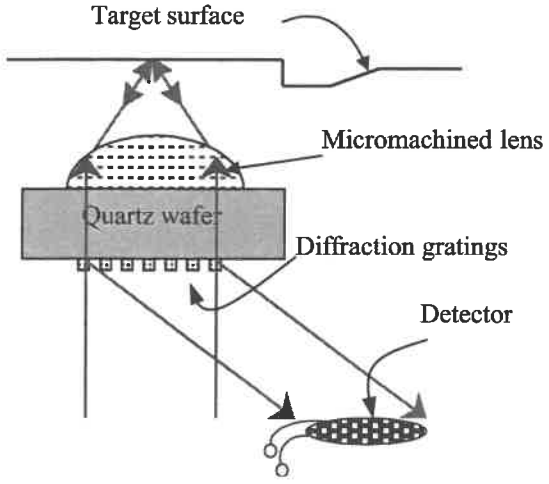


Figure 1. Schematic of a μPSGI

A particular device is fabricated on a fused silica substrate using aluminum to form the diffraction grating fingers and AZ4620 photoresist for the microlens. The details of the fabrication process can be found in reference 2. The structure also enables optoelectronics integration so that the interferometer with photo detectors can fit in a surface area of 1mmx1mm. The feasibility of μPSGI was demonstrated for measurement of moving microstructures [2] and a similar structure was also integrated to acoustic transducers for displacement detection [3].

An experimental set-up was implemented to test the microinterferometer on MEMS devices as shown in Figure 2. Experimental results were obtained on vibrating MEMS devices, such as a 1μm thick aluminum MEMS microphone membrane with 150μm diameter and 2.5μm air gap[3]. For testing purposes, the membrane was actuated electrostatically using a 40V DC bias and 10V sinusoidal burst at its resonance frequency of 726kHz. The displacement map of the membrane is obtained by digitizing the photodetector output at 10MHz while scanning the MEMS device. The results showed the expected 15nm maximum vibration amplitude as well as the vibration shape of the membrane[4]. Figure 3 shows the detector output that is equivalent to the vibrating shape of the membrane. The discontinuities of the profile in Fig. 3 are mainly due to misalignment and vibration noise in set-up.

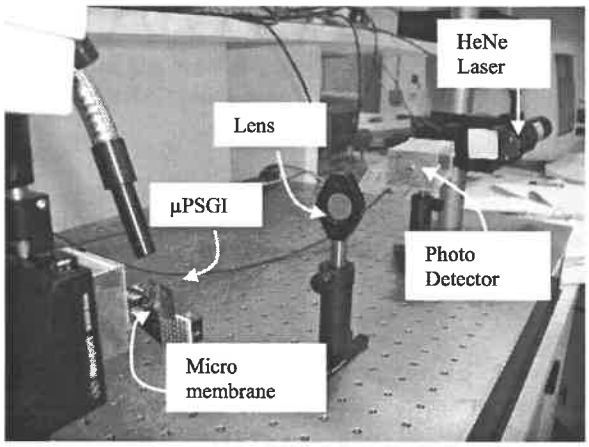


Figure 2. Experimental set-up

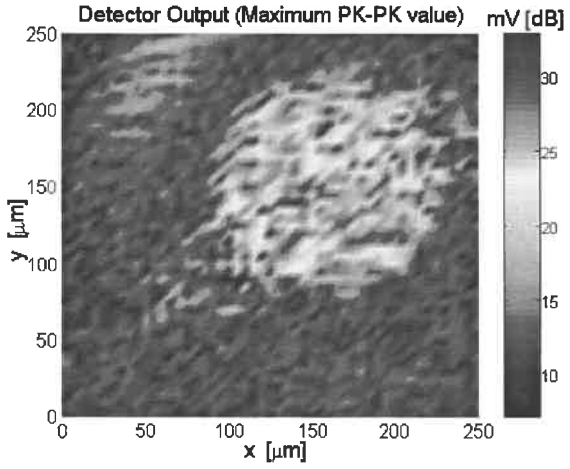


Figure 3. Vibrating membrane

## EXPERIMENTAL SET-UP AND RESULTS

To reduce the vibration noise in the signal, the experimental set-up has been improved to include a phase sensitive detector (lock-in amplifier). Similar MEMS microphone membranes have been used as the device under test. The membrane that was used in this paper has a diameter of 150 μm of diameter, a thickness of 1 μm and a 2.5 μm gap between its electrodes. In this particular case, the microlens has 200μm diameter and 0.3mm focal length. The light source was HeNe laser.

The schematic of the μPSGI scanning system set-up is depicted in Fig. 4. For the scanning purposes, X-Y plane actuator was implemented to scan the MEMS microphone and the Z direction actuator was used to adjust the distance from μPSGI to the target surface to the focal length of the lens on the μPSGI. The membrane was actuated with the same signals as the vibrating membrane of Fig. 3. For the phase sensitive detection the lock-in amplifier was locked to the AC actuation signal while the photo detector output was used as the input signal. The low pass filter removed high frequency components of the mixed signal and then only DC out which is proportional to the cosine of the phase difference between the input and the reference was remained. With this configuration, the amplitude and phase of the input signal can be determined[5]. During the experiments, the amplitude and the phase of the output from lock-in amplifier were recorded by data acquisition system at a sampling rate of 10 MHz followed by 10 averaging while the membrane was scanned in the x-y plane using a 5 μm by 5 μm grid size. Figure 5 shows mapping of R(x,y)*cos(θ), where R(x,y) is the amplitude, and θ, is the phase of the vibration at point (x,y). The resulting image shows a significant reduction in the noise outside of the vibrating membrane as well as an improved intensity pattern on the microphone membrane as compared to the previous data shown in Fig. 3. Nevertheless there are still some artifacts such as the slanted fringes superimposed on the measured vibration profile. These problems can be solved by using an active control scheme to keep the sample/diffraction grating distance at the maximum sensitivity level, i.e. the maximum slope of the fringe pattern[6].

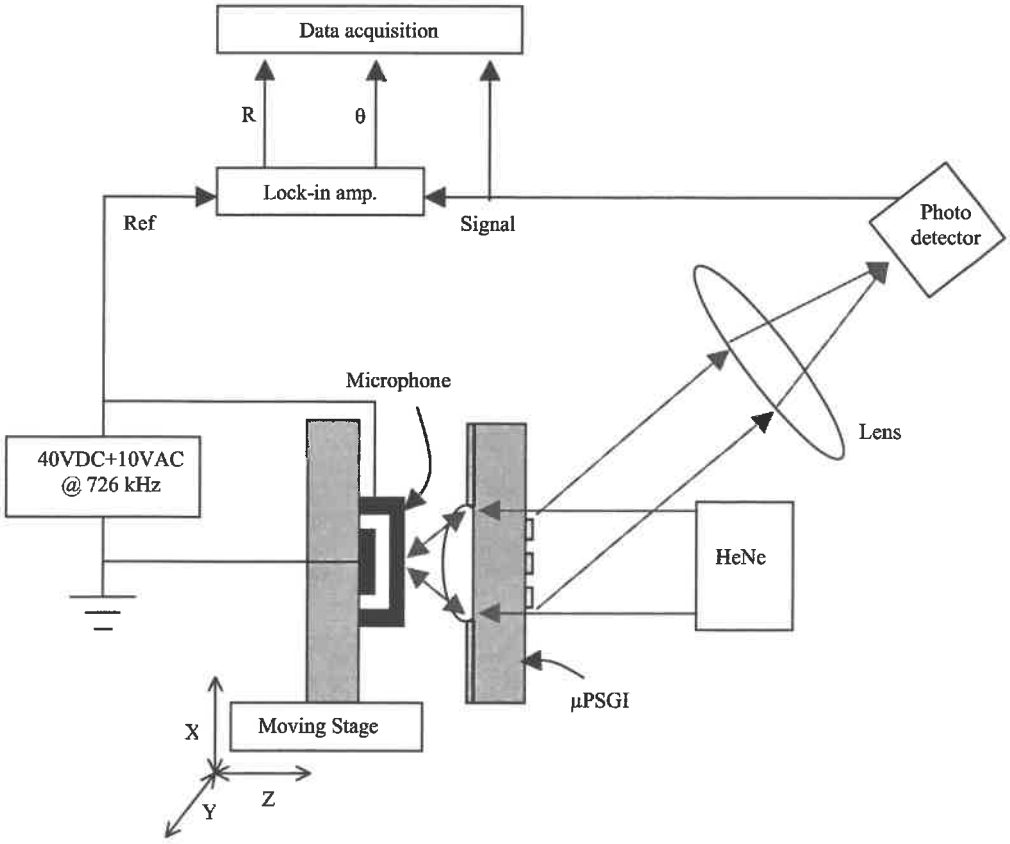


Figure 4. μPSGI scanning system

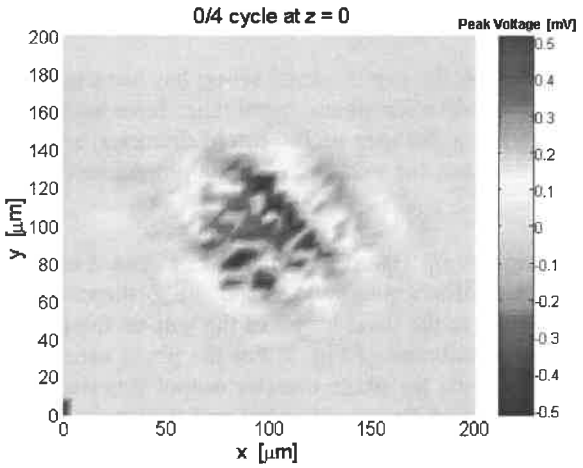


Figure 5. Scanning results using phase sensitive detector

## ARRAY IMPLEMENTATION

Due to its small volume and planar fabrication, these interferometers can be easily made into arrays. When implemented in the form of arrays, this device can perform fast, non-contact and precision static and dynamic measurements of MEMS structures in a parallel fashion to enable in-line inspection. This array structure integrated with detectors is shown schematically in Fig. 6. In order to obtain high signal to noise from each interferometer in the array, the distance between the grating and the target surface should be independently adjusted. As shown in Fig. 6, this can be achieved by using electrostatically actuated deformable diffraction gratings[7]. The optoelectronics can also be integrated using an array of photodetectors on a separate silicon chip. Such a photodetector array has already been fabricated using CMOS compatible processes. Figure 7 shows a 3x3 array of Silicon PN-junction diodes fabricated for this purpose. The location of the diodes are designed such that the 1st order of the diffraction order illuminates the detector when the gap between the µPSGI array and detector array is 1mm and the grating period is 3µm. To avoid cross talk by high order diffraction in maintaining compact size, the detectors are properly inclined. Over all size of the array is 3mmx3mm. More details of the photo detector array fabrication can be found in reference 8.

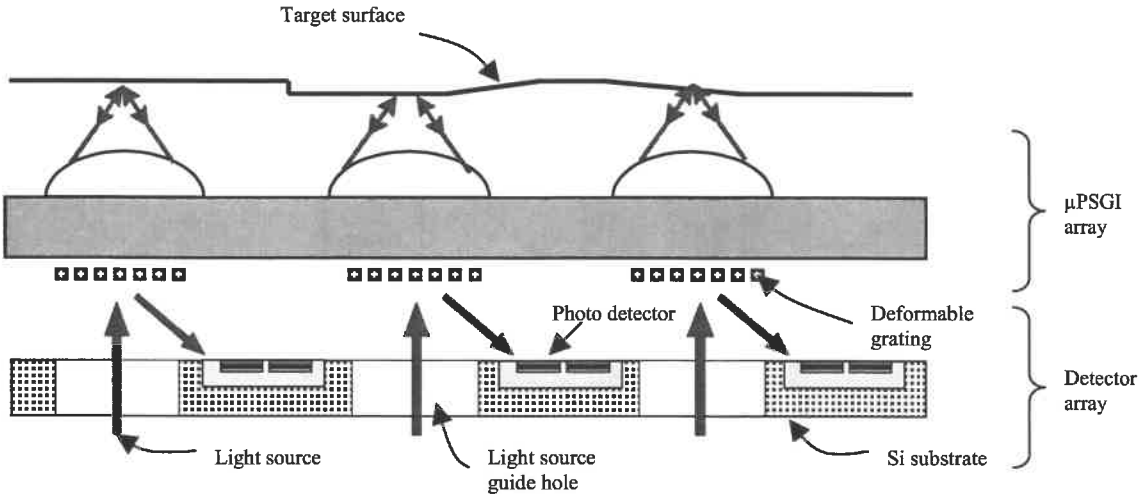


Figure 6. Schematic of an array of µPSGI integrated with detector array

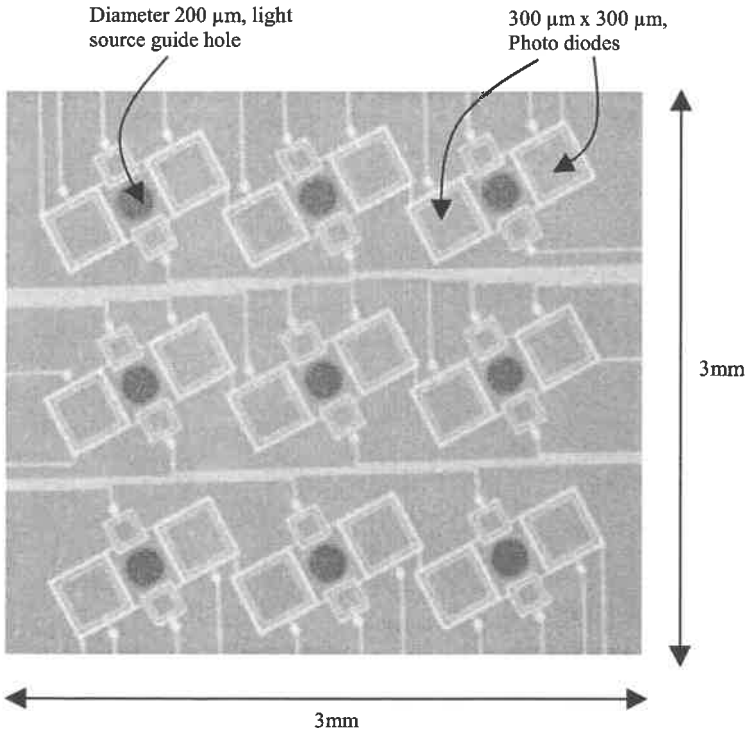


Figure 7. A fabricated array of 3x3 detectors

## CONCLUSION AND FUTURE WORK

The microscale phase sensitive diffraction grating interferometer has been used to measure the displacement of MEMS microphone structures with nm resolution in a wide frequency range. The phase sensitive detection using lock-in amplifier shows improved scanning results for the vibrating microphone during steady state operation. The performance of the interferometer can be further improved by active control of the distance to the MEMS device for maximum sensitivity. In order to operate an array of μPSGI on a typical MEMS fabrication wafer, each integrated array element needs to be optimized for displacement detection at each sensor. This is achieved by electrostatic actuation of a movable diffraction grating. This capability along with the integration of optoelectronics will eventually reduce alignment and noise problems.

## REFERENCES

1. K. Panetta, N. Aluru, S. Bart, S. Blanton, K. Böhringer, and R. Brown, "ITC 2000 Panel Discussion: Testing Challenges For MEMS," *Proceedings of ITC International Test Conference*, pp. 1130-1135 October 3-5, 2000.
2. B. Kim, H. A. Razavi, F. L. Degertekin, and T. R. Kurfess, "Microinterferometer for Noncontact Inspection of MEMS," *The 3rd International Workshop on Microfactories,* pp. 77-80 Minneapolis, Minnesota, September 16-18, 2002
3. N.A. Hall and F.L. Degertekin, "Integrated optical interferometric detection method for micromachined capacitive acoustic transducers," *Applied Physics Letters*, Vol. 80, pp. 3859-61 2002.
4. B. Kim, H. A. Razavi, F. L. Degertekin, and T. R. Kurfess, "Micromachined Interferometer for measuring dynamic response of microstructures," *Proceedings of ASME International Mechanical Engineering Congress and Exposition, MEMS Symposium*, New Orleans, Louisiana, November 17-22, 2002
5. User's Manual Model SR844 RF Lock-In Amplifier, SRS, 1997

6. J. E. Graebner, "Optical Scanning Interferometer for Dynamic Imaging of High-Frequency Surface Motion," *IEEE Ultrasonics Symposium*, pp. 733-736, 2000
7. D.M. Bloom, "The grating light valve: revolutionizing display technology," *Proc. SPIE, Projection Displays III*, vol. 3013, pp.165-171, February, 1997
8. W. Lee, N. A. Hall, and F. L. Degertekin, "Micromachined acoustic sensor array with diffraction-based optical interferometric detection", *Proceedings of SPIE Micromachining and Microfabrication*, San Jose, California, January 27-31, 2003 (to be published)

# Design and Fabrication of the MesoMill: A Five-Axis Milling Machine for Meso-Scaled parts

Jaime Werkmeister[1] and Alexander Slocum

## Introduction

With the increased prevalence of meso-scaled products, new tools are being developed to bridge the gap between fabrication processes tailored for micrometer and millimeter sized features [ 1] [ 2]. Compared to its traditional counterpart [ 3], a small machine tool designed for meso-scale could potentially have a smaller overall footprint, shorter structural loop and lower cost than a conventional machine; in addition, a small machine presents opportunities for improved machine metrology, and easier environmental control. This paper describes the design of the MesoMill: a test machine designed to evaluate the use of components new to the design of machining centers including wire capstan drives, ballscrew splines, and an air bearing spindle with an integral Z-axis.

The MesoMill machine concept is shown in Figure 1 where two ballscrew splines[2] at right angles to each other would provide four degrees of freedom. The air bearing spindle with Z-axis would provide a 5th axis. Ballscrew splines are used in robotic systems for pick and place operations, and at this time, the manufacturer was not aware of a machining application. However, by oversizing the units, their stiffness seemed appropriate. The next challenge is to drive the nuts, which can be done with direct drive at relatively high cost; thus it was decided to investigate the use of a wire capstan drive in order to obtain a backlash-free high stiffness transmission ratio. Figure 2 shows a test stand for one of the ballscrew splines whose nuts are driven by wire capstan drives. The intent was to measure the performance of a single axis, and then if the performance was desirable an entire machine could be created by assembling two such axes.

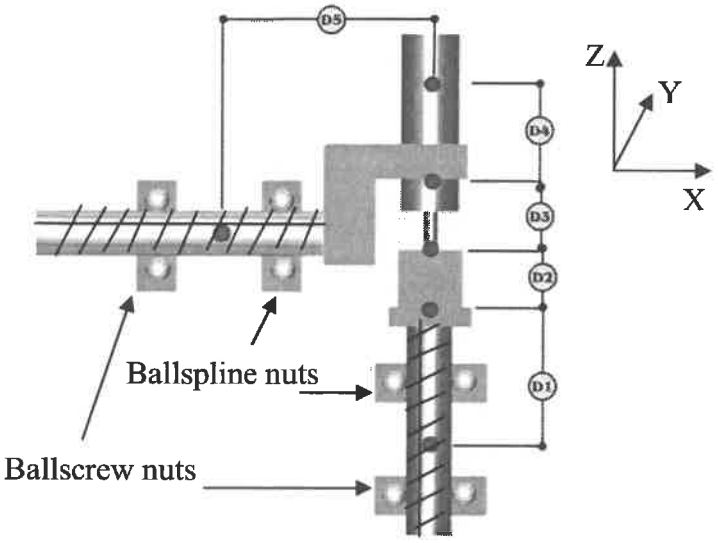


**Figure1:** Structural Loop of Mesomill: Work path is from the work piece to the center of the nuts (D1-D3), Tool path is from tip of tool to the center of the nuts (D3-D5).

The test stand is currently about 500 mm long, 300 mm wide, and 500 mm high. The machine uses a Westwind air bearing spindle with a speed range of 40,000 to 120,000 rpm [ 4]. The spindle incorporates a linear machining axis in Z with a travel of 10 mm, and it was obtained from ESI Corp., which uses these spindles for circuit board drilling operations. Position feedback to the PC-based controller is achieved close to the workpiece using a Heidenhain encoder capable of simultaneously measuring both linear and rotary movement. The error

[1] Precision Engineering Research Group, Department of Mechanical Engineering, Massachusetts Institute of Technology, 77 Massachusetts Avenue, Room 3-445, Cambridge, MA 02139. Email: jbwerkme@MIT.EDU, slocum@mit.edu

[2] A ballscrew spline is a shaft that has both helical and axial grooves ground into it for receiving both ballscrew and ballspline nuts

budget for the first prototype estimates a tool path random error of 1.4 μm for the sweet spot and 2 μm with the axes fully extended. The prototype three-axis version of the MesoMill is currently being tested, and a comparison will be presented between the calculated and measured results.

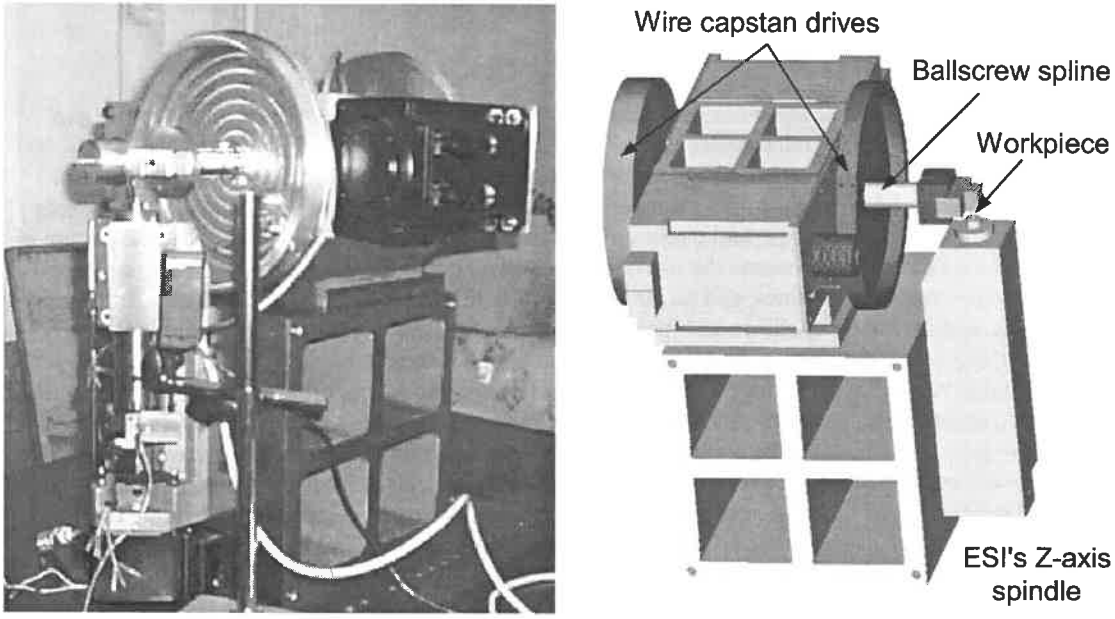


**Figure 2:** Mesomill single axis test stand and solid model

## Error analysis

Given the right angle configuration shown in Figure 1, Tables 1 and 2 show the estimated errors for the work path error and tool path respectively. The largest contributing factor to the error is from misalignment of the tool in the chuck. The farther the Z-axis is extended, the distance $D_3$, the larger the error. With the Z-axis retracted and the axes centered, the predicted accuracy is 1.4 microns. With all the axes at the limit of their travel, the predicted accuracy is 2 microns. With mapping of the axes' errors, a factor of 5-10 improvement is expected because there are only preloaded low friction joints in the machine.

**Table 1:** Work path error for retracted and extended tool. Both cases are the same. The zeros indicate no movement in direction specified (nonsenstive direction) and the rotational errors are small. Estimated as one part in 100,000. $D_1$ to the base is the origin.

| Work Path | $\Delta_x$ (μm) | $\Delta_y$ (μm) | $\Delta_z$ (μm) | $\varepsilon_x$ (rad) | $\varepsilon_y$ (rad) | $\varepsilon_z$ (rad) |
|---|---|---|---|---|---|---|
| $D_2$ (25 mm) | .25 | .25 | .25 | 1E-5 | 1E-5 | 1E-5 |
| $D_1$ (230 mm) | .16 | .16 | 0 | 1E-5 | 1E-5 | 1E-5 |
| $D_1$ to base (216 mm) | 0 | 0 | 0 | 0 | 0 | 0 |

**Table 2:** Tool path error for tool retracted (Retr) and extended (Ext). The zeros indicate no movement in direction specified (nonsenstive direction) and the rotational errors are small. Estimated as one part in 100,000.

| Tool Path | $\Delta_x$ (μm) | $\Delta_y$ (μm) | $\Delta_z$ (μm) | $\varepsilon_x$ (rad) | $\varepsilon_y$ (rad) | $\varepsilon_z$ (rad) |
|---|---|---|---|---|---|---|
| $D_3$ (16 mm) (Retr) | .1 | .1 | 0 | 1E-5 | 1E-5 | 1E-5 |
| $D_3$ (38 mm) (Ext) | .1 | .1 | 0 | 1E-5 | 1E-5 | 1E-5 |
| $D_4$ (70 mm) (Retr) | .015 | .015 | 0 | 1E-5 | 1E-5 | 1E-5 |
| $D_4$ (70 mm) (Ext) | .038 | .038 | 0 | 1E-5 | 1E-5 | 1E-5 |
| $D_5$ (215 mm) (Retr and Ext) | .5 | .5 | 0 | 1E-5 | 1E-5 | 1E-5 |
| $D_5$ to base (254 mm) (Retr and Ext) | .15 | .15 | 0 | 1.02E-6 | 1.02E-6 | 1.02E-6 |

## Stiffness Model of the Ballsplines

The principal structural elements are the ballsplines, and originally it was thought that the ballsplines could project through air bearing sleeves in order to provide a greater degree of accuracy and dynamic stiffness. The grooved portion of the shaft could be of a smaller diameter than the portion through the air bearings, and hence radial error motions induced by the nuts could be reduced. Figure 3 shows the model of the this concept [ 5], and it is found, as the length of c and d increase, the deflection ratio between the workpiece end (x= 0) and the nut end (x = c + d) decrease for a given radial deflection at the nut; however, the size of the machine grows in proportion to its workspace so the question is, how much "self coupling" is desired verses buying more accurate components in the first place?.

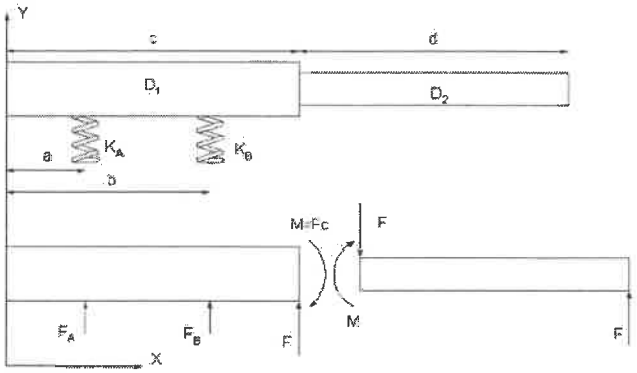


**Figure 3:** Stepped shaft model of the ballscrew spline supported at its front end by air bearings, where radial displacement from the nut closest to the air bearings is applied to the end of shaft segment $D_2$.

However, adding length to the shaft to enable it to be supported by the air bearings makes the machine very large with respect to its work volume; hence an important part of the tests are to determine if they are really even needed. Thus the initial test machine does not use the air bearings, it only uses the screw and spline nuts to support the shaft.

## Transmission System

Wire capstan drives are used as rotary transmission elements for their antibacklash and high stiffness properties, which can be on the order of $10^5$ N-m/rad. The multiple wrappings of the cable around the drum are the key in giving the transmission its stiffness [ 6]. The capstan considered in this study is made up of two drums, 76 mm input and 280 mm output, and a 3 mm diameter cable. The cable is wrapped around the drum in a figure-eight pattern twice but could be wrapped more to obtain even higher stiffness. There are several ways to analyze the stiffness of the transmission depending on how friction is considered. Figure 4 figuratively shows the cable wrapping scheme of the wire capstan drive.

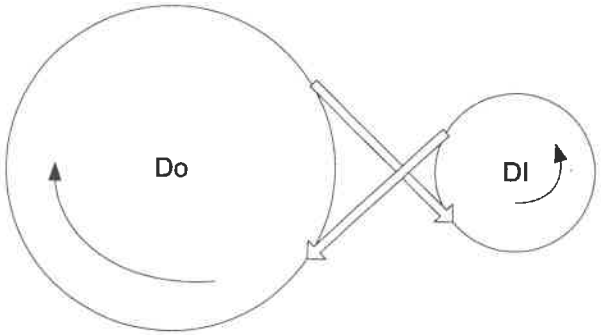


**Figure 4:** Representation of Capstan drive where arrows represent direction of drum and cable motor

The cable can exhibit traction along a particular section, or along the whole drum. These two derivations were performed and showed the stiffness is higher for the traction acting along the drum instead of a particular section. However, even though the stiffness is smaller, it is still higher than similarly sized belt or gear

transmissions. Experiments were conducted to determine the stiffness of a capstan drive. These measurements show a stiffness value less than $10^5$ N-m/rad, but as the preload in the cable is increased, the stiffness increases too as is shown in Figure 5.

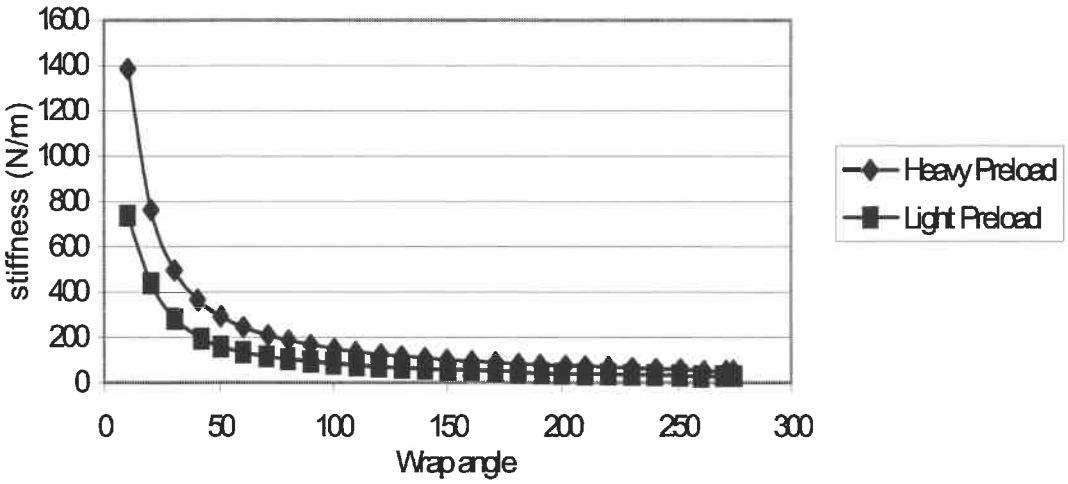


**Figure 5:** Measured stiffness vs. angle of rotation for heavy and light preload.

## Conclusions

The mesomill testbed has been assembled and is currently being integrated with the control system. Preliminary experiments on the stiffness of the wire capastan drives are very encouraging. The general ease with which the components were assembled makes us optimistic about the obtainable repeatability and accuracy of the system.

## Acknowledgements

The fabrication of the Mesomill would have not been possible without the aid of Wojciech Kosmowski and Mark Kosmowski of ESI who donated the Westwind aerostatic spindle, Thomas Massie of SensAble Technologies who donated a capstan drive to play with, THK donating the ballscrew spline, and Alkan Domez and Brad Damazo of NIST for their endless knowledge and support in seeing the Mesomill built and tested. Thank you.

## References

[ 1] Proceedings of the *Manufacturing Three-Dimensional Components and Devices at the Meso and Micro Scales: A Workshop Cosponsored by the National Institute of Standards and Technology and the National Science Foundation,* Gaithersburg Maryland, 1999

[ 2] National Science Foundation workshop on $M^4$: Micro/Meso-Mechanical Manufacturing. Northwestern University: Evanston, IL, May 2000. http://216.239.53.100/search?q=cache:gGx0lQtiaTMC:www.mech.northwestern.edu/MFG/AML/M4/M4-Files/M4-REPORT.doc++site:www.mech.northwestern.edu+machines+meso+Illinois&hl=en&ie=UTF-8

[ 3] ROBOTOOL-Project, *Advanced Kinematics for Manufacturing Applications: List of existing parallel kinematics*. Last updated July 9, 2002. http://www.ifw.uni-hannover.de/robotool/pages/listeenglisch.htm

[ 4] ASME B5.57M *Methods for Performance Evaluation of Computer Numerically Controlled Lathes and Turning Centers*, version 9.0, May 1997, ASME B5/TC52 Committee.

[ 5] Roberts, Michael, *Approximation of Air Bearings as Linear Point Springs: Verification of an Analytical Model for a New Five-Axis Machine Tool.* Massachusetts Institute of Technology, 2002.

[ 6] Sagebrush technology, Inc. Date visited 12/2002. http://www.sagebrushtech.com/tech/technology.html

# Advances in Fast Nano-Precision Motion Technologies: Practical Parallel Kinematics

Scott Jordan
Director, NanoAutomation® Technologies
Polytec PI, Inc. San José, CA
email : scottj@polytecpi.com

## 1. Abstract

Mechanical and controls advancements have long been sought to address emerging needs in industrial and optical applications for higher resolution and higher process throughputs —or, ideally, both. Today these desires are concurrent with new needs for multi-degree-of-freedom positioning in industrial applications such as alignment in MEMS and photonic-device packaging, beam-path and mask-position correction in microlithography, and scanning and tracking processes in scanned-probe and fluorescence microscopy. Such processes often require submicron accuracy in order to achieve yield and coupling-efficiency targets.

Traditionally these goals would be at cross-purposes, since the time to settle to a given positional tolerance rises exponentially with the inverse of the tolerance, all else being equal; meanwhile multi-degree-of-freedom mechanisms traditionally have traditionally necessitated massive stacks of motion stages.

Given the rapidly diminishing dimensional tolerances in a wide spectrum of industrial processes versus the "time is money" truism for any manufacturing or research endeavor, commercial advances which address these needs at the same time represent fundamental breakthroughs of keen interest to industrial engineers and researchers. In this article we review such advancements in the fields of flexure-based nanopositioners, multi-axis low-inertia parallel-kinematics mechanics designs and high-bandwidth controls engineering with application to nano-scale positioning, microfabrication, laser patterning, alignment, packaging and active optic applications:

- Integrated, parallel-kinematics microrobots with up to six degrees-of-freedom and high-level, easy-to-use controls;
- Advancements in flexure designs which improve nanometer-scale bi-directional passive trajectory control, often allowing bi-directional processing for the first time;
- Multi-axis, high-bandwidth active trajectory control, allowing out-of-plane motions in scanning applications to be controlled to Ångstrom levels;
- Industrial-class implementations of Momentum Compensation (also known as Frahm Damping) for low-order cancellation of inertial inputs to supporting structures and is of particular applicability to structures with low natural resonance frequencies;
- OEM modules and controls which implement Input Shaping®, a patented controls technique developed at the Massachusetts Institute of Technology, which provide cancellation of structural resonances in any actuation profile;
- Input Preshaping™, a technique realized in both a priori and self-learning implementations, substantially eliminates following errors in repetitive actuation.

The author reviews applications of each of these, alone and together, in a comprehensive overview of the state of the art of industrial nanopositioning techniques.

KEYWORDS: piezo, nanopositioning, parallel kinematics, microrobotics, photonics packaging, MEMS, hexapod, semiconductor, data storage, lithography, head test

## 2. Problem Statement: Settling Dominates Today's Applications

A common thread in current and emerging industrial and research applications is rapid (up to ~several kHz) physical motion. Rapid motions pose significant challenges: amplifier, interface, sensor and processing bandwidths pose obvious limitations, and the physical constraints posed by the lowest resonant frequency of the actuation mechanics provides a fundamental limit to how rapidly the workpiece may be repositioned. All of these are addressable in design choices (to a point), including: stiffer materials; optimization of moments of inertia along strategic vectors; maximization of the overall stiffness-to-weight ratio; replacement of stacked axes by multiaxis parallel-kinematics designs; mass reduction; integration of higher-bandwidth actuation technologies such as piezoelectric elements; integral damping provisions; and so on. Such improvements allow the

fixtured load to be actuated more and more rapidly. In addition, control algorithms have been developed which address phase-lags inherent in finite-bandwidth electromechanical systems.

Meanwhile, projections of system throughput often do not adequately consider the consequences of the rapid actuation on the structure, including the actuated load and its fixturing, the supporting framework and adjacent componentry. Any actuation (except a pure sinusoid without beginning or end) embodies many Fourier components which drive resonances throughout the assemblage.

The physics of recoil-driven resonant reaction is straightforward: after excitation by a force such as the actuation or recoil resulting from it, the amplitude of the resonant ringing of each element in a structure scales as $e^{-t/\tau}$, where $\tau$ is the time constant for each element's resonant characteristics. For structures with damping characteristics typical of precision motion subassemblies (see Table 1), $\tau \sim (\omega_n \zeta)^{-1}$ where $\omega_n$ is the resonant angular frequency and $\zeta$ is the damping ratio for the resonance. $\zeta$ is commonly defined as the ratio of the damping for the resonance versus critical damping ($\zeta = C/C_c$) and varies from 0 (no damping) to 1 (critical damping) (see Figure 1).

| $F_{res}$ (Hz) | $\omega_n$ (rad/sec) | $\zeta$ | $\tau$ |
|---|---|---|---|
| 75 | 471.24 | 0.0005 | 4.244 |
| | | 0.001 | 2.122 |
| | | 0.005 | 0.424 |
| | | 0.01 | 0.212 |
| | | 0.05 | 0.042 |
| | | 0.1 | 0.021 |
| 150 | 942.48 | 0.0005 | 2.122 |
| | | 0.001 | 1.061 |
| | | 0.005 | 0.212 |
| | | 0.01 | 0.106 |
| | | 0.05 | 0.021 |
| | | 0.1 | 0.011 |

**Table 1. Time constant $\tau$ for various damping coefficients, $\zeta$, and resonant frequencies, $\omega_n$**

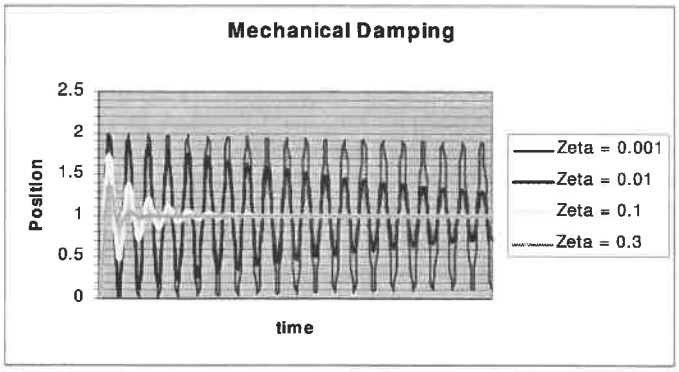


**Figure 1. Generic mechanical damping behavior after a rapid motion, shown for various material damping ratios, $\zeta$. The amplitude of the ringing diminishes with time as $e^{-t/\tau}$, where $\tau \sim (\omega_n \zeta)^{-1}$.**

Clearly, this dictates worsening process throughputs as tolerances tighten and throughput needs escalate.

Unfortunately, classical mechanical damping is of limited value in these situations, and wrapping a servo around the entire fixture is impractical for many reasons and limited by bandwidth issues. Needed are techniques which eliminate problematic motion-driven vibrations, wherever they may occur in the assemblage—on-board or even far removed from the motion device—and observable by metrology or not.

## 3. Approaches to Improving System Dynamics

### *3.1 Frahm Damping/Momentum Compensation*

This involves the integration of an equal-and-oppositely-actuated mass which opposes the motion of the load, providing net cancellation of the impulse applied to the underlying structure. It can work well as long as the real and dummy loads and actuators are reasonably identical, have identical controls, and are configured to actuate coaxially so as to eliminate couple moments. Several examples of this approach are discussed, including quantification of residual resonant response and discussion of complementary technologies.

### *3.2 Input Shaping®*

A patented, real-time feedforward technology called Input Shaping® was developed based on research at the Massachusetts Institute of Technology and commercialized by Convolve, Inc., (New York, NY; http://www.convolve.com). We present its

implementation in OEM NanoAutomation® products by PI; it is also available in motor controllers from Galil, Delta Tau and MEI. The technique scales and times transitions in the command in real-time so motion-driven vibrations are canceled throughout the system. It uses characterization of resonances as quantified during installation and does not require feedback. Unlike notch filtering, it is insensitive to variations in frequency over a range >±15%. It is effective against multiple resonances, resonances occurring outside the servo loop, and resonances exceeding system bandwidths. Its robustness makes the technique attractive for OEM usage. In particular:

- It requires no changes to application setup, software or servo parameters.
- It cannot degrade servo stability and can be used for any motion profile.
- It is does not require specific configuration for specific motions.
- It is robust with changes in operating dynamics, such as unit-to-unit variations, or moderate changes in loading.

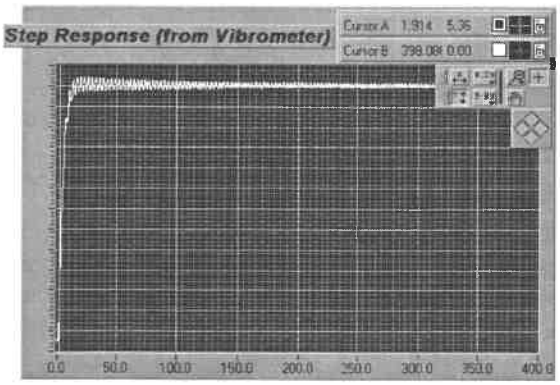


**Figure 2. Piezo devices are capable of millisecond-scale step-and settle. However, elements outside the servo loop ring (load, neighboring componentry…). External resonances are visualized here by a Polytec laser vibrometer measuring position vs. time.**

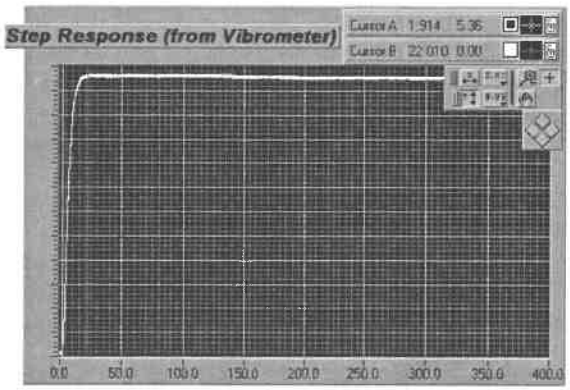


**Figure 3. Input Shaping® eliminates motion-driven ringing of components outside the servo loop. Settling after risetime completes by $t \sim F_{res}^{-1}$**

### *3.3 Complementary Implementations*

We present a simple coarse/fine angular positioner as an illustrative test-bed for demonstrating the complementary nature of Momentum Compensation and Input Shaping. This mechanism is extensively quantified using laser Doppler Vibrometry to illuminate a host of recoil-driven physical effects and illustrate how they might be addressed using these techniques.

### *3.4 Bandwidth Improvement: Input Preshaping*

For applications with continuous, repetitive periodic inputs, a new pre-shaping technique can reduce the rolloff, phase error and hysteresis of the servo, improving the effective bandwidth and allowing more accurate tracking. Input Preshaping can reduce the tracking error to the noise level and improves the effective bandwidth by a factor of 10 or more. Accuracy and tracking error improved considerably versus what can be achieved by conventional P-I-D controls. In the example presented, overall following error is reduced by approximately two orders of magnitude; this includes contributions from servo-system rolloff as well as nonlinearities such as PZT hysteresis.

## 4. The Advent of Practical Parallel Kinematics

Clearly, Hookes' Law illustrates that system throughput and settling performance are both optimized when the moving mass and structural stiffness of the motion system are maximized. In multi-axis actuation, this means the bottom axis carries the other axes in addition to the load and its fixturing. Alternatively, system dynamics can be improved by implementing a parallel actuation design (Figure 4). This improves system dynamics both through mass minimization and by stiffening the resulting structure.

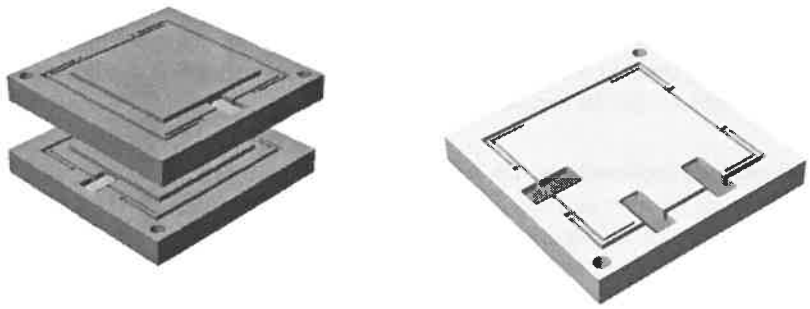

**Figure 4. Compared to multi-axis stacked approaches (such as the piezoelectric XY nanopositioning stage stack shown on the left), a parallel kinematics approach reduces the effective moving mass of the multi-degree-of-freedom actuated platform by more than a factor of two (right). Additional axes can be implemented (the right-hand drawing actually shows an $XY\theta_z$ design) without increase in the effective moving mass.**

One attraction of such an assembly is that additional axes can readily be implemented with virtually no increase in the effective moving mass. Another advantage is that direct motion metrology of the common moving platform is possible, resulting in automatic, real-time compensation of parasitic motion errors. We present examples of such mechanisms, resulting in performance as summarized in Figure 5.

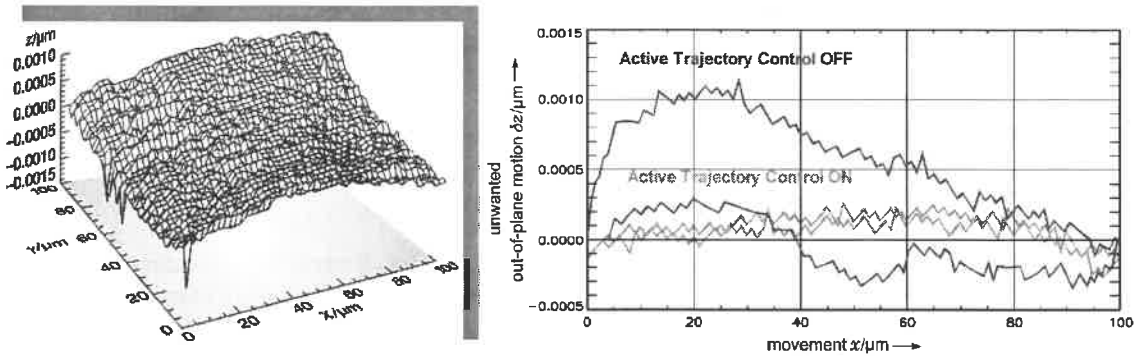


**Figure 5. Simultaneous, orthogonal sensing of platform position allows the controller to actively correct for parasitic motion errors in real time. The 6-axis stage presented thus achieves ~2Ångstrom RMS out-of-plane motion.**

Another example of parallel kinematics is hexapod configurations such as the commercially-available Stewart platform we also present. An equivalent stack of stages capable of providing similar travels and supporting similar loads can achieve a loaded resonant frequency of 50-75Hz; by supporting the load in parallel with six actuators, this hexapod achieves a 500Hz resonant frequency, facilitating greatly improved system dynamics and settling performance.

# Interferometric measuring microscopy applied to miniature machines, structures, and surface features

John Roth, Eric Felkel and Peter de Groot

*Zygo Corporation, Middlefield, CT 06455*

## INTRODUCTION - THE NEED FOR 3D SURFACE ANALYSIS

MEMS are complex microstructures such as data storage read-write heads, accelerometers, ink jet printer heads, sensors and micro-mirror arrays. Typically, measuring microscopes control and monitor MEMS fabrication, including the silicon micro-machining process. Metrology tools measure a wide variety of devices at various stages of device fabrication, including wafer, die, and packaged-level, and require flexibility and automation to meet the varied needs of R&D and production [1].

The large diversity of devices, materials, and processes, and the wide range of surface parameters create unique challenges for MEMS metrology tools. The physical dimensions and geometries of MEMS encompass a large range, from tens of millimeters down to the angstrom level. Ideally, surface characterization yields quantitative information over a variable field-of-view covering the x, y and z dimensions. Additional procedures and controls characterize mechanical parameters such as deformations.

For the past decade, optical profilers based on scanning white light interferometry (SWLI) have enabled leading edge development and commercial success of advanced MEMS devices. We review the special requirements for MEMS metrology, the general principles of SWLI microscopy, and show several examples of expanded capabilities including integrated lateral metrology, long working distance objectives, and closed-loop deflection measurement.

## SCANNING WHITE LIGHT INTERFEROMETRIC MICROSCOPY

A natural candidate for non-destructive 3D surface structure analysis of a MEMS device is an interference microscope, which provides surface height detail with sub-nm resolution. The instrument of choice is the scanning white light interferometer or SWLI microscope [2]. SWLI, also known as coherence scanning or vertical scanning interferometry, is fundamentally a multiple-wavelength technique, relying on a spectrally broadband source to remove the interference fringe order ambiguity characteristic of the previous generation of monochromatic interferometers.

In a typical application (Figure 1), a PZT or similar mechanical transducer scans an interference objective towards or away from the object surface, gathering data by electronic camera during the scan. The data are then transformed by coherence and phase analysis into a surface profile. The scan direction orthogonal to the part surface can be several mm in length, accommodating tall step heights and disconnected regions characteristic of MEMS devices. SWLI has the interesting and important property that it has the sub-nm resolution of conventional interferometers on polished surfaces [3], but is nonetheless capable of handling rough surface textures that generate complex speckle patterns that traditionally were considered inaccessible

to interferometric metrology [4]. Surface profiling microscopes are ideal for form and roughness measurements on small parts. Figure 2 illustrates an example surface topography measurement of a MEMS device using the measurement geometry of Figure 1.

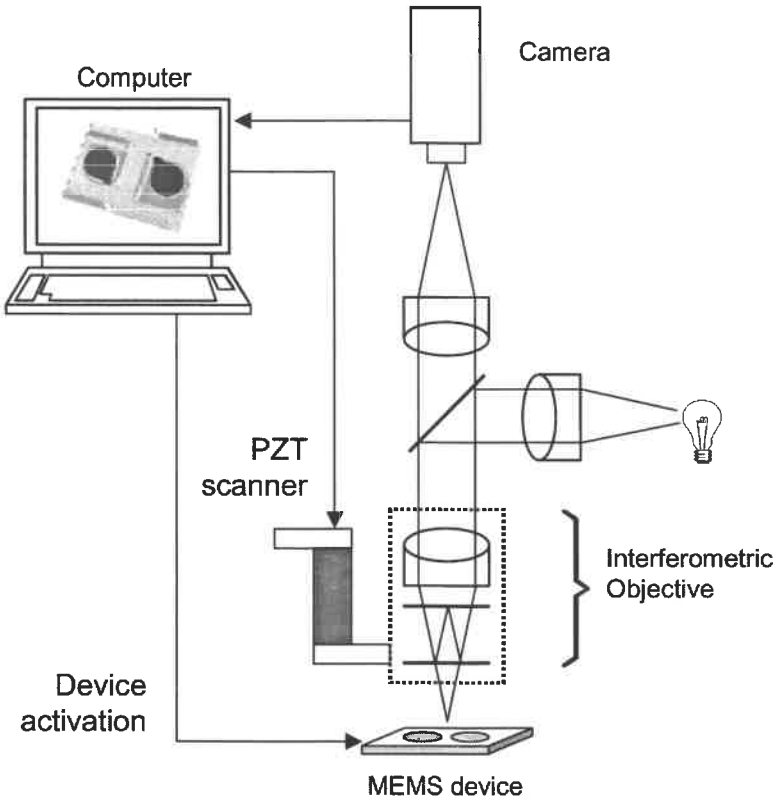


**Figure 1:** Typical MEMS metrology geometry for a SWLI type measuring microscope.

## OUT OF PLANE PARAMETERS

The function of a many MEMS devices relies on out-of-plane deflections. Wafer-level characterization of controlled deformations allows device fabrication verifies performance prior to the investment of additional processing such as dicing, packaging and bonding, leading to increased yields and cost savings. Examples include actuators, pumps, and membranes, as well as pop-up, tilt-able, and deformable mirrors. In other cases, any out-of-plane deflection is highly undesirable, for example in accelerometers and gyros.

For some MEMS devices, the objective is to characterize the micro-mechanical system as a function of applied voltage. A simple set-up performs a series of individual measurements after actuation of the device in repeated steps, without the need of mechanical contact. The data can be rapidly visualized and processed to yield quantitative information.

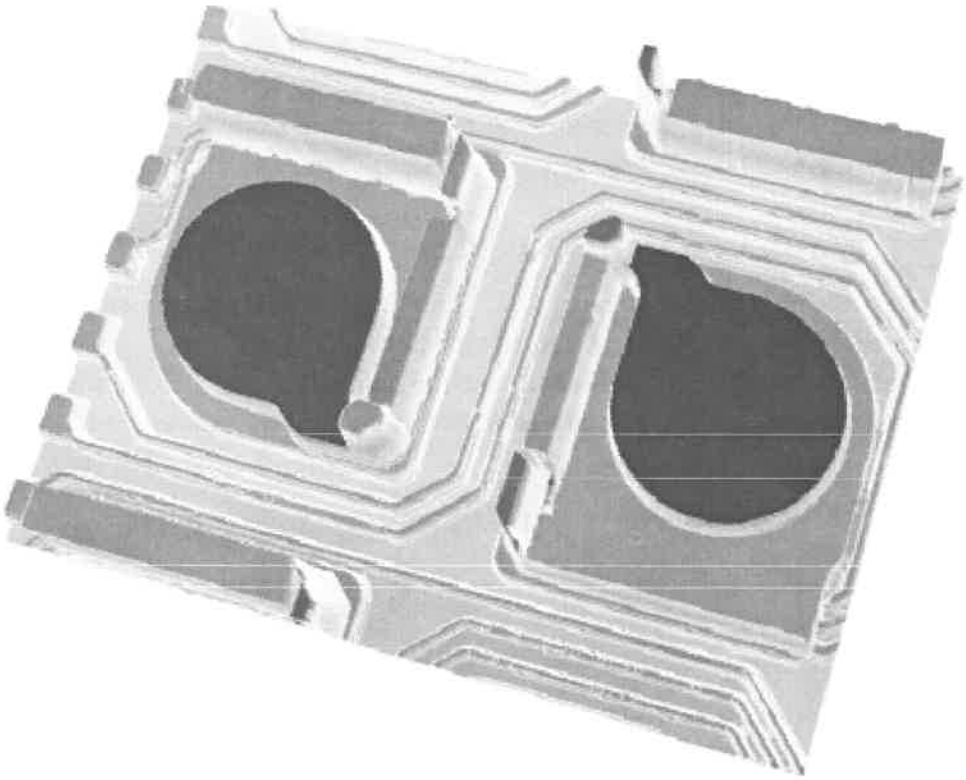

**Figure 2:** Surface topography map of a MEMS micromirror device. The lateral dimensions are 1.6 X 1.8mm, and the height range is 10 μm.

A typical scenario is a measurement tool in concert with a MEMS controller, using a flexible scripting language as the programming environment. In one example developed in collaboration with an end User, the microscope measures out of plane tilt as a function of applied voltage. The measure cycle begins with the MEMS device at the zero state, with no voltage applied. At the completion of this measurement, the profiler contacts the MEMS controller and requests a new voltage level. After applying the new voltage, the controller sends a signal back to the profiler indicating completion of its task and prompting the profiler to continue with its measure sequence. Repeating this cycle and logging the numerical data generates an applied voltage response curve for device calibration.

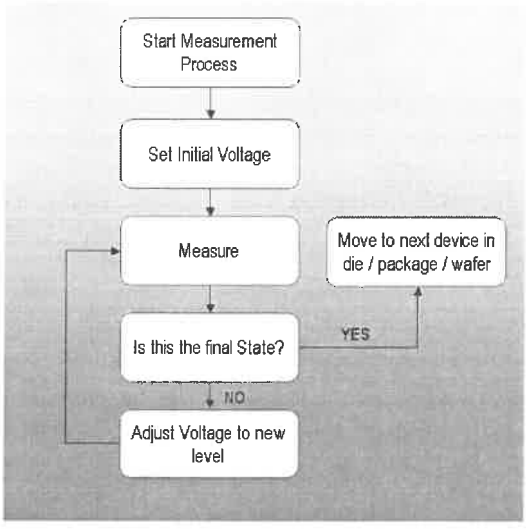


**Figure 3:** Flowchart depicting closed loop response measurement

A special consideration in these measurements is a long working distance to accommodate packaged devices and provide room for electrical probes, vacuum chucks, thermal plates, and manipulators for characterization and actuation of devices under test. Ultra-long working distance objectives (>15mm) simplify the integration of the measurement system with other experimental apparatus. It is also possible to image through a glass window to enable characterization of the device within a vacuum or sealed package.

## IMAGE ANALYSIS AND DIMENSIONAL METROLOGY

Since MEMS devices rely on mechanical properties, lateral dimensions such as size, location, diameter, shape and offset are equally as interesting as surface topography. With the complete integration of an image processing vision system, the SWLI profiler is easily used to determine x-y dimensions as well as heights in the z direction. Such a system can also perform higher-level tasks such as device rotation during activation.

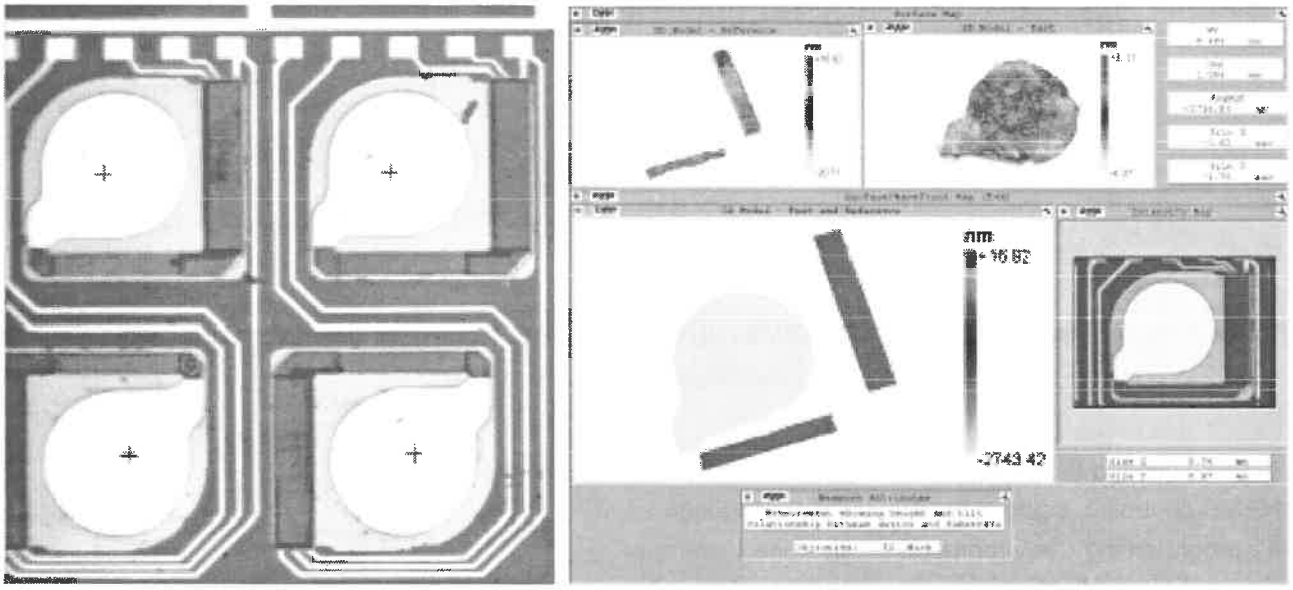

**Figure 4:** Automated feature finding. Left: The crosses indicate the defined centers of the six features identified by image analysis. Right: Image segmented by height relationships.

Advanced algorithms locate and segment complex data over a given field-of-view, without the need for hardware or software masks. The segmentation relies either on image intensity data (Figure 4a) or relative surface profile (Figure 4b). Automatic segmentation allows for several process enhancements including automation of individual and wafer level device metrology, increasing throughput and eliminating subjectivity introduced by manual masking.

Once identified, x-y metrology of specific features proceeds as illustrated e.g. by Figure 5, to determine the diameter of a round feature by detailed edge finding.

The vision system that is an integral part of a SWLI microscope also performs defect analysis. By teaching the vision system what an ideal part should look like, the actual test part can be compared to determine how closely ideal and actual parts match. The image analysis also locates defects such as pits, scratches and contaminants (Figure 6).

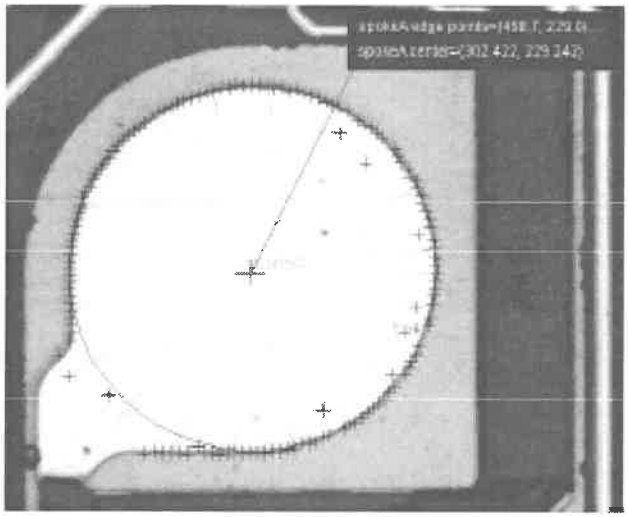

**Figure 5:** Dimensional Metrology – The round portion of the device has been fit to a circle. The measured diameter is 306.392 pixels or 513.05 µm. The measured area is 0.218907 $mm^2$

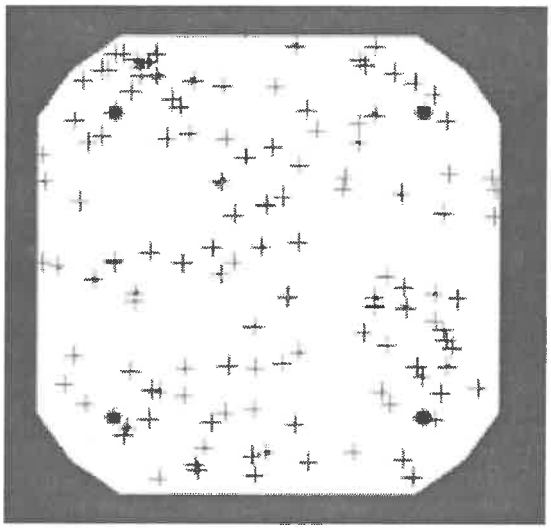

**Figure 6:** Defect analysis – 125 defects are identified as crosses within this 10.074 $mm^2$ area.

## REMOTE ACCESS

As a final note, while much of the design of MEMS devices is performed in high technology environments with high costs of manufacturing, the actual manufacture of these devices is often contracted out to a MEMS foundry. These foundries are often in a distant geographic region as compared to the design center. In order to keep manufacturing processes under control or to monitor manufacturing progress, it is often convenient to set up a profiler at the foundry which can be controlled remotely via a high-speed internet connection from anywhere in the world.

Using PC remote control software and application sharing, it is possible to access the surface profiler's GUI from a remote location (Figure 7). Operations such as moving a programmable stage or changing the position of a motorized objective turret can be programmed to occur when a button on the interface is pressed. This sort of application is quite useful when great distances separate foundries and designers and measurement turnaround time is a premium.

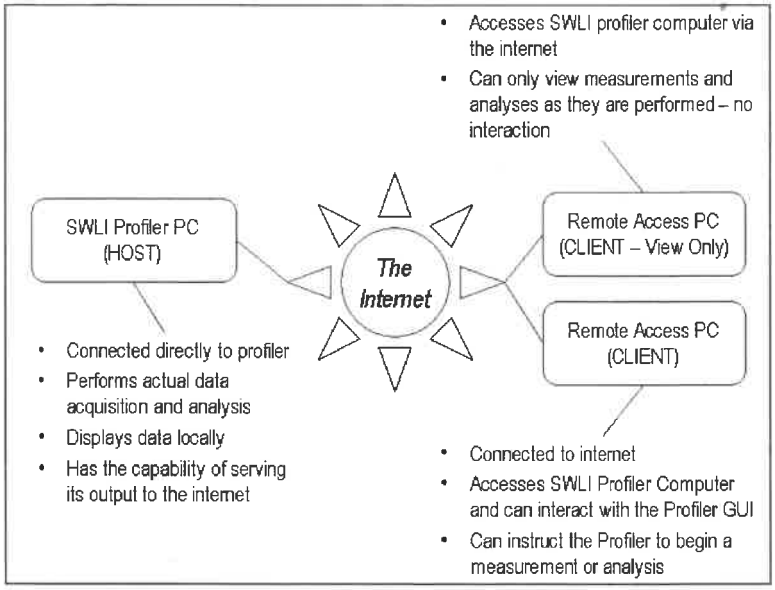
Accesses SWLI profiler computer via the internet
Can only view measurements and analyses as they are performed – no interaction
SWLI Profiler PC (HOST)
The Internet
Remote Access PC (CLIENT – View Only)
Remote Access PC (CLIENT)
Connected directly to profiler
Performs actual data acquisition and analysis
Displays data locally
Has the capability of serving its output to the internet
Connected to internet
Accesses SWLI Profiler Computer and can interact with the Profiler GUI
Can instruct the Profiler to begin a measurement or analysis

**Figure 7:** Example Remote Control Architecture allowing for remote viewing and remote use of SWLI Profiler.

## REFERENCES


[1] S. Brown, B. Gally, R. H. Grace and P. Mukai, *Electronic Design* (July 24, 2000)

[2] J. C. Wyant, Laser *Focus World* (September), 131-135 (1993)

[3] P. de Groot and Leslie Deck, *J. Mod. Opt.* 42(2), 389-401 (1995)

[4] T. Dresel, G. Häusler and H. Venzke, *Applied Optics* 31(7), 919-925 (1992)

# 3D-Analysis of Microstructures with Confocal Laser Scanning Microscopy

Eckart Uhlmann, Dirk Oberschmidt
Institute for Machine Tools and Factory Management (IWF), Technical University Berlin

Gerald Kunath-Fandrei
Advanced Imaging Microscopy, Carl Zeiss Jena GmbH

**Abstract**

The measurement of micro components and microstructures leads to special requirements of measuring gauges. State-of-the-art Confocal Laser Scanning Microscopes (LSM) are suited to meet these requirements. The paper shows examples of effective and accurate analyses of micro tools, micro components, and micro structures with a LSM. It becomes clear, that measurements with a confocal LSM lead to verifiable results in a very fast and simple way.

## Introduction

The manufacturing of micro components of a volume smaller than 1 mm³ is of increasing importance for industry. Recently achieved technological improvements for the manufacturing of these components lead to a steadily increasing number of applications. The transfer of optimized traditional manufacturing technologies to micro system technology allows the manufacturing of smallest three-dimensional structures with accurate dimensions and geometries. Though, traditional measurement principles are often not sufficient to specify the manufactured structures. In contrast, the requirements on the quality of micro products are very high and are even growing by the increasing miniaturization /1/. For the measurement of microstructures, a measurement system has to be chosen that meets the following requirements:

- measurement of structure dimensions in a range of (sub-) micrometers with nanometer accuracy,
- damage-free measurement,
- wide measuring range,
- high vertical and lateral resolution,
- 3D measuring,
- various measuring possibilities (roughness, waviness, form accuracy, macroscopic geometry characteristics),
- high measuring speed with high measuring accuracy,
- simple use and
- possibility of automation.

Components are micro-scaled components (e.g. micro gear wheels), small components with variable micro structures (e.g. lab-on-chip structures) and macroscopic components with even or uneven microstructured surfaces (e.g. dies or foils with structure dimensions in the range of a few micrometers). These examples demonstrate that the quantity, the material, and the dimensions of the basic geometry of manufactured workpieces are absolutely variable. Furthermore, measurements have to be carried out under laboratory conditions as well as under production conditions.

In case of measuring micro structures, the use of measuring systems is limited because of the dimensions of the gauge and a possible damaging of the surface. High performance measuring systems such as Atomic-Force-Microscopes (AFM) have extremely high resolutions, their measuring period, however, is far too long. It is especially the AFM, which is limited to a few micrometers in the vertical range. Optical systems such as auto-focus measuring systems or interferometers have typical disadvantages measuring steep slopes or structures with high aspect ratios.

State-of-the-art confocal laser scanning microscopes (LSM) are suited to meet the requirements listed above. The advantages like excellent contrast, the suppression of scattered light and improvement of lateral resolution are well-known /2/. The use of modern and efficient drive systems and computers results in further crucial advantages. Requirements of the daily use of confocal LSM are subject to research and are often transferred to commercial products /3/.

**Measurement Tasks**

Two representative examples of the great variety of possible measuring tasks are used to explain the functionality of confocal LSM for the analysis of micro structures. These examples are shown in figure 1 and 2 as SEM images. The measurement tasks at these components are multifaceted and challenging. The exact knowledge of the measuring task and basic knowledge about the measuring principle are the prerequisites of accurate measuring results.

Example 1 (Figure 1) shows a triple-edged micro end mill with a diameter of 0.5 mm. It serves the measurement of the topography of the face and the wear characteristics (cutting edge radius and crater wear) visible in this view.

A hot embossing tool is shown in figure 2. The tool is manufactured by path programmed electrical discharge machining (EDM) with rotating pin electrode. The dimensions x, y, z are 2 mm x 2 mm x 1 mm. One of the measuring tasks is to analyze the process and any changes in the tool length by accurate measurement of the path bottom. Another task is the analysis of the cavity profile to measure the wear of the tool diameter. This also requires the measurement and the depiction of the slopes.

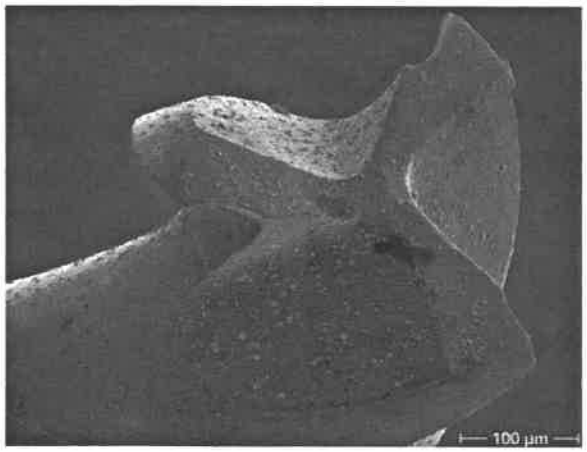


Figure 1: Micro End Mill

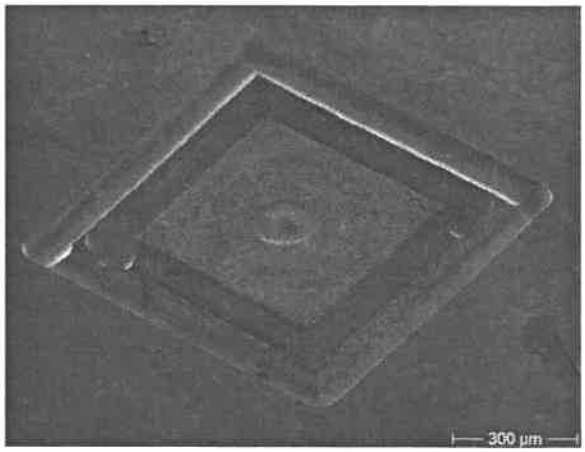


Figure 2: Hot Embossing Tool

## Measurements and Results

*Micro End mill*

The analysis of the tool leads to excellent results. The imaging of the tool is realized by a stack of 50 slices. This allows the interpretation by iso-lines and an excellent valuation of the wear. Figure 3 shows that the signs of wear are very clear and to analyzable in terms of quality and quantity. An exact statement can be made on the wear pattern of the mill through the comparison of the measured data before and after machining. Today, there is still a lack of knowledge about the wear pattern of micro end mills under manufacturing conditions. The presented method can be used close to the manufacturing process. Furthermore, the flexibility of confocal LSM allows the analysis of tool and workpiece. The measurement conditions and the results can be thus compared.

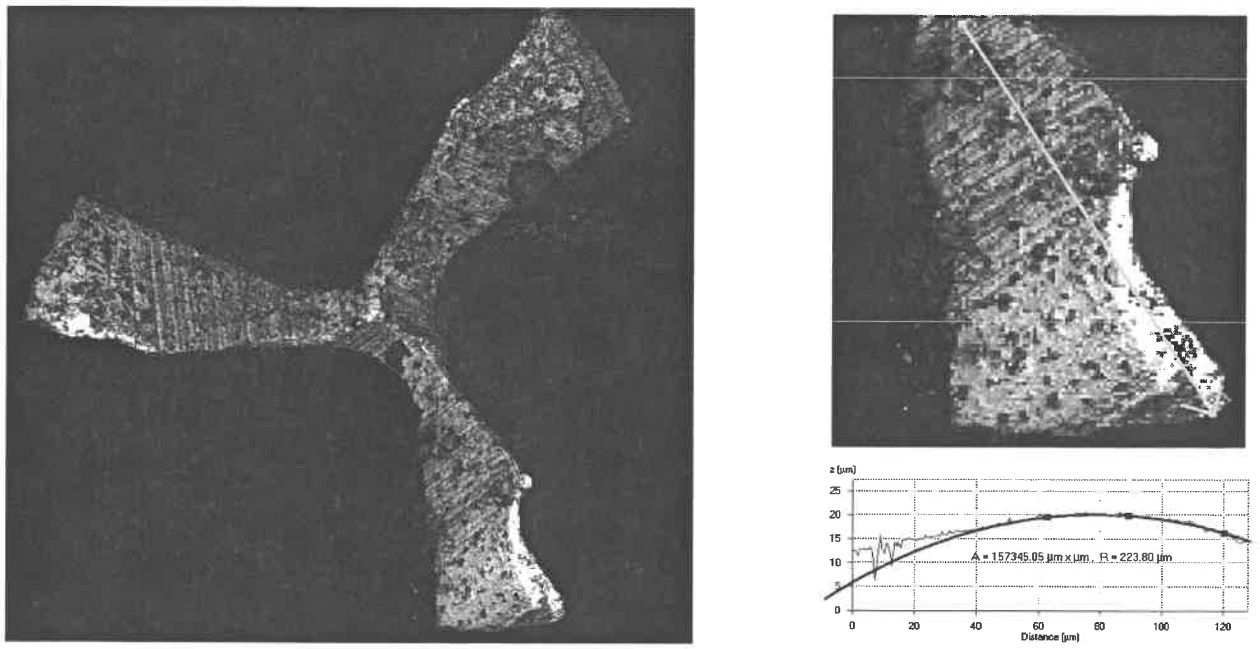


Figure 3: LSM image of the face of the micro end mill (left), resolution 512 x 512 pixel, objective 20x/0.50, median-filtered; measurement of the abrasive wear at a cutting edge (right)

*Hot Embossing Tool*

The used technology allows a determination of the summarized tool length wear by measuring the height of the path bottom at the beginning and at the end of the programmed path (figure 4, right). This value gives no information about the wear pattern of the electrode during the manufacturing process. It is, however, sufficient for the rough programming of the feed of the electrode during the process. The analysis of the proceeding tool wear requires the measurement of the whole cavity and all its characteristics.

The capability of measuring steep slopes is one of the most important advantages of confocal LSM. A minimal roughness is necessary to get an image of slopes of an angle near 90° without any extra equipment. Thus, a damage-free analysis is possible without any cleaning process. Though, an objective with high resolution and numerical aperture must be used to achieve best results. Therefore, the lateral dimensions of a measuring field are often too small to fulfill the measuring tasks. A stitching tool is used to analyze the whole hot embossing tool and the wear pattern of the electrode. Depth and width of the path

must be measured at any point of the path by the evaluation of profiles through the stitched image of the cavity (figure 5).

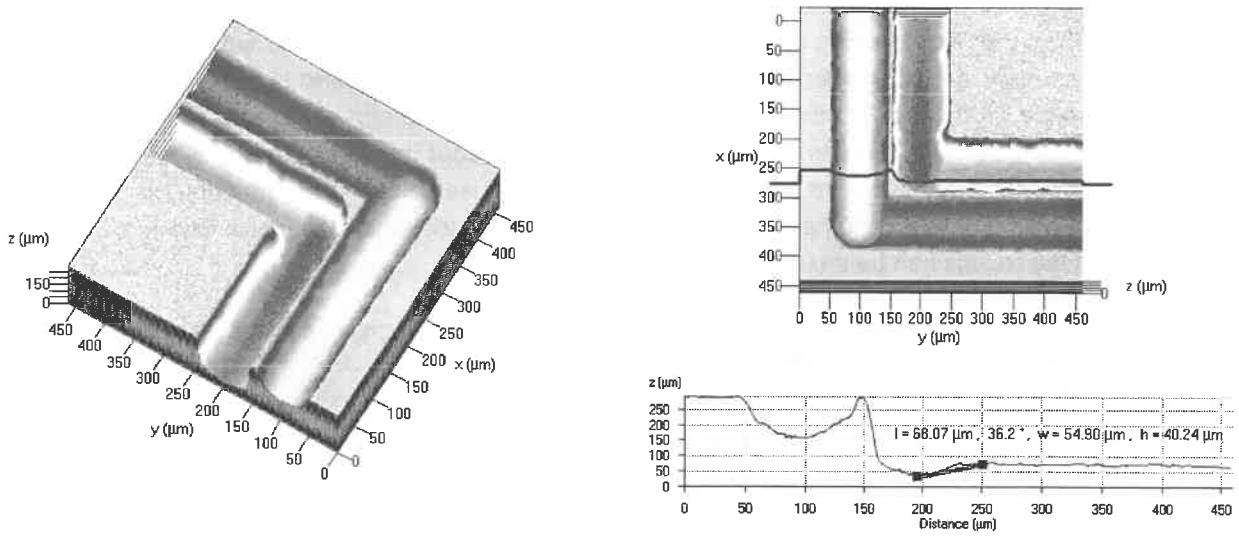


Figure 4: Single image of the hot embossing tool with points of start and end of the programmed paths (left), resolution 512 x 512 pixel, objective 20x/0.50, median-filtered; measurement of the length wear (right)

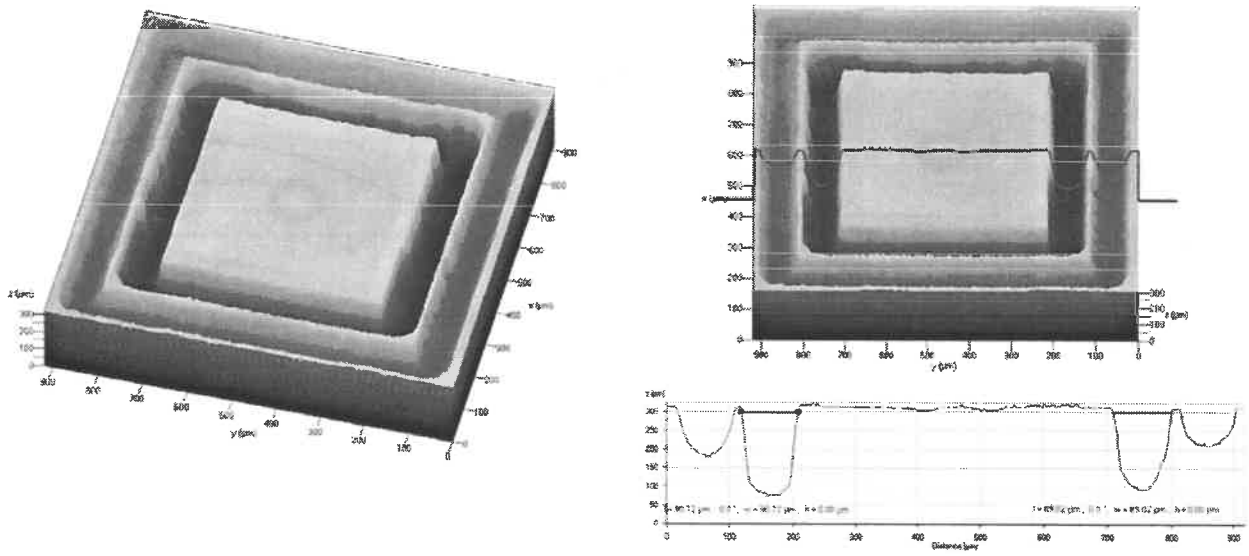

Figure 5: 3D image of the hot embossing tool, 3 x 3 single images (left), resolution 256 x 256 pixel, objective 20x/0.50, median-filtered; Measurement of the wear of the diameter (right) of the electrode

### 3D-Stitching

In material research, quality inspection, and micro production technology, there is often a rather large number of samples to be examined. Therefore, they can only be imaged with a low-power objective. Details get lost and have to be enlarged subsequently in additional detail micrographs. In combination with a motor-driven scanning stage a confocal LSM acquires, assembles, and measures height profiles over

long distances and large-area portions. Because of a large number of stacks and single measuring fields, there is a big amount of data to be processed. ZEISS is still in the process to file a patent for the algorithm that is used for the LSM series. This algorithm saves time and effort in the necessary calculation.

The most important advantage of this option is shown in figure 6. The quality of the vertical and lateral resolution of a stitched image is much higher than a single image. For the practical use, the software integrates many automatic procedures and adjusting functions, e.g. auto-focus, automatic brightness, and contrast optimization, automatic orientation of the scan field and precise correction of the objective's residual field curvature.

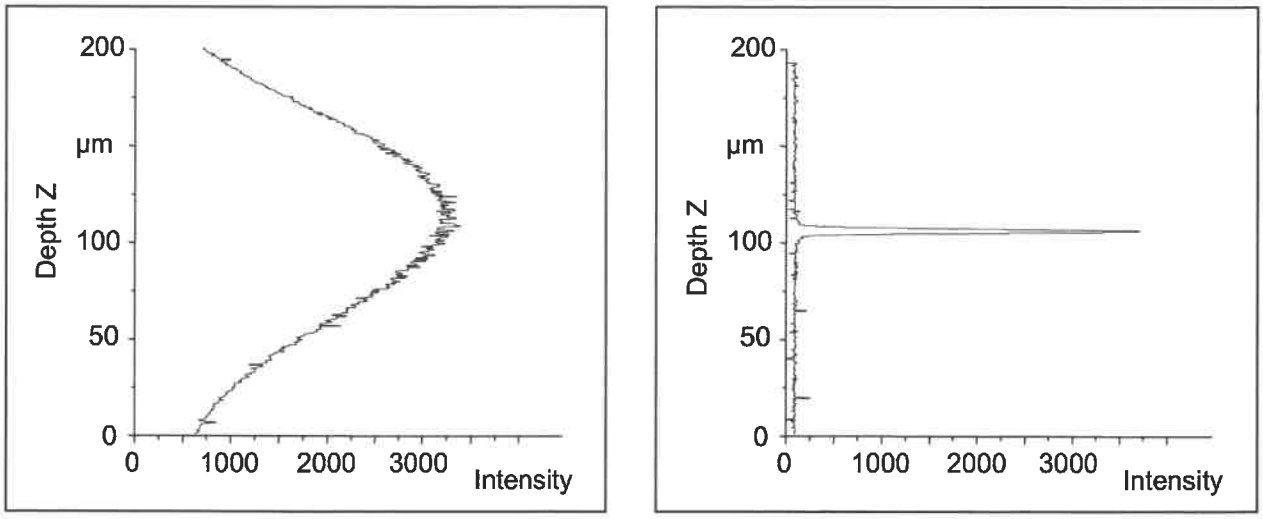


Figure 6: Detected intensity by use of the objectives 2.5x/0.075 (left) and 20x/0.5 (right)

**Conclusion**

Confocal Laser Scanning Microscopy is suitable for the measurement of microstructures. With the help of representative examples, the practical use could be demonstrated. It is clear that this measuring principle is capable of three-dimensional imaging of microstructures with high lateral and axial resolution. The imaging of steep slopes is another important advantage. The big variety of functional analyses allows a very flexible use of the gauge in laboratories and close to the manufacturing pro-cess.

The requirements of special measurement tasks result from the daily use of a gauge. Manufacturer and research institutes must work together to solve upcoming problems and to transfer the discovered solutions into commercial products.

/1/ Spath, D.; Elsner, J.: *Große Anforderungen an kleine Teile.* in QZ Qualität und Zuverlässigkeit 11/2001, 46. Jahrgang, Pages 1408-1409, Hanser Verlag.

/2/ Wilson, T.: Confocal Microscopy. Academic Press Inc., London, 1996.

/3/ Pfeifer, T.; Dussler, G.; Driessen, S.: Confocal Inspection of microscopic parts and structures. in Proceedings of the 3rd **euspen** International Conference, Eindhoven, The Netherlands, May 26th - 30th, 2002, Pages 505 - 508.

# Silicon Wafer Thickness Variation Measurements using Infrared Interferometry

Tony L. Schmitz[1], Angela Davies[2], Chris J. Evans[3]
National Institute of Standards and Technology, Gaithersburg, MD 20899
Robert E. Parks
Optical Perspectives Group, LLC, Tucson, AZ

## 1. Introduction

The continued requirement for higher personal computer processing speed calls for increasingly smaller features on integrated circuits. This need for smaller features (line widths) places greater demands on optical lithography systems and the associated metrology. Current optical lithography processes are composed of three fundamental steps. First, the silicon wafer substrate is spin-coated with an organic photoresist. Using a photomask, or reticle, the coated wafer is then exposed, typically over a number of sub-apertures or die sites located in a grid over the wafer surface, to the desired optical image. This optical image represents the geometric patterns that define the microelectronic circuit. Finally, the photoresist, which has been chemically altered by exposure to the source light, is developed to leave the desired circuit. This process combined with others, e.g., metal deposition, may be completed several times.

In this process, the minimum linewidth is diffraction limited. Equation (1) shows the relationship between linewidth, $L$, imaging lens system wavelength, $\lambda$, numerical aperture, $NA$, and a process dependent factor, $k_1$ [1]. It is clear that in order to decrease linewidth, a smaller wavelength and/or increased $NA$ may be employed. However, a smaller wavelength or increased $NA$ leads to a decreased diffraction limited depth of focus, $d$, for the imaging system. See Eq. 2, where $k_2$ is again a process dependent factor [2]. This decreased depth of focus, in turn, restricts the allowable non-flatness for the silicon wafer. At the 130 nm technology node ($\lambda = 248$ nm), for example, the allocation for wafer topography in the overall depth of focus error budget for 25 mm by 25 mm site flatness is 50 nm [3]. This will reduce to 20 nm for the 50 nm node ($\lambda = 157$ nm) [3]. In optical lithography systems, the wafer is held during production using a vacuum chuck. Therefore, three main contributors to chucked wafer flatness are the following: 1) wafer thickness variation, 2) chuck non-flatness, and 3) wafer/chuck interactions during clamping. In this research, we are focused on the former, variations in unchucked wafer thickness.

$$L = \frac{k_1 \lambda}{NA} \qquad (1)$$

$$d = \frac{k_2 \lambda}{NA^2} \qquad (2)$$

## 2. Wafer Thickness Variation

Several industry descriptors for wafer thickness variation are available. These include, for example, total thickness variation, *TTV* or *GBIR*, which is the difference between the highest and lowest elevation of the specimen front surface with respect to the back surface, and non-linear thickness variation, *NTV*, defined as the difference between the highest point above and the lowest point below an established best fit plane. Parameters are also available for describing the die sites locally exposed by the stepper system, as well as measurements of free state, or unclamped, wafers, such as bow, warp, and sori. Bow is the difference between a plane defined by three pre-determined points on the wafer, the three-point focal plane, and the height of the center point of the unclamped wafer. Warp is the maximum distance between the highest point above and lowest point below the three-point focal plane. Sori is the maximum distance between the highest point above and lowest point below the best fit plane. The International Technology Roadmap for Semiconductors (ITRS) is a good information source for wafer metrology [4].

This wafer geometry information is typically obtained using instruments based on capacitance gage technology. Capacitance-based instruments measure thickness variation by serially scanning a pair of probes located on each side of the wafer over the spinning wafer surface. Due to the increased time and potential dynamics issues involved with spinning a wafer 300 mm in diameter by 775 μm thick, a number of optical instruments have also entered the marketplace. The requirements for optical instruments are selection of an appropriate source wavelength at which the wafers are transparent (if they are to be measured in transmission) and identification of a detector with sufficient sensitivity at that wavelength. In the case of silicon, the absorption edge is near 1100 nm so infrared sources with wavelengths in the communications bandwidth, 1550 nm, are acceptable.

## 3. Infrared Interferometer Description

In our work, we have selected transmissive optical measurements of silicon wafers using the Infrared Interferometer ($IR^2$) developed at the National Institute of Standards and Technology (NIST). Various potential arrangements for $IR^2$ are demonstrated in Fig. 1. Figure 2 shows a schematic representation of $IR^2$ and its components for the 'wafer as cavity/plane wavefront' configuration, which is the current focus of our research efforts. In this setup, the interference pattern is formed from a front surface reflection and a double pass reflection from the rear surface of the wafer. Because these fringes are similar to Haidinger fringes, we will refer to them as such in this paper. Implementations of other setups are described in references [5-8]. The use of the Haidinger fringes to deduce thickness variation places two restrictions on the measurement: first, so that light is reflected from both the front and back surfaces, only double side polished wafers can be measured; and second, the traditional

[1]Now at the University of Florida, Dept. of Mechanical and Aerospace Engineering, Gainesville, FL (tschmitz@ufl.edu)
[2] Now at the University of North Carolina at Charlotte, Dept. of Physics and Optical Science, Charlotte, NC
[3] Now at the Zygo Corp., Middlefield, CT

method of phase shifting by moving the reference surface by a known amount relative to the test surface cannot be applied. In our implementation, we use a tunable wavelength source to perform the phase shifting.

Preliminary efforts have concentrated on identifying potential error contributors and quantifying an uncertainty analysis for the measurement procedure. Several possible error components have been identified including: diode wavelength calibration, phase measuring algorithm, camera/wafer coordinate system alignment, imaging system distortion, stray light, wafer holding technique, wavefront effects, diffraction, wafer refractive index and homogeneity, alignment/focus sensitivity, and camera resolution/wafer surface spatial frequency effects. Initial efforts at evaluating the measurement uncertainty have included: 1) a two day drift test with measurement performed in 15 minute measurement intervals; 2) measurement comparisons of a single wafer measured using two different collimators; 3) an investigation of the effects of phase change on reflection on the measured thickness variation; and 4) an intercomparison between thickness variation results obtained using $IR^2$, an independent optical instrument, and a capacitance gage-based instrument. These initial test results will be described in the following paragraphs. Further research will be required before a full evaluation of the measurement uncertainty can be completed.

*3.1 $IR^2$ Drift Test*

The drift test was carried out using a 150 mm aperture, approximately f/6, 2 optical element collimator that captured data from the central portion of a 200 mm diameter, 750 μm thick, double side polished wafer. The measured optical path difference, *OPD*, was converted to thickness variation in nm using an assumed, homogeneous silicon index of 3.5. The wafer thickness recorded during these measurements does not include the average thickness because the piston, or constant, term was considered a setup error and removed during data analysis. Piston was removed because the *OPD* between the front surface and back surface reflections varies with changes in the angular orientation between the wafer and collimated source.

The average of 192 phase measurements recorded at 15 minute intervals over a two day period is shown in Fig. 3. A peak-to-valley (PV) thickness variation of 1663 nm and root-mean-square (RMS) value of 414 nm were recorded over the measured aperture. Clearly, this wafer geometry is dominated by wedge, or a linear variation in thickness across the wafer face; the wafer is thinner at the top of Fig. 3. Figure 4 shows the same data, but with wedge, or tilt, removed to show the residual thickness variation. The resulting PV value is now 217 nm. The pixel by pixel (one sigma) standard deviation in the 192 measurements is provided in Fig. 5. This result, which was dominated by stray light in the interferometer, suggests repeatability at the 6 nm level for this set of tests. Temperature was also measured; however, no strong correlation between variation in the results and temperature existed due to the high stability of the measurement cavity, or wafer.

*3.2 Collimator Comparison*

A comparison of measurements of a single wafer using two different collimators was also completed. The wafer was again 200 mm in diameter, 750 μm thick, and double side polished. The two collimators were a 150 mm aperture, two optical element f/6 and a 100 mm aperture, three optical element f/6. The average of 25 measurements using the 150 mm aperture collimator with both piston and tilt removed is shown in Fig. 6. The corresponding standard deviation map is showed a maximum value of 3 nm. The averaged result using the 100 mm aperture collimator is shown in Fig. 7. The reader will note some data dropout in the lower right hand quadrant of the data in Figures 6 and 7. This is due to a combination of wafer geometric distortion and resulting high slopes, the long optical path from the wafer to detector, and inadequate imaging optics. The standard deviation map for the 100 mm aperture collimator measurements was similar to the 150 mm aperture collimator tests again with a maximum of 3 nm. The same features are identified in both Figures 6 and 7, including a high spot to the right of the triangular fiducial and two low spots to the left, and similar RMS and PV values were recorded: these are 17 nm and 85 nm for the 150 mm aperture collimator result and 16 nm and 88 nm for the 100 mm aperture collimator result, respectively. This agreement suggests that the measured thickness variation may not be highly sensitive to the incident wavefront.

*3.3 Phase Change on Reflection*

The potential impact of phase change on reflection from physical contact of the back side of the wafer with the support mechanism has also been investigated. This could be an area of concern depending on the chuck type, contact area, and camera resolution. Two cases were evaluated: 1) the current wafer holding mechanism for $IR^2$ using a small vacuum orifice, an 11 mm diameter o-ring seal that surrounds an 8 mm diameter orifice, near the bottom edge of wafer in conjunction with two cylindrical supports; and 2) metallic coatings were applied to a 50 mm diameter wafer directly to simulate intimate contact with a metallic surface and phase maps obtained. In this case, the wafer was lightly supported at the edges using a 3-jaw chuck.

A photograph of the vacuum holding method is provided in Fig. 8. $IR^2$ measurements in the local area of the vacuum orifice were obtained using a 25 mm diameter, f/3 collimator for improved spatial resolution; for the 250x250 pixel vidicon detector array, a maximum spatial resolution of 0.2 mm/pixel is available if the Nyquist criterion is applied. Figure 9 shows the average of phase measurements performed at eight different locations on a single double side polished wafer. The effect of phase change on reflection is clearly seen as the circular change in reported thickness variation where the o-ring contacts the wafer. However, in measurements with reduced resolution (e.g., Fig. 4) this effect is not visible in the data.

For typical vacuum chucks used in lithographic steppers, there is a relatively high number of small contacts between the wafer and chuck (1 % contact area is typical). To explore this intimate contact over a larger area, a gold strip was sputter-coated on the

back of a 50 mm diameter double side polished wafer. An example difference measurement of a wafer before and after applying the gold strip is seen in Fig. 10. An apparent change in thickness is demonstrated due to the relative variation in phase change on reflection from the silicon-air and silicon-metal interfaces. One potential solution to this problem is the use of 'pin-type' chucks with many low surface pin contacts between the wafer and chuck. Provided there is at least one pin per pixel, this effect may be 'averaged out'.

*3.4 Intercomparison Results*

The result for a thickness variation measurement of a 100 mm diameter, 750 μm thick double side polished wafers is shown in Fig. 11. This measurement was obtained using the f/6, 100 mm diameter collimator. The wafer shows a PV thickness variation of 204 nm, where the thickness variation is manifested as 'power' (coefficient derived from the best-fit sphere) in the phase map. This large power suggests a gradual thinning radially from the outside edge to the center of the wafer with high rotational symmetry. The phase data in Fig. 11 was again converted to nm using a silicon index of 3.5 and piston and tilt have been removed.

Next, thickness measurements of the same wafer were completed using an ADE 6033T capacitance gage-based instrument [9]. Two data sets at lower and higher spatial densities were obtained [10]. The gage repeatability was also evaluated [10]. The repeatability study included five separate measurements at a single location on four wafers, nominally 460 μm thick, by two different operators for a total of 40 tests. A one sigma standard deviation of 206 nm was recorded. Because the repeatability for this instrument is of the same order as the thickness variation recorded by $IR^2$, the intercomparison serves only to evaluate potential trends in the data.

The low spatial resolution results are shown in Fig. 12, where the values are normalized to the measured wafer center thickness of 754.2 μm. Positive values indicate measured thickness larger than the center thickness. It is seen that the wafer is thinner in the middle by 200 nm to 300 nm depending on measurement location with reasonable rotational symmetry. The higher resolution data is shown in Fig. 13. Measurements were performed at eight radial locations with data points at radii of approximately 37.5 mm, 30 mm, 22.5 mm, 15 mm, and 7.5 mm. The recorded center thickness was 754.4 μm. In this case, the measurements do not show the clear rotational symmetry demonstrated previously. However, the data does show the general trend of higher thickness near the edge than at the center (except for radial location 5, opposite the flat edge of the wafer). The thickness difference between data on the 75 mm diameter and the center is as large as 400 nm. However, the uniform 200 nm drop between the 15 mm diameter data (excluding location 5) and the center seems suspect, so the actual thickness variation may be lower.

Finally, surface reflection measurements of this wafer were performed using a phase shifting Fizeau interferometer (He-Ne 632.8 nm source). Four measurements with four repetitions each were averaged to obtain the results in Figures 14 and 15 showing phase maps from the front and back surface measurements, respectively. Tilt has also been removed from these measurements. The front surface measurement shows a slightly concave shape (6.13 μm sag), while the back surface measurement demonstrates a slightly convex shape (6.04 μm sag). The larger sag for the concave front surface suggests the wafer is thinner in the center, as demonstrated schematically in Fig. 16. This trend agrees with the $IR^2$ result in Fig. 11 and ADE 6033T results in Figures 12 and 13. Because the actual apertures for the Fizeau and $IR^2$ measurements were unequal and not well-known, a direct comparison between the data sets is not possible (i.e., sag varies with the square of measurement aperture).

## 4. Conclusions

This paper describes an interferometer developed to measure thickness variation of single or double side polished wafers using an infrared source and vidicon detector. Various possible instrument configurations, some of which have been partially evaluated previously, are described. However, the focus of this work is the 'wafer as cavity/plane wavefront' setup where a collimated wavefront is used to produce interference fringes between the front and back surfaces of the plane parallel, double side polished wafer. Experimental results are presented including: 1) an extended drift test and associated repeatability; 2) comparisons between two different collimators to determine sensitivity to the interferometer wavefront; 3) an exploration of the effect of phase change on reflection on measured thickness variation due to the wafer clamping method; and 4) an intercomparison between the NIST Infrared Interferometer ($IR^2$) thickness variation results, thickness measurements from an ADE 6033T capacitance gage-based instrument, and surface measurements obtained using a Fizeau phase shifting interferometer (632.8 nm wavelength).

## Acknowledgements

This research was supported by the NIST Advanced Optical Metrology Program. The authors would also like to recognize the contributions of L.-Z. Shao, Tinsley Laboratories, Inc., Richmond, CA, U. Griesmann, NIST, Gaithersburg, MD, and S. Jones, Virginia Semiconductor, Inc., Fredericksburg, VA, to this research.

## References

1. L.F. Thompson, C.G. Willson, and M.A. Bowden, *Introduction to Microlithography*, 2nd Ed., American Chemical Society, Washington, DC (1994).
2. http://courses.nus.edu.sg/course/phyweets/Projects99/Optical/duv_optical_elements.htm.
3. P. Langer, Personal communication, NIST Wafer Flatness Workshop, January 30, 2001.
4. http://public.itrs.net/Files/2001ITRS/Home.htm.

5. C. J. Evans and R. E. Parks, "Interferometric thickness variation test method for windows and silicon wafers using a diverging wavefront", U.S. Patent 5,739,906 (1998).
6. R. E. Parks, L.-Z. Shao, A. Davies, and C. J. Evans, "Haidinger interferometer for silicon wafer TTV measurement", *Proceedings of SPIE*, 4344, Metrology, Inspection and Process Control for Microlithography XV, 496-505 (2001).
7. C. J. Evans, R. E. Parks, L.-Z. Shao, and A. Davies, "Interferometric metrology of photomask blanks: Approaches using 633 nm wavelength illumination", *NISTIR* 6701, December (2000).
8. C. J. Evans, A. Davies, T. L. Schmitz, R. E. Parks, and L.-Z. Shao, "Interferometric metrology of substrates for VLSI", *Proceedings of 2nd International Conference of the European Society for Precision Engineering and Nanotechnology – euspen*, "Torino Incontra" Congress Centre, Torino, Italy (2001).
9. Certain commercial equipment, instruments, or materials are identified to foster understanding. Such identification does not imply recommendation or endorsement by the National Institute of Standards and Technology.
10. All ADE 6033T measurements were carried out by personnel at Virginia Semiconductor, Inc., Fredericksburg, VA, and the results reported to the authors.

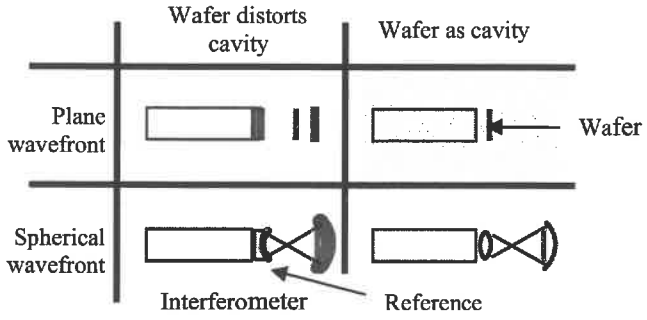


Figure 1: $IR^2$ configurations ('wafer as cavity/plane wavefront' setup is highlighted).

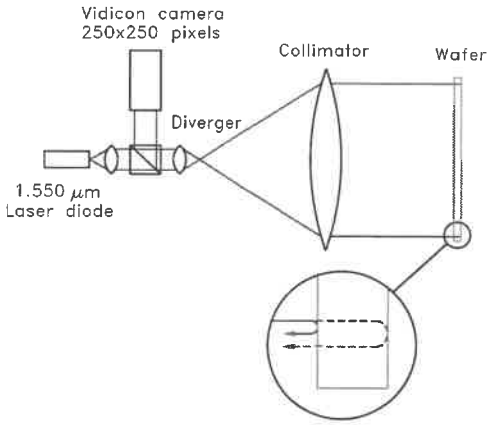


Figure 2: $IR^2$ schematic for 'wafer as cavity/plane wavefront' setup. Light from tunable wavelength infrared diode is expanded to wafer diameter. Haidinger fringes formed by the wafer cavity are then imaged on the detector.

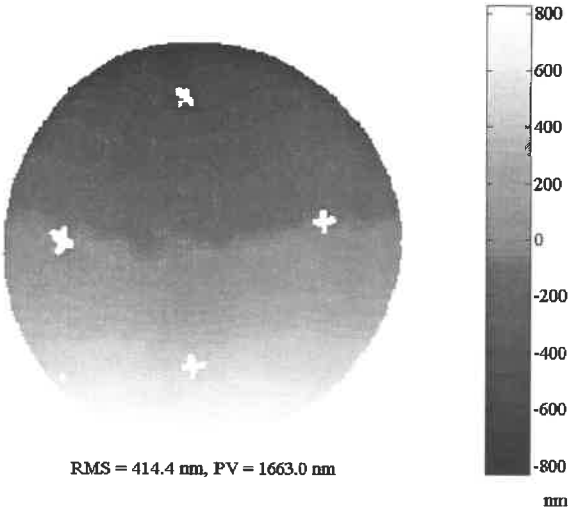


Figure 3: Phase map showing average of repeatability testing measurements with piston removed (data dropout due to fiducials on the wafer is seen).

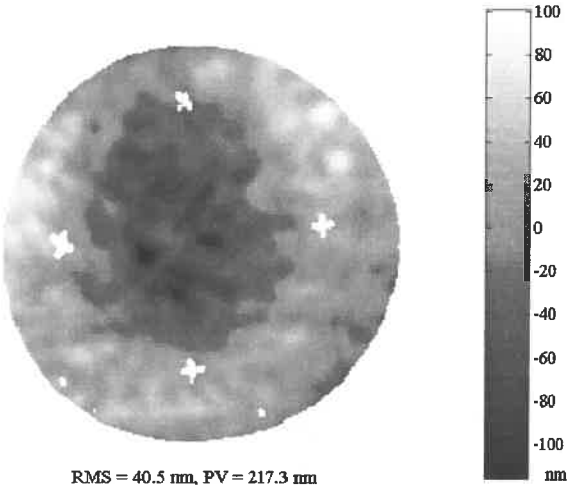


Figure 4: Phase map showing average of repeatability testing measurements with piston and tilt removed.

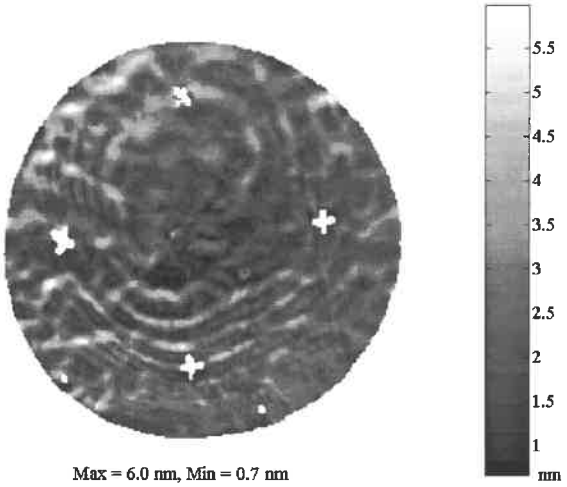


Max = 6.0 nm, Min = 0.7 nm

Figure 5: Pixel by pixel standard deviation of 192 repeatability measurements (piston removed prior to calculating standard deviation).

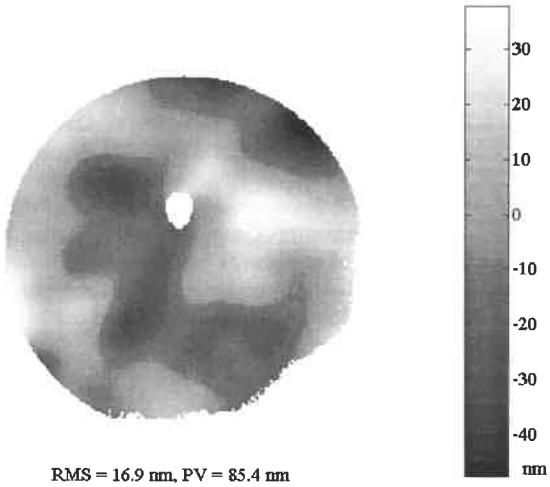


RMS = 16.9 nm, PV = 85.4 nm

Figure 6: Phase map showing average of 25 f/6, 150 mm aperture collimator measurements with piston and tilt removed (fiducial data dropout is seen).

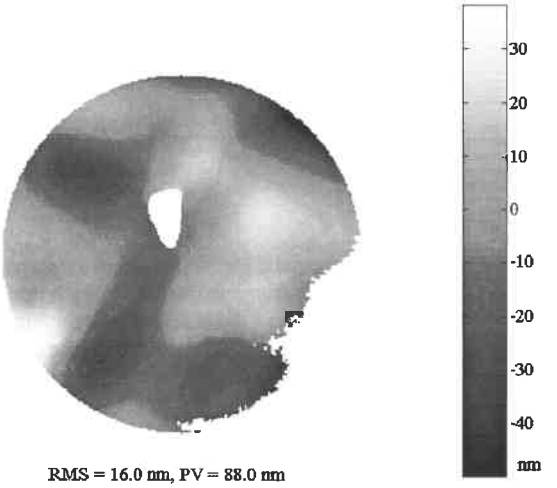


RMS = 16.0 nm, PV = 88.0 nm

Figure 7: Phase map showing average of 25 f/6, 100 mm aperture collimator measurements with piston and tilt removed.

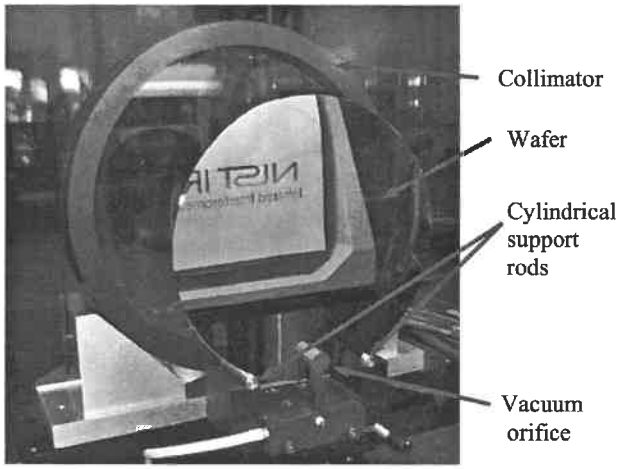


Figure 8: Photograph of vacuum orifice wafer holding mechanism employed on IR$^2$.

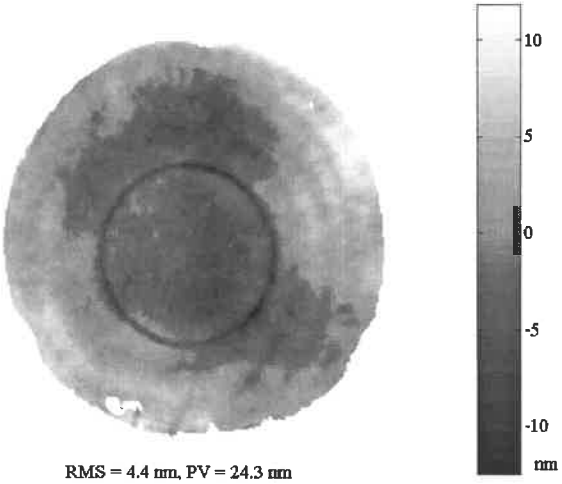


RMS = 4.4 nm, PV = 24.3 nm

Figure 9: Phase map showing effects of phase change on reflection for current vacuum holding mechanism.

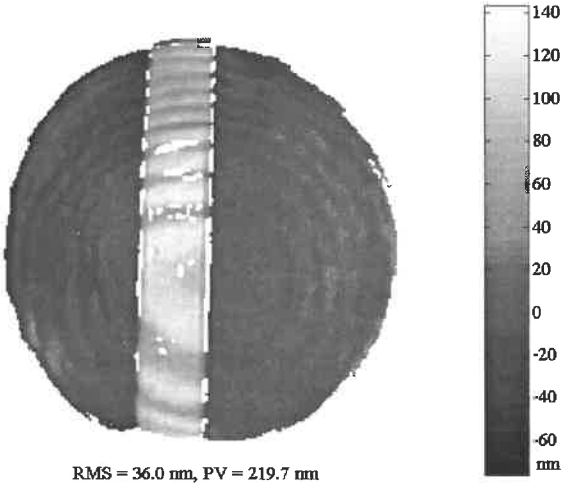


RMS = 36.0 nm, PV = 219.7 nm

Figure 10: Difference map showing apparent change in thickness for wafer with gold strip applied.

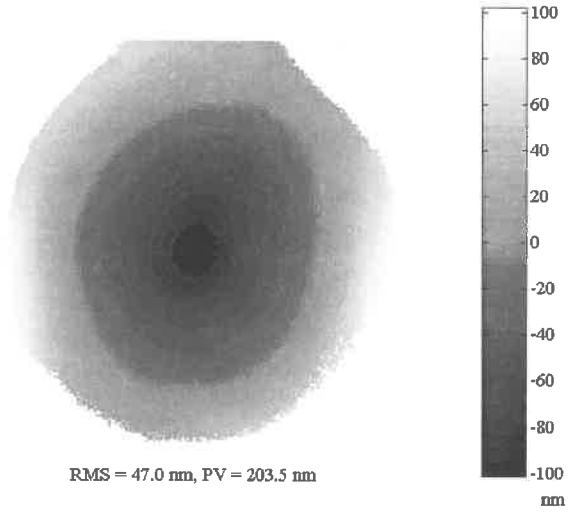


Figure 11: Phase map showing wafer thickness variation (piston and tilt removed). Wafer is thinner in center by approximately 204 nm.

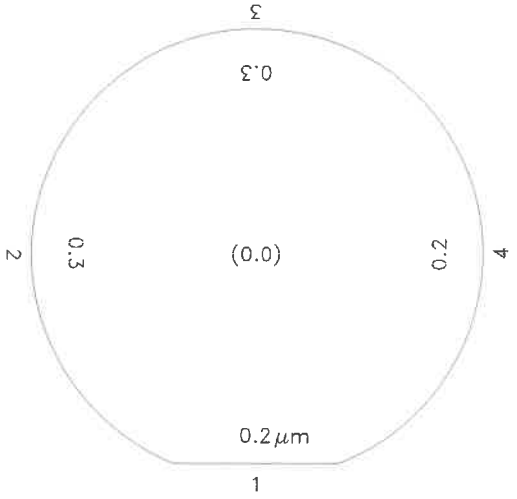


Figure 12: Lower spatial resolution ADE 6033T results.

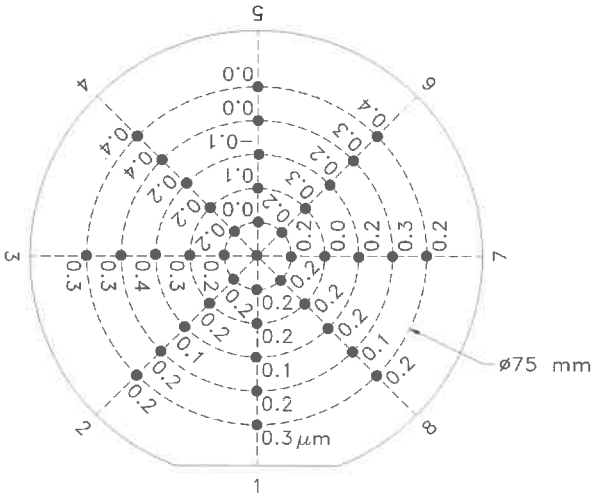


Figure 13: Higher spatial resolution ADE 6033T results.

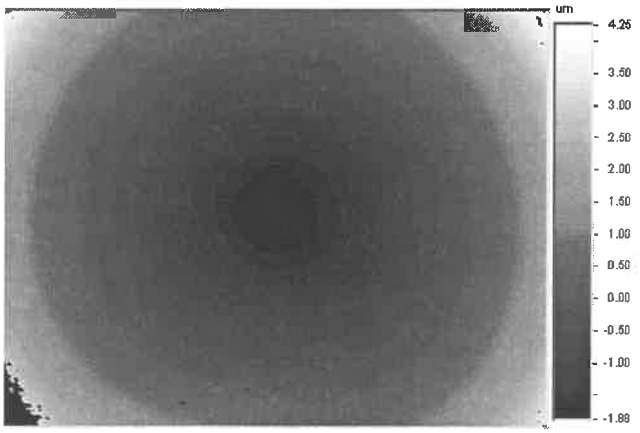


Figure 14: Phase map showing front surface measurement results using Fizeau phase shifting interferometer. Map shows that wafer is concave with front surface facing interferometer. Some data dropout is seen due to high slope of bowed wafer.

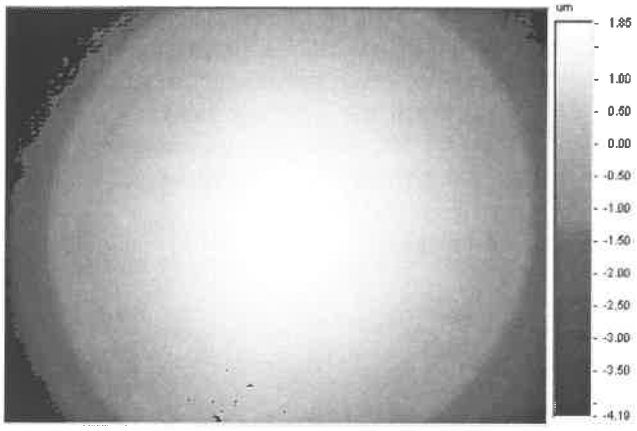


Figure 15: Phase map showing back surface measurement result. Map shows that wafer is convex with back surface facing interferometer.

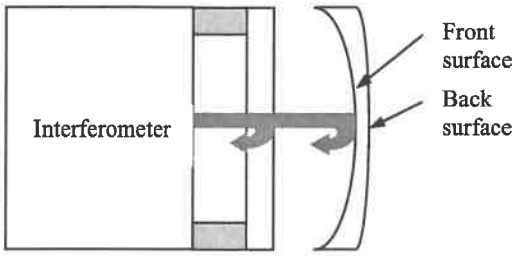


Figure 16: Schematic of wafer shape (not to scale) measurements performed on visible wavelength Fizeau phase shifting interferometer.

# Dynamic MEMS Measurement Using a Strobed Interferometric System with Combined Coherence Sensing and Phase Information

*Erik Novak, Der-Shen Wan, Paul Unruh, Joanna Schmit*
Veeco Metrology, 2650 E. Elvira Rd., Tucson, Arizona, USA
http://www.veeco.com

## 1. INTRODUCTION

While computer modeling of MEMS systems is becoming increasingly sophisticated, the delicacy and complexity of many MEMS components requires accurate metrology of the final devices to assure proper performance. Stiction, motion versus drive signal, shape changes during actuation, angular repeatability, and resonant frequencies are all items of interest. By obtaining topographic information as the drive signal phase, frequency, and voltage are varied, MEMS devices can be fully characterized over their range of operation. Strobed holographic interferometry has been employed for more than 25 years to characterize a variety of vibrating structures.[1] Only recently, however, has strobed illumination been combined with more sophisticated interferometric techniques to produce quantitative data for a large class of moving devices.

Phase-shifting interferometers and white-light profilers have gained popularity in measuring surface topology due to their generality, speed, and accuracy.[2] Phase shifting interferometry (PSI), produces topographic data with extremely low noise and high accuracy, but is limited in that height and slope of the surface to be measured must be less than one quarter of the source wavelength from pixel to pixel to avoid errors; typically the point-to-point height change limit is about 160nm. Coherence sensing interferometry, also known as white-light or vertical scanning interferometry (VSI), is based on the detection of the peak contrast of fringes which are narrowly localized about the plane of best focus. VSI techniques avoid the height and slope limitations of PSI methods, measuring steps of up to 8mm[3], but typically sacrifice some accuracy and noise rejection. The two techniques, however, may be combined for relatively smooth surfaces with large discontinuities, in a method known as enhanced VSI (EVSI), to obtain the benefits of both methods simultaneously[4]. MEMS devices are generally ideal surfaces for this combined technique, as individual features are generally high-quality, but with large steps or gaps between regions.

## 2. STROBED ILLUMINATION INTEGRATION FOR MEMS METROLOGY

Measuring even a slightly vibrating structure with any degree of accuracy is difficult with a standard optical profilometer configuration. The interference pattern to be measured will blur or distort even at low frequencies and amplitudes. The most common error associated with small vibrations is print-through of the interference fringes into the calculated surface shape, as shown in Figure 1. Thus, standard optical profilers can not accurately measure MEMS devices under actuation. However, by making the assumption that the vibrations are periodic and of primarily one frequency, which are generally design goals for MEMS products, one can use illumination strobed to match the MEMS drive frequency to effectively freeze the motion[5]. This permits standard scanning techniques and algorithms to be employed even on these moving devices.

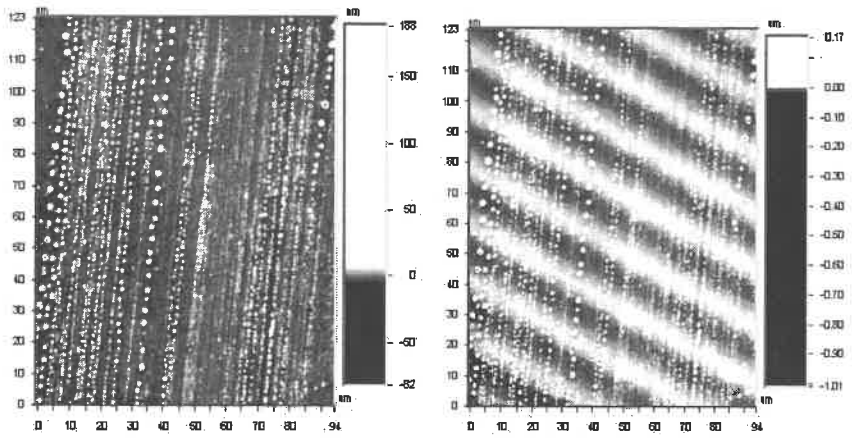

**Figure 1.** Measurement of a machined surface with (left) and without (right) motion of the test piece.

Traditional strobed illumination systems employed either pulsed lasers or varied the illumination with acousto-optic modulators or mechanical shutters. However, each of these techniques has limitations: laser illumination can lead to coherent imaging artifacts, shutters have relatively low maximum frequencies and are potential sources of vibration, and acousto-optic modulators are generally high in cost. Fortunately, recent advances in LED technology have dramatically increased their brightness; with proper integration into an optical system, they are now a viable light source for optical profilers. Also, with spectral bandwidths on the order of 30nm, LED's provide proper coherence length for EVSI techniques. Finally, rapid rise-times for LED's permit strobing at greater than one megahertz frequency, so most MEMS devices can be tested over their entire frequency range.

A standard arrangement for a white-light optical microscope is shown in Figure 2. The illumination source is traditionally a tungsten-halogen bulb, and is coupled into the system such that it best matches the various microscope objectives used to measure the test piece. The illumination is generally split in the microscope objective, with half the beam travelling to the device under test and the other portion to a high-quality reference surface. The reference surface is translated relative to the test surface, and the resulting intensity scans are analyzed using PSI, VSI, or EVSI techniques to calculate the surface profile of the device.

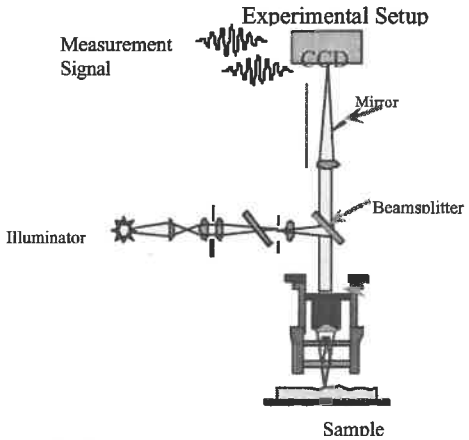


**Figure 2.** Example of a white light interferometer

To employ an LED as a strobed source for a profiler requires both careful selection of hardware as well as carefully designed software to allow efficient operation. Achieving light levels on the camera which nearly saturate it is important to maintain the quality of the surface measurement. The viewing angle of the LED must be carefully matched to the existing optical design, as even the brightest single LED's emit less than 35 candelas. By contrast, a 100W tungsten-halogen bulb emits approximately 30 times this amount.

Combinations of multiple LED's on one chip require higher currents and introduce potential pulse spreading and so are generally avoided for high-speed strobing. Thus, the optical system design becomes critical for ensuring sufficient light at high magnifications using a single LED source. The system employed in the final MEMS interferometer uses a modified Kohler illumination scheme, to allow for high efficiency and nearly uniform illumination.

While an efficient optical design is critical, the amount of light which strikes the test sample may be increased further by overdriving the pulsed LED beyond the normal maximum current or by lengthening the duty cycle of the pulse. However, higher drive currents require lower duty cycles to avoid overheating the LED, which is their primary failure mode. In addition, increasing the duty cycle of the illumination can lead to blurring of the resulting image, and this can lead to errors in the surface shape calculation. These two factors must be carefully balanced in the drive software such that good results are achieved.

## 3. EVSI TECHNIQUE WITH STROBED LED OPERATION

While the EVSI technique, which combines phase calculations and coherence peak sensing algorithms, provides high accuracy and large dynamic range, there are sensitivities to the technique which must be addressed in a MEMS measuring system. One potential source of error is having a known wavelength of the source under different operating conditions. Another is ensuring a known scanner speed throughout the scan, a requirement for accurate PSI, VSI, and EVSI measurements.

Although LED's have relatively stable center wavelengths, like tungsten-halogen bulbs and other non-laser sources, the wavelength can drift significantly with temperature and operating current. Even a few nm change in effective wavelength on a MEMS device with 100μm steps, could lead to several hundred nanometers of error. This is significantly higher than the noise floor of most optical profilers, which is generally a few nanometers or less. Combined phase and coherence sensing techniques are often more sensitive to wavelength errors, with print-through of the interference fringes when incorrect wavelengths are used. Similarly, errors in the scanner speed during the scan, or from one measurement to the next, will cause erroneous results. While either a known wavelength or scanner speed can be used to calibrate the errors in the other, one of the variables must be determined to ensure the best measurements.

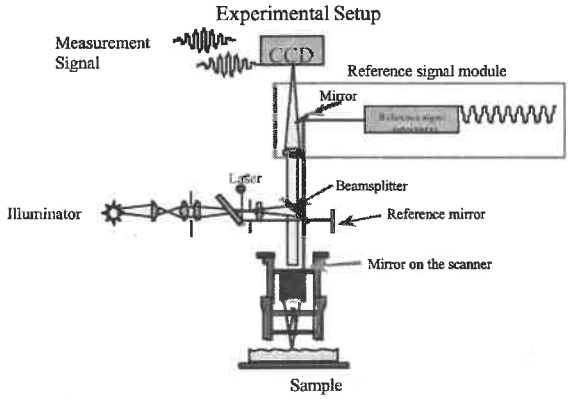


**Figure 3.** White light interferometer with internal reference signal.

Common methods for creating known correct scanner steps for PSI measurements is to employ a well-characterized narrow-band filter in the system, and use the known wavelength to adjust the scanner until steps of the correct phase difference are generated. Similarly for VSI measurements a high-quality step is measured, with the scanner speed adjusted until it measures accurately. Both techniques produce acceptable results on many parts, but suffer from effectively using the average scanner step for their calculations. Also, both calibrate the system only over one range of the scanner motion, and measuring parts at different points of the scanner's range can lead to errors.

For production systems, or ones where correlation and accuracy tolerances are tighter, it is possible to integrate a second interferometric signal into the instrument to perform real-time calibration of the scanner wavelength[3]. Such a configuration is shown in Figure 3. Such a system allows for accurate determination of the scanner motion over any range, and also can use the wavelength of the laser to ensure the effective wavelength is properly known for any scan. Thus, nanometer-level accuracy and system-to-system correlation are maintained for any surfaces within the scan range of the profiler.

## 4. EXPERIMENTAL RESULTS

A variety of devices were measured using strobed illumination for an optical profiler. Figure 4 below shows a representative measurements of an in-plane resonator provided by Sandia National Laboratories. The plot on the right shows translation of the large center section at various frequencies of actuation, but constant voltage and phase. The greater deflection at 4500 Hz represents a resonant frequency of the device. By stepping through various combinations of frequency, amplitude, and phase, MEMS devices can be completely characterized. Other plots of interest show step response of devices, translation vs. voltage for linearity calculations, and shape calculations to examine deflections in the device under the stress of actuation.

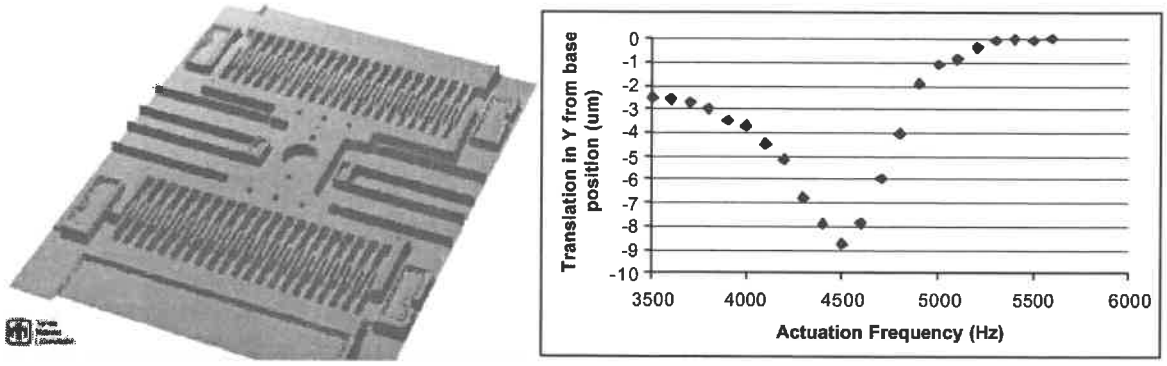


**Figure 4.** Left: in-plane resonator as measured using strobed interferometer, actuated at 4000Hz. Right: plot of translation vs. frequency at a 45 degrees phase, showing 4500 Hz resonant frequency. Resonator is courtesy Sandia National Laboratories, SUMMiT ™ Technologies, www.mems.sandia.gov

## 4. CONCLUSIONS

As more types of MEMS devices move from the laboratory to full production products, metrology for quality control and process yield improvement becomes increasingly important. Creating a system with the hardware and software required to measure these devices rapidly and accurately in a static state and during actuation is critical. Through careful opto-mechanical design and thorough software control of the strobing and device motion, an interferometric optical profiler can provide the required flexible, high-accuracy measurements needed for full MEMS characterization.

## 5. REFERENCES


[1] J.S. Harris, R.L. Fusek, J.S. Marcheski, "Stroboscopic Interferometer", *Appl. Opt. 18*, pp 2368-2371, 1979

[2] P. Caber, "Interferometric profiler for rough surfaces," *Appl. Opt. 32*, pp 3438-3441, 1993.

[3] J. Schmit, E Novak, A. Olszak "White light profiler with internal length standard", *Proceedings, ASPE 17th Annual Meeting, 2002*

[4] J. Schmit, A. Olszak, "High-precision shape measurement by white-light interferometery with real-time scanner error correction," *Appl. Opt. 41*, pp 5943-5950, 2002

[5] R. Gutierrez, K. Shcheglov, T Tang; "Interferometric system for precision imaging of vibrating structures," *US Patent 6,291,145*, 2001

# Micro and Meso Scale Robotic Assembly

Harry E. Stephanou
Center for Automation Technologies
Rensselaer Polytechnic Institute
Troy, NY 12180

The focus of this paper is on a set of meso and micro scale robotic tools for the assembly of systems in which the size of the parts being manipulated and/or the assembly tolerances are of the order of microns or less. Here, a robotic system is defined as one that includes sensors, processors and/or actuators capable of emulating some of the perceptual, cognitive and/or motor skills of humans.

The major driver for microrobotic assembly of microsystems is the combined need for high precision and high throughput at low cost. In order to accomplish this objective, we use a three-pronged approach.

- Multiscale manipulation. The goal is to combine the large motion range of low precision devices with the high positioning precision of successively smaller devices that have limited motion range.
- Parallel manipulation. The goal is to achieve orders of magnitude speed-up by using arrays of micromanipulators performing the same task, e.g. [1]. Gripper-free manipulation is an alternative method that uses force fields rather than mechanical contact, e.g. [2].
- Modularity. The goal is to reduce set-up time through modular designs that enable the rapid reconfiguration of assembly cells. This is a particularly powerful approach at the microscale, given the possibility to design an extensive library of microparts from which highly customized assembly cells can be rapidly configured to match the requirements of a broad diversity of assembly tasks.

A few illustrative examples of this approach are presented in this paper, based on work done at the Center for Advanced Technology.

## 1. Coarse - Fine Positioning

Figure 1 shows a reconfigurable robotic system for the precision assembly of components with microparts [3]. The system consists of five subsystems, tied together via a PC running a supervisory control program.

- A coarse positioning system.
- A fine positioning system.
- A gripper and fixturing system.
- A high-resolution vision system.
- An adhesive dispensing and curing system.

The main premise of this design includes the ability to quickly reconfigure assembly tasks, and replace system hardware, such as adding sensors and fixtures. The high level control application interfaces with different subsystems independently, using multithread routines coordinated via a separate assembly planning and execution thread.

A general purpose, large space positioning robot, RobotWorld by Yaskawa, is used as a coarse motion manipulator. It has four degrees of freedom (x, y, z, θ). Several "pucks" are used to hold various end-effectors. One of them is a microgripper for handling optical fiber. Another end-effector includes a syringe tip and UV curing lamp used by the adhesive dispensing and curing system. Motion parameters are transferred to the main control program via TCP/IP Ethernet communication. For achieving micron level accuracy, the system is equipped with a fine motion manipulator that has four degrees of freedom (x, y, z, θ). The same PC-based DSP motion control card is used to control the fine motion manipulator, the microgripper, the UV adhesive dispensing and curing system, as well as the part fixturing system. The relative position between the fixture and the assembled parts is determined by a vision system using a ½" CCD camera, optics, and the Intel Open Source Image processing libraries.

The system was used to pick and place microlenses, to assemble optical fiber arrays, to terminate fibers with pins and sockets, and to assemble RF diode arrays (fig.2).

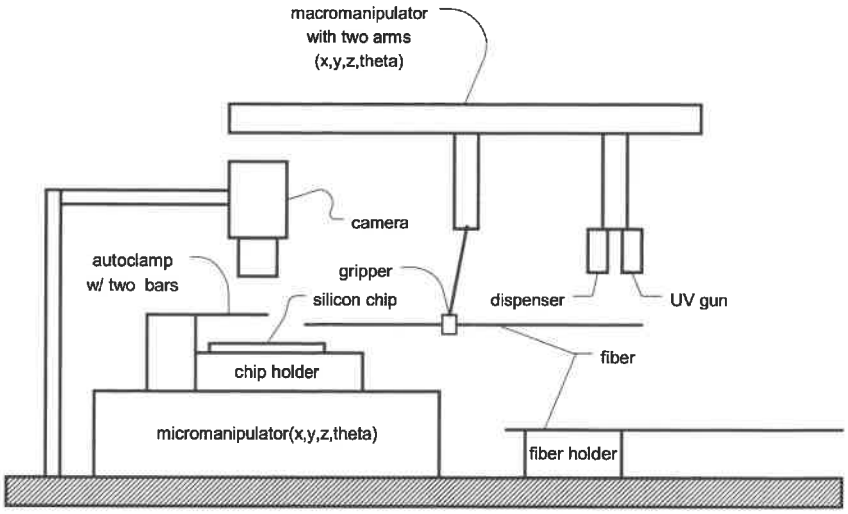


Figure 1. Reconfigurable assembly system

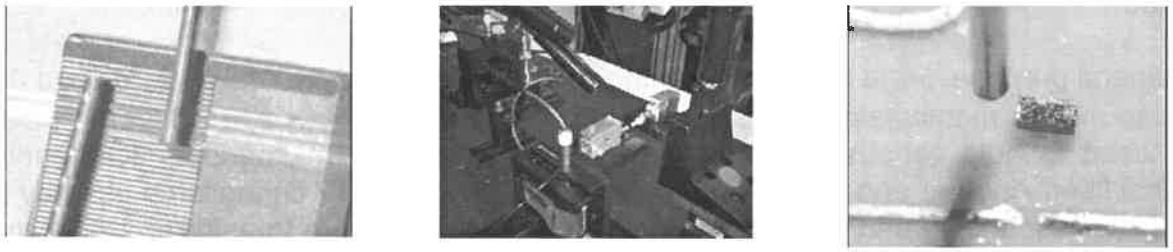

2a Fiber arrays 2b Fiber terminations 2c Diode arrays

Figure 2. Applications

Figure 3 shows a device with a two degree of freedom remote center of rotation, developed by Dr. Yves Bellouard at RPI. The joints are made with flexures, which eliminates backlash, stick-slip effects, and wear. Furthermore, the joints are linear since they use the elasticity of the material. A stainless steel prototype was built, measuring 85mm x 85mm x 60mm, with a range of motion of +/- 2.5 deg. The device was equipped with a submicron adjuster, and has a resolution of 0.9 mdeg, accuracy of 0.02 mdeg and repeatability of <0.02 mdeg. It was designed for the precise positioning of fibers by defining the center of rotation at the tip of the fiber. Because of its modular design, the mechanism can be rapidly reconfigured.

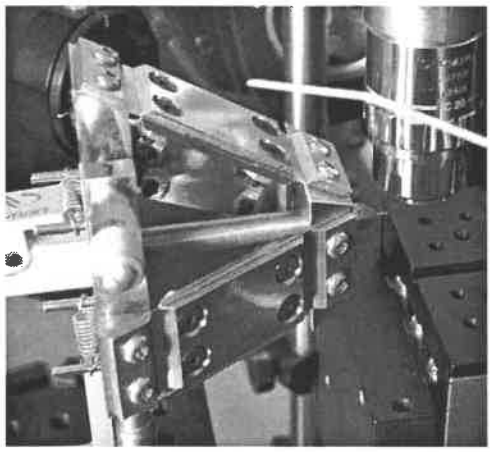

Figure 3 Remote Center of Rotation Device.

## 2. Parallel Microassembly

Figure 4 illustrates a parallel assembly architecture that is being explored as part of a collaborative effort with the Zyvex Corporation under funding from the NIST ATP. It uses a 2D array of microrobots sharing a Cartesian platform. Typical link dimensions are of the order of hundreds of microns, while typical operations may include pick and place, alignment, and compliant insertion.

Key research issues include:

- Kinematic design optimization to accommodate task dependent requirements for maximum
  - range of motion
  - stiffness or compliance along selected axes
  - positional accuracy along selected axes
- Dynamic modeling and optimum motion control
- Motion planning algorithms for compliant insertion and fault tolerance

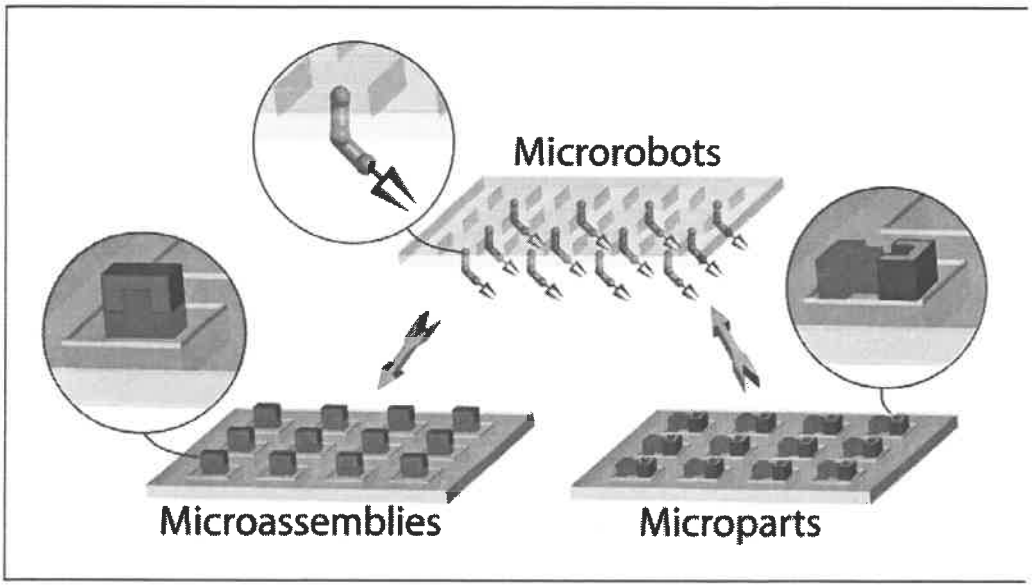


Figure 4. Parallel manipulation

## 3. Summary

The cost effective assembly of heterogeneous microsystems requires modularity, parallelism and a multiscale approach. Several examples were used to illustrate on-going work in these areas.

## 4. Acknowledgement

Work at the Center for Automation Technologies is partially funded by a block grant from the New York State Office for Science, Technology and Academic Research.

## 5. References

1. G. Skidmore, E. Parker et al., "Exponential Assembly," *Eighth Foresight Conference on Molecular Nanotechnology*, 2000.
2. H.E. Stephanou, J. Sin, K.T Winther, "Micromanipulation using a friction force field," *International Conference on Robotics and Automation,* Seoul, Korea, 2001.
3. D. Popa, B.H. Kang, J. Sin, "Reconfigurable Microassembly System for Photonics Applications," *Proc. IEEE Conf. on Robotics and Automation,* Washington, D.C., 2002.
4. Y. Bellouard, "Microrobotics, Microdevices Based on Shape-Memory Alloys" in **Encyclopedia of Smart Materials**, Wiley, pp. 620-644, 2002.

# PZN BASED NANO-POSITIONING SYSTEMS

Shane Woody
InsituTec Inc., Charlotte, NC 28210

Stuart Smith, Pavan Jain and Daisuke Iida
Center for Precision Metrology, UNC Charlotte, NC 28223

## Summary

Nano-positioning systems employed with mesoscale performances are often considerably large with respect to the work volume and as a result are slow in bandwidth, precision and accuracy limited, and settling times are marginally acceptable. One example is hydrostatic oil bearing slideways on some diamond turning machines. These often exceed 100 mm traverse range whilst maintaining 10 nm resolution or better under closed-loop control. However, due to their low velocity and acceleration, considerable fabrication costs, and large design footprints, these macro-scale machines are not suitable for routine mesoscale applications. Considering that mesoscale is generally considered to incorporate operating ranges between 10 μm – 10 mm, one limiting factor to obtaining 'tabletop' mesoscale machines is the ability to engineer multiple degree of freedom nano-positioning systems in a compact manner. Scaling down systems for mesoscale applications enables shorter measurement loops and stiffer machines, while requiring better resolutions if precision is to be maintained. We report methodologies to enhance the areas of mesoscale positioning systems using relaxor ferroelectrics (PZN-PT), innovative flexure-based lever mechanisms, capacitive sensing for absolute displacement measurement, and digital signal processing (DSP) to provide a 'smart' analog interface and data connectivity.

## PZN-PT Mesoscale Actuators

Actuator based systems such as piezoelectric (often referred to as PZT) that can provide high power densities have been employed in positioning devices over the decades. These actuators exhibit compactness, high bandwidth and favorably scale for small-volume application but are typically limited to around 0.1% strain of the stack length. Designs for longer range translations often result in unwieldy long PZT actuators (~ 100 mm to produce displacements of ~ 100 μm). For such a large range, the long stacks result in a proportionate decrease in stiffness. Alternatively, voice coils have demonstrated significant output forces to displace a platform over millimeter distances but tend to produce significant heat and are large in volume.

Recently, developments in relaxor-based ferroelectrics single crystals (PZN-PT) have exhibited ultra-high strains exceeding 1.0% in controlled laboratory settings with high piezoelectric coefficients of $d_{33}$ equal to 2500 pC/N, and exhibit lower hysteresis compared to PZTs[i]. Considering PZT actuators are capable of generating strains up to

0.1%, the PZN-PT are poised to displace an order of magnitude greater then PZT actuators. Investigations are underway within our group to explore applications of this single crystal material for mesoscale positioners, figure 1. In the investigations presented in this paper, a single crystal plate with dimensions 5.0 x 5.0 x 0.5 $mm^3$ is tested with an applied field up to 1900 volts. A strain of 0.4 % corresponding to a displacement of 2 μm are measured in this experiment, see figure 1.

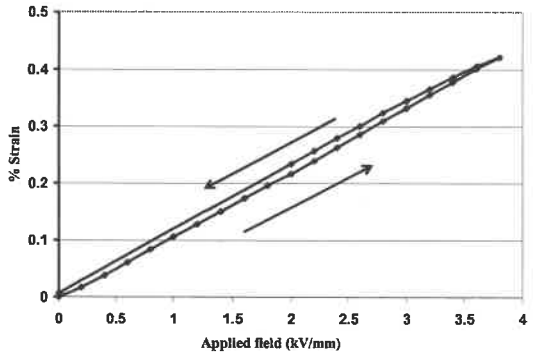


**Figure 1:** PZN-4.5% PT (5.0 x 5.0 x 0.5 $mm^3$) Extension with Applied Field

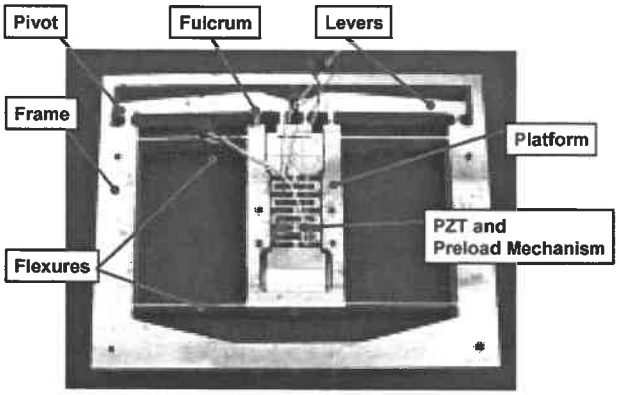


**Figure 2:** PZT based levered mechanism

We are currently investigating use of PZN-4.5% PT stacked actuators with total dimensions 5.0 mm x 5.0 mm x 5.0 mm in size[a]. The actuators consist of 10 single crystal plates which are 0.5 mm thick. Currently, these PZN ceramics require a field of 60 kV/cm for 1.1% strain and have 18 nF capacitance across the stack. Consequently, 0.5% strain will require an applied voltage of about 1.5 kV and 1.1% strain will require 3 kV. Although the potential for high strain has been demonstrated the high voltage requirement causes considerable practical problems and thinner plates will be necessary to obtain higher strains with lower voltage and higher bandwidths. At this time, thinner plates may be purchased but these are not readily available at costs that are considered economically viable for our applications. Furthermore, because of the brittle nature of these single crystalline materials, pre-stress conditions are currently being evaluated to determine if the single crystals may be used for the ultra-high strains in the flexure-based systems. An additional benefit is the single crystals have shown to generate less hysteresis compared to PZT ceramics. The energy dissipated (i.e. heat) due to hysteretic (i.e. structural) damping is predicted to be less compared to PZT materials currently used.

[a] purchased from TRS Ceramics, Inc, State College, PA 16801

## Precision High Voltage Power Supplies

Until significantly thinner single crystal plates are economically manufactured, precision power supplies and amplifiers will be necessary. Presently, our group has developed high bandwidth 1100 V precision amplifiers with up to six channels to drive multiple actuator systems. Significant power is essential to drive the high capacitive (i.e. 18 nF) loads of the actuators while rapidly sourcing and sinking current. Obtaining a symmetric source and sink circuit presents considerable problems to HV circuit design, some of which will be addressed during the presentation.

## A Symmetrical lever Mechanism for Mesoscale Systems

Meso-scale applications will require stages to move over millimeter ranges. To achieve this we have developed a unique lever mechanism employing an actuator based platform, shown in figure 2. The particular stage uses three 5.0 x 5.0 x 18.0 mm PZTs[b] which are, in turn, bonded in series resulting in a 54 mm long stack. Additionally, a mechanism is used to provide longitudinal preload to the actuator. The total length of the assembled preload mechanism is approximately 65.0 mm and the three stacks combined will produce about 54 μm of displacement. One end of the preload mechanism is mounted to the moving platform and other end is rigidly attached to two symmetrical levers, figure 2. Each lever also attaches to the platform by way of a fulcrum and the end of the lever is designed with a rotating hinge located on a fixed frame. Upon expansion, the PZT stacks generate a rotation of each lever about the fulcrum points and also about the fixed pivots which are attached to frame. Theoretically, the carriage is then displaced an amplified amount depending upon the lever ratio defined by the lever geometry, 5:1 in this particular design. The platform is also designed with four leaf flexures which are orthogonal to the principle axis of motion. The flexures' stiffness increase the natural frequency of the platform and constrain the platform's motion to a linear translation. The footprint of the flexure is 15.0 x 150.0 x 125.0 $mm^3$.

A second advantage to this lever mechanism design is reduction of 'lost motion'. Generally, lever mechanisms are inherently prone to significant fractional loss of motion as the lever ratio is increased[ii]. Figure 3 represents a mathematical model of a single lever driven flexure mechanism. The objective of the lever is to provide some form of amplification or attenuation between the force or displacement at the actuator and that produced at the moving stage of the flexure. In *Flexures* by Smith, the fractional loss of this lever mechanism is given by

$$f = \frac{\frac{k_3}{k_1} + \frac{k_3}{k_2}\left(1+\frac{1}{n}\right)^2}{\left(\frac{k_3}{k_1} + \frac{k_3}{k_2}\left(1+\frac{1}{n}\right)^2 + \frac{1}{n^2}\right)} = \frac{\alpha + \beta\left(1+\frac{1}{n}\right)^2}{\left(\alpha + \beta\left(1+\frac{1}{n}\right)^2 + \frac{1}{n^2}\right)} \qquad (1)$$

[b] purchased from Tokin™

where $n$ is the lever ratio, $\alpha$ is the stiffness ratio between the carriage flexure and actuator coupling , and $\beta$ is the stiffness ratio between the carriage flexure and the fulcrum's longitudinal stiffness. Assuming $\alpha = \beta$ and a lever ratio of 5:1, the fractional loss of motion will increase as the stiffness ratios are increased, figure 4. Using 2 levers in a symmetrical design as in figure 3 will further reduce the fractional lost motion in the system. The relaxor ferroelectric, such as the PZN-PT, will provide the same amount of displacement but in a smaller volume. Consequently, changing to this material will enable similar range of motion with a smaller footprint, higher bandwidth, and reduced fractional loss of motion. We are currently exploring a 5.0 x 5.0 x 5.0 $mm^3$ PZN-PT stacks in conjunction with a 5:1 lever mechanism. The mechanism with the PZN-PT actuator is expected to exceed 100 μm in displacements and the footprint will be 50.0 mm x 60.0 mm x 10.0 mm and results of early test will be presented. Longer PZN stacks in conjunction with the levered mechanism to provide the capability of 1.0 mm translations are currently being explored.

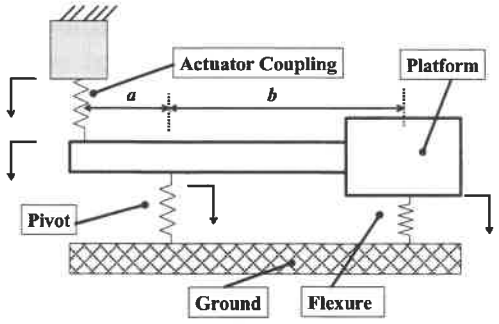


**Figure 3:** Model of a lever driven flexure mechanism

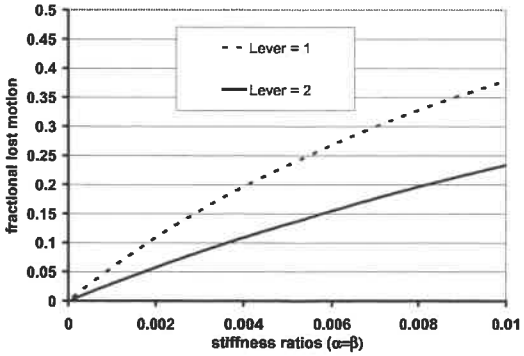


**Figure 4:** Fractional lost motion vs. stiffness ratios for single 5:1 lever and two symmetrical 5:1 levers

## Digital Closed Loop Control for Mesoscale Positioners

The absolute displacement measurement for the positioners of these studies use capacitive sensing monitored using a digital lock-in amplifier platform developed at UNC Charlotte. Generally, noise sources for capacitive sensors involve carrier signal, oscillator, and amplifier noise. The oscillator noise is a function of the oscillators chosen and will manifest as combinations of amplitude and phase components. Typically, in analog oscillators it is the amplitude that is most difficult to control. However, investigators have implemented digital signal processing (DSP) for both PID control and as a lock-in amplifier for capacitive sensing. The DSP platform is developed with 16 bit AD and DA converters while supporting 40 ksps sampling rates and a 100 ksps system is currently being evaluated. Nonetheless, fast DA and AD converters supporting 18 bit or higher precision will be necessary to achieve better than 1 part in $10^5$ accuracy. While

such resolution is possible using sigma delta converters, we have not been able to identify commercially available converters capable of providing the required performance at sufficient bandwidth.

In conjunction with the digital control system, capacitive sensors for the lever mechanism (see figure 2) have been developed. An AC bridge design using one variable capacitance and one referenced capacitor is implemented. The variable capacitor comprises two 16.0 mm diameter electrodes where one electrode is mounted to the fixed frame and the second electrode is mounted to the movable platform. The plates have a nominal gap of 230 µm and produce a capacitance variation between 20-50 pF over a displacement range of 225 µm, figure 5. The displacement is measured with a Michelson interferometer and the capacitance is measuring using the DSP lock-in amplifier. The lever mechanism's actuators and the capacitance sensor are closed loop controlled digitally. To assess the system noise the mechanism was positioned to approximately 100 µm and held stationary for 30 minutes. The gage output at a 1 kHz bandwidth is measured to be approximately 9 nm RMS, figure 6.

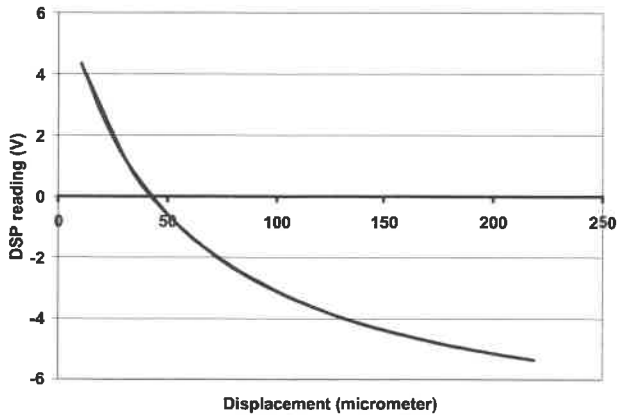


**Figure 5:** DSP voltage vs. platform displacement

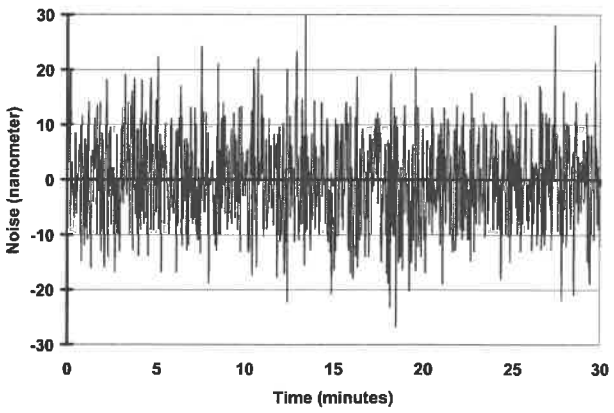


**Figure 6:** noise over 30 minutes, rms deviation = 8.6 nm for 1 kHz bandwidth

## Conclusion

The PZN-PT represents a likely candidate for nano-positioning and mesoscale applications. However, continued research is necessary to fully understand issues and implementation associated with stack pre-stress requirements and methods for economic manufacture of thinner single crystal sheets. Secondly, flexure systems appear to provide reasonable methods for frictionless motion and precision. However, many flexures are over-constrained for relatively long motions and large deformation models may be required for future designs. Assuming flexure systems are an optimal approach for nano-positioning systems with meso-scale performance, these designs will require additional modifications and perhaps new innovations in order to substantially exceed 1.0 mm ranges. Finally, we believe that alternative sensing methods may be required above 1.0

mm ranges if nanometer accuracy is to be maintained. Furthermore, while the DSP platforms developed at UNCC for software correction (i.e. PID control and Lock-in electronics) have demonstrated significant promise for digitally controlling the positioners. Nonetheless, the DA and AD converters providing DC measurements will need to be increased above 16 bit at tens to hundreds of kilo samples per second to enhance precision measurement.

## Acknowledgments

The authors would like to express their thanks to Richard Seugling and Bob Hocken, UNC Charlotte, Paul Rehrig and Dean Anderson of TRS Ceramics for many useful discussions on these developments. We would also like to thank Jeffrey Luner of Boeing, St. Louis, and NSF ( contract #DMI 2975020172) for partial support of this work.

---

[i] Seung-Eek Par and Thomas R. Shrout, Ultrahigh strain and piezoelectric behavior in relaxor based ferroelectric single crystals, J. Appl. Phys. 82 (4), 15 August 1997, pg. 1804-1811

[ii] Stuart T. Smith, Flexures, Gordon and Breach Science Publishers, 2000, pg. 345-352

# HYBRID MICRO-ASSEMBLY SYSTEM FOR TELEOPERATED AND AUTOMATED MICROMANIPULATION

Michael F. Zaeh, Dirk Jacob, Michael Ehrenstrasser, Johannes Schilp

Technische Universitaet Muenchen ,
Institute for Machine Tools and Industrial Management (*iwb*)
D - 85747 Garching, Germany

## 1 INTRODUCTION

With a compound annual growth rate of 20 % and a predicted market volume of 68 billion dollars in 2005, microsystem technology plays a decisive role in automotive, medical and telecommunication applications such as acceleration and angular rate sensors for airbag systems, optical MEMS (MOEMS) and RF-MEMS for telecommunication devices [1]. In addition to a new custom design of micro-components, research activities in MST are focused on innovative assembly strategies for hybrid microsystems in order to reduce the proportionate costs of assembly. These presently account for up to 80 % of the product costs [1]. Due to the short product life cycle of hybrid microsystems, both manual and automated assembly strategies have to be taken into account because of rapidly increasing and decreasing quantities within a short period and decreasing innovation cycle times.

During the introductionary stage and the beginning of the growth stage, prototype assembly as well as assembly in small volumes is still done manually with auxiliary devices such as magnifying glasses, tweezers etc. Because of the insufficient human tactile sense, the resulting unsatisfactory hand-eye coordination and so-called scaling effects [2], this manual and precise work is very exhausting. Telepresence technologies are a promising approach to overcome these scaling barriers and to facilitate manual assembly operations.

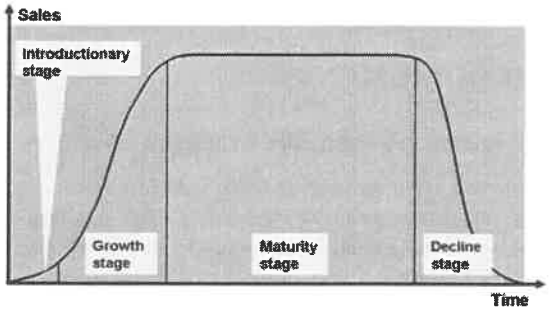


Figure 1: The Product Life Cycle

After the successful market introduction of a product, i. e. during the growth stage of the product life cycle, the required numbers rapidly increase. In order to raise economic efficiency, manual assembly processes must be replaced by automated ones. The introduction of automated systems, however, requires time for design and implementation and the training of the staff. This transition period can last up to several months. At the same time, companies have to cope with more and more decreasing innovation cycle times, which often means that a product is already obsolete within a few months after its introduction into the market.

Therefore, the time period between manual assembly in the introductionary phase and automated assembly during the growth phase has to be shortened significantly. The work reported in this paper deals with a concept for a hybrid micro-assembly system which can be used for both manual assembly processes using telepresence technology and automated assembly for production in small to mid-size numbers.

## 2 STATE OF THE ART

### 2.1 Telepresent approaches

Several research groups around the world are dealing with the use of telepresence technologies for microassembly tasks (e. g. [4], [5], [6], [7]). Most investigations deal with control engineering stability problems and measures for achieving a close-to-reality impression. [2] has developed a common micro-manipulation system for pick-and-place operations and surveys sticking-and-scaling effects during micro-manipulation. [8] describes a modular setup of a telepresent micro-assembly system for precision assembly operations. For different assembly tasks, suitable haptic devices and grippers can be connected to the system. Also, for a close-to-reality impression, both camera-based and model-based visualization of the assembly scenario can be shown. [9] has developed a teleoperated micro-assembly system, which provides a direct teleoperation mode and a task-based teleoperation

mode. The primary objective of this system is to speed up and facilitate teleoperated micro-assembly processes using semi-automatic micromanipulation technology.

However, most of the known systems are not optimized for industrial applications and can only be operated in a manual telepresent mode, but not in an automated mode.

### 2.2 Automated solutions

At present, hardly any flexible and cost efficient solutions are known for producing microsystems in small to medium-size numbers. Most automated systems are highly specialized systems. Hence reducing the costs per unit can only be achieved by increasing the number of produced units.

[10] has developed a flexible and integrated micro-assembly tool for applications with standard robots. It is suitable for both absolute positioning with the help of suitable handling equipment and for relative positioning strategies using sensors and a combination of coarse and fine manipulation by piezoelectric micro-positioners. Due to the modular design concept of this assembly tool, flexible applicability can be achieved. Expensive but frequently used components, in particular a high-precision optical system, a high-resolution force sensor and a fine-positioning actuator, are integrated in a common tool base. Specific end effectors and grippers for different processes can be attached to the tool base. Despite its flexibility and its modularity, this system is only suitable for automated series production, but not for single piece production, because the necessary effort for programming, teaching and putting the system into action still requires too much time.

[11] has developed an agile assembly architecture, which is based on intelligent, cooperating assembly agents. Assembly systems based on this architecture can be deployed with a minimum effort of time and costs. Furthermore these assembly systems can be easily adapted to changing market conditions or changes of the product design. However, this architecture was not designed for the manual, telepresent production of products in very small numbers, e.g. prototypes.

## 3 REQUIREMENTS

### 3.1 Common requirements for micro-assembly

The following requirements must be fulfilled by both automated and manually controlled systems:

Micro-assembly processes require a high position accuracy and repeatability. Therefore, the kinematic system must be very precise with robust and reliable hardware components. In addition, position sensors such as image processing systems or fiber-optical sensors have to be integrated for online-controlling the relative positions of parts. By using smart software algorithms, external interferences, e.g. assembly tolerances or thermally induced deviations can be compensated. This ensures a high availability of the micro-assembly system.

Scaling effects affect micro-assembly processes, especially during the handling of micro-parts. Because adhesive and electrostatic forces are superordinate to commonly known gravity effects, parts may be sticking to grippers and the handling of micro-parts is more difficult than the manipulation of macro-parts. Also the impression of picking up a micro-part is not common because of the missing gravity force.

In order to reduce investment costs, micro-assembly systems for both teleoperated and automated assembly tasks in small to mid-sized volumes must have a modular design and a flexible applicability for various production processes.

### 3.2 Requirements for automated assembly systems

To provide high accuracy with standard kinematic systems, relative positioning strategies have to be integrated into the assembly process ]. This means a combination of coarse positioning with absolute positioning strategies and fine positioning steps controlled by image processing or comparing sensor signals.

Controlled automatically, an online process control is required in the production system to ensure a high process quality [14]. This requires smart sensor components and intelligent software algorithms to map and evaluate all relevant process data.

### 3.3 Requirements for teleoperated assembly systems

A set of requirements has to be considered for telepresent micro-assembly applications: To ensure a high-fidelity impression, the teleoperated assembly system must provide certain minimum levels of performance in the communication rate between the operator end and the other devices. In particular the bandwidth of human perception determines the rate of data transmission. For intuitive operability, sensor information has to be adapted to

human perception. For example, micro-forces during assembly operations, e. g. adhesion forces, have to be amplified and scaled into dimensions which are familiar to humans.

Due to the usually unrestricted manual interaction in telepresent micro-assembly applications, more fail-safe features are required than in automated micro-assembly systems, which prevent collisions and damage to the work pieces and the components of the assembly system itself. In case of any irregular process conditions, e. g. when predefined force limits are exceeded, suitable safety measures, e.g. retreating movements or emergency stops, have to be activated instantly.

# 4 CONCEPT APPROACH

## 4.1 System overview

Figure 2 shows the general structure of the hybrid micro-assembly system developed at the iwb. The system was implemented in C++ and runs on a standard PC (Pentium III 500 MHz) under Windows 2000. The system offers two possible operation modes: (a) manual operation and (b) automated operation. The manual operation mode is intended for assembly processes in very small numbers, e. g. prototypes, during the introductionary stage of the product life cycle. In addition to the manual operation mode, the system enables an intuitive and interactive teaching mode for creating single elementary control steps, e. g. coarse positioning, alignment operations, force-monitored pick-and-place operations etc. By teaching single elementary operations, program scripts can be created which can be executed by an automation controller. The automated operation mode is designed for series production of micro-systems in small to mid-size volumes.

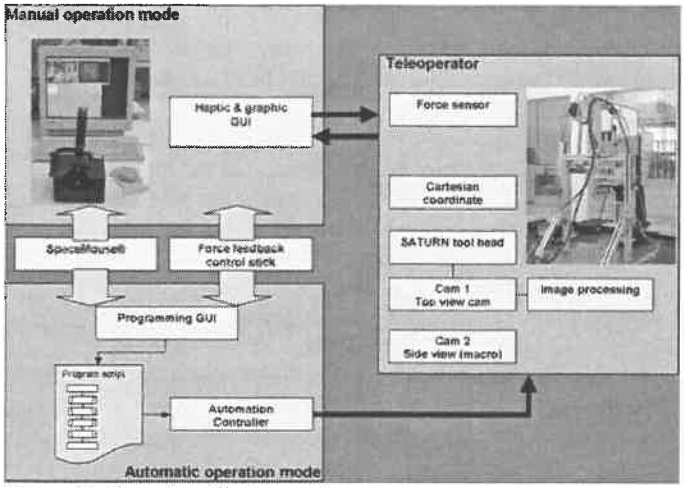

Figure 2: Overview System setup

### 4.1.1 Teleoperator

For high-precision micro-assembly tasks, a teleoperator with four degrees of freedom has been designed (see Figure 3). The assembly system consists of two core components:

The first core component is a Cartesian coordinate axes system with three precision linear tables (workspace: 204 mm x 204 mm x 204 mm). With a positioning resolution of 0.1 µm it enables very accurate positioning actions. On an assembly platform, which is attached to the precision coordinate axes, chip-trays and substrates are placed. The magazines supply the parts required for the assembly operation.

Mounting forces in z-direction can be acquired by an uniaxial precision force sensor with a measuring range of ± 50 N. In conjunction with a 12 bit data acquisition card, a maximum force resolution of ± 0.024 N can be achieved.

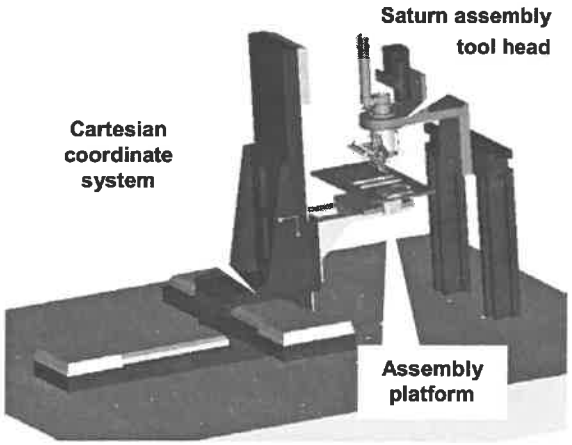

Figure 3: Hardware setup

For safety reasons, a multistage safety concept including hard- and software features was implemented. The assembly table is resiliently mounted to the coordinate axes by the use of two miniature frictionless tables and a spring. In conjunction with mechanical limit stops and

electrical limit switches, these features prevent damage to the sensitive force sensor resulting from overloads or collisions.

Furthermore, additional safety algorithms have been implemented into the controlling software. If a predefined force limit is exceeded, a further forward movement of the z-axis is stopped. This prevents a collision from occurring. However, a retracting movement is still possible in order to reduce the sensor load and to continue the assembly process. Furthermore, special safety areas can be defined within the working space. There, the maximum speed of the micromanipulator is reduced in order to minimize the danger of possible collisions.

The second main component is a modified application of the flexible and modular micro-assembly tool head SATURN (sensor-based assembly tool using robot vision), which was initially developed by the iwb for use with automated micro-assembly systems (see Figure 4[3]). The tool head can be rotated by 360° with an angular resolution of 0.005°.

The tool head provides up to four tool interfaces, which are arranged equally around the tool head cylinder. On the interfaces, process-specific tools, e. g. grippers, dispense units etc., can be flexibly mounted. The specific tools can be extended into the focus plane of the camera by pneumatic cylinders.

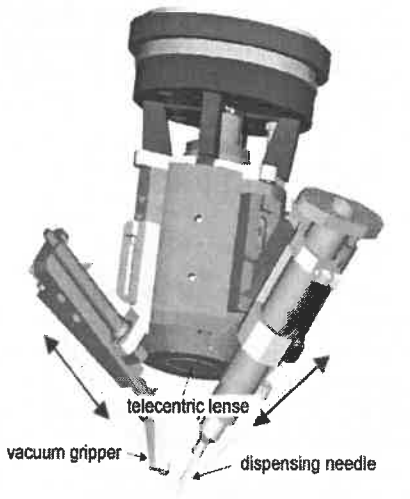

Figure 4: SATURN assembly tool head

In the centre of the tool head, a video system consisting of a CCD-camera and a highly precise telecentric lens with an coaxial illumination has been integrated. The optical system has a working distance of 34.9 mm and a magnification scale of 2:1. The field of view of the mentioned objective amounts to 1.9 x 2.5 mm and the depth of focus is ±0.5 mm. For adjusting the optical focus, the whole optical system can be moved within a range of ± 5 mm in the vertical direction. The optical system can be used for both visual monitoring by a human operator and for precise measurement tasks by image processing in automated systems. Both core components provide a total number of four degrees of freedom, which is sufficient for a multitude of micro-assembly tasks.

### 4.1.2 Operator end

The assembly station can be controlled with two input devices. For achieving a close-to-reality-impression during the manual assembly process, a force-feedback control stick is implemented in conjunction with a high-resolution force sensor. The force-feedback control stick is used for controlling the movement of the precision axes. By pushing button 1 and moving the control stick, the precision stages can be moved in the x and y-direction. The stage in z-direction can be moved by pushing button 1 and 2 and moving the control stick forward or backward.

A SpaceMouse® [13], an input device with six degrees of freedom, is used for controlling the rotation of the tool head and for adjusting the focus plane of the vision system. Furthermore, by pushing the function keys of the SpaceMouse®, the different tools of the SATURN tool head can be extended or retracted. In addition, specific tool functions, e. g. opening and closing a gripper, can be activated.

In order to provide a realistic impression of a micro-assembly process, multiple cameras with different viewpoints and zoom factors can be integrated. Visual supervision is achieved by a video system consisting of two framegrabber cards, which enable simultaneous visual output of two video displays. Up to three different cameras can be plugged into each framegrabber card. Usually one video screen image is used to display a high magnifying top view of the assembly scene.

## 5 OPERATION MODES

### 5.1 Experiment description

For testing the above-described experimental setup, a simple pick-and-place task was chosen (see Figure 5). The objective of this experiment was defined as follows: a square micro-part with edge dimensions of 1.5 mm x 1.5 mm has to be picked up from a magazine place (waffle pack) and to be moved to the desired mounting place (substrate). There the contours of the micro-part have to be aligned with reference marks on the substrate. Finally, the micro-

part has to be set down with a defined amount of force and to be placed on the substrate. For executing this task, the SATURN tool head was equipped with a vacuum gripper.

### 5.2 Manual mode

In manual operation mode, the micromanipulator can be positioned by use of the force-feedback control stick and the SpaceMouse®. For facilitating assembly operations and speeding up transport operations, the operator can define and recall way points by pushing function buttons of the SpaceMouse®. Furthermore these positions can be inserted into the automated program sequence script for later use in automated mode.

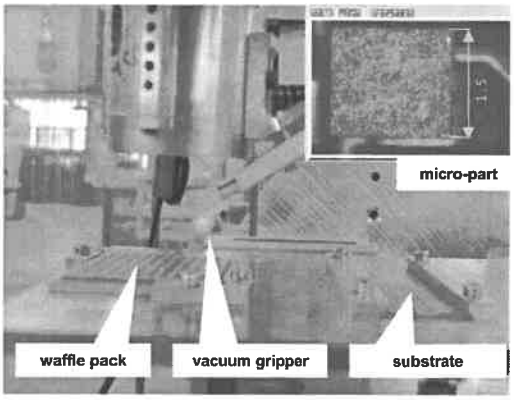

Figure 5: Assembly experiment

### 5.3 Automated mode

The described task can be divided into several elementary operations. For creating program sequences for the automated mode, a distinction must be made between open-loop operations and closed-loop operations.

| Pick-up operation | Placing operation |
|---|---|
| Coarse positioning | Coarse positioning |
| Alignment (fine positioning) | Alignment (fine positioning) |
| Extend gripper | Place gripper (touch down) |
| Place gripper (touch down) | Release part (vacuum off) |
| Grasp part (vacuum on) | Retract gripper |

Open-loop operation
Closed-loop operation

Figure 6: Pick-and-place task: elementary operations

Open-loop operations are usually used for simple elementary operations which can be executed independently from any outside process influences, e. g. assembly tolerances. For instance, the automated execution of the elementary operation "Coarse positioning" only requires the coordinates x, y and z. These positions can be intuitively programmed during the manual teleoperation mode by moving the teleoperator to the desired target position and saving the coordinates along with the desired elementary operation into the program script file. In a similar manner, the other open-loop tasks "Grasp part", "Release part", "Extend gripper" and "Retract gripper" can be easily programmed. So far the developed system makes it possible to create open-loop program sequences and initial experiments have been succesfully carried out.

However, closed-loop tasks are necessary for more complex assembly operations, e. g. for compensating assembly tolerances, or for monitoring critical process conditions, e.g. maximum allowable mounting forces. For this purpose, additional sensor data usually has to be processed during the automated program execution. For the elementary operations "Touch down gripper" and "Align gripper", the proposed system can be used for the intuitive programming of automation sequences:

The elementary operation "Touch down gripper" can be taught by moving the gripper toward the surface until there is contact. By haptic feedback and/or by observing the alphanumerical display of the acquired sensor data, the operator can intuitively define force limits for the specific assembly operation.

For teaching the elementary operation "Fine positioning", an image pattern of the part to be grasped has to be generated and saved as an input parameter to the program sequence file. During the automated assembly execution, the image processing unit then can process the relative distance between the object and the tool center point by comparing the actual video image with this image pattern. This also can be realized by the proposed system by moving the teleoperator and the top view camera to the specific target object. After making a snapshot of the target object, the operator only has to define reference edges and points within the image pattern. Both pieces of information, the image pattern along with the defined reference data, are saved to the program sequence file.

## 6 SUMMARY AND FURTHER WORK

This paper presents a hybrid micro-assembly system providing both manual teleoperation mode for single-piece production and automated operation mode for series production of microsystems.

During the manual operation mode, a force-feedback device is used in conjunction with a SpaceMouse® for controlling the position and orientation of the micromanipulator. The manual operation mode also includes the possibility to create program sequences for the automated operation mode.

During the automated operation mode, an automation controller replaces the human operator by executing the previously recorded program sequences.

The paper concludes with a short description of a first experiment based on a simple pick-and-place operation for demonstrating the abilities of the developed system. So far, program scripts for open-loop operations, i. e. coarse positioning and gripper operations, can be generated.

The integration of closed-loop operations, in particular aligning processes and force monitored placing operations, will be the very next steps of future developments. Furthermore, a series of experiments for determining the capabilities of the described system as well as a comparison of manual and automated mode in respect to cycle time and process quality will follow.

## 7 ACKNOWLEDGEMENTS

The work presented is funded within the 'SFB 453' Collaborative Research Center "High-Fidelity Telepresence and Teleaction" of the DFG (Deutsche Forschungsgemeinschaft). Furthermore, the authors wish to thank Christian Schuberth and Matthias Doerfel for their contributions to the concept and the implementation.

## REFERENCES

[1] Microsystems World Market Analysis 2000-2005 - NEXUS Task Force Market Analysis, 2002.

[2] Fearing, R.S.: Survey of Sticking effects for Micro Parts Handling. In: Proceedings of the 1995 IEEE/RSJ International Conference on Intelligent Robots and Systems, August 5 - 9, 1995, Pittsburgh, Pennsylvania, USA. Los Alamos, Calif.: IEEE Computer Soc. Press 1995, pp. 2212 - 2217.

[3] Reinhart, G.; Jacob, D.: Automated Assembly of Holder Chips to AFM Probes. In: Nelson, B. J.; Breguet, J.-M. (Eds.): Microrobotics and Microassembly III, Boston. Washington: Proceedings of SPIE Vol. 4568 (2001), pp. 310 - 317.

[4] Eme, T.; Hauert, P.; Goldberg, K. Y.; Zesch, W.; Siegwart, R.Y.: Microassembly using auditory display of force feedback. In: Nelson, B. J.; Breguet, J.-M. (Eds.): Microrobotics and Microassembly, Proc. of SPIE Vol. 3834, pp. 203-210, 1999.

[5] Alex, J; Vikramadatitya, B.; Nelson, B. J.: A Virtual reality teleoperator interface for Assembly of Hybrid MEMS Prototypes. In: Proc. of DETC'98, (Atlanta), 1998.

[6] Yokokohji, Y; Hosotani, N.; Ueda, J.; Yoshikawa, T.: A Micro Teleoperation System for Compensating Scaling Effects Based on Environment Model. In: Proc. of 1994 Japan-USA Symposium on Flexible Automation, 1994.

[7] Kunstmann, C.; Weißmantel, H.: Manual Assembly of Hybrid Microsystems - A Job for Telemanipulation with Force Feedback. In: Detter, H. (Ed.): Proc. of Symposium on Handling and Assembly of Microparts. Wien: Österreichische Tribologische Gesellschaft, 1997, pp. 30-35.

[8] Reinhart, G.; Anton, O.; Ehrenstrasser, M.; Petzold, B.: Telepresent Microassembly at a glance. In: Färber, G., Hoogen, J. (Eds.): Workshop Proceedings: Advances in Interactive Multimodal Telepresence Systems. Munich 2001.

[9] Song, E.-H.; Kim, D.-H.; Kim, K.; Lee J.: Intelligent User Interface for Teleoperated Microassembly. In: Proceedings of the 2001 International Conference on Control, Automation and System, Jeju in Korea, October, 2001, pp. 784-788.

[10] Reinhart, G.; Jacob, D.: Positioning Strategies and Sensor Integration in Tools for Assembly MOEMS. In: Motamedi, M.; Göring, R. (Eds.): MOEMS and Miniaturized Systems, Santa Clara. Washington: Proceedings of SPIE Vol. 4178 (2000), pp. 395 – 402.

[11] Rizz, A. A.; Hollis, R. L.: Opportunities for Increased Intelligence and Autonomy Systems for Manufacturing. In: Robotics Research: The Eight International Symposium of Robotics Research, Hayama, Japan, October 3-7, 1997. London: Springer 1997, pp. 141-151.

[12] Jacob, D.; Höhn, M.: Assembly of Semiconductor Based Microsystems with Sensor Guided Tools. In: Reichl, H. (Ed.): System Integration in Micro Electronics, Nuremberg. Berlin: VDE 2000, S.193 – 202.

[13] http://www.3dconnexion.com/products/Classic.htm

# Production of Direct Drive Cylindrical Targets for Inertial Confinement Fusion Experiments

Norman E. Elliott, Robert D. Day, Douglas J. Hatch, David Sandoval, Veronica Gomez, Timothy Pierce, Joyce Elliott, Ruben Manzanares
Los Alamos National Laboratory, Los Alamos, NM, 87545 USA
(505)667-1587 nee@lanl.gov

ABSTRACT

We have made targets with cylindrical geometry for Inertial Confinement Fusion (ICF) experiments. These targets are used in hydrodynamic experiments on the OMEGA laser at the University of Rochester. The cylindrical design allows the study of three dimensional hydrodynamic effects in a pseudo 2D mode, simplifying data gathering and analysis. Direct drive refers to the fact that the target is illuminated directly by approximately 50 laser beams and is imploded by the material pressure generated from ablation of the outside of the target.

The production of cylindrical targets involves numerous steps. These steps are shared in common with many other types of ICF targets but no other single target type encompasses such a wide range of fabrication techniques. These targets consist of a large number of individual parts, all fabricated from commercially purchased raw material, requiring many machining, assembly, electroplating and chemical process steps. Virtually every manufacturing and assembly process we currently possess is involved in the production of these targets.

The generic target consists of a plastic cylinder (ablator) that is roughly 1mm in diameter by 2.25mm long. The wall of the cylinder is roughly 0.07mm thick. There is an aluminum cylinder 0.5mm wide and 0.01mm thick centered on the inside of the plastic cylinder and coaxial with the outside plastic cylinder. The outside of this aluminum band has surface finishes of differing random average roughness. The required average surface roughness is determined in advance by experimental design based on the amount of turbulent mix to be observed. The interior of the cylinder is filled with low density polystyrene foam that is made in house. To produce a finished target additional features are added to each target. X-ray backlighters are cantilevered off the target that allow time resolved x-ray images of the imploding target to be recorded during the experiment. The x-ray backlighters are driven by additional laser beams that are delayed to record an image at the appropriate time after the main beams are fired. An aperture to limit the area imaged and reduce x-ray background is placed on the target opposite the backlighters. Finally, alignment fibers that allow the target to be located precisely in three dimensional space before being shot are placed in several locations on the outside of the target.

## I. INTRODUCTION

Using cylinders in hydrodynamic experiments allows the observation of interface motion along the cylindrical axis in a convergent geometry. Experiments using indirect drive in hohlraums on Nova[1] and now using direct drive on OMEGA[2] have studied low-order mode Rayleigh-Taylor growth at the ablation surface, weakly non-linear mode coupling, shock interactions at material interfaces, and Richtmyer-Meshkov turbulent mix all affected by Bell-Plesset convergent effects. Also detailed work on the techniques of comparison of hydrodynamic simulations to experimental measurements has been done using static targets.[3] To achieve sufficient quality data for significant comparison to theoretical simulations, the target dimensions, densities, surfaces, and quality must be carefully controlled and measured. A previous description of the manufacture of cylinder targets for the indirect drive Nova experiments, concentrating on the machining of perturbations, has been published.[4] Six campaigns for direct drive cylinders (DDCYLs) on the OMEGA laser over more than three years have generated a procedure for the "best practice" in making the epoxy ablators, radiographic marker layers, and foam inserts.

The description of the targets and the experimental design has been published.[2] In general the finished target consists of polystyrene foam of between 30-120 mg/cm$^3$ density and 860 μm nominal outer diameter. This CH foam has also been successfully replaced with fully deuterated foam. The foam goes inside a epoxy ablator (cylinder) of 20-73 μm wall thickness, with the outer diameter from 900-1014 μm and 2250 μm in length. At the interface of the

ablator and the foam, in the central 500-μm region is a radiographic marker layer, sometimes applied to the outside of the foam but generally embedded in the ablator during manufacture. The target is completed with assembly of backlighter, image defining aperture and alignment fibers on a target mount. Figure 1 shows an exploded view of the parts of a typical DDCYL target.

## II. PLASTIC ABLATORS AND EMBEDDED MARKERS

The primary ablator or pusher is a cylindrical shell of epoxy wrapped around a marker layer at the inside edge. This shell is made by a sequence of steps of applying layers to a central sacrificial mandrel, machining each layer, and concluding by chemically leaching away the mandrel. These steps are now described in sequence.

The mandrels are machined out of copper rods placed in a brass base used for precision installation on the diamond turning lathe. New bases must be annealed by bringing them up to the highest processing temperature they will see during subsequent steps, typically 200°C for an hour, and then they must be well cleaned before mandrels are put in them. The mandrels are made 4mm long to insure uniform coating with epoxy to produce the ablator layer. The mandrel must be removed and replaced many times on the diamond turning lathe to allow the formation of marker bands and ablator layers. An indicator band on the base is used by the machinist allowing recentering of the mandrel each time it goes back onto the lathe. This assures that all machined layers are concentric. After machining, the mandrels are cleaned initially with methanol, then Excaliber® followed by ethanol to remove any machining grease. The inner diameter of the final cylinder is determined by measuring the diameter of the mandrel using a laser micrometer. Individual targets are then tracked by a number on each mandrel base.

Targets make use of an aluminum marker layer. This layer produces radiographic contrast during the laser experiment without producing a significant density change. The aluminum is electrodeposited on the mandrels by Alumiplate, Inc. in Minneapolis, MN. The aluminum band is then produced by post machining to leave a band 500μm wide with a wall thickness between 8 and 16μm depending on the experiment being performed. The

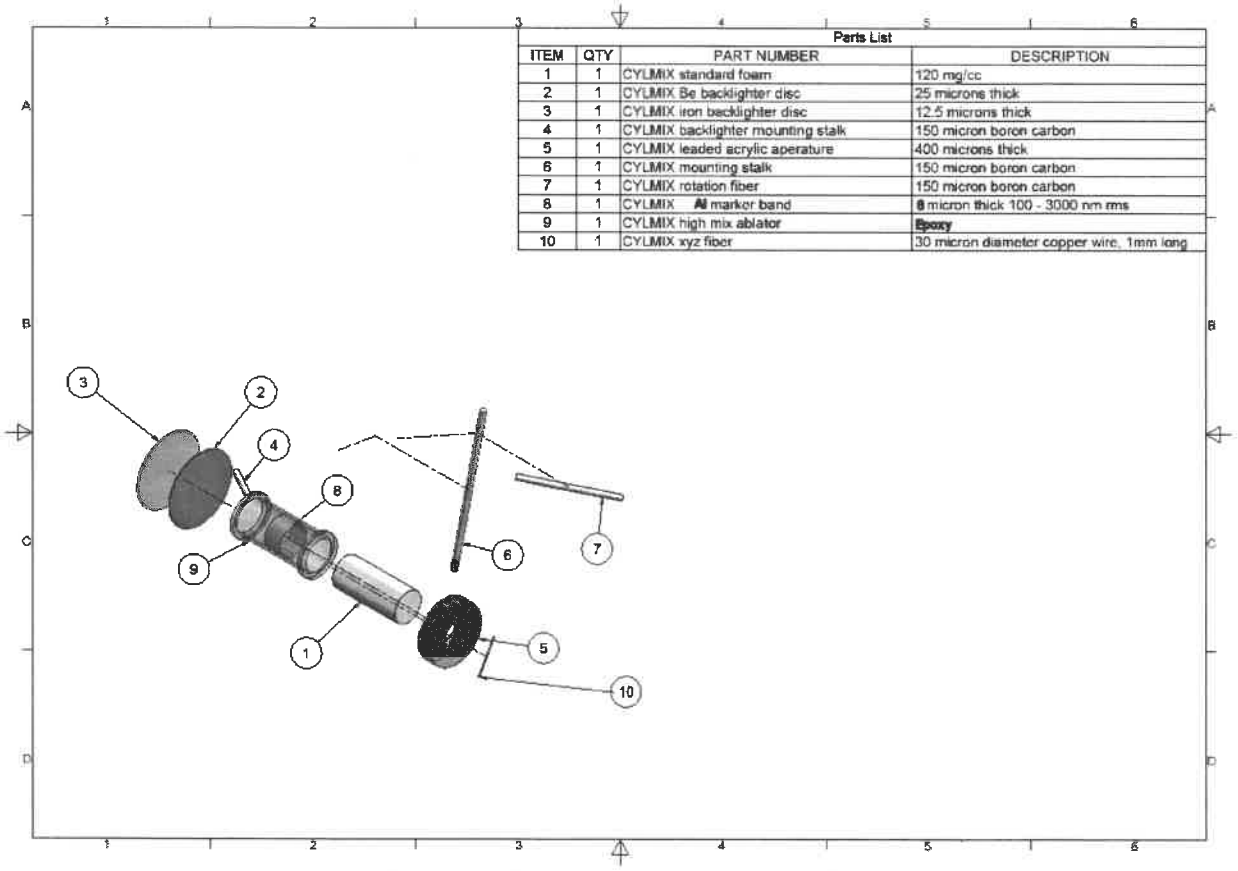
Parts List
ITEM | QTY | PART NUMBER | DESCRIPTION
1 | 1 | CYLMIX standard foam | 120 mg/cc
2 | 1 | CYLMIX Be backlighter disc | 25 microns thick
3 | 1 | CYLMIX iron backlighter disc | 12.5 microns thick
4 | 1 | CYLMIX backlighter mounting stalk | 150 micron boron carbon
5 | 1 | CYLMIX leaded acrylic aperature | 400 microns thick
6 | 1 | CYLMIX mounting stalk | 150 micron boron carbon
7 | 1 | CYLMIX rotation fiber | 150 micron boron carbon
8 | 1 | CYLMIX Al marker band | 8 micron thick 100 - 3000 nm rms
9 | 1 | CYLMIX high mix ablator | Epoxy
10 | 1 | CYLMIX xyz fiber | 30 micron diameter copper wire, 1mm long

**Figure 1:** CAD drawing of exploded DDCYL assembly

experiment measures the amount of hydrodynamic "mix" that occurs with varying amounts of initial random surface roughness imposed on the outside of the aluminum marker band. To produce this roughness a fast tool servo (FTS) is used with a diamond atomic force microscope tip as a cutting tool. Software was written to drive the FTS allowing random surface roughness of predetermined average surface roughness ($R_a$) to be produced. Variations on this theme have allowed the production of a regular feature superimposed on the random surface for some targets (Figure 2). Another variation is a "single mode" target with a sine wave produced along the cylindrical axis by FTS (Figure 4d).

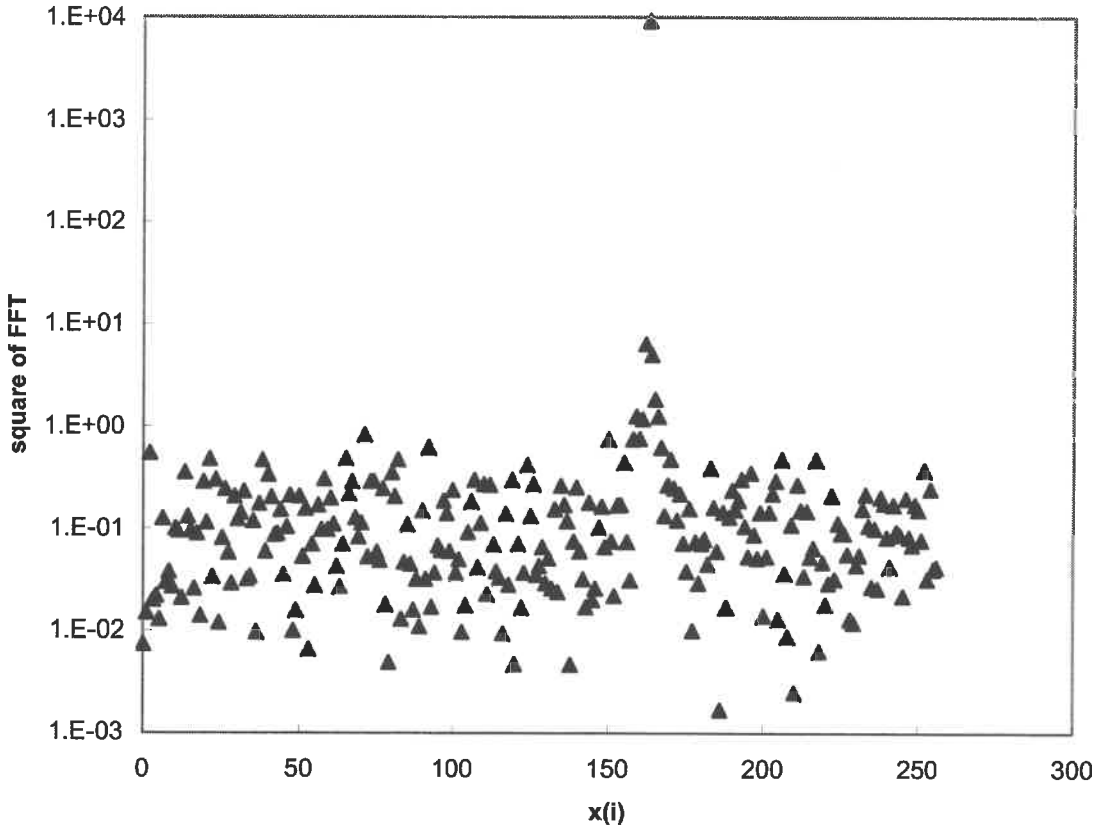


**Figure 2**: Power spectrum from numerical model of 0.5μm $R_a$ surface plus superimposed 6μm amplitude sine wave.

All epoxy layers are made by casting epoxy around the mandrel. Shrink tubing is used as a form to cast the epoxy. The epoxy is then machined to length and radius. Only diamond tool bits are used to machine the epoxy. This includes even any roughing out process, where use of high-speed steel bits induces stress in the plastic. The 500μm-long marker region should be placed relatively centered along the mandrel, so that the eventual end of the epoxy pusher should be over 500μm from the mandrel end. The precision bases are used to re-center the piece so that the 8μm-thick marker bands are concentric with the original machining of the mandrel and the outer epoxy ablator.

## III. CENTRAL FOAMS

To avoid having a vacuum and provide hydrodynamic backpressure, foam is inserted down the middle of the ablator shell. It is 2000 μm long so that the ablator hangs over its end and prevents direct illumination of the foam end. The polystyrene foams are made to the requested density and then filled with BRIJ® to allow machining.[5] After machining the BRIJ® is leached out of the foam at 50°C for up to 4 hours in ethanol in an explosion-safe oven. The foam pieces are found to shrink approximately 1%-2% after leaching, and must be machined slightly oversize to

compensate.

Double shell targets (another variation of the same general target design) are manufactured by drilling a hole into the central foam before the BRIJ® is leached. A solid cylinder (wire) of correct radius and length is inserted and centered in the foam. This wire has been made from solid metal wire of specified diameter, polystyrene or epoxy machined to a specific diameter or machined plastic that has metal vapor deposited on the outside. The final assembly should undergo static radiography in two orthogonal views to confirm correct alignment and dimensions

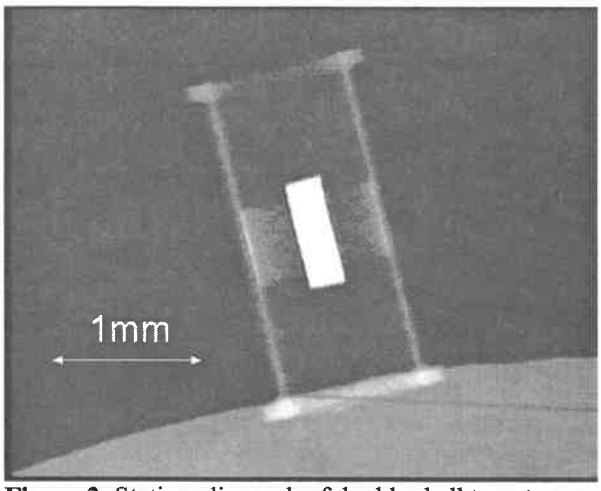


**Figure 3:** Static radiograph of double shell target showing alignment of internal wire to the cylinder outside and marker band.

(see Figure 3).

After leaching both the epoxy cylinder assembly and the foam, there is some shrinkage. Use of epoxy has minimized this but it does occur to some extent. The authors believe most of the shrinkage occurs within a few minutes to an hour after leaching; afterward the targets are demonstrably stable in their dimensions for over a year at a time. Care must be taken in inserting the foam into the cylinder to best match sizes and reduce any vacuum region between the ablator and foam and to prevent damage to the marker layer at the interface.

## IV. DIMENSIONAL MEASUREMENTS AND METROLOGY

It is important to measure and document the values as well as uncertainties in all target dimensions. This includes densities, marker thickness, length, and composition, and ablator radius and thickness, as well as target assembly angles and locations of alignment fiducials. The densities of the solid epoxy have been determined from a density gradient column to ±5% one-sigma uncertainty. Foam material density is calculated from measured volume and weight from a microbalance. Other dimensional measurements have been described above in their respective place in the processing. Because of shrinkage after leaching, final ablator radii must be determined by optical shadowography or microscopy after assembly with at best ±1μm accuracy. The characterization of the surface roughness is discussed in another paper.[6] Final documentation for each target includes dimensional metrology, surface roughness data, profilometry traces of perturbed targets, SEMs of markers or foams and assembly photographs.

## V. FINAL TARGET ASSEMBLY

With completed cylinders in hand, final targets are made by mounting on stalks, putting on backlighters and radiography apertures and alignment fibers. Angles and physical dimensions are determined using a so-called Powell scope, an optical microscope connected to a four-axis (X and Y and two angles) alignment system. This metrology can typically measure dimensions to ±5μm and ±0.1°, and allows final target alignment in the OMEGA target chamber to about 30μm and ±0.3° accuracy. Figure 4 shows photographs of the assembly of a typical target.

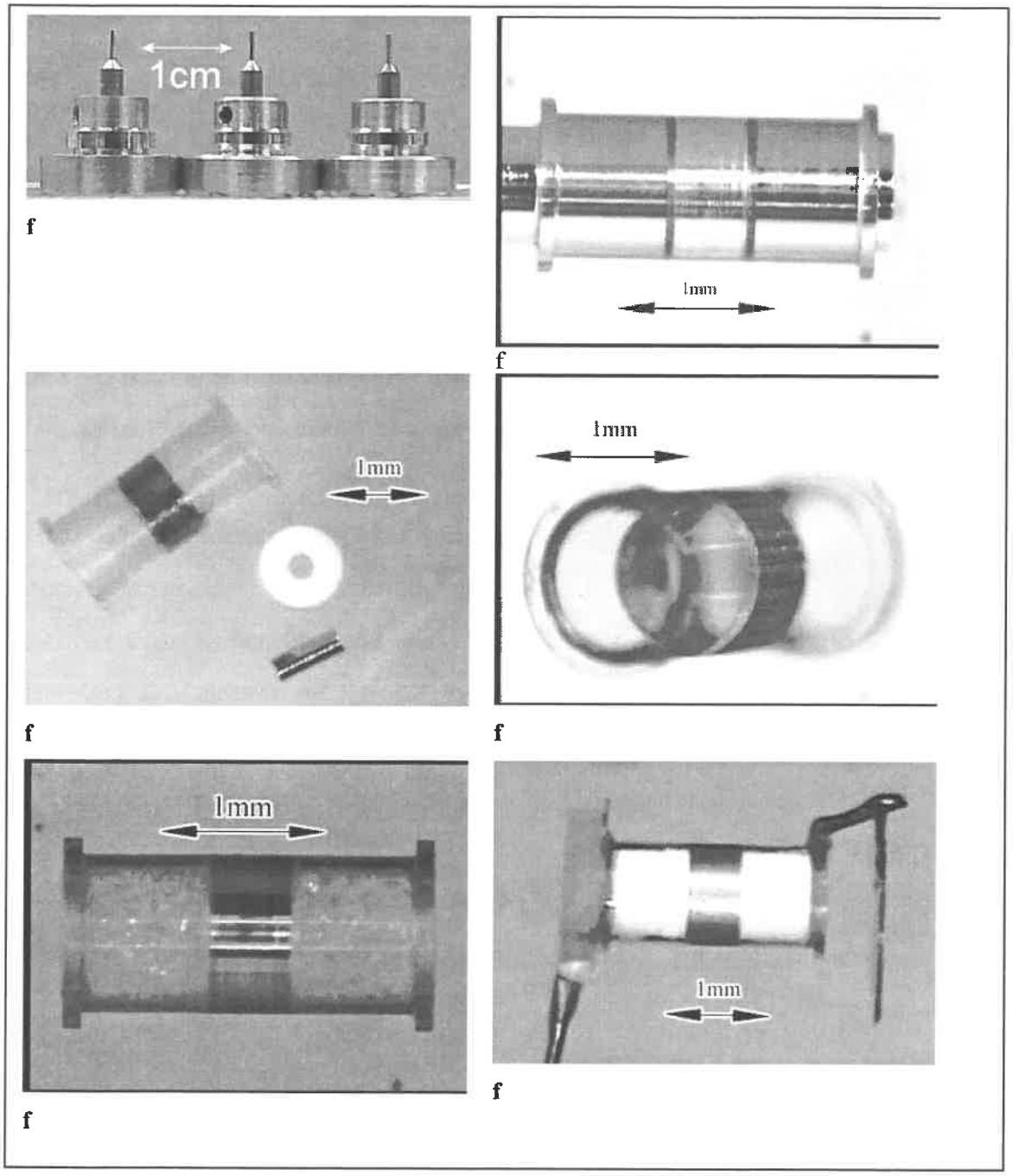


**Figure 4:** Assembly photos. a.) mandrels on bases ready for coating b.)coated mandrel with a smooth Al marker band and epoxy ready for leaching c.)pieces of double shell target ready for assembly d.) single mode sine wave target e.) partially assembled smooth target f.)finished "rough marker" target

## VI. SUMMARY

The campaign to build direct drive cylindrical targets has continued for a number of years. Typical of this work, numerous small incremental improvements in fabrication have occurred in this time. This has resulted in the current state of the art as described in this paper. Differing from most of our work, these targets encompass virtually every

fabrication method we have at our disposal. This is especially surprising after looking at the conceptually simple design of the target. As a consequence, this design presents a perfect example of our ability to produce a target of critically defined characteristics that will allow quantitative comparison to numerical simulations.

**REFERENCES**


(1)W.W.HSING, *et al.*, "Rayleigh-Taylor Instability Evolution in Ablatively Driven Cylindrical Implosions," *Phys. Plasmas* **4**, 1832 (1997); W.W.HSING AND N.M. HOFFMAN, "Measurement of Feedthrough and Instability Growth in Radiation- Driven Cylindrical Implosions," *Phys. Rev. Lett.* **78**, 3876 (1997); S. R. GOLDMAN *et al.*, "Production of Enhanced Pressure Regions due to Inhomogeneities in Inertial Confinement Fusion Targets," *Phys. Plasmas* **7**, 2007 (2000).

(2) C. W. BARNES *et al.*, "Experimental Configuration of Direct Drive Cylindrical Implosions on the OMEGA Laser," *Rev. Sci. Instrum* **70**, 417 (1999); D. L. TUBBS *et al.*, "Direct Drive Cylindrical Implosion Experiments: Simulations and Data," *Laser Particle Beams* **17**, 437 (1999); D. L. TUBBS *et al.*, "Cylindrical Implosion Experiments Using Laser Direct Drive," *Phys. Plasmas* **6**, 2095 (1999) 2095; C. W. BARNES *et al.*, "Observation of Mix in a Compressible Plasma in a Convergent Cylindrical Geometry," (submitted to *Phys. Rev. Letters*, 2001).

(3) J. M. SCOTT *et al.*, "Radiographic Image Analysis of Cylindrical Implosion Experiments," *Rev. Sci. Instrum.* **72**, 643 (2001).

(4)MICHELE H. MILLER, KENNETH P. GARRARD, THOMAS A.DOW, LAUREN W. TAYLOR, *Precision Engineering* **16**:1, 42 (1994); B. H. JARED *et al.*, "Fabrication of Hydrodynamic Instability Targets," *Fusion Technology* **31** 501 (1997).

(5) J.M. WILLIAMS, M. H. WILKERSON, A. J. GRAY, "Emulsion Stability and Rigid Foams From Styrene or Divinylbenzene Water-In-Oil Emulsions" *Langmuir* Feb 1990; **vol.6**, no.2, p.437-444.

(6) CRIS W. BARNES, R. D. DAY, N. E. ELLIOTT, *et al.*, "Characterization of Surface Roughness and Initial Conditions for Cylindrical Hydrodynamic and Mix Experiments," Fusion Science and Technology, Vol. 41, No.3, part 1, p.203 (2002).

# Nondestructive Characterization Technologies for Metrology of Micro/Mesoscale Assemblies*

Harry E. Martz, Jr. and Georg F. Albrecht
Lawrence Livermore National Laboratory, Livermore, CA 94550

## Introduction

Micro/mesoscience is an emerging area of science and engineering that focuses on the study of assemblies with small to very small dimensions (~ mm), features and structures (~ μm). Advances in micro/mesoscience will pose new challenges in experimental physics and engineering in general and will lead to new ways of information processing; require new materials with pertinent properties; and lead to new techniques for medical diagnostics and treatment. Research and development of Nondestructive Characterization (NDC) methods to "see" inside or image micro/mesoscale-size materials, components and assemblies will help enable a fundamentally new set of methods that can serve micro/mesoscale science and engineering.

To image the inside of micro/mesoscale assemblies nondestructively requires the use of penetrating electromagnetic waves, acoustic waves, or particles. Micro/mesoscale assemblies typically are of millimeter size and have complex and fragile embedded features or structures that are on the order of a few micrometers. We must be able to nondestructively verify that they are assembled correctly and are not damaged during assembly or have sufficient information to determine if the assembly is acceptable. Therefore, NDC technologies are required that can (1) penetrate into or through a few millimeters of diverse materials ranging from low-density, low-atomic-number foams to high-density, high-atomic-number metals, while providing adequate contrast; and (2) provide spatial resolutions of about a micrometer over a millimeter field-of-view to cover the size of an assembly. These micro/mesoscale requirements define the regions within the electromagnetic (keV x-rays) and acoustic (GHz) spectra and the type of particles (MeV protons) that are applicable to the NDC of micro/mesoscale materials or assemblies.

X-ray, proton and acoustic imaging methods are being developed to characterize assemblies (see Figure 1) with materials that vary widely in composition (low-Z to high-Z), density (~0.03 to 20 g/cm$^3$, i.e., aerogels to fully dense metals), geometry (planar to spherical), and embedded features (joints to subassemblies). Taken together, these techniques will form the basis for a new micro/mesoscale nondestructive characterization capability at LLNL.

* This work was performed under the auspices of the U.S. Department of Energy by University of California, Lawrence Livermore National Laboratory under Contract W-7405-Eng-48.

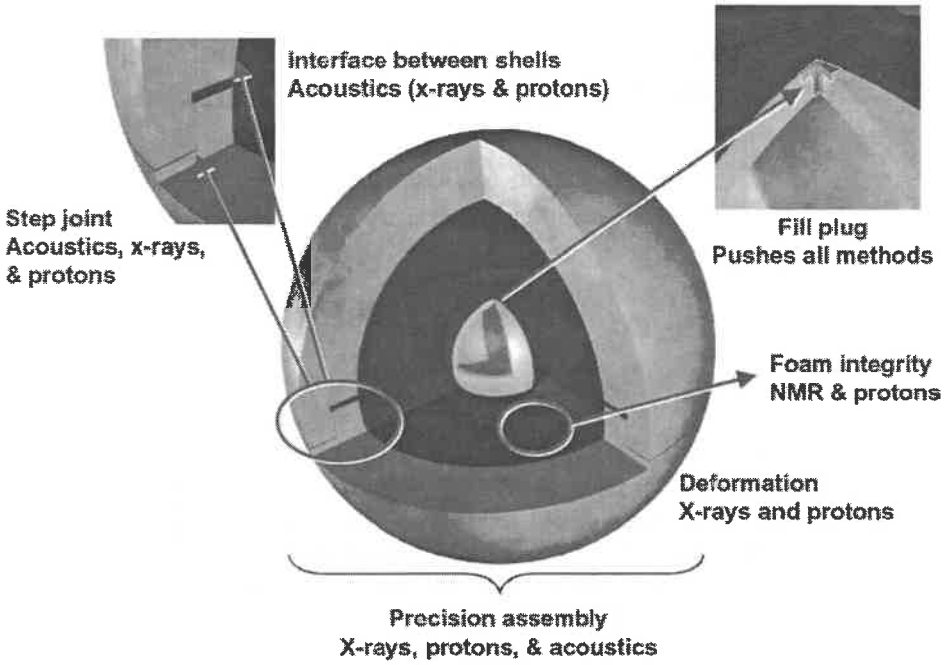


**Figure 1.** This schematic shows how a notional mm-scale double-shell laser target requires complementary NDC methods to adequately characterize its materials and assemblies. The inner shell is typically a full-density metal or plastic, the outer shell may be plastic or Be and a low-density (10's of mg/cm$^3$) aerogel is used to support the inner shell. The various characterizations required (top text) are met by the technologies shown (bottom text).

## X-Ray Microscopy

How x rays interact with matter depends on the energy of the x rays and the mass density and elemental composition of the assembly. Mass density and elemental composition of the assembly are strongly coupled in the acquired data. X-ray imaging systems can operate in three different modes: radiography, microscopy, and tomography (Martz et al., 2002). The former two result in 2-D projections of a 3-D assembly. They differ in that the short depth-of-field of the microscopy mode results in one plane being in focus with the out-of-focus planes being blurred. In tomography, the 2-D radiographs (projections at near-infinite depth of focus) are reconstructed into a 3-D representation of the assembly. X-ray microscopy and radiography (see Figure 2) are methods to measure the line-integral of the linear-attenuation coefficient, $\mu$, over the x-ray path length, $l$, (sometimes referred to as $\mu l$). In Computed Tomography (CT), many radiographs are acquired and used to reconstruct a 3-D CT model via a computer algorithm. The 3-D CT model is a measure of x-ray attenuation, $\mu$ (not $\mu l$), in the assembly.

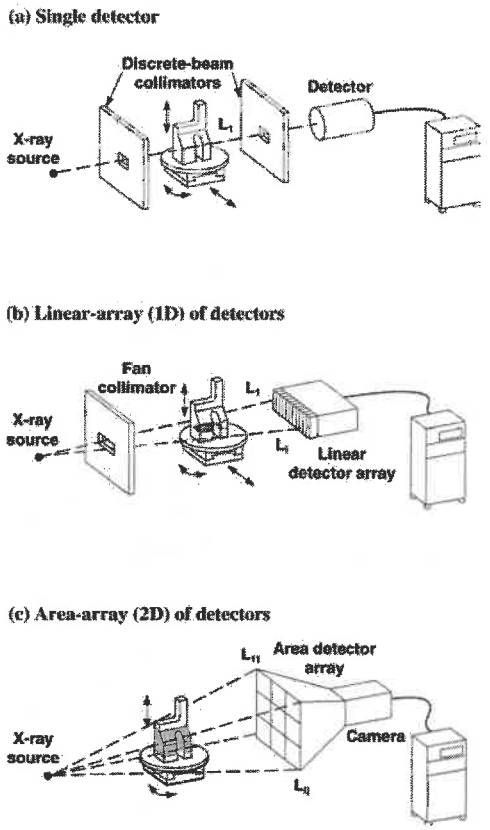


**Figure 2.** Data acquisition geometries used in industrial x-ray digital radiography and computed tomography imaging. (a) Discrete-beam translate/rotate scanner configuration using a single detector. (b) Well-collimated fan-beam configuration using a linear detector array. This geometry is the most common for industrial and medical x-ray imaging. (c) Cone-beam configuration using a area-array detector. These geometries are also employed for neutron imaging, while for protons (a) is the typical imaging geometry. An example of an x-ray microscope is shown in Figure 5.

To obtain high-resolution (~μm) x-ray images in a practical amount of time (tens of minutes), a high-collection-efficiency x-ray imaging optic and/or an extremely small, bright source should be used. For the former, we are researching a replicated Wölter multilayer x-ray optics system. For the latter, micrometer spatial resolution radiographic imaging of assemblies have been demonstrated using synchrotron x-ray sources.[1] Given the lack of targets with embedded features available for measurement we exercised the x-ray synchrotron imaging using a target with known surface features. A ruled, 1-mm diameter disk of known construction was selected for x-ray synchrotron computed tomography imaging. The disk was made of polyimide, with a brominated central insert. The surface had a three-dimensional sinusoidal pattern similar to that seen in an egg carton as shown in Figure 3. The ruling was designed to have a 50-μm period, and a peak-to-valley height of 5 μm. The specimen was placed on the rotating stage of the synchrotron radiation microtomography system at beamline 10-2 at Stanford Synchrotron Radiation Laboratory, and scanned in 0.25-degree rotational increments over 180° (Kinney and Haupt, 2002). A double crystal Si (220) monochromator was used to select an x-ray energy of 12 keV ($\Delta E/E < 10^{-4}$). As a result of the large contrast between the brominated central insert and the unbrominated disk, it has proved difficult to display a topographic image of the entire part in a single image. Therefore, we have chosen to display the insert separately in Figure 4. The surface topography along the datum line is shown in the graph to the right. The period spacing averaged 56 +/- 5 μm and the peak-to-valley height averaged 5.7 +/- 0.9 μm (averaged from line intercepts

[1] See papers in *Proceedings for the Seventh International Conference on X-ray Microscopy*, July 29-Aug.2, 2002, Grenoble, France.

perpendicular to the rule). These measurements are in line with the target (part) specifications. An underlying sinusoidal pattern runs orthogonal to the strong rule pattern seen in Figure 4. This underlying pattern, measured along a trough shown by the datum line in the image to the right in Figure 4, has a sinusoidal nature with a mean peak-to-valley height of 5 +/- 1 μm (averaged from line intercepts parallel to the rule) and a period spacing of 97 +/- 1 μm.

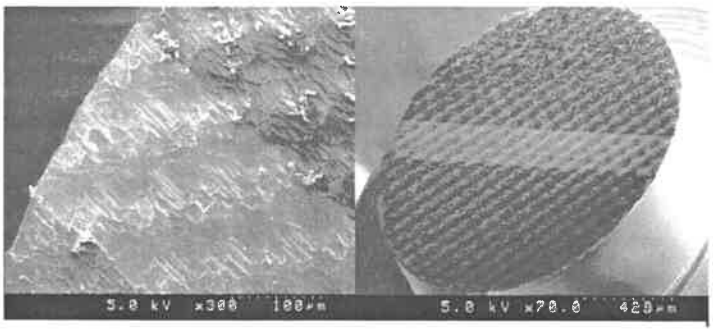

**Figure 3.** Optical micrograph at two different magnifications for a mogel surface machined into a polyimide disk with a brominated central insert used to study Super Nova Raleigh-Taylor instabilities.

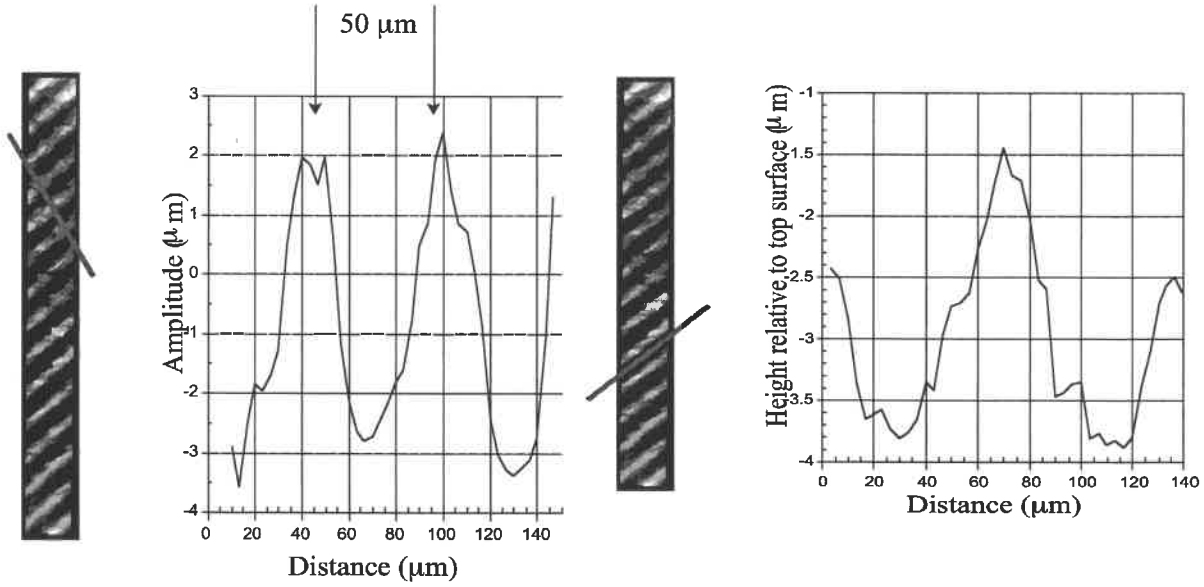


**Figure 4.** Left, a CT image of the brominated central insert surface and a graphical presentation of the surface height along the datum line perpendicular to the upper rule pattern. The amplitude is with respect to the mean surface elevation. Right, the CT image of the insert and a graphical representation of the surface height along the datum line parallel with the upper rule showing a wavelength twice that of the upper rule pattern. Only a single peak is fully shown. The negative heights indicate that the surfaces lie below the mean surface elevation.

Other researchers have used grazing-incidence Wölter imaging optics (Inoue et al., 1989 and Watanabe et al., 2001) with some degree of success, but these optics will be too slow (hours per micrograph) for our application. Xradia[2] and XRT[3], both recent start-up companies, are currently developing x-ray systems based on x-ray zone plates and projection radiography, respectively, for inspecting microchips. Their systems are impressive in their own right tens-of-nanometer resolution at Fields Of View (FOV) of tens of micrometers, but they are geared toward the specific needs of the semiconductor industry, where tens-of-nanometer-size flaws are localized to within tens of micrometers.

A replicated Wölter multilayer x-ray optics system incorporated into a mechanically stable prototype instrument (Hale, 1999) should be able to meet the micro/mesoscale characterization goals (~1-μm spatial resolution over ~1-mm FOV) (Nederbragt, 2002). Wölter optics, like other optical systems, entails a tradeoff between spatial resolution and collection efficiency. Since we are satisfied with a ~1-μm resolution, we optimized the collection efficiency for that resolution. Another key to this approach is that the multilayer coating gives it a much better collection efficiency (~100X) over grazing-incidence Wölter imaging optics. Thus, LLNL is researching and developing an x-ray microscope using Wölter I replicated multilayer x-ray imaging optics. The twofold objective of this work is to approach 1-μm spatial resolution and operate in a laboratory setting to point the way toward a high-throughput, low-operating-cost micro/mesoscale inspection system.

A super-polished, multilayer-coated, x-ray imaging optic of Wölter I design is being fabricated. Using a high brightness commercial x-ray source, the Wölter optic will project x rays through a focal plane in the assembly and onto an imaging plane, providing 12× magnification (see Figure 5). A high-resolution CCD camera, lens-coupled to a scintillator, with 3× optical magnification, will record an image of the focal plane with a detector-element size of about 0.5 μm. Our calculations show that this will take as little as 10 minutes per micrograph image. An 8-keV x-ray source was chosen initially to match low-atomic number and low-density materials of interest. Higher-energy (~60 keV) x rays and matched-energy Wölter optics will be needed to cover the large range of assembly materials and densities. A "laminate" algorithm will be developed to reconstruct a 3-D image of the assembly from successive focal plane slices through the assembly.

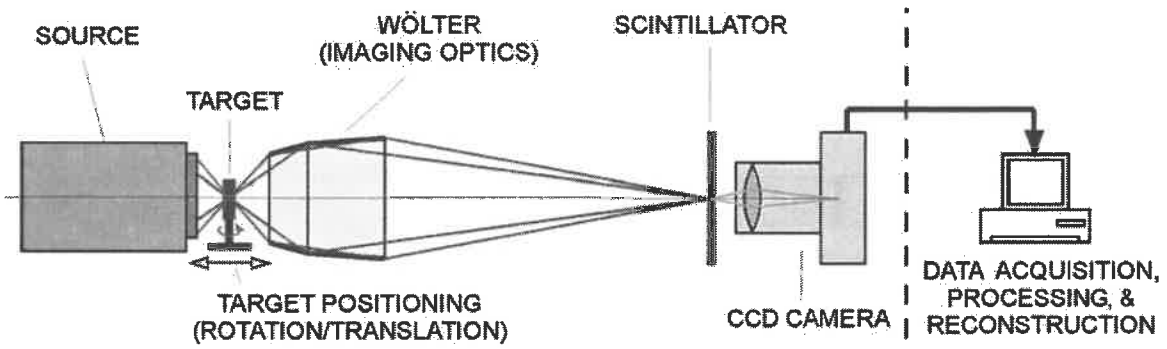


**Figure 5.** Schematic of Wölter x-ray microscope prototype. It will acquire microscope or microradiographic images using 8-keV x-rays. Its azimuthally integrated collection area has great efficiency potential that allows generation of high contrast images in a practical time frame (10's of minutes).

[2] Xradia, Concord, CA; www.xradia.com.

[3] XRT, Mulgrave,Victoria, Australia; www.xrt.com.au.

## Proton Microradiography

Ions, such as protons, in the few-to-100-MeV range lose energy continuously and predictably to matter, predominantly by electron-hole pair production. Therefore, measuring the energy loss of a beam that has traveled through the assembly provides information about the line integral of the areal electron density in the material in a single measurement (see Figure 2a). Repeating this measurement across the assembly thus provides an electron-density map of the assembly. The power of sufficiently-energetic proton beams to penetrate high-atomic-number metals, together with the potential for high-dynamic-range measurements enabled by the roughly linear energy loss mechanism in the material, makes ion beam radiography complementary to x-ray techniques, albeit at the cost of a more involved facility (Gilboy, 1995). High-resolution ion beam radiography is not offered as a commercial or near-commercial capability, however there are several institutions, mainly universities and National laboratories that have accelerator facilities.

Although the interaction of charged particle beams with matter is quite well understood (Bohr, 1913), proton radiography as a high-resolution imaging method is a more recent development (Pontau, et al 1989). In laboratories, proton beams have been used for some time to study the physics of penetration of matter by particles. Protons are useful for high spatial resolution (a few μm's) imaging, however, this method is hindered by the positional blurring of the protons (Figure 6), known as "straggling." This blurring is caused by the beam's strong interactions with the electrical charge distribution of the material through which it travels. Ion MicroTomography (IMT) (Pontau, et al. 1989) measurements were made on a direct drive inertial confinement fusion multilayered target (Antolak, et al., 1992). A focused 2-μm, 8-MeV proton beam was stepped in 0.7-μm intervals to obtain 1121 rays sums or data points per projection and 1761 projections were acquired over 360 degrees. Only 15 proton ions were obtained per ray sum and each CT slice data set required 1.5 hours to acquire. A CT slice was reconstructed and is shown in Figure 7. It is clear that the inner shell is delaminated from the target wall. A line out across the side of the target with the widest separation reveals a delamination or gap of ~ 7 μm. The total electron density is uniform across the shell wall for the slice plane shown.

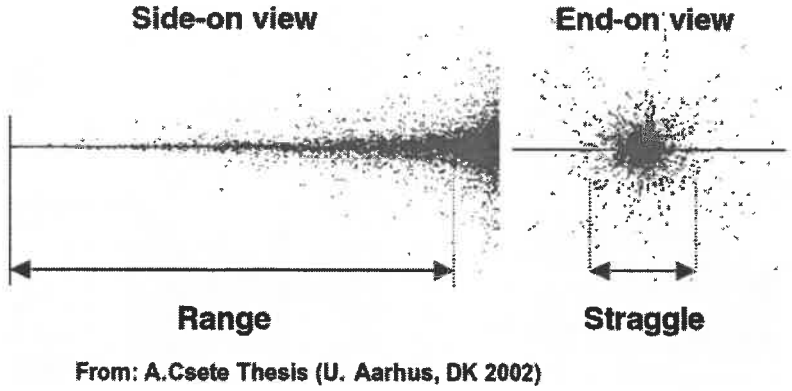


**Figure 6.** Schematic of lateral proton straggling in carbon.

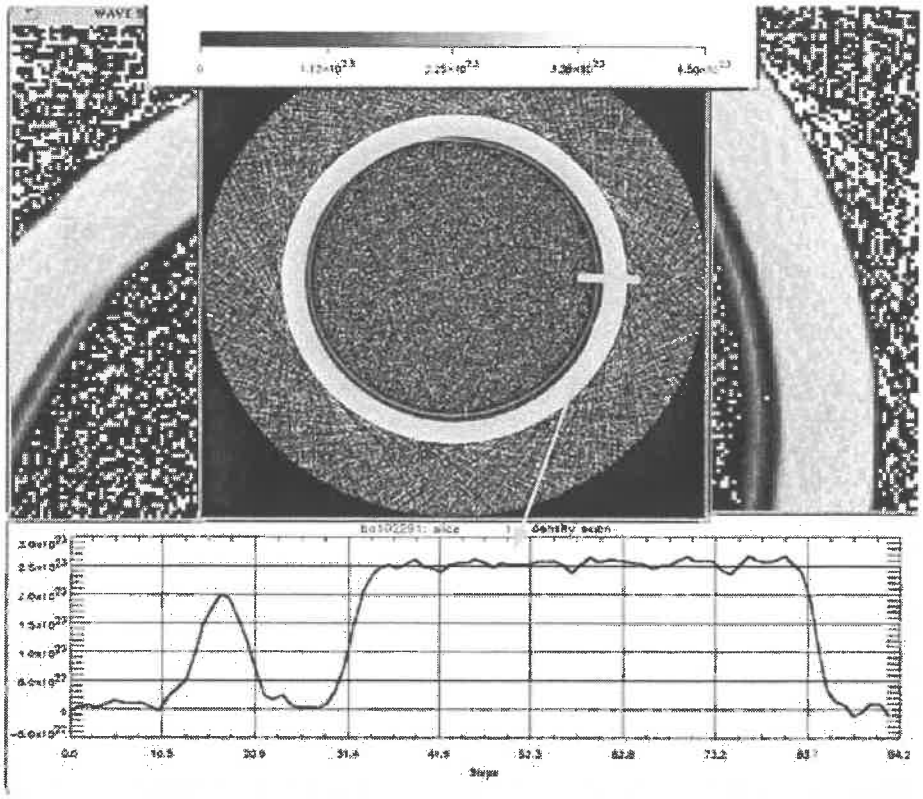

**Figure 7.** IMT slice of a direct drive inertial confinement fusion target with a delaminated inner shell flaw. A line out (shown at the bottom) is shown where the delamination is the widest. The images to the left and right are 4× enlargements of portions of the target wall showing the delamination in more detail. (*Courtesy of A. Antolak, Sandia National Laboratory, Livermore, CA.*)

A simpler concept than direct imaging by the use of a well focused proton beam (see Figure 2a) was developed even more recently by Doyle et al. (1999) and Wyss et al. (2002 and 2001), and this is the basic approach we intend to implement. This concept employs secondary electron imaging to determine the point of entry for ions impinging on samples under test. Named Ion-Electron Emission Microscopy (IEEM), it circumvents the need for focusing high-energy ions to achieve position accuracy at the micrometer level. Instead of focusing the ion beam and scanning it over the device under test, the positions of the ion impacts are determined by imaging ion-induced secondary electrons at high magnification onto a single electron position-sensitive detector as shown in Figure 8. This enables an accurate location of the proton before it enters the assembly and enables area imaging as shown in Figure 2c for protons; however, it does not overcome proton straggling. We anticipate megahertz-level counting rates that, in turn, should ultimately allow us to accumulate a radiograph of a 3-mm-by-3-mm FOV at a resolution of about one micrometer and a dynamic range of ~100:1 in ~15 min. With the IEEM method, it should eventually also be possible to extract information on chemical species by detection of characteristic x rays (Sakellariou et al., 1997; Antolak and Bench, 1994; Schofield and LeFevre, 1992).

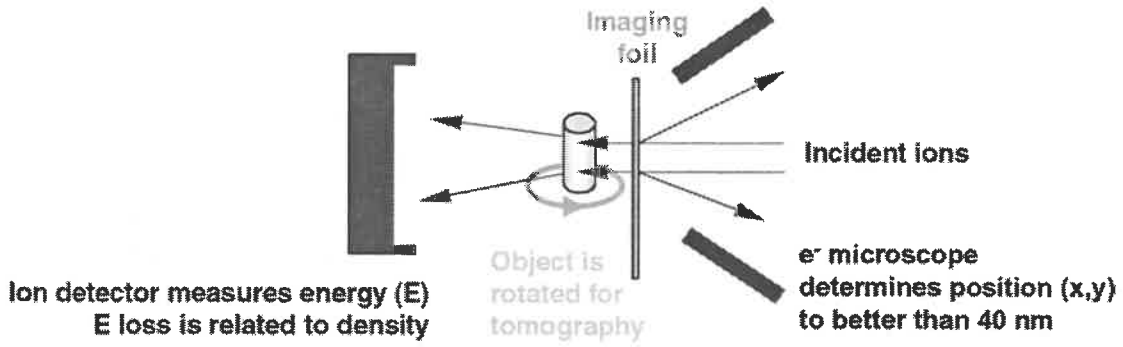


**Figure 8.** Essential components of the proposed proton microradiography prototype. Incident protons/ions (from right) strike an imaging foil, which emits secondary electrons. The electrons determine where the incident proton entered the object. The protons lose energy as they penetrate an object and their energy loss is measured in the ion detector. Signals from the entry of a proton in the foil and its subsequent energy loss are measured in coincidence.

## Acoustic Microscopy

Acoustic characterization has been in use for decades to evaluate components and materials. Most material characterization takes place in the ultrasonic frequency range, i.e., at frequencies greater than 20 kHz. Characteristics of wave propagation through a solid are determined by reflection, diffraction, or transmission by features such as defects, assembly geometry, material variations, and material attenuation. Two components contribute to material attenuation: scattering and absorption (Krautkramer and Krautkramer, 1990). Scattering accounts for the greatest portion of attenuation in solids, and is caused by material inhomogeneities such as inclusions, porosity, flaws, grain boundaries, grain orientation, and anisotropy. Absorption, resulting from the conversion of acoustic energy to heat in the material, contributes a very small part to the total attenuation in most solids.

There are three common methods of generating ultrasonic frequencies in materials: contact, immersion, and laser Ultrasonic Testing (UT). Both contact and immersion UT require coupling to the assembly by either a couplant or fluid such as water (Birks and Green, 1991), while laser UT is a noncontact method (Scruby, 1990) that does not require couplant (see Figure 9). The different frequencies and spatial resolutions achieved for each of these methods are shown in Figure 10. Immersion UT provides the best Signal-to-Noise (S/N) ratio of the three methods. However, immersion UT is limited by an assembly's geometry and its immersibility. Laser UT offers rapid, noncontact characterization of assemblies including complex geometries. Laser UT has the lowest S/N and usually requires signal processing to interpret the ultrasonic signals (Thomas et al., 1999 and Candy et al., 1999).

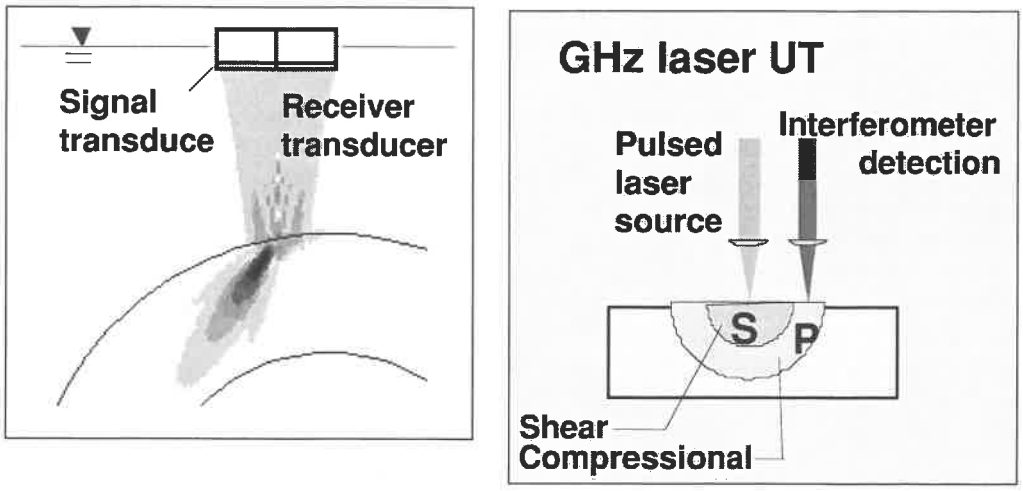


**Figure 9.** Drawing of an immersion (left) and laser (right) ultrasonic imaging set ups.

Commercial laser-based acoustic imaging systems (see Figure 10) are available at two discrete frequency ranges: 0.5–25 MHz, called laser UT[4]; and 0.1–1 THz, or femtosecond-laser UT.[5] Laser UT has insufficient spatial resolution (~0.2 mm at best) for micro/mesoscale applications. Femtosecond-laser UT has high spatial resolution (~6 nm); however, the penetration depth is inadequate for micro/mesoscale characterization (Richardson et al., 2001). The goal of this research is to achieve acoustic characterization for micrometer resolution of millimeter-sized subassemblies and features. Materials and the geometry of components used in assemblies necessitate the use of a noncontacting technique at frequencies from 100 MHz to 10 GHz. This frequency range is required to acoustically characterize features from 5 to 0.5 μm in size. At this time, laser UT in this frequency range does not exist.

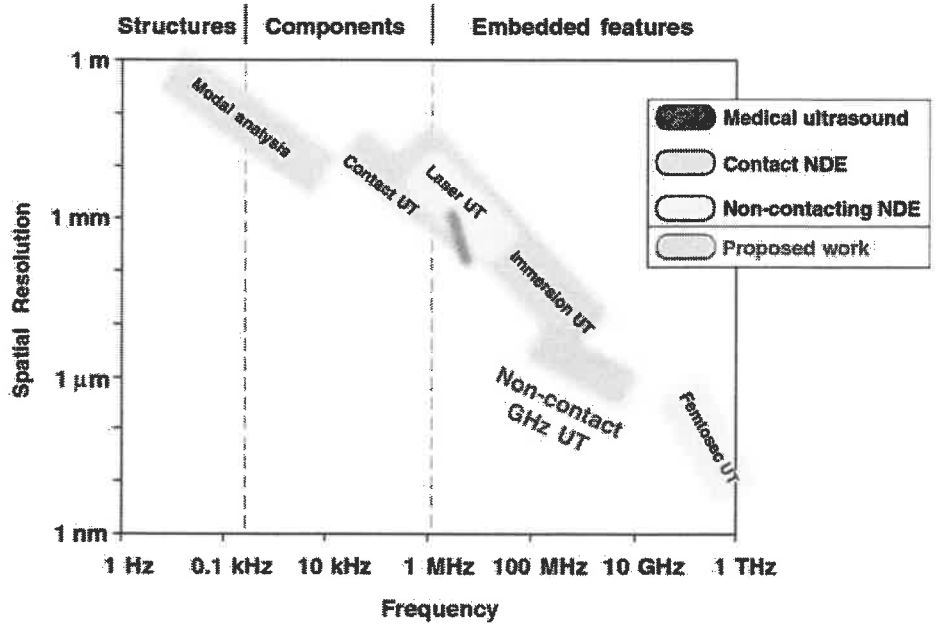


**Figure 10.** The chart shows two key parameters describing acoustic characterization, which laboratory and commercial systems exist, and what we need to research and develop, i.e., noncontact GHz UT. Also shown are relative ranges of other methods as compared to the proposed noncontact GHz laser UT method.

[4] See 'LUIS–laser ultrasound inspection system' developed by Ultraoptec, Québec, Canada; www.ultraoptec.com.

[5] See '*Meta*PULSE' developed by Rudolph Technologies, Flanders, NJ, www.rudolphtech.com/reports/tech_meta_pulse.html .

The biggest challenge for gigahertz acoustic characterization of micro/mesoscale materials is the depth of penetration. Penetration depth is determined by attenuation of the acoustic wave and is strongly dependent upon the material. For micro/mesoscale acoustic characterization, the attenuation mechanism is different for polycrystalline and amorphous materials. For polycrystalline materials, the attenuation mechanisms are understood. The polycrystalline materials acoustic characterization challenge is to detect features and structures that are on the order of the grain size. For amorphous materials, the attenuation mechanisms are not well understood. Our acoustic research will address these challenges in a three-step approach. First, we need to establish acoustic attenuation parameters at gigahertz frequencies for a variety of applicable materials, both polycrystalline and amorphous. Second, for the amorphous materials, we need to determine and understand the material attenuation mechanisms and incorporate them into existing acoustic models. Third, we need to research and develop a gigahertz laser UT prototype.

## Summary

Nondestructive characterization imaging technologies are limited in application to micro/mesoscale assemblies. At LLNL, we are researching x-ray, proton and acoustic imaging methods to characterize such assemblies with materials that vary widely in composition (low-Z to high-Z), density (~0.03 to 20 g/cm$^3$, i.e., aerogels to fully dense metals), geometry (planar to spherical), and embedded features (joints to subassemblies). Taken together, these techniques will form the basis for a new micro/mesoscale nondestructive characterization capability.

## References


Antolak, A. J., and G. S. Bench (1994), "PIXE Tomography of Samples with Inhomogeneous Elemental Composition," *Nucl. Instrum. Methods Phys. Res. Sect. B-Beam Interact. Mater. Atoms* **88**, p. 297.

Antolak, A.J., A.E. Pontau, D.H. Morse, D.L. Weirup, D.W. Heikkinen, M. Cholewa, G.S. Bench, and G.J.F. Legge, (1992), "Ion microtomography and particle induced x-ray emission analysis of directdrive inertial confinement fusion targets," J. Vac. Sci. Technol. **A 10**(4), p. 1164.

Birks, A., and R. Green, Eds. (1991), *Nondestructive Testing Handbook Vol. 7 Ultrasonic Testing*, American Society of Nondestructive Testing.

Bohr, N. (1913) "On the theory of the decrease of velocity of moving electrified particles passing through matter," *Phil. Mag.* **25**, pp.10-31.

Candy, J., R. Huber, D. Chambers, and G. Thomas (1999), "Match-field imaging of laser ultrasound using a novel correlation cancellation approach," *Journal of the Acoustical Society of America* **105** (2), p. 1252.

Doyle, B. L., G.Vizkelethy, D. S. Walsh, B. Senftinger, and M. Mellon (1999), "A New Approach to Nuclear Microscopy: the Ion-Electron Emission Microscope," *Nuc. Inst. Methods B* **158,** p. 617.

Gilboy, W.B. (1995), "Microtomography with Ionizing-Radiations," *Applied Radiation & Isotopes*, **46** (6-7), pp. 689-699.

Haddad, W. S., J. E. Trebes, D. M. Goodman, H. R. Lee, I. McNulty, E. H. Anderson, and A. O. Zalensky (1995), "Ultra High Resolution Soft X-Ray Tomography," in *Proc. SPIE Conf.*, San Diego, CA.

Hale, L. C. (1999), *Principles and Techniques for Designing Precision Machines*, Ph.D. thesis, MIT, Cambridge, MA [also Lawrence Livermore National Laboratory, Livermore, CA, UCRL-LR-133066].

Inoue, S., Y. Ogawa, K. Ueda, M. Sumiya, T. Takigawa, and S. Aoki (1989), "A Soft X-ray Microscope Using an Imaging Detector," *Japanese Journal of Applied Physics*, pp. 176-178.

Kinney, J.H., and D. L. Haupt (2002a), "Synchrotron Radiation Computed Tomography (SRCT) of Ruled Laser Targets," Lawrence Livermore National Laboratory, Livermore, CA, UCRL-ID-147653.

Krautkramer, J., and H. Krautkramer (1990), *Ultrasonic Testing of Materials* (Springer-Verlag, New York, NY).

Martz, H., C. Logan, and P. Shull (2002), "Radiology," in *Nondestructive Evaluation: Theory, Techniques, and Applications*, P. Shull, Ed., Marcel Dekker, Inc., New York, NY.

Nederbragt, W. (2002), "Wölter Instrument–Optical Design," Lawrence Livermore National Laboratory, Livermore, CA, UCRL-ID-150702.

Pontau, A. E., A. J. Antolak, D. H. Morse, A. A. Ver Berkmoes, J. M. Brase, D. W. Heikkinen, H. E. Martz, and I. D. Proctor, "Ion Microbeam Tomography," *Nucl. Instr. and Meth.*, **B40/41**(1989)646.

Richardson, C., J. Spicer, R. Huber, P. Thielen, and H. Lee (2001), "High frequency laser based NDT of extreme ultraviolet lithography masks," *Materials Evaluation* **59** (10), pp. 1223-1226.

Sakellariou, A., M. Cholewa, A. Saint, and G. J. F. Legge (1997), "Advances in 3D ion micro-tomography," *Nucl. Instrum. Methods Phys. Res. Sect. B-Beam Interact. Mater. Atoms* **1 3 0**, p. 253.

Schofield, R. M. S., and H. W. LeFevre (1992), "PIXE-STIM Microtomography — Zinc and Manganese Concentrations in a Scorpion Stinger," *Nucl. Instrum. Methods Phys. Res. Sect. B-Beam Interact. Mater. Atoms* **72**, p. 104.

Scruby, C. (1990), *Laser Ultrasonics: techniques and applications* (Adam Hilger, New York, NY).

Thomas, G., D. Chinn, R. Huber, J. Candy, and J. Spicer (1999) "Techniques for enhancing laser ultrasonic nondestructive evaluation," in *Nondestructive Evaluation Thrust Area Report*, Lawrence Livermore National Laboratory, Livermore, CA, UCRL-ID-129207.

Watanabe, N., K. Yamamoto, H. Takano, T. Ohigashi, H. Yokosuka, T. Aota, and S. Aoki (2001), "X-ray Fluorescence microtomography with a Wölter Mirror System," in *Nucl. Instr. & Meth. in Phys. Res.*, pp. 837-840.

Wyss, J., D. Bisello, A. Kaminsky, A. Magalini, M. Nigro, D. Pantano, and S. Sedhykh (2002), "The future of the SIRAD SEE facility: Ion-electron emission microscopy," *Nucl. Instrum. Methods Phys. Res. Sect. A* **476**, p. 621.

Wyss, J., D. Bisello, and D. Pantano (2001), "SIRAD: an irradiation facility at the LNL Tandem accelerator for radiation damage studies on semiconductor detectors and electronic devices and systems," *Nucl. Instrum. Methods Phys. Res. Sect. A* **462**, p. 426.

# Laser Contouring Method for Wall Thickness Metrology on OMEGA Shock Breakout Targets

R. J. Sebring[1], J. J. Bartos[1], R. D. Day[1], J. M. Edwards[1], A. Nobile[1], G. Rivera[1] and R. E, Olson[2].

1. Materials Science and Technology Division, Los Alamos National Laboratory, Los Alamos, NM 87545 2. Diagnostics and Target Physics, Sandia National Laboratory, Alb., NM. 87185

## Introduction

The National Ignition Facility (NIF) at Lawrence Livermore National Laboratory will attempt to achieve thermonuclear ignition of deuterium-tritium in approximately ten years. Ignition will be achieved by using the 1.8 MJ, 192 laser beam NIF to compress spherical targets containing deuterium-tritium fuel. An important physics issue that is being studied in experiments at the OMEGA laser facility at the University of Rochester is the manner in which laser-induced shocks propagate through target materials, and how target materials absorb and respond to x-ray radiation pulses. The Omega laser is presently the world most powerful laser with 30KJand 60 laser beams. At Los Alamos we are fabricating targets for these experiments. The metrology of these targets is a critical issue. In this paper, the unique advantages of measuring targets assembled in their ready-to fire physics targets, using dual, active confocal, lasers is described.

Because suitable technology for measuring wall thickness to the accuracy and resolution required of these mesoscale target features does not exist, our lab developed a custom contour method. In the contour method, the target is mapped at extremely high spatial density by two opposing active confocal laser displacement probes, calibrated to each other for absolute wall thickness. The probes are scanned simultaneously over both surfaces of the target, resulting in the capture of 3D surface contour and wall thickness coordinate data maps. The motion, high speed data acquisition and analysis software system has been described elsewhere [1].

## Targets

The ablator targets were copper doped beryllium (0.9 atomic %), discs, 850 μm in diameter. Three styles of targets were fabricated with electric discharge machining and measured for surface contours and wall thickness variations using the contour method. The three styles of targets fabricated were 1) flats; 25 μm thick disc (Fig. 1A), 2) single steps; 40 μm at the thin end and 80 μm at the thick end (Fig. 1B) and 3) wedges; sloped region in the center with a small flat region at both ends (Fig. 1C). The target was attached to a cylindrical gold piece called a 'halfraum' and surrounded by a ultraviolet (UV) shine shield called a 'top hat.' The assembly was mounted to a long glass fiber called a 'stalk.' Due to this assembly, the target was inaccessible to conventional contact probe stylus or triangulation based laser probes (fig. 2).

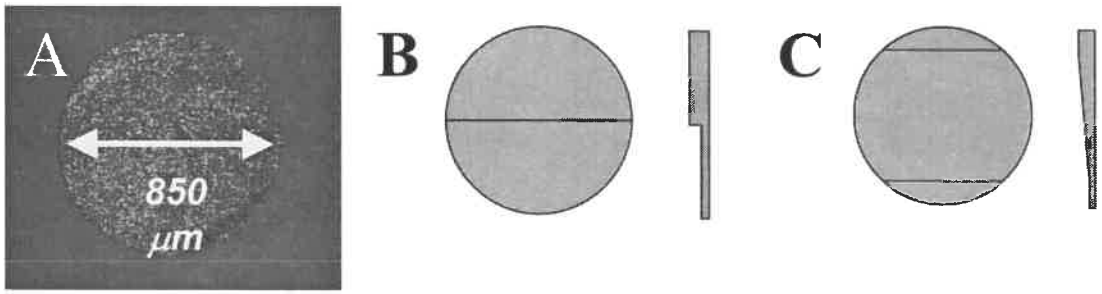


**Fig. 1:** Three styles of ablator targets were measured; A) a flat B) a step and C) a wedge

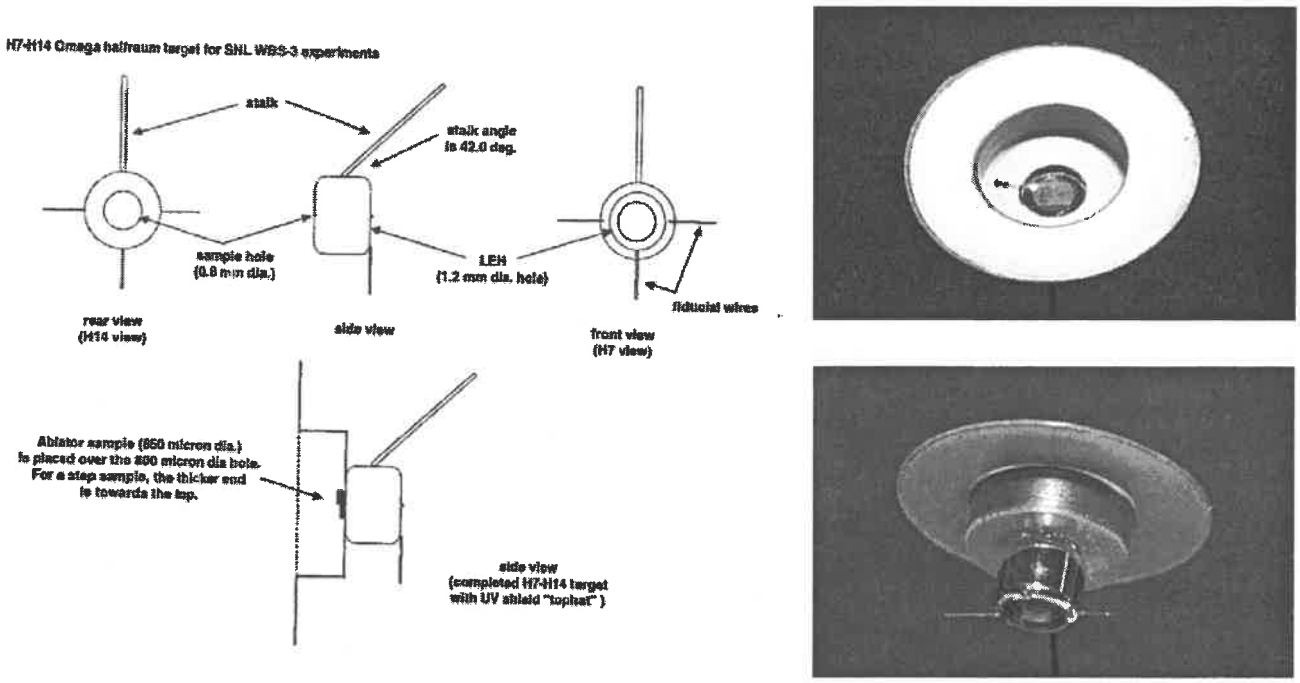
H7-H14 Omega halfraum target for SNL WSS-3 experiments
stalk
stalk angle is 42.0 deg.
sample hole (0.8 mm dia.)
LEH (1.2 mm dia. hole)
fiducial wires
rear view (H14 view)
side view
front view (H7 view)
Ablator sample (850 micron dia.) is placed over the 890 micron dia hole. For a step sample, the thicker end is towards the top.
side view (completed H7-H14 target with UV shield "topHat" )

**Fig. 2:** A line diagram and two photographs showing the placement of the ablator target relative to the halfraum, UV shield and holding stalk. The metrology challenge was to measure the contours of both sides of the target after it was assembled into this assembly.

## Measuring Apparatus

The targets were fixtured on our custom experimental measuring platform equipped with precision X and Y axes motions and high speed digital data acquisition. The motions are graphite air bearings, on round ways, mounted in a custom set of frames (Fig. 3A). Positioning is by linear motors and glass scales. The XY resolution is 100 nanometer, repeatability is ± 100 nanometers. The man/machine interface is LabView graphical programming software with Active X objects. Two opposing active laser confocal ranging probes were used to capture the part contours (Fig. 3B). These probes are commercially available and have a proven metrology record [2]. The principle of confocal is well described in the literature [3,4] and will not be described in this paper. Each probe (Keyence Corp. Model LT-8110). has a measuring range of 2 mm, a resolution of 0.2 μm, a spot size of 7 μm and a data rate of 1400 samples/sec. Data acquisition is via quadrature counters operating at 8 megahertz, and 16 bit A to D converters writing to a PC hard drive.

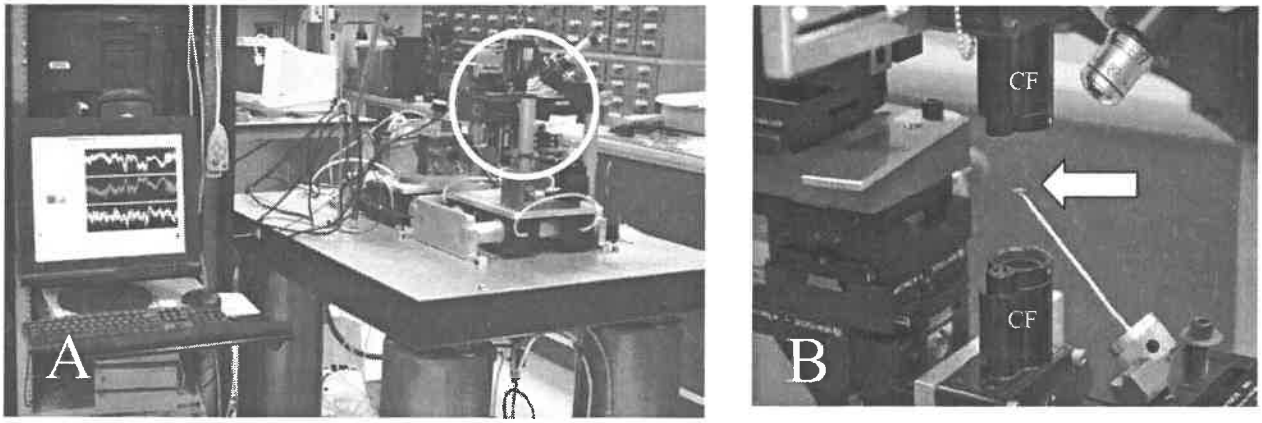


**Fig. 3:** A) The LANL custom laser contour machine mounted on an anti-vibration table and its computer for motion control and data acquisition. B) close up of machine in white circled region of Fig. 3A showing two active confocal probes (CF) configured to scan ablator target assembled in halfraum (arrow).

## Scanning

Laser active confocal probe calibration was verified for each probe using a National Institute of Standards and Technology (NIST) traceable quartz step height standard, 24.5 μm high. The two probes were carefully aligned to each other such that their optical axes were coaxial. A NIST traceable gauge block, 0.01 inch thickness, was inserted between the probes and the two opposing probes were set relative to this absolute thickness by zeroing them electronically. A motion control program was generated that created a XY raster motion over a 1.2 x 1.2 mm area. The first task the program does is to scan a 2mm length of the gauge block. This data is stored along with the target data and later used to correct the wall thickness data into an absolute thickness. The scan of the target immediately commenced following the gauge block scan. The gauge block and part were both attached to the Y axis, and moved relative to the probes at a rate of 0.2 mm/sec. while the probes remained stationary. Once a line of data 1.2 mm long is captured on the target, the probes, attached to the X axes, were stepped 0.01 mm. The whole scanning process, raster scanning and logging of data into a text file as XYZ triplets for top contour, bottom contour and wall thickness is totally automatic and takes about 15 minutes to complete. The raw coordinate data points, called clouds, were rendered and edited using reverse engineering software (Surfacer, Unigraphics Inc.) (Fig 4). A sub-section of the entire cloud, a cloud patch 150 μm wide x 860 μm long, was cut out and saved as a separate text file (Fig.5). The patch area corresponds to the exact region of the target as viewed by the diagnostic during the actual Omega shot. The 3D patch was plotted as a 2D wave, essentially collapsing the Y axis data into the X axis as a 2D plot, preserving the thickness variation data for the entire patch. A polynomial was fit to the wave and then sampled into 40 discrete, evenly spaced points. The data plot and the polynomial equation were provided to the experiment designer. The metrology was used to verify the wall thickness of the as-built target to choose the most appropriate target to shoot and assist in interpreting the post shot data.

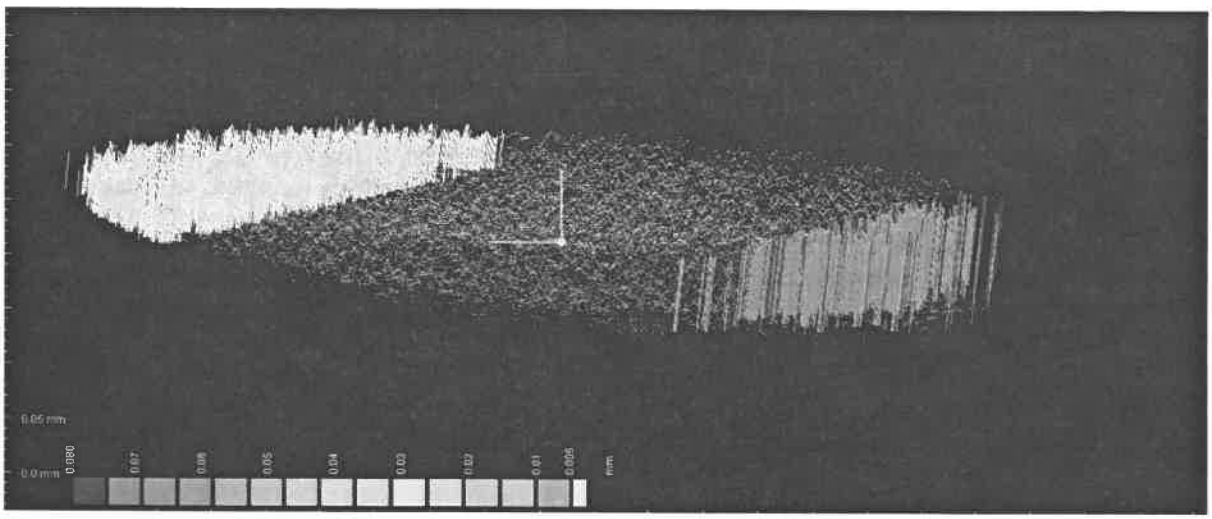

**Fig. 4**: 3D rendering of contour clouds of a wedge target. Top surface of wedge (blue colored points) and bottom surface of wedge (green colored points), lower flat region (yellow needles) and upper flat region (red needles).The needle colors and lengths represent deviations between the upper and lower surface points.

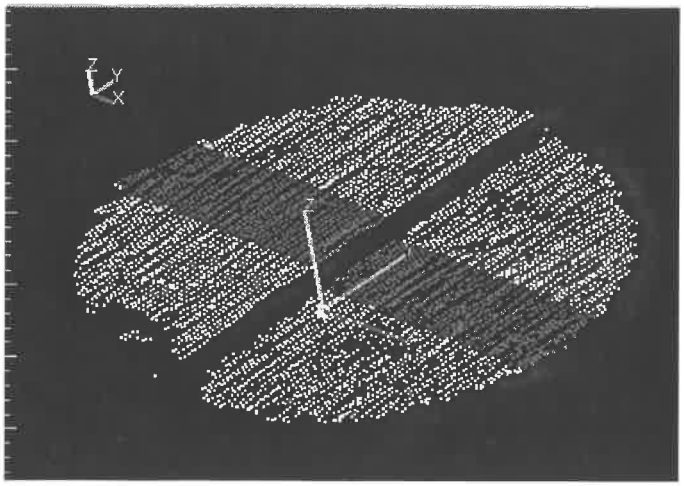

**Fig. 5:** Wall thickness cloud of ablator step target. The whole target is in white and a sub section of this cloud, a patch 15 μm wide and 850 μm long that was extracted for analysis.

## Result

Two of the three wedge shaped ablator targets, W2 and W3, varied in thickness relative to each other by about 10 microns (Fig. 6). Their wedge angles, about 4.1 degrees, were nearly identical. Their wall thickness varied considerably at the ends where the wedges were to transition into flat regions. This was more apparent for W2. Contour data from the top and bottom of the target W2 shows graphically that the majority of this unexpected wall thickness artifact is due to an uneven contour of the target's bottom surface The bottom surface is dish shaped instead of flat (Fig. 7) and would likely be caused by in the fabrication process. Even with these differences, the two targets were still within usable dimensional specifications for the experiment. But knowing the absolute wall thickness variations over the target, especially localized in the area of diagnostic interest, with this unprecedented level of detail was important to the precise interpretation of the shot breakout data. One of the three step shaped ablator targets, S1 (Fig.8 red colored line), was a few microns thinner at both the upper and lower steps but the step height was correct.

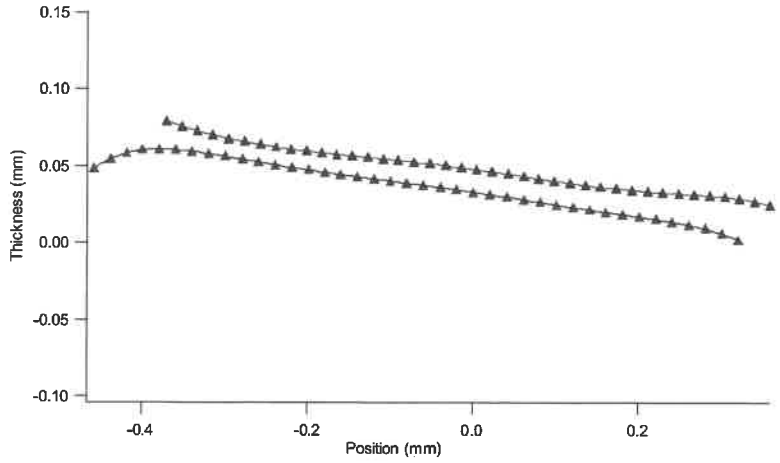


**Fig. 6:** Absolute wall thickness variation plotted as a 7th degree polynomial fit of wall thickness data with 40 discreet points along fit of ablator targets W2 and W3. These two targets are slightly different in thickness but equal in angle.

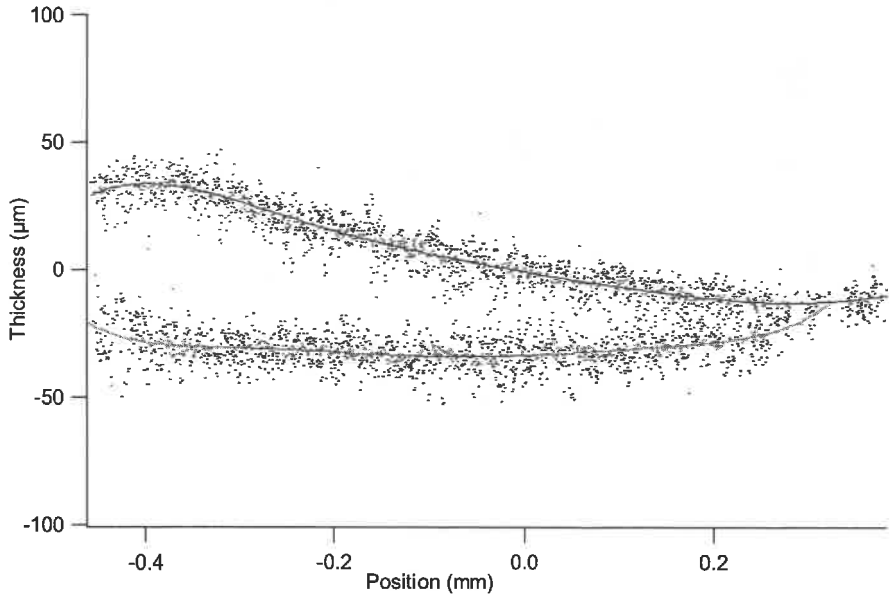


**Fig. 7** Top and bottom contour data from a 150 µm wide slice of the original 3D cloud of the entire target area. A 6th degree polynomial fit of ablator wedge target W2 is included for contour visualization purposes.

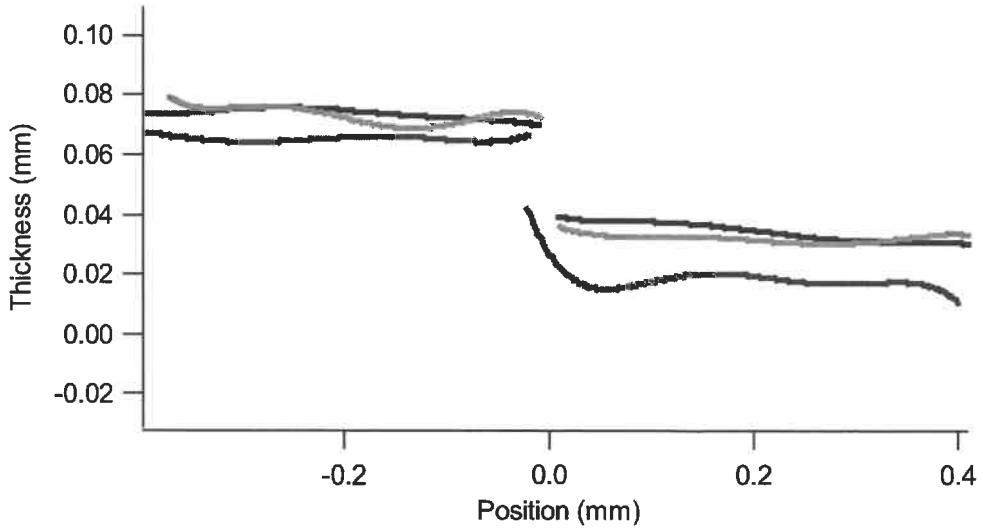


**Fig. 8** Absolute wall thickness variations plotted as a 6th degree polynomial fit of wall thickness data from 150 µm thick slice of 3 different ablator step targets. Red = S1, Blue =S2 and Green =S3 targets.

## Discussion

The primary objective of this metrology was to determine wall thickness variations in the specific area of the ablator target imaged by the ultra-violet (UV) and X-ray diagnostics during the shock breakout experiment at Omega laser in Rochester, N.Y. Step heights and wall thickness dimensions, as measured using this the contour method, varied from target to target. The results of this metrology were used to verify target dimensions, pre-select the best target assemblies, customize shot parameters for individual targets and aid in the interpretation of the shot breakout results. Prior to developing and using the contour method, wall thickness variations on these small targets could not be measured by conventional metrology. Step heights could be determined on the free standing target using a scanning white light interferometer that provided surface contour information, however the sensitive measurement for these shock breakout experiments was not step height per se but wall thickness change which can not be determined accurately by the single surface contour methods. There is also a real advantage to the experimentalist of having a full 3D record of the as-built target. Many times the shock breakout or x-ray burn though data from a highly experimental shot is not fully predicted by the design codes, so no one knows for certain whether they metrologized the target well enough to explain all the results. The ability to revisit the target and ask different dimensional questions after it was destroyed is a very powerful tool. This is an exciting new frontier in meso-metrology for fusion related physics targets.

## References

1. Sebring, R., Anderson, W., Bartos, J., Garcia, F., Randolph, B., Salazar, M. and Edwards, J. "Non-Contact Optical Three Dimensional Liner Metrology," Proc. 28th IEEE International Conference on Plasma Science and The 13th IEEE International Pulsed Power Conference, Las Vegas, NV, June 17-22, 2001, 1414-1417 (2001)

2. Kaplan, H., "Laser Gauging Enters a Submicron World," Photonics Spectra, **31** (6), 67-68 (1997).

3. Gasvik, K. J., Optical Metrology, 2nd Edition, John Wiley & Sons Ltd., Wes Sussex, England (1995).

4. Dainty, J. C., Current Trends in Optics, Academic Press Ltd., San Diego, CA (1994).

**Key words:** NIF, metrology, confocal laser, contour method, wall thickness, meso-metrology, shock

# Manufacturing of Microasperities on Thrust Surfaces using Ultraviolet Photolithography

**Kortikar, Sarang N., Stephens, Lyndon S., Hadinata, Philip C., Sirip uram, Ravinder B.**

Bearings and Seals Laboratory, Mechanical Engineering, University of Kentucky
014 RGAN Building, Lexington, KY 40506, Phone: (859) 257 6336 x 80679, Fax: (859) 257 3304

## ABSTRACT

This paper discusses the characteristics and sequences of photolithography as a means to fabricate deterministic microasperities on lubricated thrust bearing and sealing surfaces. The manufacturing process is broken down into sequences with detailed explanation for each sequence. The significance of microasperities on hydrodynamic lubrication is presented using Reynold's equation. The equation is solved using a numerical solution to find pressure distribution, load support and friction coefficient. Several aspects are discussed regarding the manufacturing process, such as human errors and difficulties in carrying out this process. Possible modifications to improve the process are also discussed.

**Keywords:** deterministic microasperities, photolithography, surface topography, hydrodynamic lubrication

## I. Introduction

Microasperities are micron-scaled protrusions and recesses on a surface that form surface roughness. The protrusions (bumps, posts) are called positive asperities, while recesses (holes) are called negative asperities. Deterministic microasperities are these surface features that have specific pattern in terms of shape, size, and spacing. This specified geometry is controllable and repeatable. Figure 1 below gives visual representation of these deterministic microasperities. The positive microasperities (Figure 1.a) were taken using SEM (scanning electron microscope), while the negative microasperities (Figure 1.b) were taken using optical microscope. These surfaces were manufactured at the University of Kentucky, Bearings and Seals Laboratory onto the end face of a thrust disc/ring.

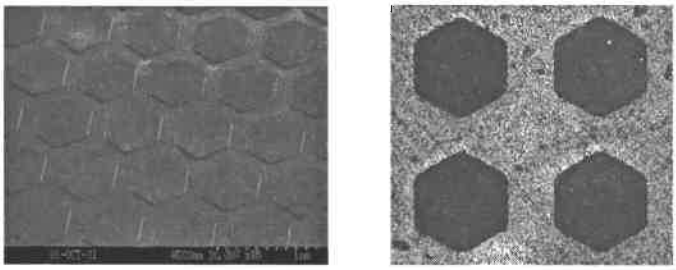

a. b.

*Figure 1: a. Positive Microasperities*
*b. Negative Microasperities*

Figure 1a. is a field of positive hexagonal microasperities in a hexagonal pattern, 15 μm tall, 165 edge-to-edge spacing and 550 μm in average diameter. Figure 1b. is a field of negative hexagonal negative asperities in a square pattern, 25 μm deep, 250 μm edge-to-edge and 600 μm in diameter. The thrust ring with asperities are tested under lubricated condition to determine their performance with hydrodynamic lubrication.

The presence of microasperities on lubricated surface has been shown to reduce friction coefficient, increase load capacity, dynamic stiffness and damping coefficients, among others. The significant increase in load support and decrease in friction coefficient in a mechanical seal had been a favorite subject for many researchers [1]-[4]. Anno, Walowit and Allen [2], in particular, stated that positive and negative microasperities produced comparable amount of load support. Negative microasperities, however, had an additional advantage to suppress leakage. Thus a suggestion to use negative microasperities to increase load capacity and prevent leakage was

presented in the paper. Etsion and Michael [4] conducted an optimization research for various parameters of the microasperities. Findlay [5] found out that microasperities could prevent leakage through "inward pumping", though this is exclusive to positive microasperities of certain geometry. It was a phenomenon which pumped the lubricant back to the center of the seal, thus keeping it from leaking out of the seal. Otto and Patterson [6], Salant and Flaherty [7] exploited this phenomenon to construct a leak-preventing elastomeric lip seal.

Microasperities fabrication also luxuriate a great deal of research and development. The manufacturing methods include laser texturing [8] and x-ray photolithography [9,10]. Stephens et.al. [10] elaborated a manufacturing process called the modified-LIGA process, which basically is the well-known LIGA process with ultraviolet (UV) light as a substitute for x-ray. The Bearing and Seals Laboratory at Mechanical Engineering, University of Kentucky has been able to engineer microasperities on mechanical seals using modified photolithography using ultraviolet light. This UV photolithography is the main subject of this paper and will be explained in detail on the next section.

## II. Manufacturing Process

Photolithography is the most widely used process of transferring geometric patterns onto the surface of a material [11]. This process is paramount in accuracy and repeatability of patterns. To date, the accuracy has been known to lie within 0.5 μm. The photolithography process is the important process in both micromachining and microelectronic fabrication, such as silicon wafer production. The authors use this process to transfer nickel patterns onto a stainless steel substrate.

The process of photolithography can be broken down into 8 sequences, as illustrated in the flowchart on Figure 2. The process differs a little for producing positive and negative asperities. The variation, as is elucidated in Table 1 and Figure 3 (similar to reference [11] with an added process of electroplating), lies in the combination of the use of mask, photoresist layer and exposure.

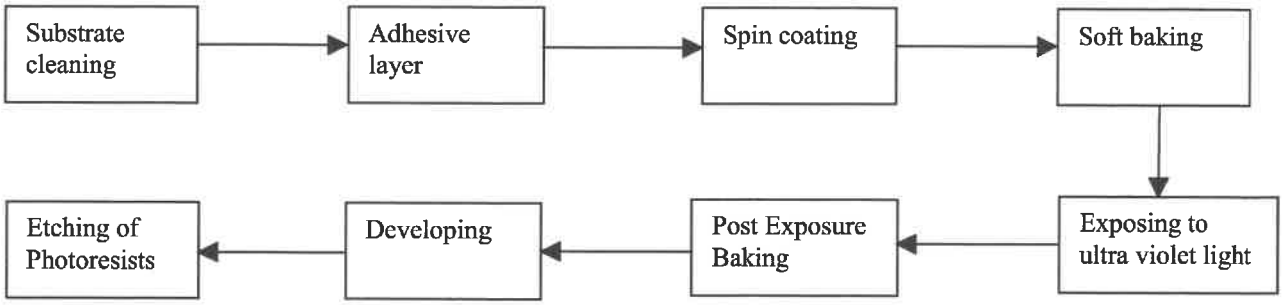


*Figure 2: Flowchart of photolithography process*

*Table 1: Chart showing the Positive and Negative asperities*

| Photoresists | Mask Type | After Developing | After Etching |
|---|---|---|---|
| Positive | Positive | Connected honeycomb grid of photoresists | Individual nickel columns (Positive Asperity) |
| Positive | Negative | Individual photoresist column | Connected grid of nickel (Negative asperity) |
| Negative | Negative | Connected honeycomb grid of photoresists | Individual nickel columns (Positive Asperity) |
| Negative* | Positive* | Individual photoresist column | Connected grid of nickel (Negative asperity) |

* Process manufactured at University of Kentucky

The first sequence in the modified photolithography process used at University of Kentucky is to clean the substrate (a stainless steel ring) using iso-propenol and acetone to get rid of contaminants such as solvent stains (methyl and isopropyl alcohol, acetone, trichloroethylene, xylene), dust, smoke particles, organic materials, ionic and metallic impurities, etc. When the substrate is cleaned, a thin layer of Microchem omnicoat® adhesive is deposited on top of the substrate. Next is the application of photoresist layer (Microchem SU8-2075®), an organic polymer sensitive to ultraviolet radiation, on top of the adhesive layer. The method to coat the substrate with the photoresist is called spin coating.

Spin coating is the most important sequence to the effectiveness of pattern transfer. This technique ensures the uniformity of the resist layer. The substrate is placed in a grappling chuck of a spinner. The photoresist solution

is dispensed on top of the substrate (at University of Kentucky, Microchem SU8-2075 is used for negative photoresist,), then the substrate is spun at the angular speed of 3000 rpm for 30 seconds to obtain 75μm thick photoresist. Such a thickness is necessary to make sure that the desired height of the asperities (10 –50 μm) is achieved after etching and lapping the final substrate.

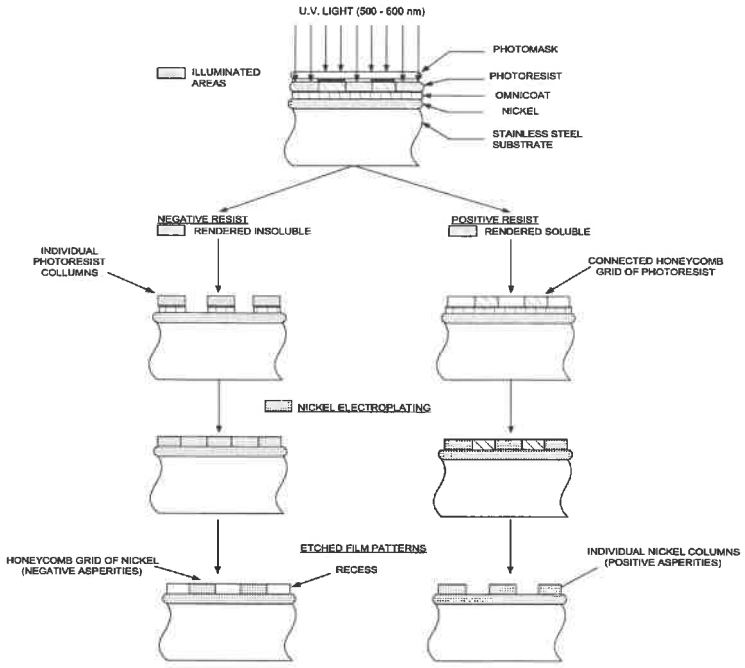


*Figure 3: Schematic diagram of contact photolithography process*

Soft baking is the process to promote adhesion of the resist layer to the substrate. This process also renders the photoresist coatings photosensitive. The substrate with photoresist is heated at 65°C for 15 minutes and 95 °C for 10 minutes. Over-soft baking (soft baking the substrate for too long) will degrade the photosensitivity of resists by either reducing the developer solubility or actually destroying a portion of the sensitizer, a photoactive compound. Under-soft baking (soft baking the substrate not long enough) will prevent light from reaching the sensitizer.

After soft baking, the photoresist-coated substrate is placed inside a MJB3 Karl Suss® mask aligner to be exposed to UV light. A mask with a desired pattern is placed between the light source and the substrate. There are three methods of exposure: contact, proximity, and projection, shown in Figure 4a. In the contact method, the photomask is in physical contact with the photoresist layer, providing very high resolution but also high wear of photomask. The substrate is exposed to UV light with wavelength 500-600 nm for 45 seconds. For the negative asperities, the photomask has a hexagonal pattern with 600μm in diameter and 250μm of equal space between cells as shown in Figure 4b. The selection of this pattern is based on the fact that hexagonal pattern has better structural stability than rectangular shape. The diameter and spacing between cells are chosen based on the friction coefficient calculation, given in Section III. This combination is the desired surface pattern, as shown in Figure 1b.

The next sequence of photolithography is post exposure baking. This step is desired for cross-linking the photoresist. The substrate is heated at 65°C for 10 minutes and 95°C for 5 minutes. After post exposure baking, the substrate is immersed in developer solution. In this process, firstly the substrate is developed using Microchem®SU8–2075 developer for 7 minutes and then substrate is developed in Microchem® Omni-coat developer for 30sec. Developing time may vary depending on the type of photoresist and speed of agitation. Hexagonal pillars of photoresist for negative asperities are generated at the end of developing process. Then a layer of nickel is deposited using electroplating on top of the photoresist. The last sequence is the removal of the photoresist called etching. The photoresist film is etched using plasma CVD (Chemical Vapor Deposition) oxygen gas used in CVD process , duration of process is 45-50 minutes but time varies depending on the thickness of photoresist film.

The result is a surface with hexagonal negative microasperities with 10.545 μm in depth and 0.256 μm of surface roughness, Figure 4b (picture taken using Zygo® Surface Texture Analyzer). Compared to the surface roughness of positive microasperities manufactured by modified-LIGA process (0.056 μm in Figure 4a), the surface roughness of UV photolithography process is somewhat bigger. A limitation of the texture analyzer is that it cannot visualize the surface texture between asperities in Figure 4a. and the surface texture at the bottom of the negative asperities in Figure 4b.

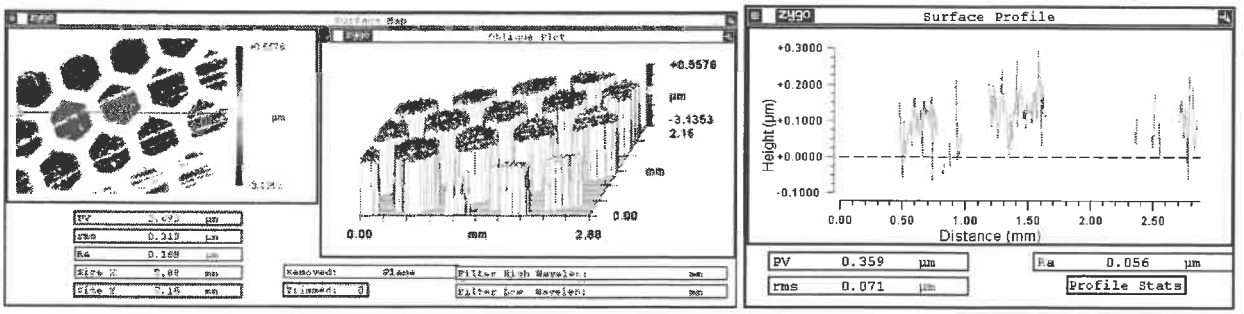


a.

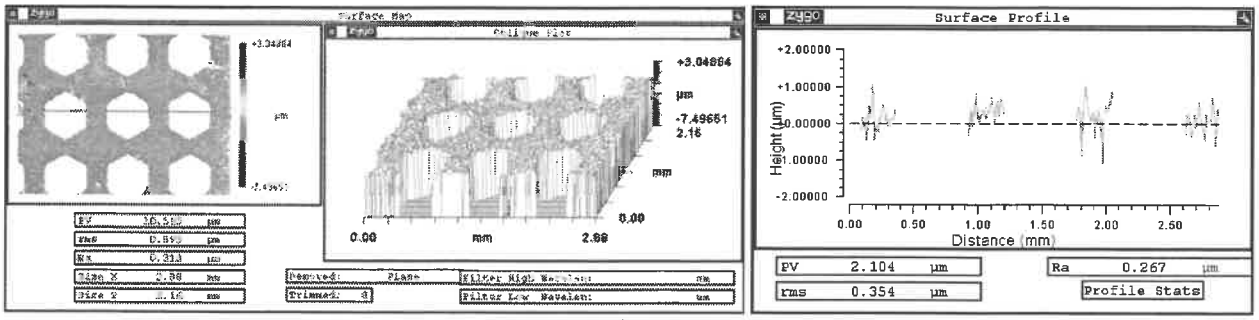


b.

*Figure 4: a. Positive microasperities with surface roughness profile*
*b. Negative microasperities with surface roughness profile*

An overall resolution of a process describes consistent ability to print a minimum size of image, a critical dimension, under condition of reasonable image of resolution, with the current manufacturing techniques. The accuracy and repeatability of patterns depends on the type and thickness of photoresist film, baking conditions, intensity of UV light, lens aberration, and mechanical stability of system. Resolution of patterns depends on swelling behavior of photoresist, thermal flow and chemical etch resistance. To increase the resolution of photolithography, shorter wavelengths must be used, since total energy incident on photoresist is a function of light source intensity, time and absorption efficiency of the exposure optics. A decrement in intensity and increment in light absorption require compensation through longer exposure dose.

## III. Effect on Lubrication

To highlight the effect of asperities on hydrodynamic lubrication, consider a slider bearing with the top slider moving with a constant velocity U. Figure 5 shows the top and side view and type of cell pattern with a square unit cell and a hexagonal asperity used for this study.

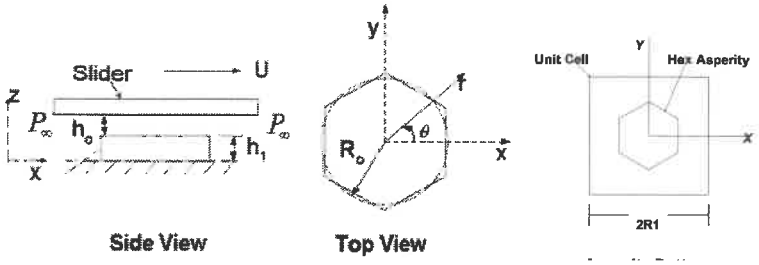

*Figure 5: Top view, side view and layout of a hexagonal slider bearing*

For a perfectly flat surface, the expression of film thickness (for the case with positive asperity) can be written as

$$h(x,y)=\begin{cases} h_o & \text{above asperity} \\ h_o + h_1 & \text{between asperities} \end{cases} \quad (1)$$

With assumptions stated in reference [8], the governing steady state Reynold's Equation for pressure distribution along the entire unit cell is given by the Poisson's Equation:

$$\frac{\partial}{\partial x}\left( h^3 \frac{\partial P}{\partial x} \right) + \frac{\partial}{\partial y}\left( h^3 \frac{\partial P}{\partial y} \right) = 6\mu U \frac{\partial h}{\partial x} \quad (2)$$

For simplicity, the boundary conditions are assumed to be zero between the asperities. Therefore,

$$P(-R_1, y) = P(R_1, y) = 0$$
$$P(x, -R_1) = P(x, R_1) = 0 \quad (3)$$

The resulting pressure distributions over a unit cell for the thrust ring sample geometry for negative asperity under full sommerfeld cavitation condition are exemplified in Figure 6a. It shows a significant drop on pressure as the lubricant flows through the recess, then an increase when the lubricant escapes the recess. Note that the pressure distribution follows the shape of the hexagonal pattern. For positive asperities, Figure 6 will be rotated 180°, because the lubricant will run into a protrusion first, as illustrated in Figure 5.

The load support for one unit cell is calculated as per the expression

$$W = \frac{1}{4R_1^2} \sum_{i=1}^{m} \sum_{j=1}^{n} P(x,y)\,dx\,dy \quad (4)$$

Coefficient of friction, in case of negative asperities is given as

$$f = \frac{\mu U}{W}\left[ \frac{(1-\delta^2)}{h_o} + \frac{\delta^2}{h_o + h_1} \right] \quad (5)$$

For full sommerfeld cavitation condition, positive and negative pressures will cancel each other, so net load support will be zero. So, for calculation of load and coefficient of friction, a cavitation condition (vaporization of dissolved gas in the lubricating fluid) other than full sommerfeld needs to be introduced during solution process. In this research, Reynold's cavitation condition is applied by replacing negative pressure with cavitation pressure (zero for simplicity) during each iteration. The result of the calculated friction coefficient under various asperity conditions is presented in Figure 6.b. It emphasizes the fact that, with proper control over asperity size and pattern, the existence of microasperities will reduce friction coefficient up to 60% [10]. The hexagonal microasperity pattern conducted using UV photolithography process has 1.34 asperities per $mm^2$ and asperity area fraction ($\delta^2$) of 0.3236. The optimal friction coefficient for this pattern is about 0.25, as is shown with the x mark on Figure 6b.

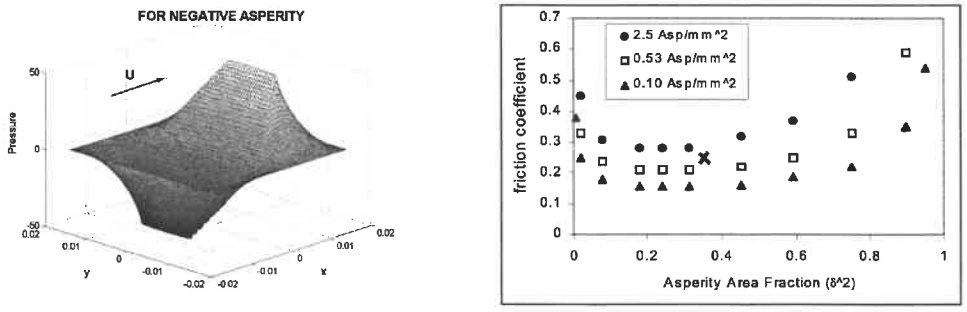


a. b.

*Figure 6: a. Full Sommerfeld pressure distribution over a unit cell of positive and negative hexagonal asperities*
*b. Theoretical Friction Coefficient under various conditions.*

## IV. Discussion

Figure 6 shows the hydrodynamic pressure distribution for one unit cell (see Figure 5). Figure 5 and Equation (1) clearly state that the film height above asperities is $h_o$, and that between asperities is $h_o+h_1$, with assumption that $h_o$ and $h_1$ are constants. In the manufacturing process, this is not always the case, especially if microasperities with very low aspect ratio are needed (such a case is in the elastomeric lip seal). The surface has

roughness, or non-deterministic asperities, so film thickness can be represented by $(h_o+\Delta h_o)$ and $(h_1+\Delta h_1)$ where $\Delta h_o$ and $\Delta h_1$ represent the random surface roughness. A problem will occur if $h_o$ or $h_1$ is in the same order as $\Delta h_o$ or $\Delta h_1$. As can be seen in Equation (2), Reynold's equation is sensitive to film height. In that case, Reynold's equation will not consider $h_o$ and $h_1$ as differences in film height, but merely as some small noise or irregularities in a flat surface. So extra attention is needed in the case of microasperities with very low aspect ratio. Lapping the surface until the desired surface roughness is achieved can reduce the surface roughness.

Another problem that might occur in manufacturing process is the flatness of the surface, i.e. $h_o$ and $h_1$ are not constants, but functions of x and y. Again, in the case of very low aspect ratio microasperities, a small changes in film height will affect the result. If the angle of deflection is large enough, Reynold's equation will see the microasperities as converging-diverging wedges, rather than step microirregularities as illustrated in Figure 5. The calculation of pressure distribution, load capacity and friction will differ significantly. This problem can be solved using lapping technique, polishing and flatness monitoring using monochromatic light to ensure a small inclination in the surface, if any, will not affect the pressure distribution, load support, and friction.

## V. Conclusions and Acknowledgment

The photolithography process is a simple and convenient method to manufacture deterministic microasperities in mechanical seal surfaces. While it offers high accuracy and resolution, it has some limitations in its sequences that will affect the result. Further research is needed to modify this method to increase the chance of fabricating good microasperites.

The authors wish to thank Dr. Kevin Kelly from Louisiana State University μSET Team for ongoing information and technical support on micro-electro-mechanical system and fabrication, particularly in photolithography process, and Mark Shaw, Technical Sales and Application Support from Microchem Inc. for giving valuable support in rectifying the technical difficulties in the process.

## VI. References

1. Hamilton, D.B.; Walowit, J.A.; Allen, C.M.; *A Theory of Lubrication by Microirregularities*, Journal of Basic Engineering, Transaction of ASME, March 1966, pp. 177 – 185.
2. Anno, J.N.; Walowit, J.A.; Allen, C.M.; *Load Support and Leakage from Miscroasperity-Lubricated Face Seals*, Journal of Basic Engineering, Transaction of ASME, October 1969, pp. 726 – 731.
3. Elrod, H.G.; *Thin Film Lubrication Theory for Newtonian Fluid with Surfaces Possessing Striated Roughness or Grooving*, Journal of Lubrication Technology, vol. 94, no. 4, 1973, pp. 484-489.
4. Etsion, I.; Michael, O.; *Enhancing Sealing and Dynamic Performance with Partially Porous Mechanical Face Seals*, STLE Tribology Transactions, Vol. 37, no. 4, 1994, pp 701-710.
5. Findlay, J.A.; *Inward Pumping in Mechanical Face Seal, Journal of Lubrication Technology*, Transaction of the ASME, July 1969.
6. Otto, Dennis L.; Paterson, Peter C.; *Wear Surface for Facilitating Lubrication of Elements in Engagement Therewith*, US Patent no. 3,572,730, March 30, 1971.
7. Salant, Richard F.; Flaherty, Andrew L.; *Elastohydrodynamic Analysis of Reverse Pumping in Rotary Lip Seals with Microasperities*, Journal of Tribology, vol 117, January 1995, pp. 53-59.
8. Etsion, I.; Burstein, L.; *A Model for Mechanical Seals with Regular Microsurface Structure*, Tribology Transaction, vol. 39, no.3, 1996, pp. 677-683.
9. Becker, E.W.; Ehrfeld, W.; Hagmann, P.; Maner, A.; Munchmeyer, D.; *Fabrication of Microstructures with Extreme Structural Heights by Synchrotron Radiation Lithography, Galvanoforming and Plastic Molding (LIGA Process)*, Microelectronic Engineering, vol. 4, 1986, pp. 35-56.
10. Stephens, L.S.; Siripuram, R.; Hayden, M.; McCartt, B.; *Deterministic Microasperities on Bearings and Seals using a Modified LIGA process*, Proceedings of ASME Turbo Expo 2002, paper number GT-2002-30289.
11. Madou, Marc; *Fundamentals of Microfabrication*, CRC Press LLC, USA 1997, pp. 1-49.

# ALUMINIDE MICROCHANNEL ARRAYS FOR HIGH-TEMPERATURE MICROREACTORS AND MICROSCALE HEAT EXCHANGERS

Brian K. Paul and Kannachai Kanlayasiri
Industrial and Manufacturing Engineering
Oregon State University
Corvallis, Oregon 97331-2407, USA

## ABSTRACT

Microtechnology-based Energy and Chemical Systems (MECS) are microsystems fabricated in engineering materials with the goal to decentralize and make portable systems such as heat pumps, chemical plants, and cytosensors. The miniaturization of MECS devices is made possible by the manifold improvement in the heat and mass transfer performance of the system due to the high surface area-to-volume ratios of the microchannel arrays within the devices. Many exothermic and endothermic chemical reactions must happen above 650 °C (e.g. gasoline steam reforming). Further, for some reaction rate-limited processes, higher temperatures are necessary to increase reaction kinetics thereby making the process mass transport-limited and a better candidate for miniaturization. For high temperature applications (above 650 °C), conventional engineering materials, such as stainless steel, are not functional. As a result, new microchannel materials, such as ceramics and intermetallic compounds, are being investigated. Microchannels produced from ceramics have faced dimensional instability problems such as sagging, porosity, and volumetric shrinkage. Among intermetallic materials, $Ni_3Al$ microchannels have been produced although the economics of the process are poor. NiAl has been investigated as another intermetallic system because of its high melting temperature and chemical inertness. However, prior investigations have found problems with warpage and device leakage. In this paper, advances in the fabrication procedure including material composition and channel metallography are reported.

Keywords: intermetallic, aluminide, microchannel arrays, high-temperature, microreactors, microscale heat exchangers

## INTRODUCTION

Microtechnology-based Energy and Chemical Systems (MECS) are meso-scale fluidic devices that rely on embedded microchannels for their function. The overall size of MECS devices places them in the mesoscopic regime, i.e. in a size range between macro objects such as automobile engines and laboratory vacuum pumps, and the intricate MEMS-based sensors that reside on a silicon chip. Thus MECS, although having micro-scale features, are large by MEMS standards straddling the size range between the macro- and micro-worlds.

The internal processes of MECS devices rely on length scales that are much smaller than traditional systems. For thermal and chemical applications, small length scales provide the benefits of high rates of heat and mass transfer, large surface-to-volume ratios, and the opportunity of operating at elevated pressures. For other applications, small dimensions imply rapid response and compact design. Because of this, MECS devices are expected to provide a number of important functions where a premium is placed on either mobility, compactness, or point application. For example, the development of miniature refrigerators could provide point cooling of high speed electronics and communication equipment for enhancing performance.[1] Also, power packs based on combustion rather than electrochemistry could extend operating times of electronic devices by a factor of ten.[2] In the area of chemical processing, miniaturized chemical reactors could provide in-situ remediation of toxic chemicals thereby eliminating the need for transport and burial.[3] Because many MECS devices rely on fluidic processes, the same technology can be applied to biological applications. Miniaturized bioreactors could provide precisely regulated environments for small groups of cells to enhance their production of therapeutic drugs or the detection of toxic compounds.

It is expected that these miniature devices can be produced in high volumes at low cost following the lead of IC devices and MEMS sensors. However, IC and MEMS manufacturing rely heavily on silicon-based processing where submicron features are routinely implemented in production. The microfluidic components in MECS

generally do not require the extremely small feature sizes available by silicon micromachining (although nanotechnology can be deployed in the deposition of engineered catalysts and nanocrystals on microreactor walls). Furthermore, for many MECS applications, silicon is not the favored base material.[4,5] It has a much higher thermal conductivity than is desired for many energy-based applications and the material, although strong, is brittle, expensive, and cannot always be tailored to specific environmental conditions. In contrast, the functionality of MECS typically require that they have the thermal, chemical, and physical properties of more traditional engineering materials such as metals or ceramics.

One subclass of MECS devices that is receiving a growing amount of research interest is high-temperature micro-heat exchangers and microreactors. Because of the environments in which these devices are used, they require materials with high melting temperatures and high-temperature corrosion resistance. A high-temperature microchannel catalytic combustor/reactor and gasoline vaporizer have been produced at Pacific Northwest National Laboratories for fuel reforming.[6] The material used in this application was type 316 stainless steel with microchannel widths on the order of 250 μm. Researchers in Germany created a microchannel heat exchanger that is used in a miniaturized reactor for the synthesis of HCN.[7] The microchannels were fabricated in stainless steel and were on the order of 60 μm wide.

Because these devices were fabricated in stainless steel, the maximum operating temperature of these devices is in the range of 550-600°C. More recently a microchannel steam reformer was produced at PNNL with combustion temperatures up to 750°C.[8] Though specific materials were not discussed, it is expected that the materials used are either superalloys or specific high-temperature stainless steel formulations. Operation above these temperatures over a sustained period of time will cause loss of device effectiveness due to either creep or corrosion. However, there exists numerous applications for microchannel devices at temperatures higher than this. Additional applications of current interest for high temperature microchannels include[9]:

- Steam superheating for driving turbines
- Hydrogen steam reforming
- Gasification of coals and heavy oils
- Flue gas desulphurisation
- Chemical, petroleum, petrochemical and metallurgical process waste heat recovery and process heating
- Incineration, especially of hazardous materials
- Domestic furnace waste recovery
- Mobile engine heat recovery

Ceramics have been identified as a possible structural material for these devices because of their very high melting temperatures, low thermal conductivity, and corrosion resistance. Some work has been conducted with the

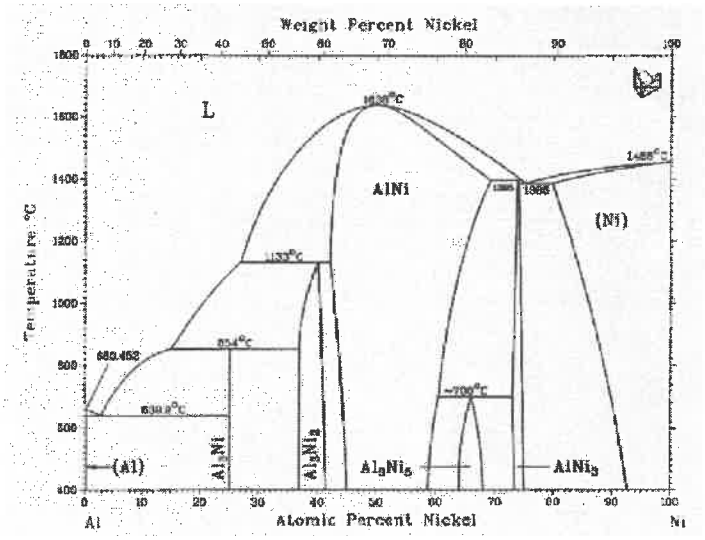


Figure 1: Nickel-Aluminum binary phase diagram.

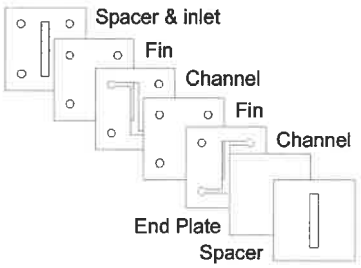


Figure 2: An exploded view of the design of the NiAl counterflow heat exchanger.

use of multi-layer ceramics to form microchannel conduits.[10] Problems with ceramics include warpage due to shrinkage during binder removal, warpage due to sagging and low fractional densities.

Another group of materials with physical properties similar to those of ceramics are intermetallics. Many intermetallics have excellent high-temperature properties.[11,12] However, like ceramics, intermetallics generally have poor formability at room temperature. Recent intermetallics research has found mechanisms to overcome these problems. Research at the Albany Research Center has shown that various intermetallics can be synthesized from elemental foils through self-propagating high-temperature synthesis (SHS) and heat treatment.[13,14] Therefore, one alternative to forming intermetallic microchannels would be to pattern the ductile elemental foils at room temperature and afterwards synthesize and bond the foils together at high temperature. This paper will present current results toward producing NiAl microchannels.

## DEVICE DESIGN AND FABRICATION

### Materials

The equilibrium binary phase diagram for the Nickel-Aluminum system is shown in **Figure 1**.[11] The non-stoichiometric NiAl phase is perhaps most desirable because of its high temperature resistance and good corrosion resistance. Although the melting temperature of NiAl is not much higher than that of Ni and $Ni_3Al$, the high temperature mechanical properties of NiAl are much better. Because of the different crystal structures (NiAl is BCC and $Ni_3Al$ is FCC), the two intermetallics have quite different mechanical and physical properties. NiAl has a higher melting point, a substantially lower density, and a higher Young's modulus than $Ni_3Al$. In addition NiAl has excellent oxidation and sulfidation resistance at high temperatures. The thermal conductivity of NiAl as compared to other NiAl intermetallics is on the higher side, where as the coefficient of thermal expansion is lower than that of other NiAl intermetallics. In general, the properties of NiAl are most desirable for most high-temperature MECS applications.

### Experimental

To evaluate the new fabrication procedure, a counter flow microchannel design was implemented as shown in **Figure 2**. Laminae were cut from a 63.5 μm thick NiAl foil. The new microlamination procedure involved blank tacking, conversion to intermetallic, laminae patterning, registration, and diffusion bonding. This procedure is

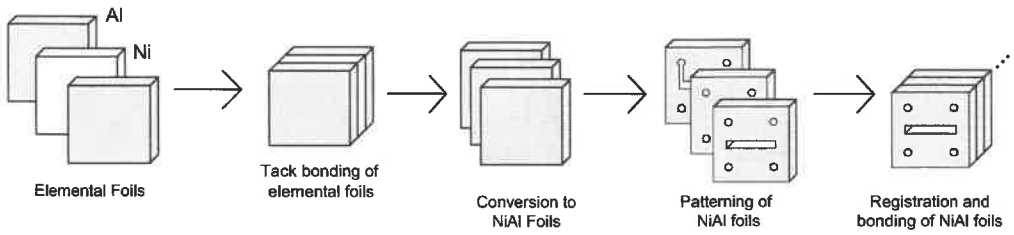


Figure 3: Illustration of the microlamination procedure used to produce an NiAl intermetallic heat exchanger.

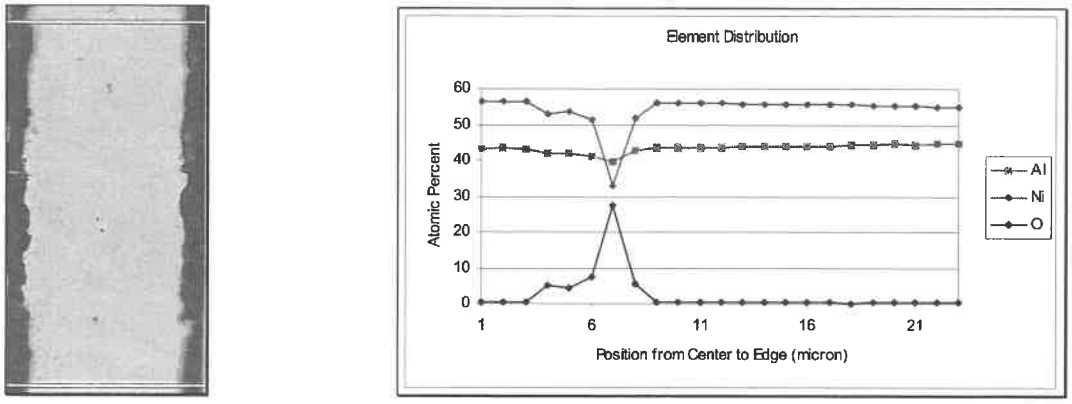


a) b)

Figure 4: a) Fully developed NiAl foil (annealed at 1000° C for 15 hr), nominal thickness of the foils is 63.5 microns. b) Wavelength dispersive spectrograph showing the composition of Al, Ni, and O in the NiAl foil. The anomaly in the graph indicates the presence of an oxide inclusion.

diagrammed in **Figure 3**. A composite blank consisting of one Ni blank sandwiched by two Al blanks was produced by low-temperature tack bonding in a vacuum hot press at 500°C and 1000 psi for 15 minutes. The blank laminae were produced using nominally 19 μm thick Al foil and 25.4 μm thick Ni foil. The blanks were cleaned using acetone, then acid soap to remove native oxides. Conversion to intermetallic involved reactive diffusion synthesis and heat treating of the tack-bonded stack of patterned laminae in a vacuum hot press, resulting in a homogeneous intermetallic structure. **Figure 4a and 4b** show homogenized NiAl foil and its corresponding element distribution, respectively. It was found that after 15 hours, the elemental foils had completely converted to intermetallic. At the start of the experiment, very little was known about the machinability and weldability of the foils. An ESI 4420 Laser Micromachining System with a 266 nm UV laser rail was used to pattern the blanks. Optical microscopy of the foils after patterning revealed no cracking in the regions immediately adjacent to the cut. Laminae registration was accomplished prior to bonding by adhesive tack bonding laminae in an edge registration fixture. Diffusion bonding of the laminae was achieved in a vacuum hot press at elevated temperature and pressure. Samples were fixtured between two graphite platens with bonding pressures ranging between 1000 and 4000 psi heated at a rate of 10°C per minute to a temperature between 600 and 1000°C in atmospheric gases at $3 \cdot 10^{-4}$ torr. Samples were held at this temperature for between 10 and 15 hours to ensure that the intermetallic foils would bond.

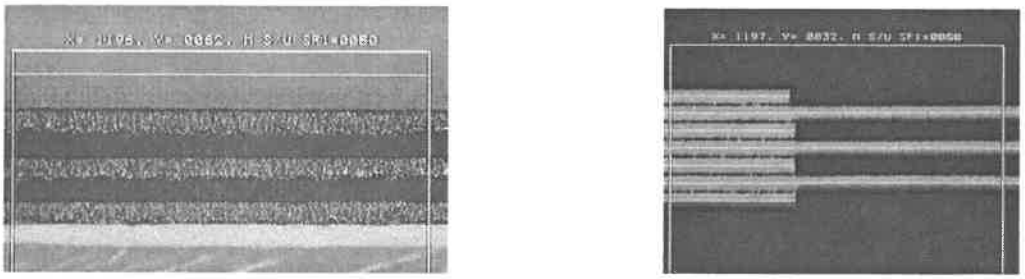

a) b)

Figure 5: a) Two 100:1 aspect ratio microchannels (~125 micron channel height) formed between three alternating NiAl fins (bonding conditions: 600 °C, 1000 psi, 10 hr) . This demonstrates the ability to control dimensions (eliminate warpage) on the fins of the microchannel array. b) Micrograph showing voids on the bond interface causing leakage.

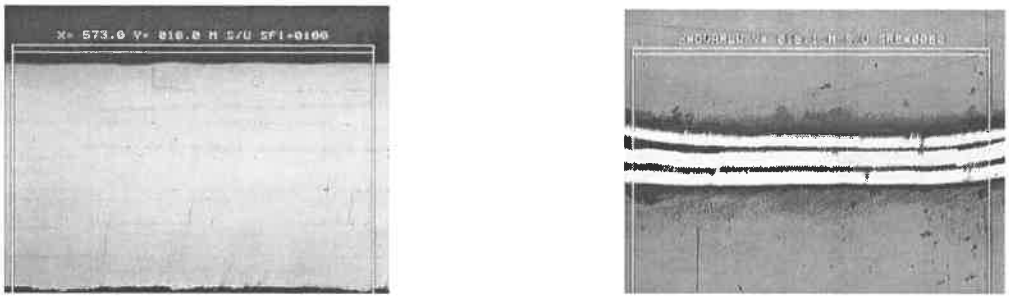

a) b)

Figure 6: a) Bonding results from diffusion bonding at 1000 °C, 4000 psi, for 15 hrs. This demonstrates the ability to diffusion bond NiAl foils. b) NiAl microchannels formed under identical conditions.

## RESULTS AND SUMMARY

Experimental results show that warpage-free NiAl microchannel structures can be produced by this fabrication method. Micrographs of the fabricated NiAl devices are shown in **Figure 5 and 6**. Stability of the intermetallic fins was obtained by using this new fabrication approach. **Figure 6a** shows a cross-section of a set of diffusion bonded laminae demonstrating some level of bond quality. Small voids at the lamina interfaces were observed. Further development is needed to ensure leak-tight bonding.

The work presented here demonstrates recent progress in the development of a more economical microlamination procedure for forming high-temperature, intermetallic microchannel devices. At low bonding pressures, the microlamination procedure using NiAl foils was found to provide good dimensional stability with large voids on the bond interface (**Figure 5a and 5b**). At high bonding pressures, voids were minimized with large fin deflection (**Figure 6b**). Future work is needed to refine the joining method for NiAl to produce leak-free microchannels while maintaining dimensional stability.

## REFERENCES


[1] Little, W. A., "Microminiature Refrigerators for Joule-Thomson Cooling of Electronic Chips and Devices," *Advances in Cryogenic Engineering*, (Vol. 35, 1990), pp. 1325-1333.

[2] Benson, R. S. and J.W. Ponton, , "Process Miniaturization- A Route To Total Environmental Acceptability?" *Trans. IChemE*, (Vol. 71, Part A, 1993), pp.160-168.

[3] Koeneman, P. B., I. J. Busch-Vishniac, and K. L. Wood, "Feasibility of Micro Power Supplies for MEMS," *J. MicroElectoMechanical Sys*, (Vol. 6(4), 1997), pp. 355-362.

[4] Peterson, R.B. "Size Limits for Regenerative Heat Engines," *Microscale Thermophysical Engineering*, (Vol. 2, 1998), pp. 121-131.

[5] Peterson, R.B, "Numerical Modeling of Conduction Effects in Microscale Counterflow Heat Exchangers," *Microscale Thermophysical Engineering*, (Vol. 3, 1999), pp. 17-30.

[6] Matson, D. W., P. Martin, D. Stewart, A. Tonkovich, M. White, J. Zilka, and G. Roberts, "Fabrication of Microchannel Chemical Reactors Using a Metal Lamination Process," *Proc. IMRET3,* (April, Frankfurt, Germany, 1999).

[7] Hessel V., W. Ehrfeld, K. Golbig, Ch. Hoffmann, H. Lowe, and M. Storz, "High temperature HCN generation in a complex integrated micro-reaction system," *Proc. IMRET3*, (April, Frankfurt, Germany, 1999).

[8] Whyatt, G.A., C.M. Fischer and J.M. Davis, "Progress on the Development of a Microchannel Steam Reformer for Automotive Applications," *Proc. IMRET6*, (March, New Orleans, 2002).

[9] Chaumat, G. F. Moret, and A. Gasse, "SiC brazing for ceramic heat exchangers," *DVS-Berichte*, (Vol. 166, 1995), pp-217-219.

[10] Kim, M., Yi, M. Zhong, J., Bau, H.H., Hu, H. and Ananthasuresh, S.G.K., "The Fabrication of Flow Conduits in Ceramic Tapes and the Measurement of Fluid Flow through These Conduits," *Proceedings of the ASME Dynamic Systems and Controls Division*, DSC- (Vol. 66, 1998), 171-177.

[11] Brandes, E.A. and Brook, G.B. (Ed.), *Smithells metals reference book*, 1992, 7th edition.

[12] Golberg, D., Demura, M. and Hirano, T., "Effects of Al-rich off-stoichiometry on the yield stress of binary Ni3Al single crystals," *Acta materialia*, 1998, 46: 2695-2703.

[13] Alman, D.E. and Dogan, C.P., "Intermetallic Sheets Synthesized from Elemental Ti, Al, and Nb Foils," *Metallurgical and Materials Transactions A*, (26A, October, 1995), 2759-62.

[14] Alman, D.E. "Fabrication, Structure and Properties of Aluminum-Aluminide Layered Composites," *Mat. Res. Soc. Proc.*, 1996, 434: 255-260.